The parameter space and signals of axions

Thesis submitted in accordance with the requirements of the University of Liverpool for the degree of Doctor in Philosophy by **Horia Petru Nicolaescu**

March 2023

Abstract

The QCD axion provides one of the best motivated solutions to the Strong CP problem of the Standard Model. Meanwhile, axion like particles appear as part of many high energy theories and could play a role in solving various puzzles of cosmology and particle physics. In particular, owing to their small couplings and their non-thermal production mechanisms, the QCD axion and axion like particles are robust candidates for cold dark matter and have been the subject of extensive research and experimental search effort.

I start by reviewing the motivation for axions and their phenomenology. I explain why an important aspect is the axion inflationary scenario, either pre- or post-inflationary, related to the time when the global $U(1)$ PQ symmetry that gives rise to the axion was last spontaneously broken. I study a precise way to separate these scenarios, characterising them based on the density of axion strings: the post-inflationary scenario corresponds to large string density at the time when the axion mass becomes relevant and domain walls form which result in the network collapsing immediately after, while the pre-inflationary scenario corresponds to negligibly low strings and domain walls density having re-entered until today. An intermediate scenario when the string network re-enters the horizon and is destroyed after the axion mass becomes relevant but before today is uncovered, and I estimate the corresponding axion abundance and discuss phenomenological consequences. Meanwhile, numerical simulations are used to find a relation between string density and the probability distribution of the radial mode over regions that have re-entered the horizon, which can be related to the size of quantum fluctuations during inflation. This allows to predict the evolution of the string density up until a value sufficient to collapse the network and estimate the time when the network would be destroyed, which prescribes the inflationary scenario. Additionally, I discuss alternative ways to restore the PQ symmetry even when quantum fluctuations are small, which can similarly result in the post-inflationary scenario, and in some cases the intermediate scenario.

I also explain how the spectrum of gravitational waves emitted by axion string networks in the post-inflationary scenario can be derived by combining effective field theory analysis with numerical simulations. The spectrum is used to determine when such axions would be detectable by gravitational waves detectors. Various constraints on axion like particles that could result in observable gravitational waves are considered. As a result axion like particles in the post-inflationary scenario with symmetry breaking scales in the range $10^{14} \div 10^{15}\,\text{GeV}$ and masses $10^{-28} \div 10^{-18}\,\text{eV}$ lead to gravitational waves observable by next generation detectors, both pulsar timing arrays and space-based interferometers, while being compatible with constraints from dark radiation, dark matter overproduction and isocurvature. I discuss the conditions under which axions with such high symmetry breaking scales can be in the post-inflationary scenario.

Declaration

The work presented in this thesis is primarily mine and I have cited the work of others where it has been used. Some of the thesis is based on papers written together with collaborators, which is noted here and in the main body of the thesis.

Chapter 4 is based on work done in collaboration with Dr Marco Gorghetto and Dr Edward Hardy and which will be the subject of a future publication. The computer code used to perform the numerical simulations in this chapter has been provided by my collaborators.

Parts of Chapter 5 follow the relevant sections of [1] which I have written in collaboration with Dr Marco Gorghetto and Dr Edward Hardy.

Chapter 6 closely follows the same paper [1] which I have written in collaboration with Dr Marco Gorghetto and Dr Edward Hardy.

I declare that the thesis has not been submitted in whole or in part for any degree or qualification at any other University or institution.

Horia Petru Nicolaescu

Acknowledgements

I would like to thank my supervisor, Dr Edward Hardy, for his support and guidance over the years of my PhD. I am grateful for the opportunity as well as the time he has given me. I appreciate his patience and calmness, which has often times helped me get over my various worries. I am also thankful for the extensive feedback he provided over versions of my thesis as well as his advice regarding time management, without which I would have severely underestimated the time required to finish my thesis.

I would also like to thank my office mates Ben, Flavio and Jamie for helping me accommodate in my first year as a fresh PhD student.

Finally I would like to thank my parents and my brother for support over the years.

Contents

Chapter 1

Introduction

1.1 The Standard Model of Particle Physics

The Standard Model of Particle Physics (in short the Standard Model or SM) describes all directly observed matter and three of the four fundamental forces affecting it, that is the electromagnetic, weak and strong forces. It is a Lorentz invariant renormalisable quantum field theory (QFT) based on the gauge group $SU(3) \bigotimes SU(2)_L \bigotimes U(1)_Y$, where the $SU(3)$ gauge group corresponds to the strong force which is described by what is known as Quantum Chromodynamics (QCD) [2–4], and $SU(2)_L \bigotimes U(1)_Y$ to the weak force and electromagnetic forces which are unified in the Glashow, Salam, Weinberg model [5–7] and are spontaneously broken down to the residual symmetry $SU(2)_L \bigotimes U(1)_Y \to U(1)_{\mathrm{EM}}$. The SM Lagrangian contains renormalisable terms[1] which obey the underlying symmetries. These are the gauge symmetry and Lorentz symmetry, which has combined CPT conservation (charge conjugation+parity transformation+time reversal) as a consequence [9]. However, charge conjugation (C) i.e. that the action is invariant under replacement of particles by antiparticles, parity (P) i.e. that the action is invariant under the flipping of the sign of an odd number of spatial dimensions and time reversal (T) i.e. the action is invariant under the flipping of the sign of the time dimension, are not imposed individually. Terms in the SM Lagrangian can be broken into four types:

- Kinetic terms corresponding to the gauge bosons that mediate the various interactions: photons for electromagnetic, W^-, W^+ and Z bosons for the weak interaction and eight gluons for the strong interactions. These terms look like $-(1/4)X_{\mu\nu}X^{\mu\nu}$ where $X_{\mu\nu}$ is replaced by the field strengths corresponding to the various interactions. These terms conserve CP.
- Dirac terms of the form $i\overline{\psi}\not{D}\psi$, where $\not{D}$ is the covariant derivative, for each of the fermions in the SM. These terms conserve CP.

[1] In $d = 4$ dimensions operators up to mass dimension 4 are renormalisable [8].

- Kinetic $(D_\mu\phi)^\dagger(D_\mu\phi)$ and potential $-\mu_\phi^2(\phi^\dagger\phi) + \lambda_\phi(\phi^\dagger\phi)^2$ terms for the Higgs boson ϕ. The Higgs is a spin 0 scalar that is charged under the weak interaction, but not the strong or electromagnetic interactions. These terms conserve CP.

- Yukawa terms $-Y_\psi\overline{\psi}_L\psi_R\phi$ for each of the fermions with the exception of neutrinos. These terms describe the fermions' ψ interactions with the Higgs boson and are responsible for giving fermions Dirac mass upon electroweak symmetry breaking [10–12]. These terms violate P and CP if there are complex phases in the Yukawa matrices, which has been observed experimentally [13–18].

Fermions of the SM are split into quarks and leptons. Quarks carry color charge of one of three colors and are thus subject to the strong force. For this reason quarks cannot generally be observed as free states, at temperatures lower than about $\Lambda_{\mathrm{QCD}} \simeq 200\,\mathrm{MeV}$ they are bound together into composite particles called hadrons, either mesons which are a quark/antiquark pairs, or baryons which are made up of three quarks or antiquarks[2]. There are in total six quark flavours which are grouped in three generations, each generation containing a quark of electric charge $2/3\,e$: the up, charm and top quarks, as well as a quark of electric charge $-1/3\,e$: the down, strange and bottom quarks. The weak interaction allows quarks to change flavour: from a quark with charge $-1/3\,e$ to any other quark of charge $2/3\,e$ by emitting a W^- boson and vice versa by emitting a W^+ boson, and this is responsible for the eventual decay of second of third generation quarks into the lighter first generation quarks. The transitions between various quarks are parametrised by the Cabibbo-Kobayashi-Maskawa (CKM) matrix.

Leptons on the other hand do not carry color charge so they are unaffected by the strong interaction, at least at tree level. They similarly also come in six flavours grouped into three generations, each generation containing one electrically charged particle: electron, muon and tau, and a corresponding neutrino which does not carry electric charge. Leptons can also change flavours via the weak interactions: a charged lepton can decay into a charged lepton and a neutrino of different flavour plus an antineutrino of the original flavour.

All fermions in the Standard Model except neutrinos come in two chiralities, either left-handed or right-handed, with only left-handed fermions interacting through the weak force. Fermion masses are generated through the Yukawa terms above containing left and right-handed fermions once the Higgs acquires a non-zero Vev [10–12]. For this reason neutrinos are exactly massless in the Standard Model, as there are no right-handed neutrinos and thus no corresponding Yukawa terms coupling to the Higgs.

Other than the residual gauge symmetry $SU(3)\bigotimes U(1)_{\mathrm{EM}}$ and the associated electric charge and color charge which are conserved, there are additional accidental symmetries in the Standard Model and correspondingly conserved quantities. These arise as a result of the truncation of the Lagrangian down to renormalizable terms and are expected to be broken once higher dimension

[2] In the following, quantities expressed in units of eV are understood to be in natural units for which $c = \hbar = k_B = 1$.

operators are introduced. Examples for these include the baryon number $U(1)_B$, the lepton number $U(1)_L$ and more specifically the lepton number of each generation.

Finally the Standard Model can be tested for experimentally and the various parameters can be measured, such as the gauge couplings, the masses of various particles and the CKM matrix, Higgs mass and self-coupling (see [19] for recent values). There has been extensive evidence for the SM such as the prediction of the existence of the Higgs boson, charm and top quarks, the prediction of the masses of $W^{\pm}$ and Z bosons, the branching ratios of Z boson's decays into fermion pairs, the agreement between the predicted and measured anomalous electron dipole moment to high precision. While the SM agrees well with particle accelerator experiments, there are various hints to physics beyond the Standard Model, coming for example from various patterns and fine tuning problems within the Standard Model or from cosmology.

1.1.1 Hints of physics beyond the Standard Model

- The discovery of neutrino oscillations [20, 21] points to a violation of the accidental lepton flavour symmetry as well as non-zero masses for neutrinos. This accidental symmetry is violated by non-renomalizable dimension five operators of the form $Z_{i,j}\phi\phi\nu_i\nu_j$ which allow for Majorana masses for the neutrinos once the Higgs acquires a Vev. Extensions of the SM to include heavy right handed neutrinos and a Higgs triplet can elegantly explain the smallness of SM neutrino masses [22–28]. Similarly models for which the neutrino acquires a Dirac mass have been considered [29, 30].

- The current best cosmological model requires that the majority of matter in the Universe is non-baryonic, which cannot be explained by the SM. This additional matter is called Dark Matter (DM) and there is extensive cosmological and astrophysical evidence for its existence, which is discussed in the next Section on the ΛCDM model, together with a few candidates for DM.

- Similarly, cosmological observations point to the Universe being filled with a substance with negative pressure called Dark Energy (DE). One explanation for this could be a scalar field stuck in a relatively flat region of its potential, which is very similar to the inflation which is discussed in Section 1.3. However no such scalar or otherwise an explanation for DE is available in the SM. Alternatively, it could be the zero-point (vacuum) energy density, however a standard calculation shows that this energy is UV divergent [31] which is typically resolved by introducing a UV cut-off M. The zero-point energy density in this case is expected to be of the order $\rho_\Lambda \sim M^4$, however natural cut-offs such as the Planck scale $M \sim 10^{18}\,\text{GeV}$ or the GUT scale $M \sim 10^{16}\,\text{GeV}$ or even the mass scale of the heaviest Standard Model particles $M \sim 100\,\text{GeV}$ lead to a disastrously large prediction, which is away from the observed value of the cosmological constant by anywhere from 56 orders of magnitude for the Standard Model

scale and up to the infamous 120 orders of magnitude for the Planck scale, which is known as the cosmological constant problem.

- As I explain in Section 1.3 the inflationary paradigm is well-established in cosmology. One of the ways this could be achieved is through the presence of at least one scalar field, the inflaton, which has decayed in the early Universe to produce the SM matter. However, the only such scalar available in the SM is the Higgs, whose self-coupling λ_ϕ is too large for it to be the inflaton while providing the right amplitude of the spectrum of primordial density perturbations. Therefore some extensions are required to allow the Higgs to be the inflaton, the minimum one being a non-minimal coupling to gravity (see [32] for a review on Higgs inflation). Alternatively, the inflationary paradigm would require the addition of at least one scalar field to the SM.

- The SM provides no explanation for the gauge group $SU(3) \bigotimes SU(2) \bigotimes U(1)$ and in particular why the electromagnetic and weak interactions are unified while the strong interactions are not. Grand Unified Theories (GUTs) have been proposed to also unify the strong interaction above a large energy scale $\Lambda_{\rm GUT} \simeq 10^{16}\,$GeV and these theories are based on larger symmetry groups such as $SU(5)$ [33] or $SO(10)$ [34].

- The SM as a quantum theory describes three out of the four fundamental forces, with gravity being described by General Relativity, which is a classical theory. Extensive research is dedicated to finding the quantum theory of gravity, with many candidates being proposed (see [35] for a recent review). Ideally such a theory would unify all four fundamental forces.

- The SM provides no explanation why there are three generations of fermions and also why the masses of successive generations differ by large factors. An interesting observation is that these factors are approximately powers of the so-called Cabibbo angle $|V_{us}| \simeq 0.225$, a coincidence known as the flavour puzzle. An attractive solution is the Froggatt-Nielsen mechanism [36] which involves the introduction of an additional flavour symmetry G_F fermions are charged under, such that renormalizable Yukawa couplings are forbidden for fermions other then the top quark. Effective Yukawa couplings for fermions are then generated by non-renormalizable couplings of the form $(\chi/\Lambda_F)^{a_L+b_R}\overline{\psi}_L\psi_R\phi$, where χ is a new scalar called the flavon, which acquires a Vev upon spontaneous breaking of the symmetry G_F at a scale Λ_F between the electro-weak and the Planck scale, while a_L, b_R are quantum numbers associated with the left and right chiralities of the fermions. This way Yukawa couplings are approximately powers of $\langle\chi\rangle/\Lambda_F$ which explains the flavour puzzle.

- The baryon and lepton number conservation means that the today matter/antimatter asymmetry must be the result of the asymmetry in the initial conditions. This is however not a very attractive explanation, particularly as the initial matter/antimatter asymmetry must

have been extremely small but not zero before they annihilated to leave only the remaining matter. Additionally this is incompatible with the inflationary paradigm, since inflation is supposed to dilute the initial matter density to a negligible amount, with matter in our Universe being the result of the decay of the inflaton. A more attractive solution is that the asymmetry is generated by interactions, which requires the well-known Sakharov conditions [37] that the responsible interactions violate baryon and lepton number conservation, C and CP and that they happen outside of thermal equilibrium. If any of these conditions does not hold the rate at which matter and anti-matter is produced are equal and thus no asymmetry can be created. The CP violating terms in the SM are however insufficient to produce the matter/antimatter asymmetry [38, 39], so this explanation requires extension of the SM to contain additional CP violation as well as baryon number violation.

- An additional CP-violating term can be written in the SM Lagrangian and is consistent with the symmetries of the model:

$$\mathcal{L} \supset \frac{\theta_{\text{QCD}} g_s^2}{64\pi^2} \epsilon^{\mu\nu\alpha\beta} G^a_{\mu\nu} G^a_{\alpha\beta} \,. \tag{1.1}$$

  While this term turns out to be a total derivative it ends affecting the physics due to the anomalous axial symmetry, and in particular can be probed be the neutron's electric dipole moment (nEDM). The vanishing of the nEDM constitutes a fine tuning problem for the parameter θ_{QCD} known as the Strong CP problem. I discuss the Strong CP problem and the QCD axion solution in more detail in Chapter 2.

- Treating the SM as an effective field theory, the mass squared of the Higgs boson receives quantum corrections for each fermion and boson it couples with. For example at leading order for a fermion the correction is of the form:

$$\delta m_\phi^2 \sim -g_{\phi,f}^2 \Lambda_{\text{UV}}^2 \,, \tag{1.2}$$

  where Λ_{UV} is some UV cut-off at which we would expect new physics to show up. However such a correction for a natural coupling $g_{\phi,f} \simeq \mathcal{O}(1)$ dominates over the measured mass of the Higgs boson $m_\phi \simeq 125\,\text{GeV}$ unless the cut-off is $\Lambda_{\text{UV}} \lesssim \mathcal{O}(1\,\text{TeV})$ which is smaller than the energy scale accessible by the LHC. This means that quantum corrections to the Higgs potential must somehow cancel to a high degree of accuracy, which constitutes a fine tuning problem called the hierarchy problem. Among the solutions proposed for this is Supersymmetry, which would ensure an exact canceling between the negative corrections from fermions and positive corrections from bosons.

1.2 The post-inflationary ΛCDM Universe

Meanwhile, the cosmological evolution of the Universe appears well described by the ΛCDM model, which is the simplest model that explains the observed abundance of light elements, the spectrum of temperature anisotropies in the Cosmic Microwave Background data, and the observed accelerated expansion of the Universe. It is based on General Relativity, which is currently the best description of gravity available, and the cosmological principle which states that the Universe is homogeneous and isotropic over large scales. The cosmological principle reduces the metric to the standard Friedmann-Robertson-Walker (FRW) form [40–42], in comoving polar coordinates (r, θ, ϕ):

$$ds^2 = dt^2 - R(t)^2 \left(\frac{dr^2}{1 - kr^2} + r^2(d\theta^2 + \sin^2\theta d\phi^2) \right) , \tag{1.3}$$

where $R(t)$ denotes the scale factor of the Universe, k parametrises the geometric curvature of the Universe, with $k > 0$ corresponding to a closed Universe and $k < 0$ to an open Universe. The standard General Relativity treatment of extracting the Christoffel connection, the Riemann tensor and the Ricci scalar from the FRW metric can be applied (see [43] for an introduction to General Relativity), resulting in the Friedmann equations:

$$3M_P^2 H^2 = \rho - \frac{3kM_P^2}{R^2} + M_P^2 \Lambda \, , \tag{1.4}$$

$$\frac{\ddot{R}}{R} = -\frac{1}{6M_P^2}(\rho + 3P) + \frac{\Lambda}{3} \, , \tag{1.5}$$

where the Hubble parameter is defined as $H = \dot{R}/R$, P is the pressure, M_P is the reduced Planck mass $M_P = \sqrt{8\pi G} \simeq 2.4 \times 10^{18}$ GeV and Λ is the cosmological constant. The Friedmann equation is sometimes divided by the critical energy density today $\rho_c = 3M_P^2 H_0^2$ to give:

$$\Omega_r(t) + \Omega_m(t) + \Omega_k(t) + \Omega_\Lambda(t) = E(t) = \frac{H^2}{H_0^2} \, , \tag{1.6}$$

which makes clear the various relative contributions: radiation $\Omega_r = \rho_r/(3H_0^2 M_P^2)$, matter $\Omega_m = \rho_m/(3H_0^2 M_P^2)$, geometric curvature $\Omega_k = -k/(H_0^2 R^2)$ and cosmological constant $\Omega_\Lambda = \Lambda/(3H_0^2)$ to the energy budget today $E(t_0) = 1$ and in the following I denote quantities today by the subscript 0. The cosmological constant term is required to be positive since observations show $\ddot{R} > 0$ today, however for ordinary matter and radiation the pressure is positive, thus either a positive cosmological constant or an additional unknown component with negative pressure is required in the Universe. Since each of these components evolves differently in time with $\Omega_r \sim R(t)^{-4}$, $\Omega_m \sim R(t)^{-3}$, $\Omega_k \sim R(t)^{-2}$ and Ω_Λ is constant, a naive expectation is that each of these components have dominated the energy budget of the Universe in this order. Under this expectation the history of the Universe can be summarised as follows.

After the end of inflation and subsequent reheating, which are discussed shortly in Section 1.3, the Universe is radiation dominated with the SM particles in thermodynamic equilibrium at a large temperature. Relatively light degrees of freedom $m \lesssim T$ are relativistic and having equal production and annihilation rates. Once the temperature decreases below their mass, they become heavy and their production is inhibited by their mass, so their equilibrium density quickly decreases due to the annihilation. Eventually when their annihilation rate falls below the Hubble parameter they freeze out and are no longer in equilibrium, even then they continue to decay if they are unstable, which is the case for most SM particles. Thus, as the Universe cools down SM particles successively become massive, annihilate as well as decay into lighter particles, culminating with electron/positron annihilation. The remaining SM matter today is primarily made up of stable particles (protons, neutrons inside nuclei and electrons) which survived annihilation with their antiparticles due to the matter/antimatter asymmetry, which is expected to have been generated by some dynamical mechanism.

Additionally, as the Universe cools down the energy of radiation becomes smaller than the binding energy of nuclei, allowing protons and neutrons to form them. This way the light nuclei (deuterium d, tritium t, helium ^{3}He and ^{4}He and lithium ^{7}Li) are produced, which is called Big Bang Nucleosynthesis (BBN), as opposed to heavier nuclei which are produced inside stars much later in the cosmological history. At temperatures below about 1 MeV the rate of interactions that turn protons into neutrons such as $p + e^- \leftrightarrow n + \nu_e$ becomes smaller than the Hubble rate, which fixes the ratio between protons and neutron at subsequent times, apart from the neutron decays. From here on the neutrons are expected to fuse with protons to form nuclei through a couple interaction chains, however both these chains require the initial production of deuterium: $p + n \to d + \gamma$ which is broken down even at temperatures significantly below the deuterium binding energy $\simeq 2\,\text{MeV}$ due to the high photon to baryon ratio. The formation of deuterium becomes possible at temperatures below $\mathcal{O}(0.05 \div 0.1)\,\text{MeV}$ and from here on formation of heavier nuclei proceeds through:

$$d + d \to {}^3\text{He} + n \qquad {}^3\text{He} + d \to {}^4\text{He} + p\,, \tag{1.7}$$

and

$$d + d \to t + p \qquad t + d \to {}^4\text{He} + n\,, \tag{1.8}$$

until the point where the temperature is too small to allow for nuclear fusion. Finally, lithium is produced by either

$${}^4\text{He} + t \to {}^7\text{Li} + \gamma\,, \tag{1.9}$$

or

$${}^3\text{He} + {}^4\text{He} \to {}^7\text{Be} \qquad {}^7\text{Be} + e^- \to {}^7\text{Li} + \nu_e\,, \tag{1.10}$$

and heavier nuclei are difficult to be produced at this stage due to the lack of stable nuclei of atomic mass 5 or 8.

After BBN the Universe continues to cool until eventually the temperature becomes of the order of the binding energy of hydrogen atoms. At this time protons and electrons bound into atoms, and from here on the photons are allowed to travel freely through the Universe. This is called recombination, or last scattering and is the source of the Cosmic Microwave Background (CMB). At later times no more energy is transferred into radiation and matter eventually comes to dominate the energy density of the Universe, since its energy density dilutes slower with the expansion of the Universe than that of radiation. Under gravitational attraction matter finally forms the galaxies and stars present in the Universe today, which in the literature is called structure formation.

Since its discovery, the CMB has become one of the most important tools to study cosmology, as it allows for very precise determination of various cosmological parameters. This is done by considering the pattern of the baryonic acoustic peaks in the CMB temperature power spectrum, which are caused by acoustic oscillations of the baryon/photon fluid at times before recombination. The position and relative amplitude of acoustic peaks can be used to determine the various components that appear in the Friedmann equation (1.6) as well as the density of baryonic matter. In particular the third acoustic peak is sensitive to the total density of matter Ω_m, the second acoustic peak to the density of baryonic matter Ω_b, these together with the position of the first peak determine the curvature and cosmological constants Ω_k and Ω_Λ respectively (see [44] for a review). The latest result are $\Omega_m(t_0) \simeq 0.3$, $\Omega_b(t_0) \simeq 0.05$, $\Omega_k(t_0) \lesssim 0.01$, $\Omega_\Lambda(t_0) \simeq 0.7$ [45]. Thus the Universe today is dominated by the cosmological constant, which has the associated problem of being too small as discussed in Section 1.1.1, or alternatively by Dark Energy, an unknown substance with a peculiar equation of state $P_{\rm DE}/\rho_{\rm DE} < -1/3$. Either way, the exact reason for the acceleration of our Universe remains an open question and is subject to intensive research.

On the other hand, there exist another puzzle related to the density of matter. The CMB is used to determine the density of baryonic matter $\Omega_b(t_0) \sim 0.05$ much smaller than the total density of matter $\Omega_m(t_0) \sim 0.3$. Additionally, the majority of baryonic matter today, and definitely all the baryonic matter at the age of recombination, is expected to come from light nuclei which have formed through BBN (such as helium), rather than heavy nuclei which formed inside stars at much later times. The BBN prediction of the baryonic matter density is consistent with the CMB determination of the baryonic matter density [46–49], which confirms that the vast majority of matter is not baryonic. This additional matter is called Dark Matter (DM), since it should have very weak coupling to radiation (and baryonic matter) in order to have evaded direct detection. The baryonic acoustic peaks could differentiate between dark and baryonic matter due to the vastly different strengths of coupling to radiation, since the baryons travel together with photons and encounter the gravitational potential generated by dark matter, which is allowed to cluster due to its vanishing couplings to radiation (and baryonic matter).

Additional evidence for DM comes from astrophysics, such as the average velocity of galaxies in the Coma cluster [50], rotation of spiral galaxies [51–53], large scale structure, gravitational lensing [54]. An in depth review of the history of DM as well as additional references can be found

in [55]. Simulations of "hot" versus "cold" dark matter further show that dark matter must be dominantly cold to explain the scale structure of the Universe [56–59], point being that if dark matter has too large velocities it would be unable to cluster under the effect of gravity in a way consistent to the observed structure of the Universe. In fact a lower bound is placed on the mass of "hot" dark matter particles in thermal equilibrium $\gtrsim 1\,\mathrm{keV}$ [60], while an upper bound on the masses of neutrinos is $m_\nu \lesssim \mathcal{O}(\,\mathrm{eV})$ [61]. For this reason Standard Model left-handed neutrinos do not make a good candidate to explain Dark Matter [57]; similarly to Dark Energy its origin lies beyond the Standard Model. However, the addition of heavier right-handed neutrinos could avoid this bound [62].

Perhaps the most well-known candidates for DM are weakly interacting massive particles (WIMPs), which constitute a large class of potential candidates from various beyond the Standard Model theories such as the lightest supersymmetric partner in the case of supersymmetric theories [63, 64] or light Kaluza-Klein particles in theories with extra dimensions [65]. These have in common the fact that they are either produced thermally or from decays of heavier particles which are themselves produced thermally[3] [66]. The main attractive feature of WIMPs is the observation that assuming weak scale interactions their freeze-out abundance is at the same level as the dark matter density [67], a coincidence dubbed the "WIMP miracle" for typical masses of the order of 100 GeV, while being predicted by theories that attempt to simultaneously solve the hierarchy problem and the unification of the strong and electroweak forces. The direct detection attempts for WIMPs have so far been inconclusive, see [68] for a recent review of the direct detection bounds, while the lack of evidence for weak scale Supersymmetry from the Large Hadron Collider has somewhat weakened the motivation for WIMPs. However, reasonably natural supersymmetric models could have evaded detection by the Large Hadron Collider [69] and there is still parameter space to be explored by direct detection.

Axion like particles (ALPs) are another class of well motivated candidates for DM. The main representative is the QCD axion, which was initially proposed as a solution to the Strong CP problem [70–76]. It involves the introduction of an additional $U(1)$ symmetry, the so-called Peccei-Quinn (PQ) symmetry, which is spontaneously broken at a high energy scale and the QCD axion is its associated pseudo Nambu-Goldstone bosons (PNGB). The QCD axion is made to couple to the topological charge $\epsilon^{\mu\nu\alpha\beta}G^a_{\mu\nu}G^a_{\alpha\beta}$ in such a way that it effectively turns the fixed parameter θ_{QCD} into a dynamic one, which then relaxes to the value that minimizes the energy $\theta_{\mathrm{QCD}} = 0$. It also turns out that axion like particles (ALPs) are numerous in string theory [77–83], with some potential candidates for the QCD axion [4] These ALPs are generically very weakly interacting with matter and radiation and are primarily produced non-thermally with relatively low momentum, as explained in more detail in Chapter 2. For this reason, axions behave as cold matter even while being very light, thus avoiding the bounds on hot DM mentioned above. Additionally more

[3] The later are called superWIMPs.

[4] Many of these string theory ALPs are not associated to a $U(1)$ symmetry in the 4D effective theory.

complex models have been suggested in which the QCD axion contributes to solving various other puzzles such as the hierarchy problem [84], the asymmetry between the abundances of baryons and antibaryons [85–89], the smallness of neutrino masses [87, 89], the flavour puzzle [90]. For these reasons ALPs and in particular the QCD axion are subject to extensive study as well as experimental attempts to detect them.

1.3 Inflation

There are two final puzzles of the ΛCDM model I would like to discuss, the so-called flatness and horizon problems, which are somehow related in that they are both concerned with the way the Universe expands in the radiation and matter domination eras. The flatness problem has to do with the surprisingly small geometric curvature of the Universe $\Omega_k(t_0) = -k/(H_0 R_0)^2 < 0.01$, which is exacerbated by the fact that in the past the curvature $\sim 1/(R^2H^2)$ was much smaller since during both radiation and matter domination the product RH decreases with time[5]. The horizon problem has to do with the extreme homogeneity of the CMB across the sky, since the fact that the size of the causal horizon increases faster than comoving length means our observable Universe today contains a large number of causal patches at the time of recombination, which have no reason to have the same temperature. Since both of these problems have a similar cause in the behaviour of RH during matter and radiation domination, they share a common solution: the inflationary paradigm [91–93]. The idea is that if sometime in the past the expansion of the Universe was accelerated and this period of so-called inflation lasted for sufficiently long, then it would solve both of these problems: in the case of flatness starting from any arbitrary curvature inflation would bring the curvature to a very small value which then increases during radiation and matter domination up to the (still small) value today, while for the horizon problem the entire Universe observable today could have been in causal contact during inflation.

A minimum condition for inflation is that the expansion of the Universe is accelerated $\ddot{R} > 0$, which requires that the Universe was dominated by some substance with similar properties to Dark Energy. The main differences to Dark Energy is that we know inflaton must have lasted for long enough to solve the horizon and flatness problem, which typically in the literature is written in term of the minimum number of e-folds $N_{\rm tot}$ that the Universe has been inflated for, while having a mechanism to eventually end, at which point the energy must transfer into radiation to allow for the standard cosmology.

To estimate the number of e-folds of inflation necessary to solve the horizon problem, notice that it is sufficient if one region the size of the causal horizon at the time $N_{\rm tot}$ e-folds before the end of inflation expanded into a region larger than the causal horizon until today. This is written

[5]The observed curvature breaks the naive expectation of a period of curvature domination between matter and cosmological constant.

simply:

$$\frac{e^{N_{\rm tot}}}{H_I}\frac{R_0}{R_I} \gtrsim \frac{1}{H_0}\,, \tag{1.11}$$

where R_I denotes the scale factor at the end of inflation. Assuming instant reheating and comoving entropy density conservation, R_0/R_I can be estimated leading to:

$$e^{N_{\rm tot}} \gtrsim \frac{H_I}{H_0}\frac{T_0}{T_{\rm RH}}\left(\frac{g_\star(T_0)}{g_\star(T_{\rm RH})}\right)^{1/3} \simeq \frac{T_0}{H_0}\sqrt{\frac{H_I}{M_P}}\left(\frac{\pi^2}{90}\right)^{1/4}\frac{g_\star(T_0)^{1/3}}{g_\star(T_{\rm RH})^{1/12}}\,, \tag{1.12}$$

where $T_{\rm RH}$ denotes the reheating temperature and $g_\star(T)$ the effective number of relativistic degrees of freedom at temperature T. The number of e-folds of inflation sufficient to solve the horizon problem is then:

$$N_{\rm tot} \gtrsim \log\left(\frac{T_0}{H_0}\right) - \frac{1}{2}\log\left(\frac{M_P}{H_I}\right) \gtrsim 60.6\,, \tag{1.13}$$

where H_I was replaced by its maximum value $H_I \lesssim 4.2\times 10^{13}\,\text{GeV}$ discussed bellow.

Similarly for the flatness problem notice that

$$\frac{\Omega_k(t_{\rm inf})}{\Omega_k(t_0)} = e^{2N_{\rm tot}}\left(\frac{R_0H_0}{R_IH_I}\right)^2\,, \tag{1.14}$$

where $\Omega_k(t_{\rm inf})$ describes the curvature $N_{\rm tot}$ e-folds before the end of inflation. Assuming at this time $\Omega_k(t_{\rm inf}) \sim \mathcal{O}(1)$ a similar condition to (1.11) is sufficient to solve the flatness problem as is for the horizon problem.

Some of the earliest proposals for inflation [93] involved a single scalar field φ, now called the inflaton, which initially starts with a value far away from the minimum of its potential, giving it a large potential energy which dominates the energy density of the Universe. In this case the energy density and pressure are respectively:

$$\rho_\varphi = \frac{1}{2}\dot\varphi^2 + V_\varphi\,, \tag{1.15}$$

$$P_\varphi = \frac{1}{2}\dot\varphi^2 - V_\varphi\,, \tag{1.16}$$

so from equation (1.5) it can be seen that the expansion of the Universe is accelerated if $\dot\varphi^2 < V_\varphi$ and the potential of the inflaton dominates the total energy density. The equation of motion for the inflaton reads:

$$\ddot\varphi + 3H\dot\varphi + \frac{dV_\varphi}{d\varphi} = 0\,. \tag{1.17}$$

Towards the end of inflation the acceleration $\ddot R$ is approaching 0. It can be shown from the inflaton's equation of motion together with the Friedman equation (1.4) as well as the condition that the expansion is still accelerated $\ddot R \gtrsim 0 \leftrightarrow \dot H + H^2 > 0$ that close to the end of inflation the term $3H\dot\varphi$

dominates over $\ddot{\varphi}$ in the inflaton's equation of motion, which becomes:

$$3H\dot{\varphi} \simeq -\frac{dV_\varphi}{d\varphi}\,. \tag{1.18}$$

The conditions that inflation is maintaned can be written in terms of the slow-roll parameters ϵ, η defined as:

$$\epsilon \equiv -\frac{\dot{H}}{H^2} = \frac{1}{2}M_P^2\left(\frac{V'}{V}\right)^2 < 1\,, \tag{1.19}$$

$$\eta \equiv M_P^2\frac{V''}{V} < 1\,. \tag{1.20}$$

These describe the slope of the potential and consequently how slowly the field φ and the energy density evolve in the region that inflation is happening. In the limit $\epsilon, \eta \to 0$ the Universe expands exponentially $R \sim e^{Ht}$ with a constant H, so the size of the causal horizon $1/H$ remains constant, while the comoving size of the horizon $1/(RH)$ shrinks.

The slow-roll parameters can be probed due to quantum fluctuations, which perturb the value of the inflaton (scalar perturbations) and of the metric (both scalar and tensor perturbations). Metric perturbations are described by a wave equation (see [94] for a review, as well as references therein), which gives them the name primordial gravitational waves. The wavelengths of these waves are rapidly stretched by the expansion of the Universe and eventually exceed the size of the horizon since expansion is accelerated. When this happens, their amplitude remains roughly constant for as long as they the wavelength is super-horizon, assuming single field inflation. This results in an approximately scale invariant power spectrum:

$$P_T(k) \equiv A_T(k)\left(\frac{k}{RH}\right)^{n_T(k)} = \frac{2H^2}{\pi^2 M_P^2}\left(\frac{k}{RH}\right)^{-2\epsilon}\,, \tag{1.21}$$

where the right hand side is evaluated at the time of horizon crossing. Similarly scalar perturbations become frozen when the wavelength of Fourier modes is super-horizon, resulting in a spectrum:

$$P_s \equiv A_s(k)\left(\frac{k}{RH}\right)^{n_s(k)-1} = \frac{1}{2\epsilon}\left(\frac{H}{2\pi M_P}\right)^2\left(\frac{k}{RH}\right)^{2\eta-6\epsilon}\,, \tag{1.22}$$

where the right hand side is also evaluated at the time of horizon crossing.

The CMB temperature anisotropy probe the scalar spectrum of curvature perturbations, while the tensor perturbations are better distinguished by combining temperature anisotropy and the polarization data [95–97]. The most recent CMB constraints on the tensor to scalar ratio, the scalar spectral index and the amplitude of the spectrum of scalar perturbations are respectively [98–100]:

$$r_T = 16\epsilon \lesssim 0.028\,, \tag{1.23}$$

$$n_s = 1 - 6\epsilon + 2\eta = 0.9649 \pm 0.0042\,, \tag{1.24}$$

$$A_s = \frac{1}{2\epsilon}\left(\frac{H}{2\pi M_P}\right)^2 = (2.105 \pm 0.029) \times 10^{-9}\,, \tag{1.25}$$

which can be used to place upper bounds $\epsilon \lesssim 1.75 \times 10^{-3}$, $H \lesssim 4.2 \times 10^{13}\,\text{GeV}$ at the time when CMB scales exited the horizon during inflation.[6] The relatively low value of ϵ allows to assume that Hubble is a constant during inflation $H = H_I$ and the Universe expands exponentially $R \sim e^{H_I t}$.

By now there are multiple proposed ways to achieve the slow decrease of energy required for inflation, see [102–104] for reviews. Many of these require more ingredients than just one simple scalar field, however in some cases the model can still be written as an effectively single field model with the values of additional fields being determined by the couplings to the inflaton and effectively contributing to its potential. This is for example the case in hybrid inflation models which we discuss later, in Chapter 5, and in this situation inflation is similarly maintained as long as the inflaton is slow-rolling.

One issue in many inflationary models is that they require somewhat special initial conditions, in particular the simplest single models with high scale of inflation require that the inflaton starts with very large initial values $\varphi \gtrsim M_P$, while many of the low scale inflation models also suffer from fine tuning problems [105, 106]. An argument in the defense of large scale models is that a small Universe with huge initial energy density is most likely to be quantum created from "nothing" through quantum fluctuations [107, 108]. A simplified version of this argument is stated in [103]: by using the uncertainty principle $\Delta E \Delta t \gtrsim 1$ it can be argued that the most likely Universe is the one that forms in the shortest possible time $\Delta t \simeq 1/M_P$ in which case the energy density of such a Universe is of the order of the Planck density $\sim M_P^4$ and thus a large energy density during and at the end of inflation is expected. A more general justification for initial conditions required for inflation is that parts of the Universe that have been inflated cover exponentially more space than those that have not been inflated at all and thus we might be more likely to find ourselves in such a region.

Regardless of the realisation of the inflationary model, eventually the inflaton is no longer stuck in a relatively flat region of its potential and it starts oscillating, relaxing to its vacuum. At this point it decays together with the various other fields that were participating in keeping the energy density approximately constant. During this time the Universe is in a phase of matter domination called reheating, which is responsible for the decay of the inflaton and the thermalisation of its decay products. This process is incredibly complicated as it depends on the exact contents of the early Universe and their interactions, which also necessarily happen outside of equilibrium. Following this phase, the Universe ends up radiation dominated and in thermodynamic equilibrium

[6] A future mission to measure CMB polarisation could detect a tensor to scalar ratio, or alternatively strengthen the upper bound down to $r_T \lesssim 0.001$ [101].

at a (presumably large) unknown temperature, which connects to the standard cosmological history as explained above.

On top of the flatness and the horizon problem, the exponential expansion of the Universe characteristic to the inflationary paradigm could also account for the lack dangerous relics which appear in many high energy theories. These often predict topological defects as a result of phase transitions at large temperatures, such as heavy magnetic monopoles which would come to dominate the energy density of the Universe and endanger the standard cosmology [109], domain walls whose energy density dilutes slower than both matter and radiation and thus would result in a phase of domain walls domination if they are stable and cosmological strings which are heavily constrained if they survive until recombination [110–113]. A way to avoid these problems is if these dangerous relics have been additionally diluted, in which case their energy density has been negligible throughout the history of the Universe, and inflation can easily do this since it introduces a potentially huge dilution as the scale factor grows by a factor $\sim e^{60}$ in order to solve the horizon and flatness problems.

1.4 Gravitational waves

Gravitational waves, first indirectly detected by observations of the orbital period of the Hulse-Taylor pulsar [114,115] and later directly detected by the LIGO/Virgo collaboration [116], provide a powerful tool to study astrophysics, cosmology and particle physics.

Indeed gravitational waves have already led to discoveries in astrophysics [117, 118] and they provide valuable insights into the early Universe, since they are the only signal that was freely propagating through the Universe at times before recombination. This could result in insights into particle physics, since the temperature and correspondingly the particles energies in the early Universe have possibly been much larger than what is achievable in particle accelerators. As explained above, gravitational waves can also be used to probe the energy scale during inflation H_I at the very beginning of the Universe.

For these reasons great effort has been dedicated to designing and improving detectors capable of observing gravitational waves on the experimental front, while on the theory front it is useful to understand the spectrum of gravitational waves predicted by various proposed extensions of the SM in order to tell whether current or near future detectors could help us gain insight into these theories, and if so what might those insights be.

Gravitational waves detectors currently working or proposed for the future can be broken down into three categories: laser interferometers, atom interferometers and pulsar timing arrays. Laser interferometers are sensitive to small changes of the arm length of the detector which are sourced by gravitational waves. These can be either ground-based such as LIGO [119] and ET [120, 121] or space-based such as LISA [122], DECIGO/BBO [123]. Space-based interferometers allow for a much larger arm length than ground-based ones and thus are sensitive to lower frequency gravita-

tional waves. On the other hand, atom interferometers such as AEDGE [124] and AION [125] use laser pulses to move cooled atoms inside two atom clouds between ground and excited states, with the interference pattern being generated by the atoms de Broglie waves. In this sense, the laser pulses act as effective mirrors and beam splitters for these interferometers. Atom interferometers are sensitive to frequencies typically between space and ground-based laser interferometers. Finally pulsar timing arrays such as EPTA [126], PPT [127], SKA [128] monitor a network of millisecond pulsars and are sensitive to changes to the times some of the pulses arrive, which is an indication of a change in distance along a direction due to gravitational waves. Since the distances between Earth and the pulsars are much larger than the arm lengths achievable by space-based laser interferometers, pulsar timing arrays are sensitive to the lowest frequency gravitational waves out of all types of detectors.

1.5 Outline of the thesis

This thesis is concerned with the dynamics of ALPs in the early Universe, an important question being when the associated $U(1)$ PQ symmetry has been broken, which is separated into two cosmological scenarios for ALPs: either the PQ symmetry has been broken before the end of inflation which is the pre-inflationary scenario, or after the end of inflation which is the post-inflationary scenario. For given values of the parameters that describe ALPs which are the mass m_a and symmetry breaking scale f_a[7] the two scenarios result in massively different phenomenological results as I will explain.

In Chapter 2 I briefly review the Strong CP problem and the QCD axion as a potential solution, as well as properties of the QCD axion and general ALPs such as the current constraints, their viability as DM candidates, the standard separation between the pre- and post-inflationary scenario and how it affects the calculation of relic abundance.

Then in Chapter 3 I review quantum fluctuations during inflation in more detail since they are an important ingredient in separating the pre- and post-inflationary scenarios, and in particular I introduce the relevant Langevin and Fokker-Planck equations which are of use in later Chapters.

Chapter 4 is dedicated to the exploration of the transition between the pre- and post-inflationary scenarios assuming quantum fluctuations are the relevant factor in restoring the PQ symmetry. This is done by using numerical simulations to empirically find a relatively simple correlation between the energy density in axion strings and domain walls and the distribution of the axion field at the end of inflation, which in turn is correlated to H_I by the Fokker-Planck equation. This way the pre- and post-inflationary scenarios can be separated more precisely. We also uncover a region of the parameter space (albeit small) at the edge between the post-inflationary and pre-inflationary that has for a long time not been considered in the literature, even if the result for the relic abundance is substantially different in this case. This is characterised by strings and domain

[7] Which are related for the QCD axion.

walls being destroyed later than in the post-inflationary, which enhances the axion abundance. I estimate the relic abundance in this intermediate region of the parameter space and the applicable isocurvature constraints, as well as consider phenomenological implications. Additionally, recent papers [129–131] have considered a similar scenario, which requires that PQ symmetry is broken during inflation at such a time that scales that correspond to it re-enter the horizon at a specific time in the early Universe. This may result in late destruction of the domain walls, resulting in a similar prediction for the axion abundance to the intermediate scenario we uncovered, and I briefly comment on their results. This Chapter is based on work done together with collaborators and will be the subject of a future paper.

In Chapter 5 I review other potential ways to restore spontaneously broken symmetries considered in the literature and apply them to the case of ALPs. They are a large temperature in the early Universe, a coupling between the PQ field and the inflaton that modifies the PQ potential, non-perturbative decay of the inflaton and multiple stages of inflation interrupted by brief radiation or matter domination. Some of these possibilities may lead to the scenario with late domain walls introduced in [130, 131] that was mentioned above.

A second objective of the thesis is to consider the possibility of probing ALPs through gravitational waves. In Chapter 6 I explain how numerical simulations can be used to calculate the spectrum of gravitational waves produced by the evolution of ALP strings in the post-inflationary scenario and discuss the possibility of detecting ALPs this way. This is possible due to a relatively simple relation between the strings' emissions to axions and gravitational waves which we have deduced analytically in the Nambu–Goto effective theory, up to numerical factors which could be extracted through numerical simulations. Meanwhile most of the network's energy loss is emitted into axions, so the rate of emissions of axions and by extension gravitational waves can be approximated by simple means of energy conservation if the energy density stored in the network is known at every time. This in turn can be done thanks to the existence of a scalling regime towards which the network evolves, whose properties can also be extracted through numerical simulations. The gravitational waves spectrum is logarithmically enhanced at low frequencies, meaning pulsar timing arrays are primarily sensitive to them and the amplitude of the spectrum increases with the symmetry breaking scale f_a. Therefore gravitational waves detectors are most sensitive to axions in a region where they are invisible to most other experimental searches, which rely on axion interactions with photons and matter, whose couplings are proportional to $1/f_a$. Various cosmological bounds applicable at large values of f_a required for detectable gravitational waves are considered, such as the axion contribution to the effective number of degrees of freedom, the DM abundance and isocurvature perturbations. Additionally, I apply the results of previous Chapters to consider the possibility of PQ symmetry restoration, which is required for the ALP string network to form, in the case of high values of the symmetry breaking scale corresponding to detectable gravitational waves.

Chapter 6 is based on [1] which was written together with collaborators, Dr Marco Gorghetto

and Dr Edward Hardy. Here I will state my individual contribution to the work presented in this Chapter:

- I have calculated the constraints from dark radiation, dark matter overproduction and the constraints due to the strings surviving until recombination presented in Figure 6.7. I have also verified the constraints from isocurvature which my collaborators have calculated.
- I have verified the theoretical derivation of the ratio between strings' emissions to gravitational waves and axions and the derivation of the gravitational waves spectrum which my collaborators initially performed.
- I have considered various ways that can result in PQ symmetry restoration for large symmetry breaking scales required for observable gravitational waves.
- I have performed the test of the systematic errors due to lattice spacing presented in Figure E.1 of Appendix E.1.
- I have produced Figures 6.1, 6.2, 6.6, 6.8 presented in this Chapter. I also clearly state in the caption of every figure whether it was produced by my collaborators.

Chapter 2

Brief review of QCD axion and ALPs

2.1 Strong CP problem

The Strong CP problem is related to the CP violating term

$$\mathcal{L}_{\rm CP} = \frac{\theta_{\rm QCD} g_s^2}{64\pi^2} \epsilon^{\mu\nu\alpha\beta} G^a_{\mu\nu} G^a_{\alpha\beta} \,, \tag{2.1}$$

where $G^a_{\mu\nu}$ is the gluon field strength, g_s is the strong interaction coupling and a sum over the gauge index a which labels the $SU(3)$ generators is understood.

This term is a total derivative as first pointed out in [132]

$$\frac{1}{2}\epsilon^{\mu\nu\alpha\beta} G^a_{\mu\nu} G^a_{\alpha\beta} = \partial_\mu K^\mu \,, \tag{2.2}$$

$$K^\mu = \epsilon^{\mu\alpha\beta\gamma} A^a_\alpha \left[G^a_{\beta\gamma} - \frac{g_s}{3} f_{abc} A^b_\beta A^c_\gamma \right] \,, \tag{2.3}$$

where A^a_μ is the gluon field which defines $G^a_{\mu\nu}$:

$$G^a_{\mu\nu} = \partial_\mu A^a_\nu - \partial_\nu A^a_\mu + f_{abc} A^b_\mu A^c_\nu \,. \tag{2.4}$$

Thus the term in (2.1) will appear in the action as an integral over a boundary surface σ_μ at spatial infinity $\sim \int d\sigma_\mu K^\mu$. Such a term would not contribute to the equations of motion under the naive expectation that the gauge field A^a_μ vanishes at spatial infinity. However the correct boundary condition must allow A^a_μ to also be a gauge transformation of zero [133]. Field configurations exist with $\int d\sigma_\mu K^\mu \neq 0$ and in particular they can be classified by their winding number

$$\nu = \frac{1}{32\pi^2} \int d\sigma_\mu K^\mu \,, \tag{2.5}$$

which is an integer. The QCD vacuum is a superposition of these vacuum states:

$$|\theta_{\rm QCD}\rangle = \sum^{\nu} e^{i\nu\theta_{\rm QCD}} |\nu\rangle \ . \tag{2.6}$$

The vacuum angle $\theta_{\rm QCD}$ has physical effects in combination with a complex phase in the quark mass matrix.[1] The point is that a chiral rotation of the phase of a quark $\psi \to e^{i\alpha\gamma_5}\psi$ results in an additional term in the Lagrangian of the same form as that in (2.1), where by ψ I denote a four component Dirac spinor. The reason is that the chiral $U(1)$ symmetry is anomalous at the quantum level, so the measure in the path integral $\mathcal{D}\psi\mathcal{D}\overline{\psi}$ is not invariant under the transformation but instead transforms as [8]:

$$\mathcal{D}\psi\mathcal{D}\overline{\psi} \to \mathcal{D}\psi\mathcal{D}\overline{\psi} \exp\left(i \int d^4x \frac{\alpha g_s^2}{64\pi^2} \epsilon^{\mu\nu\alpha\beta} G^a_{\mu\nu} G^a_{\alpha\beta} \right) , \tag{2.7}$$

which corresponds to a change in the Lagrangian

$$\delta\mathcal{L} = \frac{\alpha g_s^2}{64\pi^2} \epsilon^{\mu\nu\alpha\beta} G^a_{\mu\nu} G^a_{\alpha\beta} \, . \tag{2.8}$$

This means that the $\theta_{\rm QCD}$ angle can be moved into the quarks mass matrix phase and vice versa through chiral rotations, therefore an effective vacuum angle is defined as:

$$\overline{\theta} = \theta_{\rm QCD} + \theta_q \, , \tag{2.9}$$

where $\theta_q = \arg\det(Y_u Y_d)$ and Y_u, Y_d are the Yukawa matrices corresponding to the up and down quarks respectively.

The vacuum angle $\overline{\theta}$ has an associated vacuum energy, which at leading order comes from the neutral pion sector. This can be seen by chiral rotating the $\overline{\theta}$ angle into the lightest two quarks mass matrix, and since we are interested in the vacuum the rest of the quarks can be integrated out, leaving us with 2 flavours. The pion Lagrangian at lowest order and with derivatives terms set to zero reads [135]:

$$\mathcal{L}_\pi = \frac{B_0 f_\pi^2}{2} \left\langle U M_q^\dagger + M_q U^\dagger \right\rangle , \tag{2.10}$$

where $B_0 = -\langle\overline{q}q\rangle / f_\pi^2$ is related to the chiral condensate, f_π is the pion decay constant, the θ angle has been absorbed in the quark mass matrices, brackets $\langle\rangle$ denote summing over flavour indices and $U = e^{i\Pi/f_\pi}$, with Π parametrising the pion field for 2 flavours:

$$\Pi = \begin{pmatrix} \pi^0 & \sqrt{2}\pi^+ \\ \sqrt{2}\pi^- & -\pi^0 \end{pmatrix} , \tag{2.11}$$

[1] If the lightest quark would be massless $m_u = 0$ then this phase would have no physical effect since we could perform a chiral rotation to remove it. This is however strongly disfavored by lattice results [134].

For the leading order potential we may only consider the neutral pion sector, so in the following we replace:

$$\Pi \longrightarrow \begin{pmatrix} \pi^0 & 0 \\ 0 & -\pi^0 \end{pmatrix} . \tag{2.12}$$

The potential is then

$$V(\overline{\theta}, \pi^0) = -B_0 f_\pi^2 \Re \left\langle U M_q^\dagger \right\rangle = -B_0 \left(m_u \cos\left(\frac{\pi^0}{f_\pi} + \frac{\overline{\theta}}{2} \right) + m_d \cos\left(\frac{\pi^0}{f_\pi} - \frac{\overline{\theta}}{2} \right) \right) . \tag{2.13}$$

Evaluating $V(\overline{\theta} = 0, \pi^0)$ and expanding to second order in π^0 allows us to write B_0 in terms of the neutral pion mass

$$m_\pi^2 = B_0 (m_u + m_d) . \tag{2.14}$$

Replacing B_0, equation (2.13) can be re-written as

$$V(\overline{\theta}, \pi^0) = -m_\pi^2 f_\pi^2 \sqrt{1 - \frac{4 m_u m_d}{(m_u + m_d)^2} \sin^2\left(\frac{\overline{\theta}}{2} \right)} \cos\left(\frac{\pi^0}{f_\pi} - \phi_\theta \right) , \tag{2.15}$$

where ϕ_0 is defined by

$$\tan(\phi_\theta) = \frac{m_d - m_u}{m_d + m_u} \tan\left(\frac{\overline{\theta}}{2} \right) . \tag{2.16}$$

To minimize the potential the pion acquires a Vev $\langle \pi^0 \rangle = f_\pi \phi_\theta$, so the θ-vacuum energy is:

$$E(\overline{\theta}) = -m_\pi^2 f_\pi^2 \sqrt{1 - \frac{4 m_u m_d}{(m_u + m_d)^2} \sin^2\left(\frac{\overline{\theta}}{2} \right)} . \tag{2.17}$$

One way for the vacuum angle $\overline{\theta}$ to be observable is through the neutron electric dipole moment (nEDM), which is generated by the CP violating pion neutron interaction. Initial estimates of the nEDM [136, 137] give $d_n \simeq 5.2 \times 10^{-16}\, \overline{\theta}\, e\text{cm}$. Various other estimates of the nEDM exist in the literature [138–142] and the results differ by at most one order of magnitude. Thus we can compare to the experimental limit $d_n \lesssim 3.6 \times 10^{-26} e\text{cm}$ [143] to find $\left|\overline{\theta}\right| \lesssim 10^{-10}$.

This fine tuning of the $\overline{\theta}$ angle constitutes the Strong CP problem, as there is no apparent reason why both the topological contribution θ_{QCD} and the quark mass phase θ_q are simultaneously so small, or alternatively why are they connected in a way as to cancel to such a level of accuracy.

2.2 The axion solution to the Strong CP problem

One of the best motivated solutions to the Strong CP problem is the introduction of an additional $U(1)$ global symmetry [70–76], called the PQ symmetry after R. Peccei and H. Quinn. The axion a is the (pseudo) Nambu-Goldstone boson of this spontaneously broken $U(1)$ symmetry and as

such has a shift symmetry $a \to a + \alpha v_a$, where $v_a = N_{\rm DW} f_a$ and in the following I will call f_a the axion symmetry breaking scale and $N_{\rm DW}$ is the number of non-equivalent minimums of the axion potential and is related to the colour anomaly of the PQ symmetry:

$$N_{\rm DW} = \delta_{\rm ij} \sum_j Q_{\rm PQ,\,j}\, {\rm Tr}(T_i T_j)\,, \tag{2.18}$$

where T_j are the $SU(3)$ generators and $Q_{\rm PQ,\,j}$ the PQ charge of the fermions that are summed over.

The axion couples to the topological charge $\epsilon^{\mu\nu\alpha\beta} G^a_{\mu\nu} G^a_{\alpha\beta}$ in a similar manner as the $\overline{\theta}$ angle

$$\mathcal{L} \supset \frac{a g_s^2}{64\pi^2} \epsilon^{\mu\nu\alpha\beta} G^a_{\mu\nu} G^a_{\alpha\beta}\,, \tag{2.19}$$

The idea is that the Strong CP problem vanishes at $\overline{\theta} = 0$, which is the minimum of the vacuum energy in (2.17), but the $\overline{\theta}$ cannot minimize its potential alone since transitions between different θ-vacua are topologically forbidden. The axion however contributes to the effective vacuum angle $\overline{\theta} \to \overline{\theta} + a/f_a$ which now has the advantage of being dynamical rather than a fixed parameter. Then it can evolve towards the minimum of the potential where the nEDM vanishes and the Strong CP problem is solved. Due to the shift symmetry we can define the axion field such that we absorb the $\overline{\theta}$ angle and the vacuum energy eq. (2.17) now gives the axion potential:

$$V_a(a) = -m_\pi^2 f_\pi^2 \sqrt{1 - \frac{4 m_u m_d}{(m_u + m_d)^2} \sin^2\left(\frac{a}{2 f_a}\right)}\,, \tag{2.20}$$

with minimums at $a = 2\pi n f_a$ with n being any integer between $-N_{\rm DW}/2 < n < N_{\rm DW}/2$, the axion fundamental domain is $(-\pi N_{\rm DW} f_a, \pi N_{\rm DW} f_a)$ and $N_{\rm DW}$ is a parameter that depends on the details of the model that realises this, called the colour anomaly, which is a positive integer setting the number of minimums of the axion potential.

Expanding this we find the standard result for the mass of the axion at leading order [72]:

$$m_a^2 \simeq \frac{m_\pi^2 f_\pi^2}{f_a^2} \frac{m_u m_d}{(m_u + m_d)^2}\,, \tag{2.21}$$

$$m_a \simeq 6.2\,{\rm eV} \left(\frac{10^6\,{\rm GeV}}{f_a}\right)\,. \tag{2.22}$$

More precise calculations carried out at NLO [144] and NNLO [145] improve on this result:

$$m_a \simeq 5.69\,{\rm eV} \left(\frac{10^6\,{\rm GeV}}{f_a}\right)\,. \tag{2.23}$$

It is worth mentioning the two benchmark classes of models that give rise to the QCD axion. These are the KSVZ (Kim–Shifman–Vainshtein–Zakharov) [73, 74] and DFSZ (Dine–Fischler–Srednicki–Zhitnitsky) [75,76] models[2]. They differ in the additions to the Standard Model that realise the coupling between the axion and the topological charge $\epsilon^{\mu\nu\alpha\beta}G^a_{\mu\nu}G^a_{\alpha\beta}$, in particular KSVZ model introduces two heavy quarks Q_L, Q_R which couple to the PQ field ϕ as

$$\mathcal{L} \supset -\lambda\phi\overline{Q}_L Q_R + \text{h.c.}\,, \tag{2.24}$$

while the DFSZ model introduces two Higgs doublets H_u, H_d which couple to the PQ field

$$\mathcal{L} \supset -\lambda\phi^2 H_u H_d\,. \tag{2.25}$$

In any case QCD axion models of these types have in common the complex PQ field ϕ with a $U(1)_{\text{PQ}}$ symmetric potential which contains the axion a as the angular degree of freedom. The QCD axion potential is the same as it is given by the pion potential and the relation between its mass and symmetry breaking scale eq. (2.23) is also model independent with our definition of f_a. Since these are the main ingredients required in the remainder of the thesis it is fine to remain agnostic to the exact details of the coupling between the QCD axion and the Standard Model and instead work with a simplified model where the PQ field is expressed as:

$$\phi = |\phi|\, e^{\frac{ia}{v_a}} = \frac{r + v_a}{\sqrt{2}} e^{i\theta}\,, \tag{2.26}$$

with $v_a = N_{\text{DW}} f_a$, $\theta = a/v_a$ and $r(x)$ is the radial mode defined as:

$$r(x) = \sqrt{2}\,|\phi(x)| - v_a\,. \tag{2.27}$$

With this definition $r(x)$ will be a real field with canonically normalised kinetic term.

The classical Lagrangian is invariant under the $U(1)$ PQ symmetry

$$\mathcal{L} = |\partial_\mu\phi|^2 - V_\phi(\phi)\,, \tag{2.28}$$

with the simplest form for the potential being

$$V_\phi = \lambda\left(|\phi|^2 - \frac{v_a^2}{2}\right)^2 = \frac{m_r^2}{2v_a^2}\left(|\phi|^2 - \frac{v_a^2}{2}\right)^2\,, \tag{2.29}$$

and m_r is the mass of the radial mode defined above.

We allow $f_a, \lambda, N_{\text{DW}}$ to be free parameters in the simple potential above. Model dependence

[2]The original PQWW (Peccei-Quinn-Weinberg-Wilczek) [70–72] introduced the PQ field as a Higgs doublet, with the PQ symmetry being spontaneously broken at the electroweak scale $f_a = 250\,\text{GeV}$. This has been since ruled out, as the axion couplings would be too large.

will show up in the axion's couplings, which in turn affect various bounds on the axion mass as we discuss in the following Section.

2.3 ALPs

Similarly to the QCD axion, axion-like-particles (ALPs) are pseudo Nambu–Goldstone bosons of spontaneously broken global $U(1)$ symmetries, however without an anomalous coupling to QCD. Given the standard lore that global symmetries are always explicitly broken in quantum gravity [146–148] the ALPs are expected to acquire mass due to effects that break their residual shift symmetry. Global (approximate) $U(1)$ symmetries appear in many extensions of the Standard Model such as grand unified theories, theories of leptogenesis and neutrino masses, as well as in string theory constructions.

For the remainder of the thesis it is fine to remain agnostic about the exact model realisation of the QCD axion/ALPs and work with the simplest ALP potential given by equation (2.29) above. For our purposes the only difference between an ALP and the QCD axion is the fact the mass of ALPs is not related to their symmetry breaking scale, instead it is an additional free parameter, which means there is more parameter space allowed for ALPs.[3]

2.3.1 ALPs from string theory

An important motivation for the QCD axion and ALPs is the fact that they arise from compactifying string theory down to four dimensions, as Kaluza-Klein zero modes of antisymmetric tensor fields (forms) [77, 78]. Specifically a $(p+1)$–form field strength F_{p+1} appearing in the ten dimensional action as

$$S \supset \int \frac{1}{2} d^{10}x F_{p+1} \wedge \star F_{p+1} \,, \tag{2.30}$$

has an associated p-form potential A_p defined by $dA_p = F_{\mathrm{p+1}}$, which decomposes into a basis of harmonic p-forms $\omega_{p,i}$:

$$A_p = \frac{1}{2\pi} \sum_i a_i(z) \omega_{p,i}(y) \,. \tag{2.31}$$

In the above $\star F_{p+1}$ denotes the Hodge dual of F_{p+1} and is a $10-(p+1)$ form and $\wedge$ denotes the wedge product between forms[4]. Additionally, z denotes coordinates in four dimensions, y in the compact space and $\omega_{p,i}$ are dual to p-cycles $\mathcal{C}_i$, which are closed, homologically non-equivalent, submanifolds of the Calabi-Yau manifold that the theory was compactified on:

$$\int_{\mathcal{C}_i} \omega_j = \delta_{\mathrm{ij}} \,. \tag{2.32}$$

[3] For this reason I will do my best in the remainder of the thesis to separate m_a and f_a to allow the results for the QCD axion to be easily generalised to ALPs.

[4] I adopt the notation for differential forms in [43].

The gauge invariance of the action of the antisymmetric tensor field F_{p+1} guarantees that the ALPs a_i have no potential to all orders of perturbation theory. The number of such ALPs is the number of p-cycles $\mathcal{C}_i$ of the Calabi-Yau manifold that the theory was compactified on, which is typically of the order tens or higher [83,149,150]. Thus a large number of ALPs is expected, leading to a "string axiverse" [79–83].

The mass and symmetry breaking scales of ALPs resulting from string theory compactifications are given by the volume of the corresponding submanifolds (cycles), in units of string length, which is related to the action of non-perturbative effects that break the ALPs shift symmetry $S_{\rm inst}$, such as strings instantons. The symmetry breaking scale in many string theory constructions is parametrically [78, 151, 152]

$$f_{a,i} \sim \frac{M_P}{S_{\rm inst,i}}\,, \tag{2.33}$$

while the mass

$$m_{a,i} \sim \frac{\mu^2}{f_a} e^{-\frac{S_{\rm inst,i}}{2}}\,, \tag{2.34}$$

where μ is a UV scale. Since the action $S_{\rm inst}$ is related to the volume of submanifolds it is expected that the symmetry breaking scales of the ALPs are not so different, while the masses scan many orders of magnitude as they are exponentially sensitive to $S_{\rm inst}$ (see the detailed analysis in [153]).

Meanwhile we would like one of the ALPs in the axiverse to be the QCD axion. This is possible since the terms required for the Green–Schwarz mechanism for anomaly cancellation [154] could give rise to couplings to gauge fields of the type (2.19) [77, 155, 156], so one of these ALPs could play the role of the QCD axion [77, 78, 157, 158]. This places an additional requirement for the size of the non-perturbative effects that generate the potential of the QCD axion so that it solves the Strong CP problem:

$$S_{\rm inst,QCD} \gtrsim \mathcal{O}(200)\,, \tag{2.35}$$

for a UV scale $\mu \sim M_P$, which translates into $f_{a,\rm QCD} \lesssim 10^{16}\,\text{GeV}$ for a QCD axion arising from string theory and similar symmetry breaking scales for the rest of ALPs.

2.4 Axion DM

In this Section I briefly explain why the QCD axion and ALPs in general are viable candidates for DM and then discuss the main methods to produce axion DM. They are the misalignment mechanism and the decay of topological defects. I discuss the standard separation in the literature between the pre-inflationary scenario, in which topological defects have negligible contribution, and the post-inflationary scenario in which topological defects are the dominant production mechanism for axions.

For ALPs to be DM candidates they require to be stable on cosmological timescales, to be "cold" and to have weak interactions with baryonic matter and radiation. As we will see ALPs

are primarily produced non-thermally, by either misalignment or decay of topological defects, and in both these mechanisms a majority of ALPs are produced when their mass becomes significant, making them candidates for CDM even while being very light.

Meanwhile, thermally produced axions contribute sub-dominantly to dark radiation. Owing to its small couplings, the QCD axion decouples before the QCD phase transition for values of $f_a \gtrsim 10^7\,\mathrm{GeV}$ [159], while in Section 2.5 we see that supernova 1987a constraints on axion nucleon coupling limit the QCD axion symmetry breaking scale to $f_a \gtrsim 10^8\,\mathrm{GeV}$. Thus for values of f_a that are not already ruled out, the number density of thermally produced axions today is suppressed compared to that in photons by a factor $\mathcal{O}(g_\star(T_0)/g_\star(\Lambda_{\mathrm{QCD}})) \simeq 30$, where $g_\star(T)$ denotes the effective number of relativistic degrees of freedom at temperature T.

For DM candidates with masses of less than about $\mathcal{O}(30\,\mathrm{eV})$, which is the case for the QCD axion and much of the parameter space for ALPs, their de Broglie wavelength in the galactic halo exceeds their average inter-particle separation, assuming representative values for the local DM density of $0.45\,\mathrm{GeVcm}^{-3}$ and the velocity dispersion of the galactic halo $v \simeq 250\,\mathrm{km/s}$. Meanwhile their occupation number per de Broglie volume is $\sim (30\,\mathrm{eV}/m_a)^4$, which for QCD axion and light ALPs is very large. Thus light ALPs can generally be treated as classical waves (see [160] for a review).

I now move to discuss the question of ALPs stability and the main mechanisms to produce them.

2.4.1 Axion stability

An estimate of the lifetime of the QCD axion and ALPs involves the decay into two photons through a coupling of the form [161]

$$\mathcal{L} \supset -\frac{c_{a\gamma\gamma}\alpha_{\mathrm{EM}}}{8\pi f_a} a F_{\mu\nu}\tilde{F}^{\mu\nu}\,, \tag{2.36}$$

where $c_{a\gamma\gamma}$ is a model dependent parameter, $c_{a\gamma\gamma} \simeq \mathcal{O}(1)$ for both KSVZ and DFSZ models [162].

The associated lifetime is

$$\tau_{a\gamma\gamma} = \frac{256\pi^3 f_a^2}{m_a^3 c_{a\gamma\gamma}^2 \alpha_{\mathrm{EM}}^2}\,. \tag{2.37}$$

For the QCD axion we can replace m_a in term of f_a via eq. (2.23) and find that axion's lifetime exceeds the age of the Universe for QCD axion with symmetry breaking scales $f_a \gtrsim \mathcal{O}\left(10^6\,\mathrm{GeV}\right)$. As explained in Section 2.5 there are astrophysical constraints that insure this for the QCD axion.

Meanwhile for more generic ALPs the question of stability also depends on their mass, which is no longer related to the symmetry breaking scale and it is possible that some ALPs are not stable over the age of the Universe, specifically ALPs with relatively large mass $m_a \gtrsim \mathcal{O}(100)\,\mathrm{eV}$. Most light ALPs however are stable, see Figure 2.1. In particular the QCD axion and ALPs that give rise to string networks that can be detectable via gravitational waves we discuss in Chapter 6 are always stable over cosmological timescales. Additional decay channels are not expected to

significantly shorten the lifetime and alter this conclusion, since the corresponding couplings are also similarly suppressed by a factor $1/f_a$.

2.4.2 Misalignment

The PQ symmetry is spontaneously broken when the temperature of the Universe decreases below $\mathcal{O}(f_a)$ and correspondingly the Hubble $H \gtrsim \mathcal{O}(f_a^2/M_P) > \mathcal{O}(10^7\,\mathrm{eV})$. Thus there exist a period for which the symmetry is spontaneously broken while the value of the axion field across space is frozen with $H \gg \mathcal{O}(m_a)$. During this time the background axion energy density is approximately constant. The axion begins oscillating around the time when $H \simeq H_\star \equiv m_a(T_\star)$ and its equation of state defined as:

$$w_a = \frac{\dot{a}^2 - V(a)}{\dot{a}^2 + V(a)}\,, \tag{2.38}$$

oscillates between $w_a = \pm 1$. On average the equation of state is $w_a = 0$ and thus the axion starts to behave like matter. By releasing the potential energy on the way down to the bottom of its potential, the axion always makes a contribution to DM [163–165]. Taking into account that due to the temperature dependent axion mass it is the axion number density is adiabatically conserved, and not the energy density, this contribution is:

$$\rho_{\mathrm{mis}}(t_0) = \rho_{\mathrm{mis}}(t_\star)\frac{R_\star^3}{R_0^3}\frac{m_a}{m_a(T_\star)}\,, \tag{2.39}$$

where the dilution due to the expansion can be calculated under the standard assumption that the comoving entropy density is conserved between the $t_\star$ and today i.e. $T \sim g_\star(T)^{-1/3}R^{-1}$. Entropy injection would reduce the axion abundance, which was previously considered in [166, 167]. The axion energy at the time when oscillations begin is purely potential energy, which at leading order $a^2 \ll \pi^2 f_a^2$ can be estimated:

$$\rho_{\mathrm{mis}}(t_\star) \simeq \frac{m_a(T_\star)^2 a^2}{2} = \frac{m_a(T_\star)^2 f_a^2 \left\langle\theta^2\right\rangle}{2}\,, \tag{2.40}$$

where $\left\langle\theta^2\right\rangle$ is the spatial average of the vacuum angle at the time when oscillations begin.

At temperatures much larger than the QCD phase transition before the non-perturbative effect switch on the mass of the axion will be suppressed. The axion mass varies with temperature approximately as a power law [168–170]:

$$m_a(T) = \begin{cases} m_a & \text{for } T \lesssim \Lambda_{\mathrm{QCD}}\,, \\ m_a C\left(\frac{\Lambda_{\mathrm{QCD}}}{T}\right)^n & \text{for } T \gtrsim \Lambda_{\mathrm{QCD}}\,, \end{cases} \tag{2.41}$$

where m_a is the zero temperature mass given by eq. (2.23), $C \simeq 0.01$ is a model dependent

numerical factor and $n \simeq 4$. Then the misalignment abundance can be computed [171]:

$$\Omega_a h^2 \sim 0.01 \left\langle \theta^2 \right\rangle \left(\frac{f_a}{10^{11}\,\mathrm{GeV}} \right)^{7/6} . \tag{2.42}$$

At the time when PQ symmetry breaking happens the axion will acquire a random value in each causally connected Hubble patch. Since by the time oscillations begin the size of the horizon has increased massively, by a factor $f_a^2/(M_P\ m_a(T_\star))$, the Universe at this point contains a large number these Hubble patches from the time of symmetry breaking, so the axion can be seen as uniformly distributed over its fundamental domain. This corresponds to an average vacuum angle $\langle\theta^2\rangle = \pi^2/(3N_{\mathrm{DW}}^2)$. The caveat to the above argument is that symmetry breaking might have been followed by a period of inflation, in which case a small number of Hubble patches at the time of symmetry breaking, potentially a single one, would have expanded to cover our Universe today. This has the effect of making the field homogeneous over large scales, however the field will also be affected by quantum fluctuations in de Sitter space which act to randomize its value, which are discussed in more detail in Chapter 3. Therefore depending on the size of the quantum fluctuations the field can be anywhere from approximately homogeneous across the observable Universe, in which case $\langle\theta^2\rangle$ is simply a free parameter, to fully randomised which behaves as if the PQ symmetry was restored at the end of inflation and $\langle\theta^2\rangle = \pi^2/(3N_{\mathrm{DW}}^2)$ is fixed.

This situation has led to the distinction of two scenarios. The pre-inflationary scenario requires that PQ symmetry breaking was followed by a sufficiently long period of inflation, that the quantum fluctuation are not strong enough to randomize the field for which the standard condition in the literature is $H_I \lesssim 2\pi v_a$, and that the symmetry was not subsequently restored after the end of inflation, for example by thermal fluctuations. Conversely the post-inflationary scenario requires either that the quantum fluctuations are large enough to randomize the field $H_I \gtrsim 2\pi v_a$ or that the symmetry was restored after the end of inflation in another way. These scenarios have important consequences for the axion abundance and the allowed values of the mass and symmetry breaking scale. For example, in the case of the QCD axion the misalignment contribution in the post-inflationary scenario exceeds the total DM density and is thus ruled out if $f_a \gtrsim 10^{12}\,\mathrm{GeV}$. Moreover, as I explain below the relic abundance in the post-inflationary scenario is likely dominated by the decay of topological defects which means an even stronger upper bound on f_a. On the other hand in the pre-inflationary scenario the vacuum angle $\langle\theta^2\rangle$ can be taken to be arbitrarily small and topological defects have negligible contribution, so with sufficient fine tuning the axion density can be made smaller than the total DM density all the way up to the black-hole superradiance bound discussed in Section 2.5.[5]

[5]This type of fine tuning is not as bad as the initial Strong CP problem the axion was introduced to solve. Firstly, even with symmetry breaking scale as large as the maximum allowed by the superradiance bounds the vacuum angle needs only be fine tuned to be below 10^{-3} compared to 10^{-10} for the Strong CP problem. Secondly this type of fine tuning can be subject to anthropic arguments, as it is required to not overclose the Universe.

2.4.3 Topological defects

Topological defects are field configurations that appear as a consequence of phase transitions associated to breaking of symmetries via the Kibble mechanism [172–174]. For our purposes the relevant topological defects are axion strings and domain walls, since their decay contributes the most to the axion relic abundance.

Axion strings form at the centre of closed loops in space for which the axion field wraps around the fundamental domain $(-\pi v_a, \pi v_a)$ with non-trivial winding, which inevitably will exist at the time when PQ symmetry is broken [175], or if fluctuations in the radial mode push the field over the top of the symmetry breaking potential (which effectively restores PQ symmetry). By the continuity of the axion field, if we shrink these loops down to arbitrarily small radius the winding will remain, signalling the existence of a region at the centre of the loop where the field is kept in the unbroken phase at $\phi = 0$. These are the axion strings, and they must either form closed loops or be infinitely long (again due to the continuity of the field). More precisely, axion strings serve to minimize the average Hamiltonian density:

$$\langle \mathcal{H} \rangle = \left\langle \left|\dot{\phi}\right|^2 + |\nabla\phi|^2 + V_\phi(\phi) \right\rangle , \tag{2.43}$$

which can be decomposed in terms of the axion and radial mode defined in eq. (2.27) as

$$\langle \mathcal{H} \rangle = \left\langle \left|\frac{1}{2}\nabla r\right|^2 + V_\phi(\phi) + \left(\frac{r^2}{2v_a^2} + \frac{r}{v_a} + \frac{1}{2}\right)|\nabla a|^2 \right\rangle , \tag{2.44}$$

where the potential only depends on r and is given by (2.29) and I have set the time derivatives to zero to obtain a static solution. It is clear that at the centre of the loops that wrap the full fundamental domain there exist regions for which $|\nabla a|$ becomes arbitrarily large, so the way to minimize the Hamiltonian is to have the term that multiplies it be equal to zero, which corresponds to $r = -v_a$ or $|\phi| = 0$. At larger distance from this singularity the term $|\nabla a|$ drops and at about $\mathcal{O}(m_r^{-1})$ it becomes more efficient to set the potential energy to zero, meaning this is the approximate thickness of the strings.

Domain walls are the boundaries between regions in space in which the axion field has settled into different minima of its potential for $N_{\rm DW} > 1$ or between region that were initially on the opposite sides of the maximum of the potential at $a = \pm\pi f_a$ for $N_{\rm DW} = 1$ before they settled in the minimum at $a = 0$. By the continuity of the axion field the regions across these boundaries are kept at the maximum/maxima of the axion potential. Therefore the domain walls store energy, having an associated energy per unit area which can be calculated from the potential eq. (2.20):

$$\sigma_{\rm DW} \simeq 9 m_a f_a^2 , \tag{2.45}$$

and they form after $H \lesssim H_\star$ when the field starts oscillating and it settles into the various minima.

I now introduce the properties of the string network that forms in the early Universe as a result of spontaneous PQ symmetry breaking that allow the calculation of the resulting axion abundance. A very useful result is that the string network evolves towards an attractor solution, also called the scaling regime, regardless of the initial conditions. The way this is typically written in the literature is in terms of the dimensionless string density ξ defined as

$$\xi \equiv \lim V \to \infty \frac{l(V)t^2}{V}\,, \tag{2.46}$$

where l is the length of strings inside a box of volume V. If ξ is smaller than about $\xi_{\rm int} \sim \mathcal{O}(1)$ then strings are rare enough that their interactions are inefficient and their density increases over time. However, if ξ becomes greater than $\xi_{\rm int}$, the strings start interacting, which in general decreases their total length. Thus there is a value of ξ that the network converges to, where the rate at which the density is increasing due to extra strings entering the horizon is balanced by the loss due to string interactions.

The existence of this scaling solution has been used to estimate the contribution of strings to the axion density [176–189]. The idea is that in the post-inflationary scenario the scaling solution is reached fairly quickly, (long) before $H = H_\star$, when the axion field starts oscillating and domain walls form. Since the field around a string explores the full fundamental domain it is clear that once the field starts oscillating each string will be connected to $N_{\rm DW}$ domain walls. In the case $N_{\rm DW} = 1$ the strings/domain walls network is unstable, strings are rapidly pulled together by the tension of domain walls attached to them and they "chop" each other up, which destroys the network. Therefore, once the string density in the scaling solution has been estimated and the spectrum of axion emissions from strings is found from numerical simulations, the contribution of strings in the final e-folds before network destruction can be derived and appropriately redshifted until today. Earlier emissions are more diluted such that the axion emissions at later times dominate, which in principle allows an estimation of the strings' contribution regardless of the initial distribution, as long as this initial distribution reaches the scaling regime sufficiently quickly.

In the case $N_{\rm DW} > 1$ on the other hand the strings/domain walls network is stable. This is a problem, since in the scaling regime there is on average at least one large domain wall across each causal horizon. The energy density of domain walls in the scaling solution decreases roughly as the inverse squared of the scale factor. This is slower than radiation or matter, so the walls will easily dominate the energy density of the Universe if they survive until today. In the post-inflationary scenario a solution is to introduce additional symmetry breaking such that the axion field remains with a single minimum [190]. This is in itself severely restricted in order not to reintroduce the Strong CP problem: either the position of this minimum has to be fine tuned close to $a = 2n\pi f_a$ for some integer n or the size of this additional breaking has to be very small [191]. Thus in the following I will assume $N_{\rm DW} = 1$, which corresponds to $v_a = f_a$, and substitute this whenever a numerical value is required for $N_{\rm DW}$. However I will keep the differentiation between v_a and f_a

inside expressions to allow the results to be easily adapted to the case $N_{\rm DW} > 1$.

In the following I review the estimation in [186, 188] for the strings' contribution to the axion density, however I should mention that other groups report results that differ by up to an order of magnitude. There are two main factors that contribute to this difference, first of all there is not full agreement on what the emission spectrum is. Secondly, in [186] a logarithmic violation of scaling has been observed using numerical simulations, in other words the string density in the scaling regime was found not to be exactly constant, but rather:

$$\xi_{\rm scal} = c_1 \log(\frac{m_r}{H}) + c_0 \,, \tag{2.47}$$

with $c_1 = 0.24$ extracted numerically. This is also found in other recent works [182–185, 187, 189] and it makes a difference of a factor $c_1 \log(m_r/H_\star)$ in the axion abundance compared to estimations in which $\xi_{\rm scal} \simeq 1$ is taken to be constant.

The energy density in the network once scaling is reached is:

$$\rho_{\rm str}(t) = 4H^2 \xi(t) \mu(t) \,, \tag{2.48}$$

where μ is the average string tension (their energy per unit length). For strings resulting from a global symmetry, which is the case for ALPs, the tension is logarithmically divergent due to the energy stored in the gradient of the axion field. This divergence is cut-off by the presence of a nearby string, so the theoretical expectation would be:

$$\mu_{\rm th} = \pi v_a^2 \log\left(\frac{m_r \eta(t)}{H\sqrt{\xi}}\right) \,, \tag{2.49}$$

where $\eta(t)$ is parameterizing the shape of the strings and it was found in simulations to be approximately constant and of order 1. Thus at large values of the log applicable at network destruction the tension can be estimated:

$$\mu \simeq \pi v_a^2 \log\left(\frac{m_r}{H}\right) \,, \tag{2.50}$$

which matches the prediction for infinitely long, straight strings at distance $\mathcal{O}(H^{-1})$.

The energy in the network at scaling grows slower than that of a network evolving freely with strings remaining at fixed comoving coordinates and $\xi \sim R^2$, since strings interactions reduce their total length and keep ξ constant up to the log scaling violation. By comparing the energy density in the network to that of a free network of long strings which matches the actual network at time t' and later evolves by keeping the strings at fixed comoving coordinates:

$$\rho_{\rm free}(t) = 4H' H \xi(t') \mu(t) \,. \tag{2.51}$$

The energy of the free network of long strings evolves as $1/R^2$ as the long strings are stretched by

a factor R and the above formula assumes radiation domination. The emission rate of the network can be found, with the emitted energy going primarily into axions:

$$\Gamma_a \simeq \dot{\rho}_{\rm free} - \dot{\rho}_{\rm str}\,, \tag{2.52}$$

$$\Gamma_a = \rho_{\rm str}\left[2H - \frac{\dot{\xi}}{\xi} - \frac{\pi f_a^2}{\mu_{\rm th}}\left(H + \frac{\dot{\eta}}{\eta} - \frac{1}{2}\frac{\dot{\xi}}{\xi}\right)\right] \simeq 2H\rho_{\rm str}\,. \tag{2.53}$$

This can be integrated to find the energy density of axions:

$$\rho_a(t) = \int^t \Gamma_a(t')\left(\frac{R(t')}{R(t)}\right)^4 dt' = \frac{4\pi}{3}H^2 v_a^2 c_1 \log^3\left(\frac{m_r}{H}\right)\,, \tag{2.54}$$

at times before the network destruction when the axion is effectively massless and behaves like radiation.

However, to find the axion energy density today the momentum distribution of emissions is required. It is convenient to define this in the following way:

$$\frac{\partial\Gamma_a}{\partial k} = \frac{\Gamma_a}{H}F\left(\frac{k}{H}, \frac{m_r}{H}\right)\,. \tag{2.55}$$

The spectrum is expected to have two characteristic cut-offs: an IR cut-off at $k \simeq x_0 H$ and a UV cut-off at $k \sim m_r$ and a function that matches the simulations well between these cut-offs is:

$$F\left(\frac{k}{H}, \frac{m_r}{H}\right) = \frac{1}{x_0}\left(\frac{x_0 H}{k}\right)^q \frac{q-1}{1-\left(\frac{x_0 H}{m_r}\right)^{q-1}}\,, \tag{2.56}$$

which is a simple power law between these limits. This means for the axion number density at the time the field starts oscillating and the network is destroyed:

$$n_a(t_\star) \simeq \frac{8\pi c_1 H_\star v_a^2 \log^2\left(\frac{m_r}{H_\star}\right)}{x_0} \times \begin{cases} 1 - \frac{1}{q} & q > 1 \\ \frac{1}{\log\left(\frac{m_r}{H x_0}\right)} & q = 1\,. \end{cases} \tag{2.57}$$

There is not yet consensus on what the exact power q of the spectrum is. For example [188] find $x_0 \simeq 10$ and $q \simeq 1$ at values of $\log(m_r/H)$ accessible in the simulation, however they show evidence for an increase of q with $\log(m_r/H)$, so at late times $q \gg 1$. However [189] find $q \simeq 1$ and no evidence for an increase. The difference between these extrapolations introduces another potential factor of $\log(m_r/H_\star)$ in the relic abundance estimate. Since $\log(m_r/H_\star)$ could be as large as $\log(f_a/m_a) \sim \mathcal{O}(70)$, and there is up to a factor of $c_1 \log^2$ that is not yet agreed upon, there is a range of estimates for the string contribution, which by comparing (2.57) to (2.39) can be seen it is anywhere from the same order as the misalignment contribution to much higher. Meanwhile

the contribution from the destruction of domain walls at $t_\star$ assuming order one domain walls per horizon at this time is bounded by:

$$n_a(t_\star) \lesssim \sigma_{\rm DW} \frac{H_\star}{m_a(T_\star)} \simeq 9 m_a(T_\star) f_a^2 \,, \tag{2.58}$$

which ranges from somewhat larger than the string contribution to much lower depending on the relevant factors of $\log(m_r/H_\star)$ for the string contribution.

The difference between various estimates is somewhat mitigated due to the nonlinear transient as the axion mass becomes relevant at $H_\star = m_a(T_\star)$ [188]. The point is that most of the axion energy density at that time is still contained in the gradient part of the Hamiltonian and for this reason IR modes that would normally redshift non-relativistically actually continue to redshift relativistically up until a later time, when the potential becomes comparable to the energy density in these modes. The result of the nonlinear transient is a reduction of the axion abundance from $\sim c_1 \log(m_r/H)^2$ to $\sim \sqrt{c_1 \log(m_r/H)^2}$. Overall, given that the string relic abundance has a $f_a^{7/6}$ dependence[6], the upper bound on f_a differs by about a factor of 20 depending on the various assumptions about the spectrum and the string density in the scaling regime mentioned above, between $f_a \lesssim 10^{10}$ to $f_a \lesssim 2 \times 10^{11}$. Further in the remainder of the thesis I will assume that the strings' contribution dominate over the misalignment and domain walls at the time $t_\star$.

The situation is completely different in the pre-inflationary scenario. Since the axion field is homogeneous in this case the loops required to form axion strings do not appear and the field throughout space relaxes into the same minimum, so no domain walls appear either. In other words, any potential topological defects at the time of symmetry breaking have been inflated away, (far) outside our causal horizon today and the time required for a string network to form and reach scaling exceed the age of the Universe. For this reason the misalignment contribution dominates the axion abundance in the pre-inflationary scenario and there is no need to worry about the domain walls problem even for $N_{\rm DW} > 1$.

2.4.4 Summary of pre- and post-inflationary scenarios

Here I briefly summarise the standard pre- and post-inflationary scenarios.

Pre-inflationary scenario:

- Axion field homogeneous across space.
- Requires weak quantum fluctuations $H_I/v_a < 2\pi$ and no symmetry restoration by other means.

[6]This is true for the QCD axion, since the temperature dependence of the mass (2.41) means $T_\star$ has a $f_a^{-1/6}$ dependence when the axion begins oscillating before the QCD phase transition.

- Negligible topological defects, axion abundance dominated by misalignment.
- No domain walls problem.
- Average angle $\langle\theta^2\rangle$ is a free parameter, so the misalignment contribution can be fine-tuned.
- Isocurvature perturbations in the misalignment population [192–203] which are heavily constrained by the CMB [204, 205].

Post-inflationary scenario:

- Axion field fully randomised.
- Requires either strong quantum fluctuations $H_I/v_a > 2\pi$ or that PQ symmetry was restored in another way.
- Strings reach a scaling regime, domain walls form when the axion begins oscillating.
- Average angle $\langle\theta^2\rangle = \pi^2/(3N_{\rm DW}^2)$ is fixed, so misalignment contribution is fixed.
- Topological defects (likely) dominate over the misalignment contribution. Upper bound on v_a (subject to uncertainties).
- Large domain walls would dominate energy density unless $N_{\rm DW} = 1$ or additional bias is introduced.
- Isocurvature constraints are modified by the presence of strings and no longer depend on H_I,[7] only on f_a and m_a, see Section 6.3.3 for a detailed calculation and eq. (6.17). In particular, for values of f_a, m_a allowed for the QCD axion in the post-inflationary scenario so that DM is not overproduced, they do not constrain the parameter space any further.

One natural question is how we get from the pre-inflationary to the post-inflationary scenario and what happens in between. The idea is that the post-inflationary scenario is the limit when the axion field is fully randomized across the horizon while the pre-inflationary scenario is the limit when the axion is fully homogeneous. Thus it would be useful to find a quantity that describes the degree of "randomness" of the field and be able to correlate it to the contribution of topological defects. Such a quantity could then be used to describe the transition between the pre- and post-inflationary scenario in a continuous way.

I proceed to introduce quantum fluctuations in more detail in Chapter 3, since they can be an important ingredient in the formation of topological defects. Then in Chapter 4 I show how the axion and radial mode field distributions at the end of inflation and the density of topological defects are related, and give further details on when the pre- and post- inflationary scenarios arise and the intermediate region between them.

[7] Other than the role it plays in selecting this scenario in the first place.

2.5 Astrophysical and direct detection bounds on axions

Various ways to probe the QCD axion as well as ALPs in general have been proposed, which so far resulted in bounds on the allowed parameter space. Many of the traditional ways to detect ALPs are based on the Primakoff process [206] which involves an ALP conversion into two photons in the presence of a magnetic field. Classic methods exploiting this are helioscopes and haloscopes [207], as well as "light shining through wall" (LSW) experiments [208].

Helioscopes, such as CAST [209–211] and in the future IAXO [212] search for axions produced inside the Sun which would convert into detectable photons in the presence of a strong magnetic field. For this reason they are an effective detection method regardless of the fraction of DM that axions account for.

Alternatively, "light shining through wall" experiments point a laser at a wall and apply a magnetic field to convert photons into axions. As these axions pass the wall, they are converted back into photons on the other side by a magnetic field. The Any Light Particle Search experiment [213] currently places the strongest bounds on the axion photon coupling out of this type of experiments. As axions in this case are produced inside the laboratory, these limits are also applicable regardless of the axion density.

On the other hand, haloscopes detect DM axions by converting then into photons due to an applied magnetic field, inside a cavity that is designed such as to make the conversion resonant and enhance its rate. So far the ADMX experiment [214–217] has put the strongest limits on axion photon coupling inside a narrow mass window $m_a \sim 10^{-6}\,\text{eV}$, which for the QCD axion specifically corresponds to $f_a \sim 10^{12}\,\text{GeV}$, the value roughly required for the misalignment population to make up all of DM for initial $\overline{\theta}$ angles of order one. Projected improvements of ADMX and other haloscopes [218–222] are going to cover the axion mass window $10^{-6}\,\text{eV} \lesssim m_a \lesssim 10^{-2}\,\text{eV}$. Haloscopes rely on a large density of DM axion, so the quoted bounds are calculated under the assumption that axions make up most of DM.

Aside from direct detection bounds mentioned above there are important bounds coming from stellar astrophysics. Photon conversion into ALPs which subsequently escape stars results in cooling, which alters the lifetime of stars in a phase of core helium burning (also known as horizontal branch stars) [223]. This can be probed by observing the ratio between stars in the core helium burning phase and red giants, whose luminosity is supported by hydrogen burning in their shells, inside globular clusters. Such observations have so far put constraints on the axion photon coupling [224], which for the QCD axion are roughly $10^7\,\text{GeV} \lesssim f_a$.

Meanwhile the QCD axion coupling to nucleons is strongly constrained by the duration of the neutrino burst of supernova 1987a. The idea is that nucleon-nucleon bremsstrahlung produces axions, which depending on their nucleon coupling would not be trapped inside the supernova core and thus could be cooling the supernova more efficiently than neutrinos. The limits for QCD axions in the KSVZ model translate to $m_a \lesssim 15\,\text{meV}$ or $f_a \gtrsim 4\times10^8\,\text{GeV}$ [225–227], while for DFSZ axions

$m_a \lesssim 15 \div 20\,\text{meV}$ depending on the value of $\tan(\beta)$ [227], which is stronger than that from the ratio of horizontal branch stars and red giants. However, these limits are based on supernova core collapse simulations and their reliability is being disputed [228].

Having considered some of the bounds on axions that are dependent on the strength of their interaction to light and matter, let us now discuss black hole superradiance which is based completely on gravitational interactions and thus places bounds on axions that depend only on their masses. For the QCD axion such bounds rule out a region at high symmetry breaking scale, which is otherwise inaccessible to observations that rely on axion's couplings. The point is that light bosonic field such as the QCD axion and ALPs extract energy and angular momentum from spinning black holes of size comparable to their Compton wavelength through the Penrose process [229, 230]. Such bosons are trapped into energy levels around the black hole, allowing them to continuously take away its energy, which in turn exponentially amplifies their occupation numbers [231, 232]. Thus spinning black holes that have been observed can be used to exclude the existence of light bosons of specific masses, which would have otherwise resulted in the black holes losing much of their rotational energy [79, 233–238]. For stellar mass black holes this excludes a range of masses $10^{-13}\,\text{eV} < m_a < 10^{-11}\,\text{eV}$, which for the QCD axion translate into a bound $f_a \lesssim 2 \times 10^{17}\,\text{GeV}$.

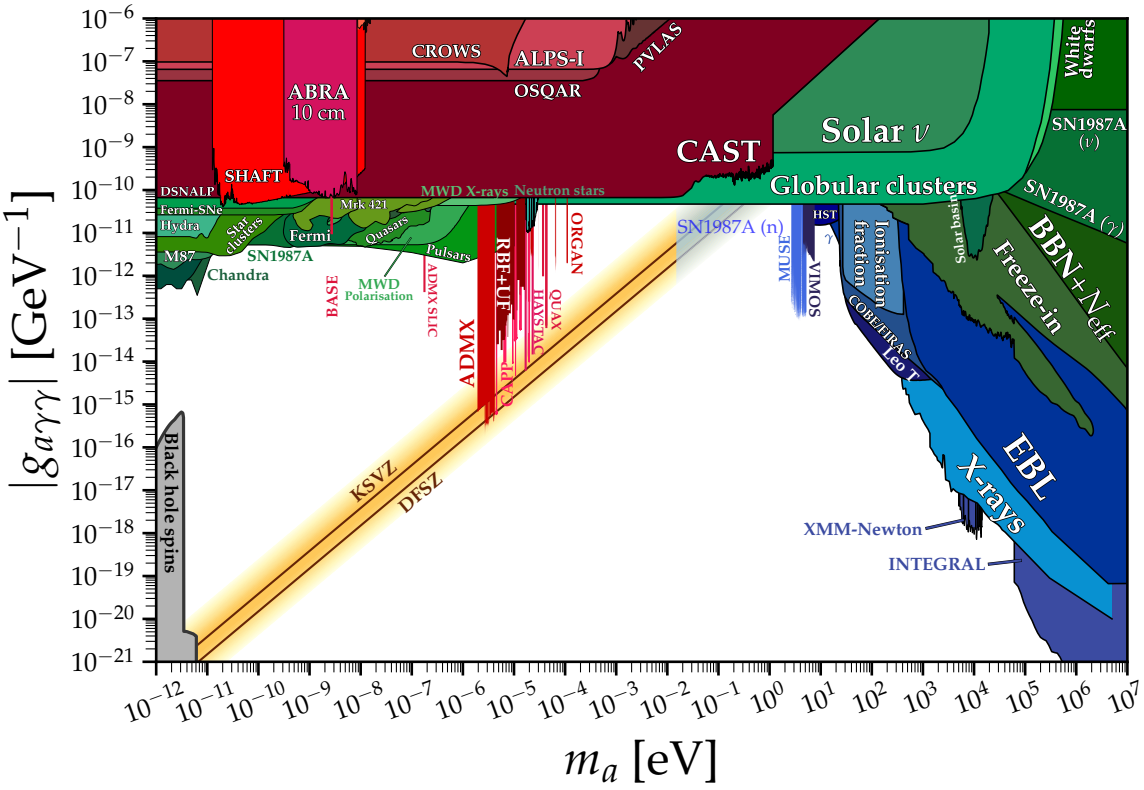

Figure 2.1: Axion parameter space in terms of mass m_a and coupling to photons $g_{a\gamma\gamma}$. Figure reproduced by using the Python notebook available at [239], where complete references to the data can be found. Red regions mark exclusions by direct detection experiments (helioscopes, haloscopes, LSW). Green regions represent exclusions from astrophysical searches for axions which are independent of the fraction of DM that axions make up. Blue regions represent exclusions from astrophysical searches which rely on DM axions. The grey region labeled "Black hole spins" represents the bounds from black hole superradiance in [238], which assume a relation between the self-coupling of the ALP field λ_a and the coupling to photons $g_{a\gamma\gamma}$ that is the same as for the QCD axion (normally for a generic ALP the symmetry breaking scale does not fix the ALPs couplings, but for the QCD axion it does, up to model dependent order 1 constants). Additionally I have modified the plot to include the blurred light blue region labeled "SN1987A (n)", which does not represent bounds on the axion-photon coupling but instead approximate model dependent bounds on QCD axion mass from the supernova 1987a, which restricts axion nucleon coupling as explained in the text.

Chapter 3

Quantum fluctuations

3.1 Introduction

In this Section I review quantum fluctuations of scalar fields during inflation following the relevant sections of [240,241] and explain how the field configuration at the end of inflation can be determined through the Langevin and Fokker-Planck equations. By applying this to the radial mode and axion I show how this relates to the formation of strings and domain walls in the following Chapter.

For this we consider a real scalar field Ψ that is not the inflaton, with a potential $V(\Psi)$ that is sub-dominant during inflation, i.e. $V(\Psi) \ll H_I^2 M_P^2$, and we express it in the Heisenberg representation in terms of mode functions:

$$\Psi(\mathbf{x},t) = \int d^3\mathbf{k} \left(a_{\mathbf{k}} \Psi_{\mathbf{k}}(t) e^{-i\mathbf{kx}} + a_{\mathbf{k}}^\dagger \Psi_{\mathbf{k}}^\star(t) e^{i\mathbf{kx}} \right) , \tag{3.1}$$

where $a_{\mathbf{k}}^\dagger$, $a_{\mathbf{k}}$ are creation and annihilation operators. The mode functions satisfy the equation:

$$\ddot{\Psi}_{\mathbf{k}} + 3H_I \dot{\Psi}_{\mathbf{k}} + \left(\frac{k^2}{R^2} + m_\Psi^2 \right) \Psi_{\mathbf{k}} = 0 \, , \tag{3.2}$$

where H_I is the Hubble parameter during inflation, which is a slow varying function of time (in the sense that $\left|\dot{H}_I\right| \ll H_I^2$) and for simplicity we take to be a constant, R is the scale factor, k is the comoving momentum of the modes and m_Ψ is the mass of the field.

To gain some qualitative understanding let us start by looking at the effectively massless case. Consider a mode that is initially sub-horizon, with a wavelength much smaller than the size of the horizon $k \gg RH_I$, then (3.2) simplifies to:

$$\ddot{\Psi}_{\mathbf{k}} + \frac{k^2}{R^2} \Psi_{\mathbf{k}} = 0 \, , \tag{3.3}$$

so the mode function oscillates with time dependent frequency. However, during inflation the

comoving wavelength of momentum modes rapidly increases and eventually it ends up much larger than the horizon $k \ll RH_I$. In this case (3.2) can be written as:

$$\ddot{\Psi}_{\mathbf{k}} + 3H_I\dot{\Psi}_{\mathbf{k}} = 0\,, \tag{3.4}$$

which is straightforward to integrate:

$$\Psi_{\mathbf{k}}(t) = A(\mathbf{k}) + B(\mathbf{k})e^{-3H_I t}\,. \tag{3.5}$$

The time dependent part quickly becomes negligible, meaning the mode function is constant in time on super-horizon scales.

It is said that modes "exit" the horizon when their wavelength becomes larger than the Hubble length $k \lesssim RH_I$ and these modes are "frozen" since their amplitude will remain constant until after the end of inflation, when the size of the horizon increases to be again larger than the wavelength $k \gtrsim RH$ and modes "re-enter".

To see this in a more precise way it is useful to work in terms of the conformal time $\tau = -1/(H_I R_0 e^{H_I t})$, which can vary from $-\infty$ in the limit of far past $t \to -\infty$ to zero at the end of inflation, and re-scale the mode functions $\nu_{\mathbf{k}} = R\Psi_{\mathbf{k}}$. We now re-write eq. (3.2) in the form of the Mukhanov equation:

$$\frac{d^2\nu_{\mathbf{k}}}{d\tau^2} + \left(k^2 - \frac{1}{R}\frac{d^2R}{d\tau^2}\right)\nu_{\mathbf{k}} = 0\,. \tag{3.6}$$

This is the general form of the Mukhanov equation, however in the case of constant H_I it simplifies to:

$$\frac{d^2\nu_{\mathbf{k}}}{d\tau^2} + \left(k^2 - \frac{2}{\tau^2}\right)\nu_{\mathbf{k}} = 0\,. \tag{3.7}$$

This is a good time to introduce a subtlety relating to quantum fields in curved space-time: there is not a unique choice for the mode function and thus no unique vacuum. To solve this we need to specify an extra boundary condition to fix the vacuum, the standard choice in the literature being the Bunch-Davies vacuum [242]. This requires that in the limit $\tau \to -\infty$ the vacuum state is the Minkowski vacuum, which for the mode function means $\nu_{\mathbf{k}} = e^{-ik\tau}/\sqrt{2k}$, fixing the solution of (3.7) to:

$$\nu_{\mathbf{k}} = \frac{e^{-ik\tau}}{\sqrt{2k}}\left(1 - \frac{i}{k\tau}\right)\,. \tag{3.8}$$

Taking (3.9) in the limit $t \to \infty$ or equivalently $\tau \to 0$ we find:

$$|\Psi_{\mathbf{k}}| = |\nu_{\mathbf{k}}/R| \to \left|\frac{1}{\sqrt{2k^3}R\tau}\right| = \frac{H_I}{\sqrt{2k^3}}\,, \tag{3.9}$$

which confirms our qualitative understanding that after sufficiently long time momentum modes end up frozen.

If we now move to the case where Ψ is a massive non-interactive field of mass m_Ψ eq. (3.7) is modified to:

$$\frac{d^2\nu_{\mathbf{k}}}{d\tau^2} + \left[k^2 - \frac{1}{\tau^2}\left(\chi_\Psi^2 - \frac{1}{4}\right)\right]\nu_{\mathbf{k}} = 0\,, \tag{3.10}$$

where $\chi_\Psi^2 = 9/4 - m_\Psi^2/H_I^2$. This can be solved generally in terms of the Hankel functions of the first and second kind $H^{(1)}_{\chi_\Psi}$, $H^{(2)}_{\chi_\Psi}$ when χ_Ψ is real, which is the case for both the axion and radial mode in the region we are interested in. Indeed axions are typically massless during inflation, while for the radial mode relevant values of m_r, H_I for string formation are such that $m_r^2/H_I^2 \lesssim \mathcal{O}(0.5)$, as can be seen in the summary of our results in Figure 4.9.

Similarly to the massless case the solution is fixed by the Bunch-Davies vacuum: in the limit $\tau \to -\infty$ to $\nu_{\mathbf{k}} = e^{-ik\tau}/\sqrt{2k}$. This boundary condition is enough to fix the solution to:

$$|\Psi_{\mathbf{k}}| = \frac{\sqrt{\pi}}{2R\sqrt{RH_I}}\left|H^{(1)}_{\chi_\Psi}\left(\frac{k}{H_I R}\right)\right|\,, \tag{3.11}$$

where $H^{(1)}_{\chi_\Psi}$ is the Hankel function of the first kind. We then take this solution in the super-horizon limit $k \ll RH_I$:

$$|\Psi_{\mathbf{k}}| = \frac{H_I}{\sqrt{2k^3}}\left(\frac{k}{RH_I}\right)^{3/2-\chi_\Psi}\,. \tag{3.12}$$

The solutions (3.11) and (3.12) are valid if χ_Ψ is real i.e. $m_\Psi/H_I < 3/2$. As a side note, if the field has large mass $m_\Psi/H_I > 3/2$ super-horizon modes are no longer frozen, instead their amplitude decreases exponentially:

$$|\Psi_{\mathbf{k}}| = e^{-\pi\mu_\Psi/2}\frac{\sqrt{\pi}}{2R\sqrt{RH_I}}\left|H^{(1)}_{i\mu_\Psi}\left(\frac{k}{H_I R}\right)\right|\,, \tag{3.13}$$

where $\mu_\Psi = \sqrt{m_\Psi^2/H_I^2 - 9/4}$ is real in this case.

3.2 Langevin equation

A standard method to consider quantum fluctuations is the stochastic formalism [243, 244], which involves the introduction of a momentum cutoff to separate the far IR modes that have left the horizon from the modes that are either sub-horizon or have just left the horizon[1]. It has been shown that far super-horizon modes behave classically [243], contributing a c-number to the average value of the field inside the horizon $\overline{\Psi}$, while the short wavelength modes are quantum fluctuations that act as a small perturbation of the average $\delta\Psi$. The point is that for super-horizon modes $k < H_I R$

[1]This is required because for self-interacting fields it was found that a divergence appears in the 4-point and higher correlation functions [245].

the occupation numbers are of the order [240]:

$$n_{\mathbf{k}} \sim \left(\frac{H_I R}{k}\right)^4 , \tag{3.14}$$

which become very large for modes that have left the horizon for a long time $H_I R \gg k$, while being $\lesssim \mathcal{O}(1)$ when the modes were sub-horizon. As the sub-horizon modes exit the horizon, they end up contributing a random amount to $\overline{\Psi}$, corresponding to their phase at the time they become "frozen".

It is standard to re-write eq. (3.1) in the following way:

$$\Psi(\mathbf{x},t) = \overline{\Psi}(\mathbf{x},t) + \delta\Psi = \overline{\Psi}(\mathbf{x},t) + \int d^3\mathbf{k}\,\Theta\left(k - R\epsilon H_I\right)\left(a_{\mathbf{k}}\Psi_{\mathbf{k}}(t)e^{-i\mathbf{kx}} + a^\dagger_{\mathbf{k}}\Psi^\star_{\mathbf{k}}(t)e^{i\mathbf{kx}}\right) , \tag{3.15}$$

where $\overline{\Psi}(\mathbf{x},t)$ represents the average value of the field inside a region of radius $1/(\epsilon H_I)$, which is meant to be somewhat larger than the horizon. Meanwhile, the step function Θ separates modes that have wavelength shorter than this radius from those with wavelength larger than this radius. As explained, the short wavelength modes are quantised and are treated as perturbations of the long wavelength modes, which in turn contribute to the average value $\overline{\Psi}(\mathbf{x},t)$ and behave classically. Here ϵ is a parameter that distinguishes whether a mode is considered "long" or "short" wavelength in this approximation and is not to be confused with the slow-roll parameter $-\dot{H}_I/H_I$.

We perform a so-called coarse graining procedure, dividing our space into patches of size $1/(\epsilon H_I)$, each having a corresponding value for $\overline{\Psi}(\mathbf{x},t)$ which is uniform inside the patch. It is convenient to absorb the (slow) time dependence of H_I into the parameter ϵ such that the product ϵH_I is constant, this way the patches we divided the space into are of constant size. We would like these patches to be sufficiently larger than the size of the horizon during inflation so that the amplitude of the modes with wavelength the size of the patch can be estimated by (3.9) or (3.12) for massless and massive field respectively, this corresponds to $\epsilon < 1$.

Let us now derive an equation for the evolution of the average field value over patches of size $1/(\epsilon H_I)$, which is $\overline{\Psi}(\mathbf{x},t)$ from eq. (3.15) above. A detailed derivation is given in [246], which I am following here while adding discussion regarding some points. Upon breaking $\Psi = \overline{\Psi} + \delta\Psi$ as above we can re-write the equation of motion for Ψ, expanding around $\overline{\Psi}$ up to the first order in $\delta\Psi$:

$$\ddot{\overline{\Psi}} + 3H_I\dot{\overline{\Psi}} - \frac{1}{R^2}\delta^{ij}\partial_i\partial_j\overline{\Psi} + \frac{dV(\overline{\Psi})}{d\overline{\Psi}} + \delta\ddot{\Psi} + 3H_I\delta\dot{\Psi} - \frac{1}{R^2}\delta^{ij}\partial_i\partial_j\delta\overline{\Psi} + \delta\Psi\frac{d^2V(\overline{\Psi})}{d\overline{\Psi}^2} = 0\,. \tag{3.16}$$

In the following we can neglect the spatial derivative of the average value of the field $\frac{1}{R^2}\delta^{ij}\partial_i\partial_j\overline{\Psi}$ compared to $H_I\dot{\overline{\Psi}}$ [243]. Additionally we neglect the second time derivative $\ddot{\overline{\Psi}}$, which is self-consistent if $\partial_{\Psi\Psi}V(\Psi) \ll 9H_I^2$. For light fields compared to H_I this happens in the vicinity of the minimum of the potential, and since in Chapter 4 where we apply these results we work with the radial mode initially starting in the vacuum, this is a safe assumption to make.

Expanding this using (3.15) and the fact that the time derivative of the step function is:

$$\frac{\partial}{\partial t}\Theta\left(k - R\epsilon H_I\right) = \frac{\partial\left(k - R\epsilon H_I\right)}{\partial t}\frac{\partial\Theta}{\partial\left(k - R\epsilon H_I\right)} = -\epsilon R H_I^2 \delta\left(k - R\epsilon H_I\right) , \tag{3.17}$$

results in a rather long equation. Fortunately some of the terms in this equation also appear in the equation of motion for the short wavelength modes (3.2), so they can be cancelled out[2]. After this the remaining equation is:

$$3H_I\dot{\overline{\Psi}} + \frac{dV(\overline{\Psi})}{d\overline{\Psi}} - 3H_I^3\epsilon R\int d^3\mathbf{k}\,\delta\left(k - R\epsilon H_I\right)\left(a_{\mathbf{k}}\Psi_{\mathbf{k}}(t)e^{-i\mathbf{kx}} + a_{\mathbf{k}}^\dagger\Psi_{\mathbf{k}}^\star(t)e^{i\mathbf{kx}}\right) = 0\,. \tag{3.18}$$

We write the above in the form of a Langevin equation:

$$3H_I\dot{\overline{\Psi}} + \frac{dV(\overline{\Psi})}{d\overline{\Psi}} = \Delta(\mathbf{x},t)\,, \tag{3.19}$$

where we have denoted the integral by $\Delta(\mathbf{x},t)$. The function $\Delta(\mathbf{x},t)$ represents a stochastic (random) noise, the effects of the perturbations due to the short wavelength modes exiting the patch and becoming long wavelength.

The left hand side of eq. (3.19) correspond to the evolution of the average value of the field toward a minimum of its potential under the influence of the potential alone, which is continuously affected by the random noise described by the right hand side of the same equation. Additionally the space expands and existing patches split up into new ones, which up until the point of splitting share the history of the noise that the original patch received, but from there on evolve independently. We show this by calculating the two-point correlation $\langle\Delta(\mathbf{x_1},t_1)\Delta(\mathbf{x_2},t_2)\rangle \equiv \langle 0|\,\Delta(\mathbf{x_1},t_1)\Delta(\mathbf{x_2},t_2)\,|0\rangle$, which also sets the typical size of the noise. The first step is to replace $\Delta(\mathbf{x},t)$ and use the standard way the creation and annihilation operators act on the vacuum as well as their commutation relation[3] $\left[a_{\mathbf{k}}, a_{\mathbf{k}'}^\dagger\right] = 1/(2\pi)^3\,\delta^3(\mathbf{k}-\mathbf{k}')$. The result of this is:

$$\begin{aligned}\langle\Delta(\mathbf{x_1},t_1)\Delta(\mathbf{x_2},t_2)\rangle =& \frac{9H_I^6\epsilon^2 R_1 R_2}{(2\pi)^3}\int\frac{d^3\mathbf{k_1}d^3\mathbf{k_2}}{(2\pi^3)}\delta\left(k_1 - R_1\epsilon H_I\right)\delta\left(k_2 - R_2\epsilon H_I\right)\\ &\times\delta^3\left(\mathbf{k_1}-\mathbf{k_2}\right)e^{i(\mathbf{k_2x_2}-\mathbf{k_1x_1})}\Psi_{\mathbf{k_1}}(t_1)\Psi_{\mathbf{k_2}}(t_2)^\star\,,\end{aligned} \tag{3.20}$$

where we have denoted $R_i \equiv R(t_i)$. We chose to define the product ϵH_I to be constant in time by absorbing the time dependence of H_I into ϵ and for simplicity we also treat the extra factors of H_I^4 as constant due to the condition that the Hubble only evolves slowly during inflation as discussed in the introductory Section 1.3[4].

[2] One such term is $\delta\ddot{\Psi}$.

[3] The factor $1/(2\pi)^3$ appears in the commutation relation due to the convention for the Fourier transform in (3.1).

[4] Earlier noise is stronger as it happened when H_I was larger. This difference is not too significant if inflation proceeds in one go, but crucial if inflation is interrupted and restarted with a significantly lower H_I, as we briefly consider in Section 5.5.

After integrating the $\delta^3(k_1 - k_2)$ we move to polar coordinates, setting the z-axis along the direction $\mathbf{x_1} - \mathbf{x_2}$:

$$\begin{aligned}\langle\Delta(\mathbf{x_1}, t_1)\Delta(\mathbf{x_2}, t_2)\rangle =& \frac{9H_I^6\epsilon^2 R_1 R_2}{(2\pi)^2}\int k_1^2 dk_1 \delta\left(k_1 - R_1\epsilon H_I\right)\delta\left(k_2 - R_2\epsilon H_I\right) \\ & \Psi_{\mathbf{k_1}}(t_1)\Psi_{\mathbf{k_2}}(t_2)^\star \int_0^\pi d\theta \sin(\theta) e^{-k_1|\mathbf{x_1}-\mathbf{x_2}|\cos(\theta)}\,.\end{aligned} \tag{3.21}$$

The θ integral is straightforward to evaluate. Additionally, one of the two delta functions can be turned into $\delta\left(R_1\epsilon H_I - R_2\epsilon H_I\right) = \delta(t_1 - t_2)/(\epsilon H_I^2 R_1)$ and the integral over the momentum can be performed:

$$\langle\Delta(\mathbf{x_1}, t_1)\Delta(\mathbf{x_2}, t_2)\rangle = \frac{9H_I^6\epsilon^3 R_1^3}{2\pi^2}\left|\Psi_{\epsilon R_1 H_I}(t_1)\right|^2 \delta(t_1 - t_2)\mathrm{sinc}\left(\epsilon H_I R_1\left|\mathbf{x_1} - \mathbf{x_2}\right|\right)\,, \tag{3.22}$$

where we denote $\mathrm{sinc}(x) \equiv \sin(x)/x$. The mode with momentum $k_1 = \epsilon R_1 H_I \lesssim R_1 H_I$ is a super-horizon mode for $\epsilon < 1$ required in the stochastic formalism. As an approximation we replace the solutions that we have discussed above, for mode functions for a massless field (3.9) and for a massive non-interacting field (3.12). Upon this replacement the noise correlation becomes

$$\langle\Delta(\mathbf{x_1}, t_1)\Delta(\mathbf{x_2}, t_2)\rangle = \frac{9H_I^5}{4\pi^2}\delta(t_1 - t_2)\mathrm{sinc}\left(\epsilon H_I R_1\left|\mathbf{x_1} - \mathbf{x_2}\right|\right)\,, \tag{3.23}$$

for the massless case and

$$\langle\Delta(\mathbf{x_1}, t_1)\Delta(\mathbf{x_2}, t_2)\rangle = \frac{9H_I^5}{4\pi^2}\delta(t_1 - t_2)\mathrm{sinc}\left(\epsilon H_I R_1\left|\mathbf{x_1} - \mathbf{x_2}\right|\right)\epsilon^{3-2\chi_\Psi}\,, \tag{3.24}$$

for the massive non-interactive case.

We are interested in the distribution of the field inside the horizon at times after the end of inflation to relate it to the formation of topological defects. Thus it would be useful if we could approximate $\Psi(\mathbf{x}, t)$, the value of the field at a point after inflation, by $\overline{\Psi}(\mathbf{x}, t_{\mathrm{end}})$, the average value over the patch at the same position at the end of inflation (apart from the evolution of the field post inflation). This is possible at times after the end of inflation when a very large number of patches used in the coarse graining have re-entered the horizon, such that each patch can be treated as an infinitesimally small region, and the larger ϵ is the earlier this approximation holds in the post-inflationary Universe. Meanwhile an upper bound on ϵ comes from the fact that we replace the super-horizon limit (3.12) into equation (3.22). This works if the dominant term in the expansion of the Hankel function in equation (3.11) is the one proportional to $\epsilon^{-\chi_\Psi}$, which corresponds to $\epsilon < 2\sqrt{\chi_\Psi - 1}$. For values of H_I and m_r that are relevant to string formation (see Figure 4.9) we find that we are allowed to perform the coarse graining procedure for $\epsilon \simeq 1$ in a self-consistent way and the factor $\epsilon^{3-2\chi_\Psi}$ introduces at most an order 1 uncertainty which can be

absorbed into H_I^5 in equation (3.24)[5]. Thus in the following we use (3.23) as an approximation for the noise correlation function.

We now move to the factor sinc $(\epsilon H_I R_1 |\mathbf{x_1} - \mathbf{x_2}|)$ in (3.23) and, given that it only makes sense to consider points at distances $|\mathbf{x_1} - \mathbf{x_2}| > 1/(\epsilon H_I)$ to be distinct due to the coarse graining procedure, we see that for such points this factor quickly becomes very small due to the exponentially large R_1. On the other hand in the limit $|\mathbf{x_1} - \mathbf{x_2}| \to 0$ it is equal to 1. Thus we further approximate the correlation function

$$\langle \Delta(\mathbf{x_1}, t_1)\Delta(\mathbf{x_2}, t_2)\rangle = \frac{9H_I^5}{4\pi^2}\delta(t_1 - t_2)\delta_{\mathbf{x_1},\mathbf{x_2}}\,. \tag{3.25}$$

This is zero for points in different patches while for points in the same patch

$$\langle \Delta(\mathbf{x}, t_1)\Delta(\mathbf{x}, t_2)\rangle = \frac{9H_I^5}{4\pi^2}\delta(t_1 - t_2)\,. \tag{3.26}$$

Also it is straightforward to show:

$$\langle \Delta(\mathbf{x}, t)\rangle = 0\,. \tag{3.27}$$

Unfortunately it is impossible to solve the Langevin equation to find a unique spatial distribution of $\overline{\Psi}$ at the end of inflation, since the noise inside each patch takes a random value at each time. What we can do however is to use the Langevin equation (3.19) together with the correlations of the noise function above (3.26,3.27) to find a deterministic equation for the probability distribution of $\overline{\Psi}$.

3.3 Fokker-Planck equation

Here we derive the Fokker-Planck equation which describes the evolution of the probability distribution of $\overline{\Psi}$. As opposed to the Langevin equation which contains a stochastic noise term, the Fokker-Planck equation is fully deterministic and can thus be solved, either analytically for simple potentials of Ψ, or otherwise numerically. This however comes at the cost of losing some of the information encoded in the Langevin equation, such as the spatial distribution of the field.

For future convenience the time during inflation will be measured by the number of e-folds that have passed starting from the moment when scales that re-enter the horizon today have exited the horizon, and we denote the number of e-folds at the end of inflation by $N_{\rm tot} \simeq \mathcal{O}(60)$, which is required to solve the horizon and flatness problems. With the assumption of constant H_I the conversion from time to number of e-folds is simply $\Delta t = \Delta N/H_I$.

With this convention, we define the probability density $\rho_\Psi(\overline{\Psi}, N, \overline{\Psi}_0, N_0)$ i.e. the probability

[5] As will be seen in Section 4.5.4, it is useful to interpret various uncertainties as an equivalent uncertainty in the value of H_I that corresponds to the string network being destroyed at a given time, and these will correspond to $\mathcal{O}(1)$ factors.

that the field in a patch has average value between $(\overline{\Psi}, \overline{\Psi}+d\overline{\Psi})$ is $\rho_\Psi(\overline{\Psi})d\overline{\Psi}$ at time labeled N, with the initial condition that the distribution at some initial time labeled by N_0 was a delta function $\rho_\Psi(\overline{\Psi}, N_0, \overline{\Psi}_0, N_0) = \delta\left(\overline{\Psi} - \overline{\Psi}_0\right)$. Here N_0 and Ψ_0 do not mean quantities today, but rather at some initial time during inflation, which is convenient to be identified by the time when scales the size of the horizon today exited the horizon. The reason for this choice of initial conditions is that if we look at the probability distribution ρ_Ψ over a region of size $L \gg 1/(\epsilon H_I)$ which contains a large number of patches at moment labeled N, then if we set $N_0 \lesssim N - \log(L\epsilon H_I)$ at this time this region was the size less than one patch, which had an average value of the field $\overline{\Psi}_0$. But then it is trivial that at the time N_0 the distribution was a delta function, since we sample over a single patch. Thus the reason to always consider delta function configurations for initial conditions is that for any region over which we are interested in the probability distribution during inflation, we can set our initial time far enough in the past when it was the size of (less than) a single patch. This works only if between the times of interest and the corresponding initial times the Universe is in a period of inflation with approximately constant H_I, which is reasonable given that it only makes sense to evolve the probability density for at most the number of e-folds that re-entered the horizon until today $N_{\rm tot}$.

We will now derive the Fokker-Planck equation, which describes the evolution of the probability density ρ_Ψ. I follow the steps of the derivation in [247], which is done in the context of Brownian motion and involves following a particle over the possible paths that it could have gone through due to the various noise realisations to find the probability distribution of the position of the particle. The position of particles in Brownian motion and the average value of the field $\overline{\Psi}$ are analogous in the sense that their evolution are both described by a corresponding Langevin equation.

One may be worried about what happens to the distribution as patches continuously creating other new patches during inflation. This however is not a problem once we observe that the process of patches expanding into new patches has no effect over the probability distribution. To see this, let us follow some initial set of causal patches for the time it takes for the scale factor to double and for simplicity take them to be cubic. As the scale factor doubles, each of these causal patches have expanded into 8 causal patches, so the number of patches with a specific value of $\overline{\Psi}$ increased by a factor of 8 as the scale factor doubled, but so did the total number of patches. Patches "splitting" this way as the scale factor grows does mean that regions that are located closer together have somewhat similar values of $\overline{\Psi}$ as they have shared some of the stochastic noise at earlier times, however this is the kind of information that is lost when moving from the Langevin to the Fokker-Planck equation, as the Fokker-Planck equation is only concerned with the probability distribution of $\overline{\Psi}$ over all the patches and not the spatial distribution of the field.

With the observation above it is enough to simply follow the evolution of a single initial patch over all possible noise realisations for a number of e-folds $N - N_0$. Let us start by looking at the distribution at an intermediate time and its evolution for a short time $\rho_\Psi(\overline{\Psi}, N + \delta N, \overline{\Psi'}, N)$. The

field starting from $\overline{\Psi}'$ has moved an amount:

$$\delta\overline{\Psi}(\mathbf{x}) = \frac{1}{3H_I^2}\left(-\frac{dV(\overline{\Psi})}{d\overline{\Psi}}\delta N + \int_t^{N+\delta N}\Delta(\mathbf{x},t')dN'\right), \tag{3.28}$$

where $\Delta(\mathbf{x},t')$ is the stochastic noise function appearing in the Langevin equation (3.19) and $t' = N'/H_I$ is the corresponding time to N'.

Of course if we were to know the exact noise the patch went through this probability distribution would be trivial $\rho_\Psi(\overline{\Psi}, N+\delta N, \overline{\Psi}', N) = \delta\left(\overline{\Psi} - \overline{\Psi}' - \delta\overline{\Psi}\right)$, but since multiple noise realisations are possible we must average over all of them $\rho_\Psi(\overline{\Psi}, N+\delta N, \overline{\Psi}', N) = \left\langle\delta\left(\overline{\Psi} - \overline{\Psi}' - \delta\overline{\Psi}\right)\right\rangle$.

We now proceed to Taylor expand the delta function above, only keeping the terms that are at most $\mathcal{O}(\delta N)$:

$$\rho_\Psi(\overline{\Psi}, N+\delta N, \overline{\Psi}', N) = \left(1 + \left\langle\delta\overline{\Psi}\right\rangle\frac{\partial}{\partial\overline{\Psi}'} + \frac{1}{2}\left\langle\delta\overline{\Psi}^2\right\rangle\frac{\partial^2}{\partial\overline{\Psi}'^2}\right)\delta\left(\overline{\Psi} - \overline{\Psi}'\right). \tag{3.29}$$

The mean and the correlation of the noise eqs. (3.26, 3.27) can be used to calculate

$$\left\langle\delta\overline{\Psi}\right\rangle = -\frac{\delta N}{3H_I^2}\frac{dV(\overline{\Psi})}{d\overline{\Psi}}; \qquad \left\langle\delta\overline{\Psi}^2\right\rangle = \frac{H_I^2\delta N}{4\pi^2}, \tag{3.30}$$

while further terms such as $\left\langle\delta\overline{\Psi}^3\right\rangle$ only contain terms of order $\mathcal{O}(\delta N^2)$ or higher.

Additionally, we can write the probability distribution at the final time as a conditional probability that the field is at $\overline{\Psi}$ after N e-folds given that it was at $\overline{\Psi'}$ after N' e-folds:

$$\rho_\Psi(\overline{\Psi}, N, \overline{\Psi}_0, N_0) = \int\rho_\Psi(\overline{\Psi}, N, \overline{\Psi}', N')\rho_\Psi(\overline{\Psi}', N', \overline{\Psi}_0, N_0)d\overline{\Psi}'. \tag{3.31}$$

Instead of N we write $N+\delta N$ in the above so that we can replace $\rho_\Psi(\overline{\Psi}, N+\delta N, \overline{\Psi}_0, N_0)$ from eq. (3.29) and after integrating by parts the derivatives will move from acting on delta function:

$$\rho_\Psi(\overline{\Psi}, N+\delta N, \overline{\Psi}_0, N_0) = \rho_\Psi(\overline{\Psi}, N, \overline{\Psi}_0, N_0) + \frac{1}{3H_I^2}\frac{\partial\left(\frac{dV(\overline{\Psi})}{d\overline{\Psi}}\rho_\Psi(\overline{\Psi}, N, \overline{\Psi}_0, N_0)\right)}{\partial\overline{\Psi}} + \frac{H_I^2}{8\pi^2}\frac{\partial^2\rho_\Psi(\overline{\Psi}, N, \overline{\Psi}_0, N_0)}{\partial\overline{\Psi}^2}. \tag{3.32}$$

It is straightforward to Taylor expand $\rho_\Psi(\overline{\Psi}, N+\delta N, \overline{\Psi}_0, N_0)$ directly and compare with eq. (3.32) to arrive at the Fokker-Planck equation:

$$\frac{\partial\rho_\Psi(\overline{\Psi}, N, \overline{\Psi}_0, N_0)}{\partial N} = \frac{1}{3H_I^2}\frac{\partial}{\partial\Psi}\left(\frac{dV(\overline{\Psi})}{d\overline{\Psi}}\rho_\Psi(\overline{\Psi}, N, \overline{\Psi}_0, N_0)\right) + \frac{H_I^2}{8\pi^2}\frac{\partial^2\rho_\Psi(\overline{\Psi}, N, \overline{\Psi}_0, N_0)}{\partial\Psi^2}. \tag{3.33}$$

The first term on the right side of the Fokker-Planck equation (3.33) is related to the evolution of the field under the influence of the potential alone, while the second term describes the random walk

behaviour of the field due to the random noise. In the presence of a potential the Fokker-Planck equation predicts that the probability distribution evolves towards an equilibrium distribution with $\partial\rho_\Psi/\partial N = 0$ [244]:

$$\rho_{\Psi,eq}(\overline{\Psi}) = \frac{1}{Z}\exp\left(-\frac{8\pi^2 V(\overline{\Psi})}{3H_I^4}\right), \tag{3.34}$$

where $Z = \int_{-\infty}^{+\infty}\exp\left(-\frac{8\pi^2 V(\overline{\Psi})}{3H_I^4}\right)d\overline{\Psi}$ is the appropriate normalisation factor.

In the following we are interested in applying the Fokker-Planck equation (3.33) above to the axion and radial mode of the complex PQ field. The axion will correspond to a massless non-interacting field, while the radial mode is interacting and we work with numerical solutions of the Fokker-Planck equation. Either way, it is useful to discuss the massive non-interactive case, if only to gain an intuitive understanding, and in this case the Fokker-Planck equation can be solved analytically.

We start by noticing that the solution in the massless case is a normal distribution and we check if this is a solution for the massive case as well. We start with an ansatz:

$$\rho_\Psi(\overline{\Psi}, N, \overline{\Psi}_0, N_0) = \frac{1}{\sqrt{2\pi}\sigma}e^{-\frac{(\overline{\Psi}-\Psi_m)^2}{2\sigma^2}}, \tag{3.35}$$

where $\sigma \equiv \sigma(N)$ is the standard deviation and $\Psi_m \equiv \Psi_m(N, \overline{\Psi}_0, N_0)$ is the mean of the distribution, both of which we allow to be time dependent.

By taking the average of the Langevin equation (3.19) and using eq. (3.27):

$$3H_I\left\langle\dot{\overline{\Psi}}\right\rangle + \left\langle\frac{dV(\overline{\Psi})}{d\overline{\Psi}}\right\rangle = \langle\Delta(\mathbf{x},t)\rangle = 0\,. \tag{3.36}$$

Replacing the potential $V(\Psi) = (1/2)m_\Psi^2\Psi^2$ we find that we can treat the mean of the distribution $\Psi_m = \left\langle\overline{\Psi}\right\rangle$ as a field of mass m_Ψ evolving only under the influence of the potential (the noise average is 0).

Replacing the ansatz into the Fokker-Planck equation (3.33) we also find a condition for σ:

$$\frac{1}{\sigma}\frac{d\sigma}{dN} + \frac{m_\Psi^2}{3H_I^2} - \frac{H_I^2}{8\pi^2\sigma^2} = 0\,, \tag{3.37}$$

which we can re-write as:

$$\frac{d\sigma^2}{dN} = \frac{H_I^2}{4\pi^2} - \frac{2m_\Psi^2}{3H_I^2}\sigma^2\,. \tag{3.38}$$

The solution is Gaussian with mean evolving towards $\Psi_m = 0$ as described in equation (3.36) and variance increasing over time given our usual initial condition for the distribution which is a delta function. It eventually reaches an equilibrium distribution, which is Gaussian with mean $\Psi_m = 0$ and variance $\sigma^2 = 3H_I^4/(8\pi^2 m_\Psi^2)$. The solution for the massless, non-interacting case

follows by setting $m_\Psi = 0$ and is a Gaussian distribution with mean the initial value of the field and variance continuously increasing:

$$\sigma^2 = \frac{N H_I^2}{4\pi^2} \,. \tag{3.39}$$

3.4 Approximate field distribution from the Langevin equation

It should be clear that we cannot solve the Langevin equation (3.19) exactly, as the noise function $\Delta(\mathbf{x}, t)$ takes random values at different positions and times. If we knew the exact probability distribution of the noise we would in principle be able simulate the evolution of the field corresponding to the Langevin equation numerically, by simply applying random kicks to the field over infinitesimal times δN and then solving for the evolution between kicks. Such a procedure would produce one of the many possible realisations of the evolution of the field.

Unfortunately we do not know the exact distribution of the noise, which would require to calculate the higher point correlation functions of $\Delta(\mathbf{x}, t)$ just like we did for the two-point correlation. While for odd point the correlation function is trivially zero as all the terms contain an odd number of creation and annihilation operators, the correlation function for even point are quite difficult to calculate. Fortunately a Gaussian distribution for the noise function is a good approximation, to see this more precisely let us start by following the evolution of one patch for negligible potential. Over a time interval $\Delta N = n\,\delta N$ the field has moved by a random amount $K = \delta\overline{\Psi}_1 + \delta\overline{\Psi}_2 + ... + \delta\overline{\Psi}_n$, where $\delta\overline{\Psi}_i$ are small random kicks, each corresponding to the effect of the noise over an infinitesimally small time step δN. The exact distribution of $\delta\overline{\Psi}_i$ is unknown, however its mean and variance are given by equation (3.30). It follows from the Central Limit Theorem that in the limit $n \to \infty$ the distribution for their sum K is Gaussian with mean 0 and variance $\Delta N H_I^2/(4\pi^2)$. Thus in the absence of the potential we can approximate the evolution of $\overline{\Psi}$ by kicking the field by an amount K distributed as above every ΔN e-folds.

Moving to a non-zero potential the situation is complicated by the fact that at intermediate times between N and $N + \Delta N$ the value of the field is unknown due to the distribution of $\delta\overline{\Psi}$, which translates into unknown field evolution due to the potential $-\delta N/(3H_I^2)\left(dV(\overline{\Psi})/d\overline{\Psi}\right)$. We show in Appendix B that if the gradient of the potential is small enough

$$\left|\frac{dV(\overline{\Psi})}{d\overline{\Psi}}\right| \ll \frac{H_I^3}{2\pi\sqrt{\Delta N}} \,, \tag{3.40}$$

then the evolution of the field is well approximated by kicking the field by an amount K and then following the evolution in the absence of noise for a time ΔN.

A procedure to simulate the Langevin equation (3.19) would thus be as follows. We discretise the space on a grid where each point corresponds to a coarse graining patch of physical size $1/(\epsilon H_I)$ and discretise time in steps of size ΔN which we choose such that the inequality in eq. (3.40) holds. We then apply a kick K to each grid point which is a random quantity normally distributed with

mean 0 and variance $\Delta N H_I^2/(4\pi^2)$ as explained above and compute the evolution in the absence of noise at each point until the next time step when another kick is applied. Additionally when the scale factor would double in size which happens every log(2) e-folds, we split each point into 8 grid point with the same value of the field initially and which subsequently evolve independently. To do this splitting it is convenient to pick ΔN such that the ratio between the time it takes for the scale factor to double in size and the time step ΔN is an integer.

This procedure will be useful when generating realistic initial conditions at the end of inflation for numerical simulations of the PQ field. The probability distribution of the field values obtained this way clearly obeys the Fokker-Planck equation (3.33), for which only the correct mean and variance of the noise function are necessary. Additionally, this procedure has an advantage over simply allocating to each grid point a random value distributed according to the Fokker-Planck equation in that it retains some of the information encoded in the Langevin equation that is otherwise lost, in particular the field in closer grid points takes similar values since they have shared some of the earlier kicks.

Chapter 4

The edge of symmetry restoration

4.1 Introduction

In this Chapter we consider in more detail the boundary between the pre- and post-inflationary scenarios. To do so we focus on the simplest axion theory that consists of a complex scalar with a potential (2.29), and we comment at the end of the Chapter on how our results and analysis could be adapted to more general axion theories. Here we assume that quantum fluctuations during inflation are the main ingredient that result in the formation of strings and domain walls, i.e. we assume that PQ symmetry has not been restored after the end of inflation by thermal or non-thermal fluctuations and also that it has not been restored by other mechanisms during the last $N_{\rm tot}$ e-folds of inflation which have re-entered the horizon up until today, such as a coupling between the inflaton and the PQ field. In particular, this is the case provided

$$\Gamma_\varphi \lesssim \mathcal{O}\left(\frac{v_a^4}{H_I M_P^2}\right), \tag{4.1}$$

for the inflaton decay rate Γ_φ to not generate a too large temperature, which is discussed in Section 5.3, as well as a sufficiently small coupling of the PQ field to the inflaton which is discussed in Section 5.1. Additional details on alternative ways to restore PQ symmetry can be found in Chapter 5.

As discussed in Section 2.4, it is typical in the literature to consider two extreme scenarios. The post-inflationary scenario for $H_I \gtrsim 2\pi v_a$ is associated with the formation of numerous topological defects such as strings and domain walls that reach a scaling regime, as well as a fully randomised axion field. Meanwhile the pre-inflationary scenario $H_I \ll 2\pi v_a$ is associated with negligible topological defects and an approximately uniform axion field. The idea is that during inflation each e-fold kicks the axion and the radial mode by random amounts of typical size $H_I/(2\pi)$, so the post-inflationary scenario is roughly equated with the radial mode moving over the top of the symmetry breaking potential and the axion exploring the full fundamental domain over order one e-folds, while the pre-inflationary scenario corresponds to negligible spatial changes in the axion field due

to small quantum fluctuations.

Here we focus on the region between these two scenarios, in which fluctuations accumulated over many e-folds of inflation are significant to form strings and domain walls, but not so large as to fully randomise the field over one e-fold. In doing so, we pin down the boundary between the pre- and post-inflationary scenarios more precisely, up to uncertainties due to the not fully known details of the destruction of strings/domain walls network as discussed in Section 4.5.4 and under the assumption that the behaviour of the string network we observed in numerical simulations and present in Section 4.4 is applicable to later times, which are otherwise inaccessible to numerical simulations. We also uncover an intermediate regime interpolating between the post- and pre-inflationary scenarios that allows the QCD axion to comprise the full dark matter relic abundance with a larger mass than would otherwise be possible.

Intuitive summary of our results

Before proceeding to our detailed analysis, which will be backed up by results from numerical simulations, it is useful to give a simple intuitive description of the intermediate regime at the edge between the post- and pre-inflationary scenarios.

An important observation is that strings will form at points where quantum fluctuations have pushed the radial mode over the top of the potential, as once the field around these point settles around the various vacua there must be some region kept at the top of the potential due to the continuity of the field. It would be ideal if we could also quantitatively connect the size of quantum fluctuations in the radial direction to the formation of strings by relating the probability that the radial mode has been pushed over the top of the potential inside a causal region some time after the end of inflation to the density of strings inside the same region. We show using numerical simulations how this can be done, which for a particular UV completion of the QCD axion would give a sharp prediction of the conditions for strings to form.

To explain what is meant by the fluctuations "accumulating", we start by assuming the Universe is radiation dominated instantly after the end of inflation, i.e. immediate decay of the inflaton and thermalisation, and we leave a brief discussion on how our results could be adapted to an early period of matter domination during reheating to Section 4.5.4. Let us follow a specific patch of the Universe that exited the horizon N e-folds before the end of inflation and denote the average value of the radial mode and axion over this patch at the time of exiting by r_0, a_0 respectively. By the end of inflation this patch will be inflated into an exponentially large number of causally disconnected new patches, which will all re-enter the horizon at a time when the Hubble parameter H is given by:

$$\frac{1}{H} = \frac{1}{H_I} e^N \frac{R}{R_I}\,, \tag{4.2}$$

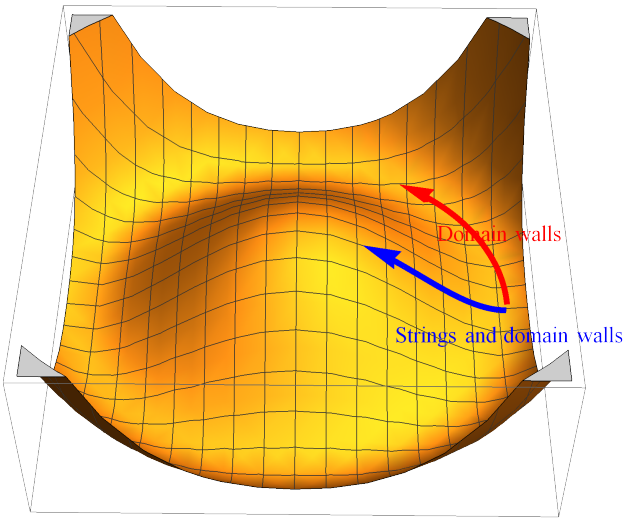

Figure 4.1: Schematic representation of the role of quantum fluctuations in the formation of topological defects. Radial fluctuations form strings when the pass over the top of the potential, and subsequently domain walls resting on them. Angular fluctuations form closed domain walls as they pass $\theta = \pi$, but not necessarily strings.

where R_I is the scale factor at the end of inflation and in a radiation dominated Universe we have

$$\frac{R}{R_I} = \sqrt{\frac{H_I}{H}}\,, \tag{4.3}$$

which means

$$e^N = \sqrt{\frac{H_I}{H}}\,. \tag{4.4}$$

The radial mode and axion fields inside these patches that have re-entered up to this point were distributed at the end of inflation according to the solutions of Fokker-Planck equations (3.33) which evolved for N e-folds, corresponding to their respective potentials. As explained in Section 3.3 the initial condition for the probability distribution before the final N e-folds of inflation was a delta function for both the radial mode $\delta(r-r_0)$ and the axion $\delta(a-a_0)$. The distributions of radial mode and axion that solve the respective Fokker-Planck equations are wider at the end of inflation the larger N is.[1] Thus the more e-folds re-enter the horizon the more randomized the axion and radial mode are inside the horizon, so the more likely the radial mode has passed over the top of the potential to form strings, and similarly the more likely the angle θ passed over π to form domain walls. This is both because we are taking more samples of the probability distribution as more patches of size $1/H_I$ that were causally disconnected at the end of inflation have re-entered, but primarily because the probability distributions we are sampling over have spread with the number

[1] Up to an eventual equilibrium distribution if N is large enough.

of e-folds. We can see that the way the fluctuations accumulate as the Hubble horizon grows after inflation leads to the possibility that a network of strings forms only late, once the probability the radial mode has passed over the top of the potential inside the horizon is sufficient[2]. Likewise, even for small radial mode fluctuations and consequently in the absence of strings, angular fluctuations similarly accumulate and may create domain walls.

Since we expect radial mode fluctuations to lead to strings (and consequently domain walls), while angular fluctuations lead to domain walls without strings, it is time to consider the fluctuations in these directions separately.

4.2 Negligible radial mode fluctuations

First let us consider the case of small radial mode fluctuations, where the axion field at the end of inflation is given by the solution to the Fokker-Planck equation (3.33) with the field $\Psi = a$ replaced by the axion and no strings form. This corresponds to the case of a radial potential that is sufficiently steep so fluctuations in this direction are negligible even if they accumulated over $N_{\rm tot}$ e-folds.

In typical theories of inflation $m_a \ll H_I$ as well as $\Lambda_{\rm QCD} \ll H_I$, so the axion has effectively no potential. However it is interesting to mention the results for the situation $H_I \lesssim \Lambda_{\rm QCD}$ which has been considered in [248, 249]. In this case the axion has a mass and will eventually reach an equilibrium distribution if inflation lasts for a large number of e-folds $\gtrsim \mathcal{O}(H_I^{10}/m_a^2\Lambda_{\rm QCD}^8)$. The equilibrium distribution is strongly peaked in the minima of the axion potential with very small variance controlled by the size of H_I. This means that the initial misalignment angle is no longer a free parameter as in the usual pre-inflationary scenario, but rather $\langle\theta^2\rangle \sim 10^{-6}\,(H_I/\Lambda_{\rm QCD})^{12}$, which is naturally small while the usual isocurvature constraints present in the pre-inflationary scenario are satisfied since $H_I \lesssim \Lambda_{\rm QCD} \ll f_a$.

Back to the case of negligible axion potential, as we have seen in Section 3.3 the solution to the Fokker-Planck equation (3.33) for a massless field starting from a delta function initial distribution is a Gaussian distribution with constant mean and a variance increasing linearly with the number of e-folds elapsed $\sigma_a^2 = NH_I^2/(4\pi^2)$. At a time after the end of inflation when $N_{\rm re}$ e-folds have re-entered the horizon, the axion fluctuations inside the horizon have been produced during the final $N_{\rm re}$ e-folds of inflation. It was argued in [197, 198] (see also [250]) that if the variance of the distribution of the field inside the horizon is sufficiently large

$$\sigma_a = \frac{\sqrt{N_{\rm re}}H_I}{2\pi} \gtrsim \pi f_a\,, \tag{4.5}$$

then domain walls will form that are larger than the size of the horizon at the time when $N_{\rm re}$

[2]By a network forming we mean that strings are at a distance typically the size of the horizon. Strings still exist even before, but they are very rare and far apart, at distances much larger than the horizon.

e-folds re-enter. The problem with these walls is that, in the absence of the strings that would collapse them, they will be stable while they are larger than the size of the horizon and they will dominate the energy density at late times, even if $N_{\rm DW} = 1$ or if an energy bias is present reducing the number of inequivalent minimums of the axion potential to one. The point is that even with a single minimum of the potential, walls form at places where the axion was at the maximum of its potential and interpolate between regions that have reached the same vacuum while the complex PQ field moved over opposite sides of the bottom of the Mexican hat potential described by (2.29).

Therefore, in the absence of strings there is a necessary condition that there is no such domain wall larger than the horizon today

$$\frac{\sqrt{N_{\rm tot}} H_I}{2\pi} \lesssim \pi f_a \,. \tag{4.6}$$

Additionally an estimation of the number density of wall bubbles of any size in [197] translates to less than one bubble having re-entered the horizon if:

$$\frac{\sqrt{N_{\rm tot}} H_I}{2\pi} \lesssim \frac{\pi f_a}{12} \,. \tag{4.7}$$

The situation between these limits is rather complicated and we do not consider it in detail. However we remark that such values of $H_I/v_a \sim \mathcal{O}(1)$ would be ruled out by isocurvature in the absence of domain walls if the axion makes up a significant fraction of DM [201], and the presence of decaying domain walls can only tighten these bounds, as they are located at regions where the axion is close to the top of the potential $a = \pi v_a$, precisely where the largest contribution from the misalignment is coming from.

We conclude that in the case of small radial fluctuations domain walls can only have a negligible contribution to axion density compared to the DM density, as all the other possibilities are ruled out either by stable domain walls dominating the energy density today or by isocurvature. A necessary condition for the standard pre-inflationary scenario is eq. (4.7) which corresponds to the absence of walls, together with the characteristic isocurvature constraints [192–199, 201–203], which require $H_I \ll f_a$ if the axion makes up a significant fraction of DM. If condition (4.7) holds it is also likely that strings do not re-enter the horizon until today, as we discuss in subsequent Sections.

4.3 Radial mode fluctuations

Once radial fluctuations are large enough for the field to go over the top of the PQ potential the distribution of the axion field is no longer determined by the fluctuations in the angular direction alone. Firstly, the field displacement required to go from $a = 0$ to $a = \pi v_a$ is larger when going around the circle than over the top. Additionally, the effect of axion fluctuations is also enhanced when the radial mode is closer to the top of the potential, since a kick of the same size of the axion field now results in a larger angular displacement due to the reduced radius. This leads to a

complicated description of the axion spatial distribution at the end of inflation and consequently at the time the axion mass becomes relevant, which we do not attempt to consider in detail.

Instead, we recognize that radial fluctuations are the important ingredient to the formation of strings, during which the axion field around strings is adjusted in such a way as to explore the full fundamental domain around a closed loop. Meanwhile the complicated distribution of the axion field away from the strings is only relevant to the calculation of the axion misalignment contribution, which is not the dominant one in the post-inflationary and the intermediate scenario we will uncover. On the other hand in the pre-inflationary scenario the radial mode remains approximately in the vacuum so the treatment of the previous Section 4.2 can be applied.

The effect of quantum fluctuations in the radial mode has been previously considered in [251] which finds approximate solutions to the Fokker-Planck equation in the limits $H_I^4/v_a^4 \ll \lambda$ and $H_I^4/v_a^4 \gg \lambda$ and identifies these with the pre- and post-inflationary scenario respectively.[3]

More specifically, in [251] the complex PQ field is written in term of its real and imaginary part $\phi = (\phi_1 + i\phi_2)/\sqrt{2}$ with ϕ_1 and ϕ_2 being real fields with canonically normalised kinetic terms, each evolving according to a respective Langevin equation (3.19) during inflation. This gives rise to an individual Fokker-Planck type equation for each field, which after moving to polar coordinates $(\phi_1, \phi_2) \to (\sqrt{2}\,|\phi|\,, \theta)$ and integrating over θ results in an equation for the probability distribution of $|\phi|$ reproduced here:

$$\frac{2\pi}{v_a}\sqrt{\frac{3}{\lambda}}\frac{\partial \rho_{|\phi|}}{\partial N} = \frac{1}{4\sqrt{2}}\frac{\partial^2 \rho_{|\phi|}}{\partial\,|\phi|^2}\zeta^2 v_a + \frac{1}{4}\frac{\partial}{\partial\,|\phi|}\left[\left(\frac{4\sqrt{2}\,|\phi|\,(\sqrt{2}\,|\phi| + v_a)(\sqrt{2}\,|\phi| - v_a)}{\zeta^2 v_a^3} - \frac{v_a\zeta^2}{\sqrt{2}\,|\phi|}\right)\rho_{|\phi|}\right], \tag{4.8}$$

where $\zeta = \left(\frac{3H_I^4}{2\pi^2\lambda v_a^4}\right)^{1/4}$, and $\rho_{|\phi|}$ is the probability distribution for the absolute value of the complex PQ field.

In the limit $\zeta \ll 1$ the equilibrium distribution of eq. (4.8) is strongly peaked in the vacuum, which corresponds to the field being stuck in the vacuum with fluctuations too small to bring it over the top of the potential and form strings.[4] Additionally if $\zeta \ll 1$ and perturbative self-coupling $\lambda \lesssim \mathcal{O}(1)$, the condition to avoid domain walls in the absence of strings (4.7) we have discussed in Section 4.2 holds, so this limit clearly leads to the standard pre-inflationary scenario.

Conversely in the limit $\zeta \gg 1$ the distribution is very spread and large values $|\phi| \gg v_a$ are common, meaning it is likely that the radial mode was pushed over the top of the potential inside regions the size of the horizon $1/H_I$ at the end of inflation. This is expected to lead to the formation of numerous strings once many Hubble patches at the end of inflation will have re-entered the

[3] It is interesting that even though the radial mode is self-interacting, a qualitatively similar conclusion could be reached by comparing the equilibrium variance for a massive non-interactive field discussed in Section 3.3 $\sim H_I^4/m_r^2 \sim H_I^4/(\lambda v_a^2)$ to the distance squared between the vacuum and the top of the potential v_a^2.

[4] In fact in our single field approach that is introduced bellow, it can be shown that fluctuations would need to accumulate for an exponentially large number of e-folds $N \sim e^{1/(2\zeta^4)}$ before the probability that the field passed over the top of the potential is $\mathcal{O}(1)$ [244].

horizon, which interact to reach the scaling regime characteristic to the standard post-inflationary scenario.

Our approach differs from that in [251] since we are interested in exploring the situation between the limits $\zeta \gg 1$ and $\zeta \ll 1$. Since we expect that string formation corresponds to the radial mode passing over the top of the potential we consider the fluctuations in the radial direction separately from the angular fluctuations to find the condition to form strings. We do so by looking at a slightly modified theory in which we consider a real field which we denote $\tilde{r}$ with a potential:

$$V_{\tilde{r}}(\tilde{r}) = \frac{\lambda}{4}\left(\tilde{r}^2 - v_a^2\right)^2 . \tag{4.9}$$

The field $\tilde{r}$ has a similar potential to that of the radial mode, with the exception that its potential exhibits a $\mathbb{Z}_2$ instead of a $U(1)$ symmetry and it is allowed to take any value (compared to the radial mode as defined in eq. (2.27) which only takes values larger than $-v_a$). We would then apply the Fokker-Planck equation (3.33) by replacing the generic field Ψ with $\tilde{r}$ to find the probability distribution of $\tilde{r}$ and relate this to the string density via numerical simulations presented in Section 4.4. While this one field system is not identical to the complex PQ field it has some advantages:

- The solution of the Fokker-Planck equation for the field $\tilde{r}$ quantitatively captures the difficulty of pushing $\tilde{r}$ over the top of the potential, which we expect is necessary to form strings. Meanwhile the Fokker-Planck solution to the full complex potential does not distinguish between the field passing over the top of the potential through radial fluctuations and rotating to the other side along the flat axion direction.

- It is numerically less demanding to solve the Fokker-Planck equation for the one field $\tilde{r}$ than it is for the two component PQ field. This is helpful when exploring the parameter space, for example to produce a contour plot such as Figure 4.9 we have solved the Fokker-Planck equation for a large number of parameters $(H_I/v_a, \lambda)$.

- Finally for the typical parameters that are relevant for the edge of the post-inflationary scenario which can be seen in Figure 4.9 (i.e. $H_I/v_a \sim 2$, however there order 1 uncertainties), the difference between the solution to the one field Fokker-Planck equation and two field Fokker-Planck equation is not very dramatic, an example is shown in Figure A.3 in Appendix A.

Another difference between our approach and that in [251] is that we are looking for a more precise condition to form strings which does not necessarily involve reaching the equilibrium distribution. In fact if the equilibrium distribution of $\tilde{r}$ has been reached it is expected that numerous string would form, since the equilibrium distribution has equal amount of probability on both sides of the $\mathbb{Z}_2$ symmetric potential (4.9), see equation (3.34) and Figure 4.2. Since strings form even if the equilibrium distribution of $\tilde{r}$ is not reached, that means that initial conditions for $\tilde{r}$ matter

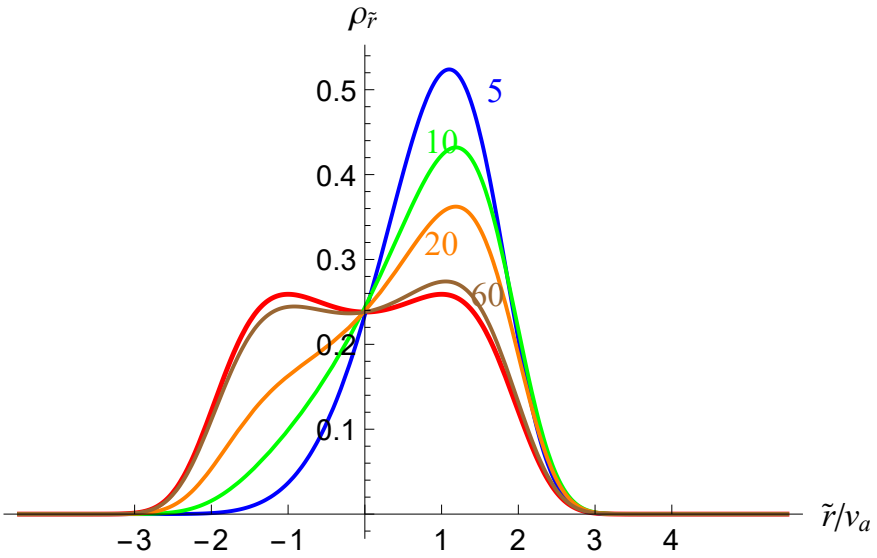

Figure 4.2: An example of the evolution of the probability distribution of $\tilde{r}$ with potential (4.9) following the Fokker-Planck equation (3.33) for $H_I/v_a = 2.5$ and $\lambda = 0.5$. Different colors correspond to different number of e-folds the distribution evolved for as labeled, while initial condition are $\rho_{\tilde{r}}(\tilde{r}, N = 0) = 50\ \mathrm{sech}^2(100\ (\tilde{r}/v_a - 1))$, which is a narrow distribution around $\tilde{r}/v_a = 1$. The thicker red plot corresponds to the equilibrium distribution, which is calculated by replacing the potential (4.9) into equation (3.34).

for the precise boundary of the post-inflationary scenario. As explained in Section 3.3 the initial distribution at the time $N_{\rm tot}$ e-folds before the end of inflation is a delta function on the average value of $\tilde{r}$ over the Hubble patch that will expand to be the size of our Universe today, but this value is unknown. In the following we present results assuming initially $\tilde{r} = v_a$, corresponding to the PQ field starting in the vacuum, although our approach can be in principle adapted to different initial conditions.

Additionally, in Appendix C we discuss the situation where $\tilde{r}$ starts very far away from the vacuum. This is possible if the quantum fluctuations are large and the radial mode can take large values with significant probability, which is likely to lead to the post-inflationary scenario. Alternatively, with additional model building it is possible to have simultaneously large radial mode and low H_I during inflation, which has an interesting consequence of suppressing the otherwise strong isocurvature constraints typical to the pre-inflationary scenario [252, 253].

4.3.1 Solution to Fokker-Planck equation

In the simulations presented in the next Section we will show how the string density at some time after inflation when N e-folds re-entered the horizon is correlated to the probability distribution (in particular the variance of the distribution seems to be a good measure) of $\tilde{r}$ at the end of inflation over regions that would be the size of the horizon at the time when the same N e-folds re-entered.

To find the radial mode distribution over regions that re-enter the horizon at a time N e-folds re-entered, we would ideally solve the Fokker-Planck equation (3.33) multiple times with initial conditions sampling over the distribution of the field $\tilde{r}$ at the time N e-folds before the end of inflation for a given pair $(H_I/v_a,\, \lambda)$, weighting the initial conditions appropriately, i.e. by their own probability distribution which is the solution of the Fokker-Planck equation this time starting at $N_{\rm tot}$ before the end of inflation and evolving until N e-folds before the end of inflation. Unfortunately it would be very difficult to achieve this weighting numerically, since we also need to do so for many pairs $(H_I/v_a,\, \lambda)$ to explore the parameter space. Instead we use the fact that for parameters of interest on the edge of the post-inflationary scenario, i.e. fluctuations that are relatively small over one e-fold and affect the string formation through accumulation over many e-folds, the probability distribution of the radial field N e-folds before the end of inflation is expected to be peaked in the vacuum, as it also obeys a Fokker-Planck equation, having evolved from the start of inflation. As an approximation we always set the initial conditions for the Fokker-Planck equation as a delta function in the vacuum and we checked numerically that a proper accounting for the initial conditions does not change the results by a large amount and it is likely not the dominant source of uncertainty.

We solved the Fokker-Planck equation (3.33) for various $(H_I/v_a, \lambda)$ numerically using Mathematica NDsolve [254], method "BDF" and a maximum step size of 0.1. The initial condition is a sharp function $\rho_{\tilde{r}}(\tilde{r}, N = 0) = 50\ \mathrm{sech}^2(100\ (\tilde{r}/v_a - 1))$ and the equation is solved inside a box between $(-3.5v_a, 4.5v_a)$ with boundary conditions $\rho_{\tilde{r}}(-3.5v_a, N) = 0$ and $\rho_{\tilde{r}}(4.5v_a, N) = 0$ at all times. Convergence checks for the maximum step size and box size can be found in Appendix A. Then for each pair $(H_I/v_a, \lambda)$ we extracted the variance as a function of e-folds re-entered $N_{\rm re}$, which as we show in the next Section is correlated to the string density.

We plot as a representative example the way variance calculated grows with the number of e-folds $N_{\rm re}$ for various H_I/v_a, λ in Figure 4.3. In general, the variance grows at most linearly with the number of e-folds, the fastest growth corresponding to $\lambda = 0$.

We now present the results of numerical simulations and then explain how they can be used to explore the edge of the post-inflationary and pre-inflationary scenarios.

4.4 Results of numerical simulations

The claim we would like to check using numerical simulations of the underdense string networks is that the string density is simply a function of the probability that the radial mode went over the top of the potential inside causally connected regions. We will do this by plotting the string density as a function of the variance of $\tilde{r}$ over regions the size of the causal horizon for various pairs $(H_I/v_a, \lambda)$.

Our numerical simulations of the string network incorporate two phases. First there is a phase of generating the initial conditions, which involves populating a cubic lattice of size $N_{\rm grid}^3 = 2048^3$

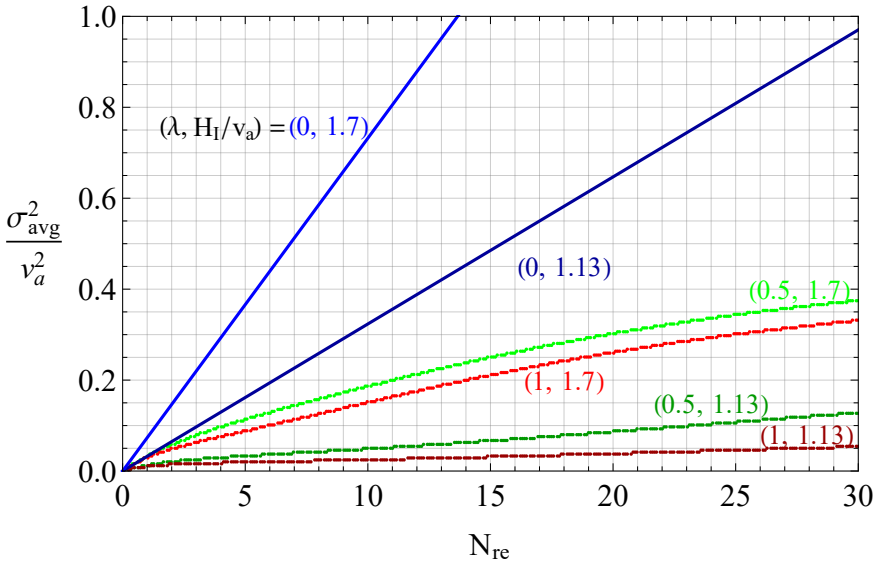

Figure 4.3: Plot showing the variance of the solution of the Fokker-Planck equation (3.33) for various values of parameters $\lambda, H_I/v_a$ as a function of e-folds during inflation, color coded by the value of λ. The initial condition for the distribution is a delta function centered on the minimum of the potential as explained in the text. As expected, larger values of H_I and smaller values of λ lead to faster growth of the variance, which grows at most linearly with the number of e-folds. As explained in the text, we use this as an estimate for the average variance over regions that will be the size of the horizon when N_{re} e-folds have re-entered during the radiation dominated era.

points by assigning values for the components ϕ_1, ϕ_2 of the complex PQ field at each point, i.e. $\phi = (\phi_1 + i\phi_2)/\sqrt{2}$. We use a procedure to populate the grid that is meant to simulate the evolution of the Langevin equation (3.19) as follows:

- We start by setting a grid point in one corner of the lattice to $\phi_1 = v_a$, $\phi_2 = 0$. This corresponds to some initial Hubble patch during inflation with the complex PQ field in the vacuum. Further grid points correspond to a Hubble patch during inflation each.[5]

- Then we apply random "kicks" to ϕ_1 and ϕ_2 at this point, distributed according to a Gaussian distribution with mean 0 and variance $\log(2)H_I^2/(4\pi^2)$. As explained in Section 3.4 this corresponds to a duration of $\log(2)$ e-folds of inflation, which is the time it takes for the scale factor to double.

- We then copy the values of ϕ_1 and ϕ_2 from this grid point to the seven neighbouring grid points. This "splitting" of the initial grid point correspond to the fact that over $\log(2)$ e-folds an initial Hubble patch has expanded into eight Hubble patches, which then evolve independently.

[5]Since we set the distance between grid points to the size of the horizon during inflation $1/H_I$ this corresponds the coarse graining procedure discussed in Section 3.2 after setting the parameter $\epsilon = 1$.

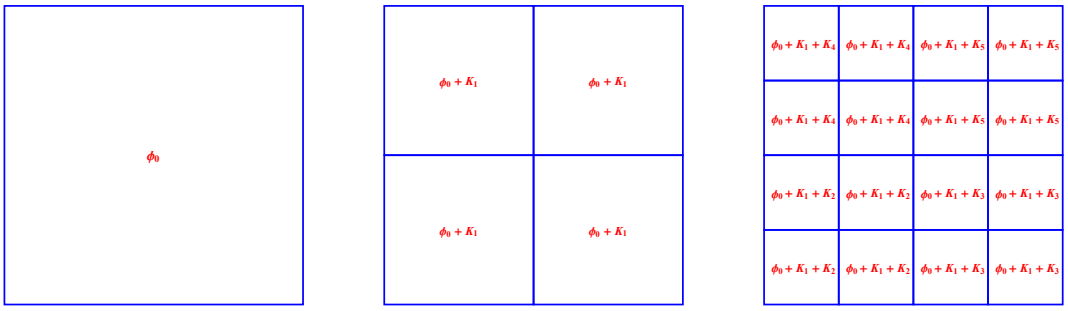

Figure 4.4: Schematic representation of the first two steps of the procedure to generate initial condition in the case of no potential. At each step a Hubble patch "splits" into two along each dimension, which share the history of random kicks up until that point but then evolve independently. For a non-zero potential the evolution of the field due to the gradient of the potential also has to be applied.

- We allow the field to evolve under the potential term (i.e. the evolution of the field in the Langevin equation in the absence of random kicks) for a duration of $\log(2)$ e-folds. As shown in Appendix B we can apply the kicks and the relaxation separately and approximate the Langevin evolution if:
$$\lambda \ll \frac{3\sqrt{6}}{8\pi\sqrt{\log(2)}} \frac{H_I^3}{v_a^3} \,. \tag{4.10}$$
- We continue this procedure of applying kicks, allowing the field to relax and splitting the grid points until the entire grid is populated. Since we started with one populated grid point and end up with 2048, this corresponds to the scale factor doubling 11 times, or $11\log(2) \simeq 7.6$ e-folds of inflation.

In Figure 4.4 we show a schematic representation of the field going through two "splits", while in Figure 4.5 we show a 2D slice through a realisation of the Langevin equation according to the procedure discussed above.

By construction the probability distribution of the fields (ϕ_1, ϕ_2) for initial conditions generated in this way is expected to obey the Fokker-Planck equation (for two fields there are two coupled equations, see equation (A.1)), since the procedure mimics the evolution of the fields under the Langevin equation. The reason we chose this procedure is that some of the spatial information about the field distribution is maintained, as opposed to the Fokker-Planck equation. We show that indeed the field distribution obeys the Fokker-Planck equation in Figure 4.6.

We generate initial conditions in this way for various values of the relevant parameters H_I/v_a and λ and then for each realisation of the initial condition we proceed to the second phase of the simulations, which is following the formation and evolution of strings after the end of inflation. We do so by integrating the equations of motion resulting from the action (2.28) on the discrete cubic lattice that we populated. The code for used to do this phase was written and provided to me by

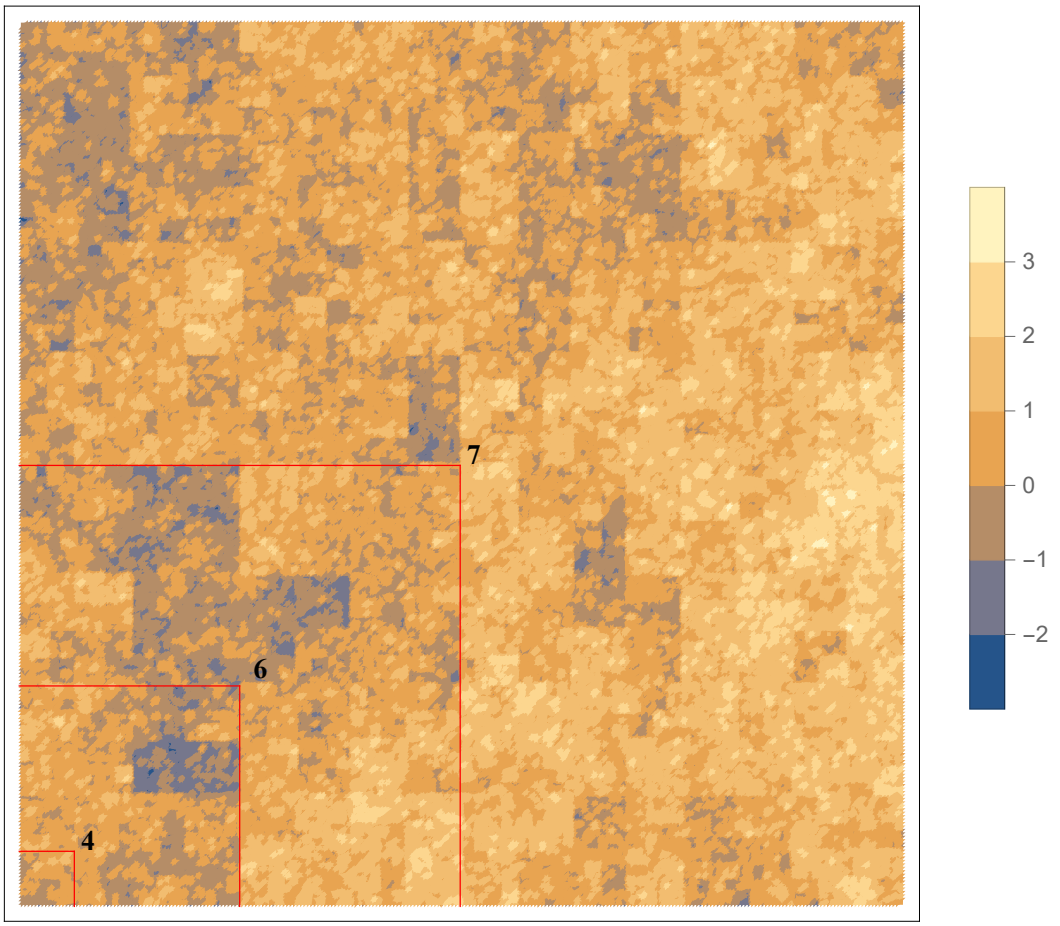

Figure 4.5: Two dimensional slice through a realisation of a Langevin evolution for 8 doubling of the scale factor (or $8\log(2) = 5.5$ e-folds), $H_I/v_a = 2.5$ and $\lambda = 0.5$. Colours represent the value of ϕ_1 in units of v_a, while initial conditions were $\phi_1 = v_a$, $\phi_2 = 0$. Red squares mark regions corresponding to $4, 6, 7$ doubling respectively. Points at the edge of red lines have only been distinct and received different kicks for the corresponding number of doubling.

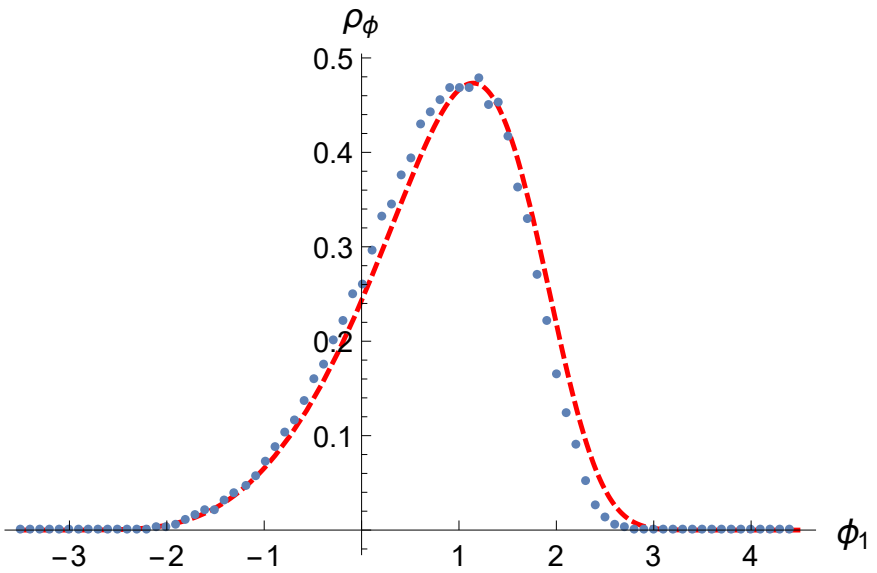

Figure 4.6: Comparison of the probability distribution of the field ϕ_1 generated by the Langevin procedure explained above (blue dots) and the prediction from the two-field Fokker-Planck equation (A.1), which we solved numerically as explained in Appendix A. Additionally, we show in Appendix A that the probability distribution of ϕ_1 found by solving the two-field Fokker-Planck equation is numerically very similar to that of the field $\tilde{r}$ found by numerically solving the one field Fokker-Planck equation as explained in the main text (see Figure A.3). For definiteness we plotted for $H_I/v_a = 2.5$, $\lambda = 0.5$, and the field was evolved for $11\log(2)$ e-folds, which is the same as in the evolution of the initial conditions used in simulations, i.e. the network size doubled 11 times, from initial conditions $\phi_1 = 1$, $\phi_2 = 0$. Kicks were applied every $\log(2)$ e-folds, i.e. every time the network size doubled, the same as in the generation of initial conditions used in simulations. In Appendix B we also provide a check that applying kicks every $\log(2)$ e-folds is sufficiently often, see Figure B.1.

my collaborators, Dr Marco Gorghetto and Dr Edward Hardy. More details about this phase can be found in Appendix E as well as in the Appendices of [186, 188].

We employ the fat string model, which involves replacing the constant self-interaction coupling λ to a time dependent one:

$$\lambda(t) = \lambda_{\rm ini}\frac{R_{\rm ini}^2}{R^2} = \lambda_{\rm ini}\frac{t_{\rm ini}}{t}\,, \tag{4.11}$$

where the subscript ini denotes quantities at the time when the simulation of the string network starts and we assume radiation domination at the start of the simulation. A period of matter dominated during reheating can be accounted for as we explain briefly in Section 4.5.4. The fat string model has the advantage that the number of grid points inside the string cores remains constant, in particular one grid point per string core in our simulations, which was found to be sufficient to resolve the string core for simulations of scaling networks (see Appendix B.1 and Figure 15 of [186]) and we also show evidence for that in Appendix E.1. For this reason we expect that

one grid point per string core is also sufficient resolution to resolve strings in the case of underdense network, however as we briefly discuss in Appendix E.1 there are some complications if we wish to test this directly. Nevertheless, the test that we show in the Appendices points to the fact that the error due to our choice of resolution is not too large. Conversely in the physical case a large number of grid points would be inside string cores at the initial time and the initial conditions would lose some of their resolution.

We initialise the value of the Hubble at the start of this second phase of strings evolution to be equal to the initial mass of the radial mode $H = m_{\rm r,ini}$ and set $\lambda_{\rm ini} = 1$. This means that there is a time discontinuity between the end of inflation when $H_I \simeq 1.7 \div 3.4 v_a$ in the various simulations, and $H = m_r \simeq \sqrt{2\lambda} v_a$ at the start of the post-inflationary evolution. We do this because the formation and subsequent evolution of strings happen after $H \lesssim m_r$, so this way we can follow the string network for the longest time possible inside the simulation, which otherwise would have been a problem particularly for $\lambda \ll 1$ simulations. During this time additional fluctuations would re-enter physically, so there is a difference between the distribution we are simulating and the exact distribution for small λ. However given that we find that the string density depends on the variance of the distribution and not time it is likely that this is not a problem, and that the empirical relation we find also holds for the physical distribution.

For each realisation of the initial conditions the quantity we are interested in is the string density ξ defined as in equation (2.46). First we performed simulations with various $H_I/v_a, \lambda$ on smaller grids ($N_{\rm grid} = 512$) to find the most relevant values of the parameters to simulate on the largest grids. In particular we are looking for parameters such that the fluctuations are large enough for the network to evolve and ξ to grow, while small enough so that network remains in the underdense regime $\xi \lesssim 1$ throughout the simulation. Due to the random nature of the initial conditions, we also generated multiple realisations for each such pair of parameters while only changing the random seed, allowing us to have some idea about the size of statistical errors.

In Figure 4.7 we plot the string density for various values of $(H_I/v_a, \lambda)$ used in the generation of initial conditions as a function of the variance $\sigma^2_{\rm avg}$ of the probability distribution for the field $\tilde{r}$ defined in Section 4.3. The string density ξ is extracted directly from the numerical simulations as a function of time, while the variance is computed from the solution of the Fokker-Planck equation as a function of $H_I/v_a, \lambda$ and time. The key result is that the growth of ξ as a function of variance overlaps and aligns for different simulations with different initial conditions, which reach equal variance at different times. Therefore this shows evidence for a linear relation between $\log(\xi)$ and $\sigma^2_{\rm avg}$:

$$\log(\xi(t)) = \alpha \frac{\sigma^2_{\rm avg}(N_{\rm re})}{v_a^2} + \beta \,, \tag{4.12}$$

with $\alpha = 3.72 \pm 0.03$, $\beta = -3.41 \pm 0.01$ extracted from the fit.

For simulations with $\lambda = 0$ this may not come as unexpected, since in this case the variance fully describes the probability distribution, which is a Gaussian with mean in the initial value of $\tilde{r}$

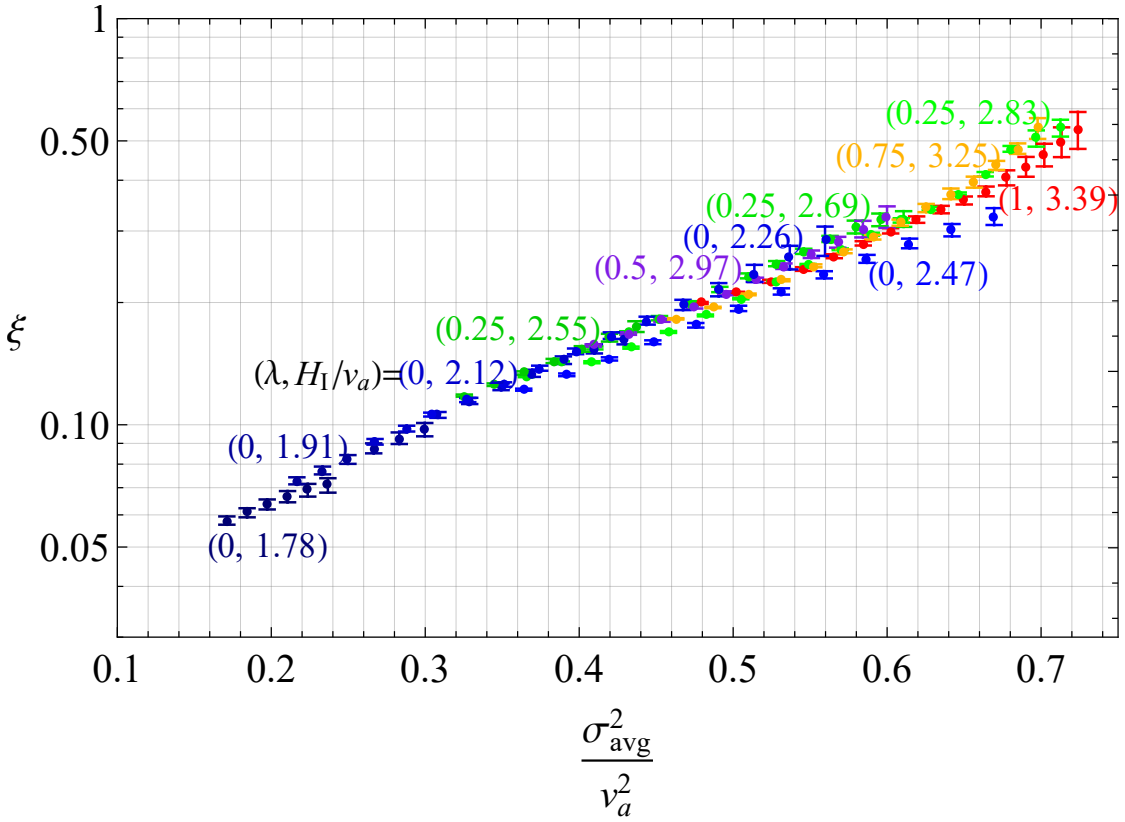

Figure 4.7: Plot of $\xi(t)$ versus average variance over causal regions as explained in the main text. Various colours represent different values of λ and different shades represent different H_I/v_a at the same λ. For each pair of parameters the evolution of ξ has been averaged over multiple simulations which differ only in the random seed. The exact number of simulations we have averaged over varies between 4 and 20 for each pair of parameters, depending on the size of statistical errors towards the end of the respective simulations, which is discussed in more detail in Appendix E, and we have plotted only for values of H_I/v_a for which 20 simulations were enough to have at least 6 data points with reasonable statistical errors. The fact that the evolution of the string density in simulations for various $H_I/v_a, \lambda$ partially overlap and align when plotted as a function of variance provides evidence for the claim that string formation is associated with the probability that the radial mode has been pushed over the top, more specifically by the relation (4.12), and that the variance is a good measure for this probability.

which we took to be v_a. The plot in Figure 4.7 also points to the variance being a good measure of the probability that $\tilde{r}$ passes over the top of the potential even for $\lambda > 0$, since simulations with $\lambda > 0$ and $\lambda = 0$ do overlap.[6]

[6]We have tested and the variance actually provides a better fit than the integral of the probability distribution between $\tilde{r} = -\infty$ and $\tilde{r} = 0$. This is because there is another way the field can be pushed over the top, namely that the field is pushed to values $\tilde{r} > \sqrt{2}v_a$ where its potential is greater than that at the origin. In this case $\tilde{r}$ can also pass over the top of the potential by the oscillations of the field after the end of inflation, and the actual calculation of the probability that $\tilde{r}$ passes over the top must take this into account. We discuss this in more detail in Appendix C.

In the following we assume this relation holds in the underdense regime $\xi \lesssim 1$ for larger ξ and $\log(m_r/H)$, that are otherwise inaccessible in the simulations, including after the time the axion mass becomes relevant. We extrapolate this relation and use it to estimate the contribution of the string network to the axion relic abundance in the following Section.

For comparison the evolution of ξ with time rather than variance would proceed differently for each pair $H_I/v_a, \lambda$, generally growing faster with larger H_I/v_a and smaller λ as one would expect. This can be seen in Figure 4.8 for a selection of pairs $H_I/v_a, \lambda$.

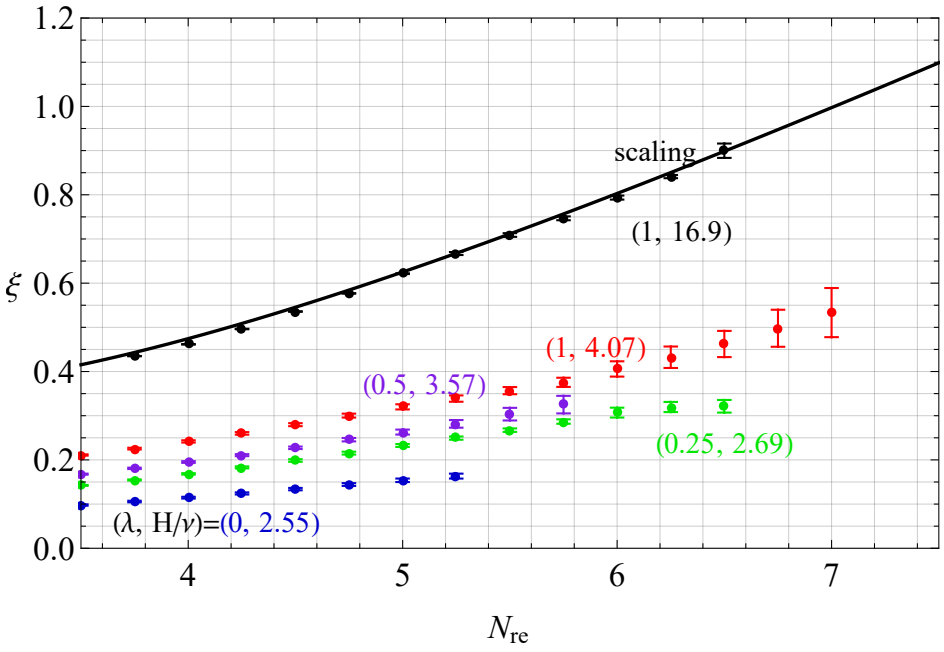

Figure 4.8: Comparison of a selection of simulations in the underdense regime to the evolution in the scaling regime. The scaling regime corresponds to initial conditions obtained by evolving the Langevin equation for a large value $H_I = 16.9 v_a$. Such large values of H_I introduce additional complications in the simulations, which we explain in Appendix E.2. The black line corresponds to a fit of the black data points to the expression $\xi = c_{-2}\log(m_r/H)^{-2} + c_{-1}\log(m_r/H)^{-1} + c_0 + c_1\log(m_r/H)$, where $\log(m_r/H) = N_{\rm re}$ for the fat string model applicable to these simulations. We find $c_1 = 0.22 \pm 0.13$ which is consistent to the result $c_1 = 0.24$ in [188] for the fat strings in the scaling regime.

4.5 Late strings and the edge of symmetry restoration

We now have the tools necessary to estimate the relic abundance as a function of H_I, v_a, λ. First of all, as we will show in Section 4.5.1, the dominant contribution of strings and domain walls to the axion density is the energy released by the domain walls when the network is destroyed, if that happens sufficiently late. Thus the time when the network is destroyed is an important quantity and we discuss how it can be estimated.

We start by recognizing that there exist some minimum value $\xi_{\rm crit} \sim \mathcal{O}(1)$ that is required for the network to be destroyed. This is because for a domain wall larger than the horizon the strings it rests on are outside of causal contact, and they cannot "chop" up each other in order for the wall to decay. Then at the time of network destruction each long string must be away from the closest other long string by at most the radius of the horizon. This means at least order one long strings inside each causal horizon, which corresponds to $\xi_{\rm crit} \sim \mathcal{O}(1)$. Thus we define the time the network is destroyed $t_{\rm des}$ as either the time the axion mass becomes relevant and domain walls form when $H = H_\star = m_a(T_\star)$, where $m_a(T)$ is given by equation (2.41), or the time when $\xi = \xi_{\rm crit}$, whichever happens later.

For a given $\xi_{\rm crit}$ we can estimate the time the network is destroyed as a function of H_I/v_a and λ, by taking the corresponding $\sigma^2_{\rm crit}$ directly from Figure 4.7 or alternatively by extrapolating the expression (4.12) to $\xi = \xi_{\rm crit}$ and the corresponding $\sigma^2_{\rm crit}$ in case $\xi_{\rm crit}$ is above the values of ξ represented.[7] Then we numerically solve the Fokker-Planck equation (3.33) to find the number of e-folds $N_{\rm des}$ that re-enter until this specific value of the variance is reached. In Figure 4.9 we show the number of e-folds before the network is destroyed for various $H_I/v_a, \lambda$ and a set value $\xi_{\rm crit} = 1$, focusing primarily on the region that corresponds to the intermediate scenario.[8] If the Universe was radiation dominated immediately after inflation the network is destroyed at a time when the Hubble parameter is

$$H_{\rm des} = \frac{1}{2t_{\rm des}} = \frac{H_I}{e^{2N_{\rm des}}} \,. \tag{4.13}$$

The time the network is destroyed also sets the inflationary scenario. Large values of H_I for a given λ and v_a result in the network reaching scaling before the axion starts oscillating so that $N_{\rm crit} \lesssim N_\star$ and thus the network is destroyed approximately at $H_{\rm des} \sim H_\star$. This would be the standard post-inflationary scenario and in this case the dominant contribution to axion density is from strings and can be estimated as explained in Section 2.4.3. The resulting upper bound $f_a \lesssim 10^{10} \div 10^{11}\,{\rm GeV}$ [188, 189] depends on the value of the network's density while scaling and the details of the emissions spectrum. Somewhat lower values of H_I result in the network being underdense at $H_\star$, this is an intermediate scenario interpolating between the post- and pre-inflationary scenario. As we show in Section 4.5.1, the later the network is destroyed the larger the domain walls contribution to axion abundance is, and it dominates the strings contribution if $H_{\rm des} \ll H_\star$. Eventually the network is destroyed so late that the walls contribution saturates the DM abundance today, later destruction times and correspondingly lower H_I are ruled out. Alternatively, if the network would be destroyed too late the intermediate scenario could also be in tension with isocurvature constraints discussed in Section 4.5.2. Finally if the network has

[7] We expect equation (4.12) to hold in the underdense regime defined as $\xi \lesssim \xi_{\rm int} \simeq 1$ which is the limit of inefficient string interactions. We also expect $\xi_{\rm crit} \lesssim \xi_{\rm int}$ since the presence of domain walls is expected to enhance the string interactions as walls pull strings together.

[8] In producing Figure 4.9 we have actually solved for the number of e-folds required for the average displacement away from the minimum squared to be equal to $\sigma^2_{\rm crit}$ rather than the variance, to account for the change in the mean of the distribution.

not developed sufficiently and topological defects have negligible contribution we are in the pre-inflationary scenario.

The precise transition between the region of the intermediate scenario ruled out by DM abundance or isocurvature and the pre-inflationary scenario would be challenging to estimate, because the domain walls emissions to gravitational waves become relevant if the network survives to very late times. In this situation the walls emissions to axions would be difficult to estimate and the DM abundance and isocurvature bounds would be modified in an unknown way, on top on the fact that the backreaction of gravitational waves could modify the behaviour of the network's evolution in eq. (4.12). Similarly, as discussed in Section 4.2, there may exist a region in which small domain walls form in the absence of strings due to the angular fluctuations, which subsequently decay into axions. We do not consider any of these situations further.

4.5.1 The dark matter parameter space

In this Section we explain how the axion abundance in the intermediate scenario can be estimated which allows us to consider the corresponding axion masses allowed and phenomenological consequences later on in Section 4.5.3.

We start by writing the energy density of strings and domain walls at times before network destruction. For strings the energy density stored in the network is simply the length of the strings times the tension:

$$\rho_{\rm str} = 4\pi v_a^2 H^2 \xi \log\left(\frac{m_r}{H}\right) . \tag{4.14}$$

For domain walls it is useful to define a dimensionless wall density $\mathcal{A}$, analogous to ξ for strings:

$$\mathcal{A} \equiv \lim V \to \infty \frac{A(V)t}{V} , \tag{4.15}$$

where $A(V)$ is the total area of domain walls inside the volume V. Then the energy density in domain walls is:

$$\rho_{\rm DW} = 2\sigma_{\rm DW} H \mathcal{A} , \tag{4.16}$$

where $\sigma_{\rm DW}$ is the domain walls tension in (2.45).

In order for the network to maintain the relation (4.12) it is clearly emitting some of the stored energy, otherwise ξ would grow as $\xi \sim t$. Additionally once walls form the loss of energy and therefore length of strings also translates in a loss of area and energy of the attached walls. This will go primarily into axions rather than gravitational waves, as long as the network is not destroyed too late, while emissions of strings to heavy radial mode are expected to be suppressed by a factor of $\log(m_r/H)$ compared to axions, and we will see that the emissions of walls dominate those of strings anyway. The ratio between the rate of energy transfer to gravitational waves and axions can be estimated using the quadrupole formula and is $\mathcal{O}(v_a^2 N_{\rm des}^2/M_P^2)$ for strings as we explain in

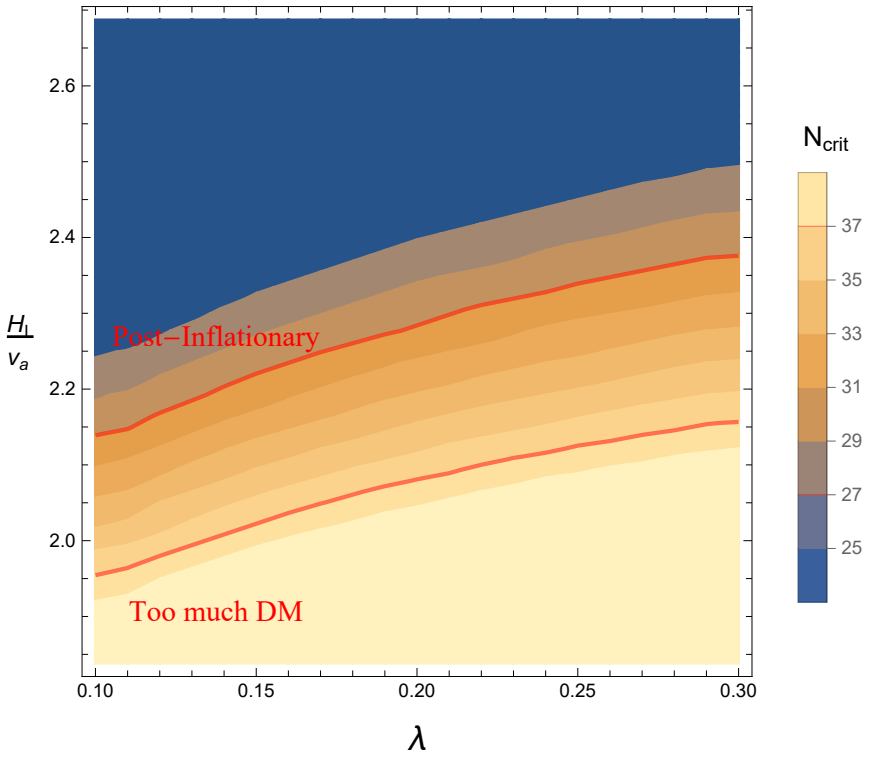

Figure 4.9: Contour plot showing the number of e-folds $N_{\rm crit}$ that re-enter before the average variance is $\sigma^2_{\rm crit}$ corresponding to $\xi_{\rm crit} = 1$. Marked in red are the contour that corresponds to the edge between the intermediate and post-inflationary scenario, as well as the contours that corresponds to axions produced by walls saturating the DM bound, both for $f_a = 10^7\,\text{GeV}$. For this value of the symmetry breaking scale the intermediate scenario is allowed between the red lines. Higher values of f_a result in a narrower parameter space for the intermediate scenario. The precise transition between the region labeled "Too much DM", which is ruled out, and the pre-inflationary scenario for even lower H_I is difficult to estimate as we explain in the main text, primarily due to the backreaction of gravitational waves becoming relevant if the network survives to very late times. However a sufficient condition for the pre-inflationary scenario is given by (4.7), corresponding to $H_I \lesssim 0.4 f_a$. Values for which $m_r/H_I > 3/2$ resulting in the stochastic formalism no longer being valid as explained in Chapter 3 correspond to the pre-inflationary scenario and are located outside the range of this plot.

more detail in Section 6.2.1 and $\mathcal{O}\left[(m_a f_a^2)/(H_{\rm des} M_P^2)\right]$ for domain walls [255]. Thus let us denote:

$$H_{\rm grav} \equiv \frac{m_a f_a^2}{M_P^2} \simeq 10^{-27}\,\text{GeV}\left(\frac{f_a}{10^{12}\,\text{GeV}}\right), \tag{4.17}$$

which parametrises the time when the walls start emitting comparable amounts of their energy into gravitational waves and axions. In the following calculations we assume that $H_{\rm des} \gg H_{\rm grav}$ i.e. that almost all of the energy emitted by the network goes into axions, so we ignore gravitational waves backreaction. The case when the domain walls network survives to much later times so

that gravitational waves emissions become relevant is subject to many uncertainties, such as the exact time the network would decay to gravitational waves and the fraction of its energy that went into axions and gravitational waves respectively. Additionally it is unclear if the behaviour of the network described by eq. (4.12) which we use to estimate the time the network would be destroyed continues to hold in the presence of significant gravitational waves backreaction.

We first estimate the axion abundance from the evolution and final destruction of domain walls assuming that $\mathcal{A}$ is a general monotonically increasing function of time. This can be done by setting an upper and lower bound for the total domain wall contribution, which are within a factor of 2 of each other. Similarly we estimate an upper bound for the contribution of strings during their evolution and final destruction and show that it is in general much smaller than that of domain walls in the intermediate scenario.

The relevant scales to the emissions of the domain walls are the size of the horizon $1/H > 1/m_a$ after walls form and their thickness $1/m_a$. Thus we expect that axions produced by the domain walls are at most mildly relativistic in which case we can convert from the energy emitted by the walls to the number of axions emitted by dividing by m_a, up to an order 1 correction. A lower bound on the domain walls contribution to the axion density is obtained simply by the energy in the network at the time it is destroyed:

$$18 f_a^2 H_{\rm des} \mathcal{A}(t_{\rm des}) < n_{\rm a,DW}\,. \tag{4.18}$$

Domain walls also emit axions during the network evolution, at a rate which can be estimated by comparing the evolution of the network of walls to that of a free network which is identical to the actual network at a time t' is later described by the walls staying at fixed comoving coordinates:

$$\Gamma_{\rm DW} = \dot{\rho}_{\rm DW,\ free} - \dot{\rho}_{\rm DW}\,. \tag{4.19}$$

The energy density of the free network of walls larger than the horizon evolves as $\sim 1/R$ since the walls are stretched by a factor R^2 and we assume radiation domination:

$$\rho_{\rm DW,\ free} = 2\mathcal{A}(t')\sigma_{\rm DW}\sqrt{H'H}\,, \tag{4.20}$$

$$\Gamma_{\rm DW} = H\rho_{\rm DW} - \frac{\dot{\mathcal{A}}}{\mathcal{A}}\rho_{\rm DW}\,. \tag{4.21}$$

The total domain walls contribution is then:

$$n_{\rm a,DW}(t_{\rm des}) = 18 f_a^2 H_{\rm des}\mathcal{A}(t_{\rm des}) + \int_{t_\star}^{t_{\rm des}} \frac{\Gamma_{\rm DW}(t')}{m_a(t')}\left(\frac{R(t')}{R(t_{\rm des})}\right)^3 dt'\,. \tag{4.22}$$

Replacing $\Gamma_{\rm DW}$ from eq. (4.21) the integral above breaks into:

$$n_{\rm a,DW}(t_{\rm des}) = 18 f_a^2 H_{\rm des}\mathcal{A}(t_{\rm des}) + \frac{18 f_a^2}{t_{\rm des}^{3/2}}\left(\int_{t_\star}^{t_{\rm des}} \frac{\mathcal{A}}{4\sqrt{t'}}dt' - \int_{t_\star}^{t_{\rm des}} \frac{\sqrt{t'}\dot{\mathcal{A}}}{2}dt'\right), \tag{4.23}$$

where the first integral can be performed by parts to give:

$$n_{\rm a,DW}(t_{\rm des}) = 18 f_a^2 H_{\rm des}\mathcal{A}(t_{\rm des}) + \frac{18 f_a^2}{t_{\rm des}^{3/2}}\left(\frac{\mathcal{A}(t_{\rm des})\sqrt{t_{\rm des}}}{2} - \frac{\mathcal{A}(t_\star)\sqrt{t_\star}}{2} - \int_{t_\star}^{t_{\rm des}} \sqrt{t'}\dot{\mathcal{A}}dt'\right). \tag{4.24}$$

For positive $\dot{\mathcal{A}}$ this means an upper bound as well:

$$18 f_a^2 H_{\rm des}\mathcal{A}(t_{\rm des}) < n_a(t_{\rm des}) < 36 f_a^2 H_{\rm des}\mathcal{A}(t_{\rm des}), \tag{4.25}$$

i.e. the contribution from the evolution of the network is at most equal to that from the final destruction of the network.

For the contribution of strings an upper bound can be obtained by noticing that the rate of emission during the evolution of the network is lower than that of a network with constant $\xi = \xi_{\rm crit}$:

$$\Gamma_{\rm str} < 2H\rho_{\rm str} < 8\pi v_a^2 H^3 \xi_{\rm crit}\log\left(\frac{m_r}{H}\right). \tag{4.26}$$

As opposed to the domain walls, the strings are also evolving at times before $t_\star$, when axions emitted would have been relativistic. We estimate the axion density from the energy emissions as $dn/dt \sim \Gamma_{\rm str}/H$ at times before $t_\star$ and $dn/dt \sim \Gamma_{\rm str}/m_a \lesssim \Gamma_{\rm str}/H_\star$ at times between $t_\star$ and $t_{\rm des}$. Upon performing the integrals and discarding the negative terms as we are interested in an upper bound, we find:

$$n_{\rm a,str} < 4\pi v_a^2 \xi_{\rm crit} H_{\rm des}\left(\log\left(\frac{m_r}{H_{\rm des}}\right)\frac{H_{\rm des}}{H_\star} + 4\sqrt{\frac{H_{\rm des}}{H_\star}}\log\left(\frac{m_r}{H_\star}\right)\right). \tag{4.27}$$

Comparing the upper bound on the contribution of strings to the lower bound on the contribution of domain walls (4.25) we find that indeed the domain walls contribution dominates in the intermediate scenario if the network is destroyed somewhat later than $t_\star$ such that:

$$\sqrt{\frac{H_{\rm des}}{H_\star}} \lesssim \frac{18}{16\pi}\frac{\mathcal{A}(t_{\rm des})}{\xi_{\rm crit}}\frac{1}{\log\left(\frac{m_r}{H_\star}\right)} \sim \mathcal{O}(10^{-3}), \tag{4.28}$$

assuming $\xi_{\rm crit}$ and $\mathcal{A}(t_{\rm des})$ are of order 1. Thus we can estimate the axion number density at the time the network is destroyed in the intermediate scenario as:

$$n_a(t_{\rm des}) \simeq 18 f_a^2 H_{\rm des}\mathcal{A}(t_{\rm des}). \tag{4.29}$$

The axion number density above redshifts until today as $1/R^3$ and can be multiplied by the mass of the axion to give the energy density. This must not exceed the total DM energy density, which results in a minimum value for Hubble when the network is destroyed:

$$H_{\rm des} \gtrsim H_{\rm min} = 2.1 \times 10^{-16}\,{\rm GeV}\sqrt{\frac{10}{g_\star(T_{\rm des})}}\left(\frac{f_a}{10^{12}\,{\rm GeV}}\right)^2 \mathcal{A}(t_{\rm des})^2\,, \tag{4.30}$$

where the network being destroyed at $H_{\rm min}$ corresponds to axions making up the entirety of DM. Notice that $H_{\rm min} \gg H_{\rm grav}$ for values of f_a allowed for the QCD axion, so the assumption that the majority of the domain walls energy goes into axions that was used to calculate $H_{\rm min}$ is self-consistent.

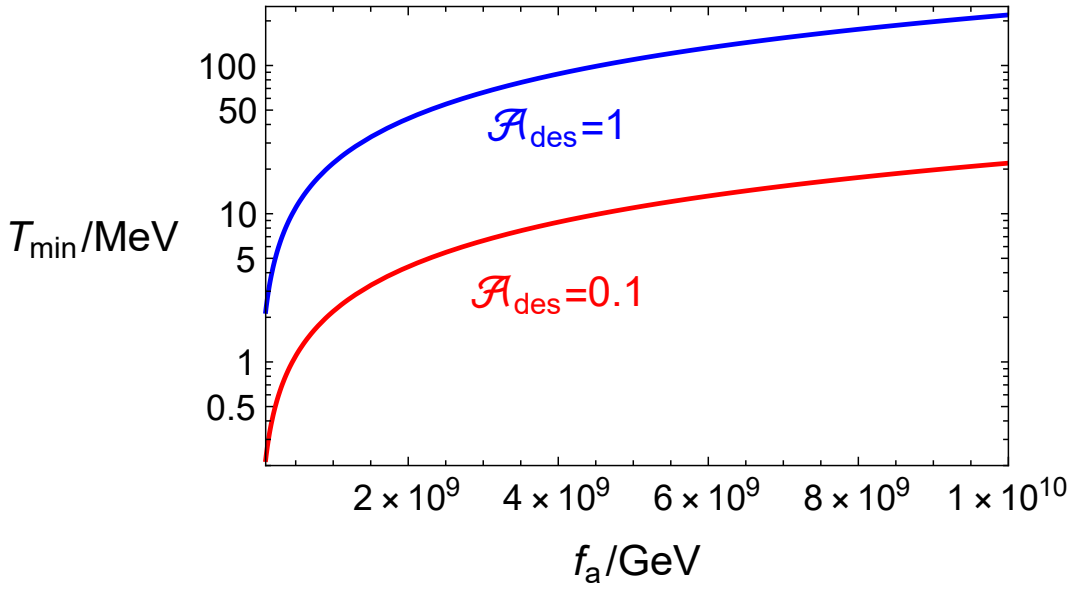

Figure 4.10: The minimum temperature at which the domain walls are allowed to collapse in order to not overproduce dark matter as a function of the symmetry breaking scale f_a, in the range allowed by astrophysical constraints $f_a \in (10^8\,{\rm GeV}, 10^{10}\,{\rm GeV})$. This is calculated by converting $H_{\rm min}$ of eq. (4.30) into a temperature. We have plotted two different values of $\mathcal{A}(t_{\rm des})$ to show that for sufficiently low density of walls at network destruction, this is potentially allowed to happen around the time of the BBN.

4.5.2 Isocurvature constraints

During the evolution of the network and at the time domain walls annihilate, the axion field contains inhomogeneities. Since these involve only the axion energy density, they correspond to isocurvature perturbations [256], which could potentially be in conflict with cosmological observations, even if the axion makes up only a fraction of the total dark matter. An analysis of such perturbation has previously been carried out for the QCD axion [257] and axion-like particles in [258, 259] in the

post-inflationary scenario. In this Section we explain in more detail how to calculate the potential isocurvature constraints in the intermediate scenario, while in Section 6.3.3 we apply the same to the post-inflationary scenario of ALPs which are relevant in our analysis in Chapter 6. The calculation in these two scenarios is qualitatively very similar, the only difference being the dominant source of axions: domain walls in the intermediate scenario, strings in the post-inflationary scenario.

The perturbations in the axion energy density ρ_a are most easily studied using the overdensity field $\delta_a(x) \equiv (\rho_a(x) - \langle\rho_a\rangle)/\langle\rho_a\rangle$, where the brackets indicate the spatial average. It is useful to express δ_a in terms of the (dimensionless) power spectrum $\Delta_a^2(k)$, defined by

$$\langle\tilde{\delta}_a(\mathbf{k})\tilde{\delta}_a(\mathbf{k}')\rangle = \frac{2\pi^2}{k^3}\Delta_a^2(k)\delta^3(\mathbf{k}-\mathbf{k}') \ , \tag{4.31}$$

where $\tilde{\delta}_a$ is the Fourier transform of δ_a and we assumed statistical homogeneity and isotropy. It is straightforward to show that $\langle\delta_a^2\rangle = \int \Delta_a^2(k)/k \ dk$.

After the strings/domain walls network is destroyed, Δ_a^2 is expected to have a non-zero (and order one) value at momenta $k \simeq H_{\rm des}$, since $H_{\rm des}$ sets the typical size of fluctuations, and therefore the typical correlations between momentum modes. At these scales, the precise shape of Δ_a^2 depends on the dynamics of the network at $H \simeq H_{\rm des}$. Conversely, fluctuations at scales larger than the horizon at that time, i.e. $k \ll H_{\rm des}$, are expected to be uncorrelated. From eq. (4.31), this fixes the form of $\Delta_a^2 \propto k^3$, which is the prediction from a white noise spectrum, so Δ_a^2 is suppressed at large scales. We therefore parametrise $\Delta_a^2(k) = C(k_{\rm com}/H_{\rm des})^3$ at comoving momenta $k_{\rm com} \equiv kR/R_{\rm des} \lesssim H_{\rm des}$, where C is a dimensionless coefficient.

It is worth noting that the isocurvature perturbations in the post-inflationary scenario as well as those produced by the domain walls in the intermediate scenario differ from the scale invariant isocurvature perturbations characteristic to the pre-inflationary scenario. For this reason they are not necessarily constrained if the scales probed by the CMB lie in the k^3 part of the spectrum of $\Delta^2(k)$ above. For the QCD axion in the post-inflationary scenario this means no constraints on the parameter space and we derive bellow potential contraints in the intermediate scenario.

During the network's evolution and destruction Δ_a^2 changes. However, once all the strings and domain walls have vanished and the axion field has mostly settled down to have amplitude $\ll f_a$, the axion energy density is redshifting non-relativistically, so the k^3 part of Δ_a^2 is constant leading to a time-independent C.[9]

The CMB is the longest standing source of constraints on isocurvature perturbations, with the best currently available data coming from Planck [204, 205], from modes close to the pivot scale $k_{\rm CMB} = 0.05$ MPc^{-1}. Such observations bound the fraction of isocurvature fluctuations $f_{\rm iso}$ relative to the curvature perturbations at these scales, defined by $f_{\rm iso}^2 \equiv \Delta_{\rm iso}^2(k)/\Delta_{\mathcal{R}}^2(k)$, where $\Delta_{\rm iso}^2$ is the spectrum of isocurvature perturbations and $\Delta_{\mathcal{R}}^2(k) = A_s(k/k_{\rm CMB})^{n_s-1}$ is the (almost scale invariant) spectrum of curvature perturbations. For the QCD axion in the intermediate scenario,

[9] We neglect the effect of gravity, which is expected to not affect the far IR-momenta [259].

the network decays at $H_{\rm des} \gtrsim H_{\rm min}$ given in eq. (4.30) which is before CMB decoupling, therefore $k_{\rm CMB}$ is inside the k^3 part of $\Delta_a^2(k)$. An order of magnitude limit can be obtained by calculating $f_{\rm iso}$ at the scale $k_{\rm high} = 0.100\ {\rm MPc}^{-1}$ and comparing this to the limit reported in Table 14 of [205] at this scale, either in a general model with a free spectral tilt for isocurvature perturbations (which is named "axion II" in [205], and we are taking the strongest limit reported) or the model with scale independent spectral tilt corresponding to the pre-inflationary scenario ("axion I" in [205]). The k^3 suppression of the isocurvature spectrum insures that limits derived in this way at the scale $k_{\rm high}$ are stronger than those that would be derived at lower k, which can be easily seen from Table 14 of [205] after converting from $\beta_{\rm iso}$ to $f_{\rm iso}$ by $f_{\rm iso} = \sqrt{\beta_{\rm iso}/(1-\beta_{\rm iso})}$, i.e. that the upper bound on $f_{\rm iso}$ increases slower with momentum than k^3, even for the free spectral model. A comparison of the k^3 spectrum of the isocurvature produced by the destruction of the domain walls and the scale invariant spectrum constrained by the CMB can be seen in Figure 4.11.

In general the axions only comprise a fraction of the total dark matter, so there is a factor of $\Omega_a^{\rm st}/\Omega_{\rm DM}$ in their contribution to $f_{\rm iso}$. Consequently, assuming there are no isocurvature fluctuations in the remainder of the DM:

$$f_{\rm iso}(k) = \frac{\Omega_a}{\Omega_{\rm DM}} \sqrt{\frac{C k^3 R_0^3}{A_s H_{\rm des}^3 R_{\rm des}^3}}\,. \tag{4.32}$$

Leading to a limit for "axion I":

$$H_{\rm des} \gtrsim 1.8 \times 10^{-24}\,{\rm GeV} \left(\frac{f_a}{10^{12}\,{\rm GeV}}\right)^{\frac{4}{5}} C^{\frac{2}{5}} \mathcal{A}(t_{\rm des})^{\frac{4}{5}} \left(\frac{3.9}{g_\star(T_{\rm des})}\right)^{\frac{1}{10}}\,, \tag{4.33}$$

and "axion II" respectively:

$$H_{\rm des} \gtrsim 1.6 \times 10^{-24}\,{\rm GeV} \left(\frac{f_a}{10^{12}\,{\rm GeV}}\right)^{\frac{4}{5}} C^{\frac{2}{5}} \mathcal{A}(t_{\rm des})^{\frac{4}{5}} \left(\frac{3.9}{g_\star(T_{\rm des})}\right)^{\frac{1}{10}}\,. \tag{4.34}$$

However the limits above are derived by fitting either a free spectral tilt model for the isocurvature spectrum or a scale invariant model and to obtain precise limits we would need to fit a model with a k^3 isocurvature spectrum. This has already been done in [258, 259] and we can directly apply the limit $f_{\rm iso}(k_{\rm CMB}) < 0.64$ obtained in [259].[10] This corresponds to a lower bound on $H_{\rm des}$:

$$H_{\rm des} \gtrsim 3.3 \times 10^{-25}\,{\rm GeV} \left(\frac{f_a}{10^{12}\,{\rm GeV}}\right)^{\frac{4}{5}} C^{\frac{2}{5}} \mathcal{A}(t_{\rm des})^{\frac{4}{5}} \left(\frac{3.9}{g_\star(T_{\rm des})}\right)^{\frac{1}{10}}\,. \tag{4.35}$$

In addition to CMB bounds, it has recently been shown that isocurvature fluctuations at smaller scales are constrained by Lyman-α observations [260], and that these can be important in post-inflationary axion dark matter models [261]. We use the constraint from [260], which assumes a

[10] The precise numerical bound depends on the cosmological data that is combined. Interestingly the analysis in [259] shows a mild preference for a non-zero isocurvature component.

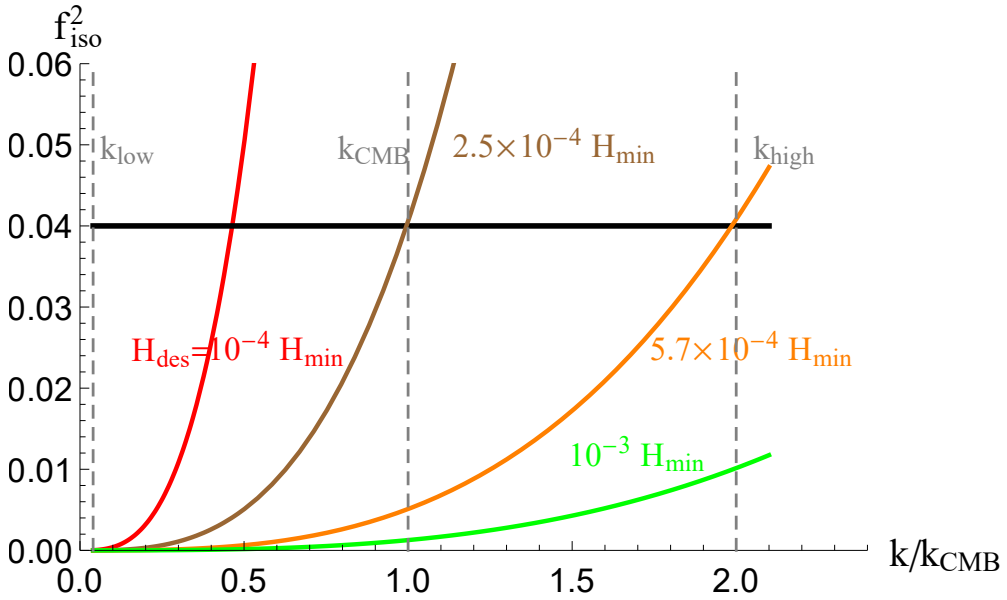

Figure 4.11: Comparison between the fraction of isocurvature perturbations produced by the destruction of domain walls relative to curvature perturbation as defined in equation (4.32) for various network destruction times (colored lines), and the scale invariant isocurvature fraction constrained by the CMB [205] (black line). The various isocurvature fractions are represented as functions of momentum in units of $k_{\rm CMB} = 0.05\,{\rm Mpc}^{-1}$. We have also plotted the values of $k_{\rm low} = 0.002\,{\rm Mpc}^{-1}$ and $k_{\rm high} = 0.1\,{\rm Mpc}^{-1}$ at which the CMB limits on the isocurvature fraction are reported in [205]. Due to the k^3 momentum dependence of Δ_a^2 and $f_{\rm iso}^2$, if the CMB limits are satisfied at the highest momentum $k_{\rm high}$, they are automatically satisfied at lower momentum. We represent the various destruction times as $H_{\rm des}$ in units of $H_{\rm min}$ defined in equation (4.30), which is the latest time the network could be destroyed in order to not overproduce DM. It can thus be seen that the isocurvature constraints are weaker than those from DM overproduction. Stronger constraints come from Lyman-α forest observation, see equation (4.36), which are sensitive to higher momentum scales $k_{\rm L\alpha} \simeq 10\,{\rm Mpc}^{-1}$. For definiteness we have set $f_a = 10^8\,{\rm GeV}$, $C = 1$, $\mathcal{A}(t_{\rm des}) = 1$ to produce this figure.

k^3 power spectrum. Expressed in terms of the isocurvature fraction at the Planck pivot scale, this requires $f_{\rm iso}(k_{\rm CMB}) < 0.004$. For axion masses such that the observed modes are in the k^3 part of Δ_a^2, this can be immediately converted into a bound on $H_{\rm des}$ similarly to eq. (4.35). However, the dominant scales in Lyman-α studies correspond to momenta of order $k_{\rm L\alpha} \sim 10\ {\rm MPc}^{-1}$ much larger than those relevant to CMB observations [261] (and more sophisticated analyses are potentially sensitive to even smaller scales). Given the bound on $H_{\rm des}$ in eq. (4.30), Lyman-α observations are relevant for the QCD axion in the intermediate scenario, since $k_{\rm L\alpha}$ is also in the k^3 part of Δ_a^2. This tightens the isocurvature constraints to:

$$H_{\rm des} \gtrsim 1.9 \times 10^{-23}\,{\rm GeV} \left(\frac{f_a}{10^{12}\,{\rm GeV}}\right)^{\frac{4}{5}} C^{\frac{2}{5}} \mathcal{A}(t_{\rm des})^{\frac{4}{5}} \left(\frac{3.9}{g_\star(T_{\rm des})}\right)^{\frac{1}{10}} . \tag{4.36}$$

The isocurvature bound is weaker than the bound from DM abundance in eq. (4.30) if

$$f_a > 1.3 \times 10^6 \,\mathrm{GeV}\, C^{\frac{1}{3}} \mathcal{A}(t_{\mathrm{des}})^{-1} \,, \tag{4.37}$$

where $C \ll 1$ and $\mathcal{A}(t_{\mathrm{des}}) \sim \mathcal{O}(1)$ is expected. Given the bound on axion nucleon coupling from supernova 1987a and the bound on axion photon coupling from the ratio of horizontal branch stars to red giants discussed in Section 2.5 we expect that the isocurvature bound is weaker than the DM abundance bound for a QCD axion in the intermediate scenario.

We stress that the results of this Section should be taken as a conservative estimate and that there are many potential uncertainties. Since we do not know the exact way the domain walls density evolves over time, we only considered the isocurvature perturbations in the axions produced by the destruction of the domain walls at the final time. Meanwhile, for the destruction of the network it is difficult to extract the quantitative details precisely since it happens at times far out of the reach of numerical simulations.

4.5.3 Observational implications

An interesting feature of the intermediate scenario is that the axion abundance is larger the later the network is destroyed. Therefore for values of f_a below the upper bound in the post-inflationary scenario discussed in Section 2.4.3 $f_a \lesssim 10^{10} \div 10^{11}\,\mathrm{GeV}$, it is possible that axions make up the entirety of DM if the network is destroyed at the corresponding time H_{min} in eq. (4.30). The lowest f_a for which this is possible is found by equating H_{min} to the lowest H_{des} allowed by isocurvature in eq. (4.36), i.e. $f_a \gtrsim 1.3 \times 10^6\,\mathrm{GeV}\, C^{\frac{1}{3}}$, where C is the amplitude of the spectrum of isocurvature perturbations. This means that the QCD axion can be all of DM in the intermediate scenario down to the lowest values of f_a allowed by astrophysics, such as the model dependent supernova 1987a bound $f_a \gtrsim 10^8\,\mathrm{GeV}$ [225, 227] or the bound from the ratio of horizontal branch stars to red giants $f_a \gtrsim 10^7\,\mathrm{GeV}$ [224] which were discussed in Section 2.5. Thus the intermediate scenario would be of interest in the case of a detection of the QCD axion with mass anywhere inside the region allowed in the post-inflationary scenario $0.5\,\mathrm{meV} \lesssim m_a \lesssim 20\,\mathrm{meV}$. This is especially so if the detection happens by means of a method which relies on axions being a significant fraction of the dark matter, as is the case of haloscopes.

Most of the axions are produced by the destruction of the network in the intermediate scenario, and at that time the number of domain walls per horizon is expected to be of order 1. Therefore we expect axion density to have order 1 fluctuations on scales the size of the horizon at network destruction $1/H_{\mathrm{des}}$. These fluctuations subsequently collapse into bound objects at the time of matter-radiation equality [256, 262, 263], which are axion miniclusters of typical mass:

$$M_{\mathrm{mc}} \simeq \frac{4\pi}{3} \overline{\rho}_{\mathrm{a,eq}} \frac{R_{\mathrm{eq}}^3}{R_{\mathrm{des}}^3 H_{\mathrm{des}}^3} = 2.2 \times 10^{-14} M_\odot \frac{g_\star(T_{\mathrm{des}})}{10} \frac{1}{\mathcal{A}(t_{\mathrm{des}})} \left(\frac{10^{12}\,\mathrm{GeV}}{f_a} \right)^3 \,, \tag{4.38}$$

where $\overline{\rho}_{\rm a,eq}$ and $R_{\rm des}$ denote the axion density and the scale factor at the time of matter-radiation equality respectively, $M_\odot$ is the solar mass and we set $H_{\rm des} = H_{\rm min}$ from eq. (4.30), i.e. axions make up the entirety of DM.

Other possibilities exist that also allow the QCD axion to be all of DM even for larger masses $m_a \gtrsim 0.5\,\text{meV}$ than that in the post-inflationary $N_{\rm DW} = 1$ scenario. One such possibility is that the misalignment angle is close to the top of the axion's potential $a \simeq \pi f_a$ in the pre-inflationary scenario, in which case the misalignment abundance is enhanced [171, 198, 264–266] as well as the characteristic isocurvature perturbations [201]. Simultaneous requirements that H_I is small enough to be allowed by isocurvature constraints in this case and that it is larger than m_a so that the misalignment angle can remain large during inflation limit this scenario to $0.5\,\text{meV} \lesssim m_a \lesssim 1.5\,\text{meV}$ [188]. Inside this range the intermediate scenario and the large misalignment pre-inflationary scenario could be in principle still be separated if miniclusters are observed, as the predictions of the typical mass of miniclusters in these scenarios are expected to be different. The typical mass of miniclusters in the pre-inflationary scenario for $f_a \simeq 10^{10}\,\text{GeV}$ is about $10^{-18} M_\odot$, see [267], while in the intermediate scenario they would be typically much heavier according to eq. (4.38), at about $10^{-8} M_\odot$. Of course such a distinction would require a quantitative understanding of the mass distribution of miniclusters in the intermediate scenario.

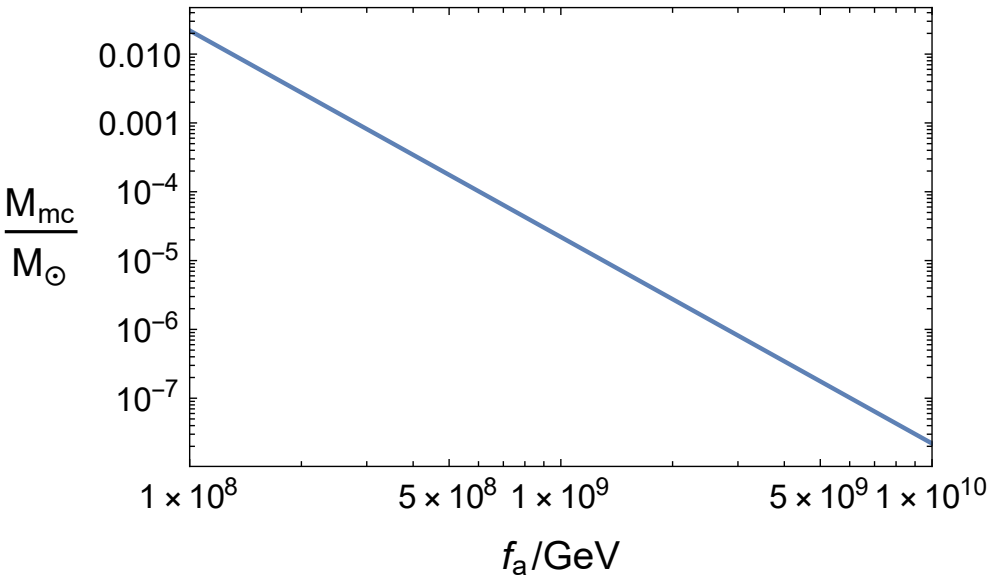

Figure 4.12: The typical mass of axion miniclusters produced in the intermediate scenario as a function of the axion symmetry breaking scale f_a, described by equation (4.38), in the range allowed by astrophysical constraints $f_a \in (10^8\,\text{GeV}, 10^{10}\,\text{GeV})$. For definiteness we have set $\mathcal{A}(t_{\rm des}) = 1$.

On the other hand, the intermediate scenario shares many similarities to the post-inflationary scenario for $N_{\rm DW} > 1$, since in both cases the domain walls network is stable at the time when the axion begins oscillating $t_\star$. The domain walls must eventually decay, or they will end up dominating

the energy density of the Universe; for $N_{\rm DW} > 1$ this is done by introducing an additional explicit symmetry breaking of the remaining symmetry [268], which can be sourced for example by Planck suppressed operators [146, 147, 269]. If the bias is parametrised as $V_b = \delta V \cos(\theta - \delta\theta)$, the walls are collapsing roughly when the pressure due to the energy difference between vacua is comparable to the energy density of the walls [190, 268, 270], parametrically corresponding to:

$$H_{\rm des} \sim \frac{\delta V}{\mathcal{A}(t_{\rm des}) m_a f_a^2} \,. \tag{4.39}$$

Similarly to the intermediate scenario for $N_{\rm DW} = 1$, the domain walls will dominate axion production for $H_{\rm des} \ll H_\star$, which corresponds to $\delta V \ll m_a^2 f_a^2$, and the walls contribution can be estimated in the same way as in Section 4.5.1. This also requires lower values of f_a for axions to make up all of DM than in the post-inflationary scenario with $N_{\rm DW} = 1$, and the miniclusters formed in the post-inflationary scenario for $N_{\rm DW} > 1$ will have similar mass as in the intermediate scenario for $N_{\rm DW} = 1$.[11] The difference is that, while in the intermediate scenario $H_{\rm des}$ is given by the density of the network and can in principle take any value between $H_{\rm min} \lesssim H_{\rm des} \lesssim H_\star$, in the post-inflationary scenario with $N_{\rm DW} > 1$ the size of the bias sets $H_{\rm des}$, while it is constrained as to not re-introduce the Strong CP problem. This also puts an upper bound on $H_{\rm des}$:

$$H_{\rm min} \lesssim H_{\rm des} < \frac{N_{\rm DW}^2 \left|\overline{\theta}\right| m_a}{\mathcal{A}(t_{\rm des}) \sin(\delta\theta)} \,, \tag{4.40}$$

where $\overline{\theta}$ is the effective QCD vacuum angle which parametrises the CP violation in the strong sector, as defined in Section 2.1, and it is bounded by the requirement that a neutron electric dipole moment has not been observed $\left|\overline{\theta}\right| < 10^{-10}$. Replacing $H_{\rm min}$ from eq. (4.30) we find this is only possible for:

$$\sin(\delta\theta) \lesssim \left|\overline{\theta}\right| \frac{N_{\rm DW}^2}{\mathcal{A}(t_{\rm des})^3} \left(\frac{10^{12}\,{\rm GeV}}{f_a}\right)^3 \,, \tag{4.41}$$

which would be tight for $\sin(\delta\theta) \sim \mathcal{O}(1)$ and $10^8\,{\rm GeV} \lesssim f_a$. The post-inflationary scenario for $N_{\rm DW} > 1$ might require fine tuning of the $\delta\theta$ angle to be close to one of the minimums of the axion potential and could also be potentially detectable if a non-zero value of the nEDM, and thus a vacuum angle $\left|\overline{\theta}\right|$ close to its current upper limit, is measured in the future. A definite conclusion would require a more precise expression for the time the network is destroyed as a function of the size of the bias.

[11] For $N_{\rm DW} > 1$ we expect the final walls density $\mathcal{A}$ to be larger by up to a factor $N_{\rm DW}$ compared to the case $N_{\rm DW} = 1$, as there are $N_{\rm DW}$ walls attached to each string.

4.5.4 Uncertainties

Here we summarise the various assumptions and simplifications we have made and discuss associated uncertainties in our results.

- As we have discussed, we require the value of $\xi_{\rm crit}$ to calculate the axion relic abundance in the intermediate scenario, as it sets the time when the network is destroyed. While $\xi_{\rm crit} \simeq \mathcal{O}(1)$ has been found to be sufficient to collapse the network in simulation with accessible $\log(m_r/H)$, see for example [271] and we also performed simulation of domain walls collapse at $\log(m_r/H) = 5$ for a scaling network with corresponding $\xi \simeq 0.5$ (see Appendix F.4), we cannot exclude that a significantly different value is necessary at large log that is relevant in the intermediate scenario and not accessible in simulations. Additionally, we have not performed dedicated simulations in which we turn on the axion mass at various point of the evolution of an underdense network to find the exact necessary density to collapse it. The uncertainty in the value of $\xi_{\rm crit}$ translates straightforwardly into an uncertainty in the critical variance from eq. (4.12) or Figure 4.7. This in turn translates to an uncertainty in $N_{\rm des}$ and thus $H_{\rm des}$, which is non-obvious to calculate since it depends on the numeric solution to the Fokker-Planck equation. For a specific λ and $H_{\rm des}$, this can alternatively be seen as an uncertainty on the value of H_I that would result in the network being destroyed at this time. To give a simple example, the difference between $\xi_{\rm crit} \simeq 0.1$ and $\xi_{\rm crit} \simeq 1$ which we represented in Figure 4.9 corresponds to a difference of the variance of the radial mode distribution at the time the network is destroyed between $0.3v_a^2$ and $0.9v_a^2$. For $\lambda = 0$ which allows for an analytic solution of the Fokker-Planck equation, this corresponds to factor of order $\sqrt{3}$ decrease in H_I to maintain the same $H_{\rm des}$.

- In interpreting the result of numerical simulations we have solved the Fokker-Planck equation assuming a one dimensional field space, i.e. we have replaced the radial mode's potential (2.29) into the Fokker-Planck equation (3.33) while keeping the axion at a constant value. This was done because we wanted a measure of the probability that quantum fluctuations in the radial direction have pushed the field over the top of the potential. We think this approximation was reasonable for our purpose, especially given the results presented in Figure 4.7 together with the procedure to generate initial conditions discussed in Section 4.4. The point is that, while the calculation of the variance in Figure 4.7 was done by only considering the one dimensional Fokker-Planck equation in the radial direction, the distribution of the field inside the simulation box which results in the string density ξ has been simulated in the full two dimensional field space, both in the phase of generating initial conditions and the phase of evolving the string network.

- A source of uncertainty is the simplification in our calculation of the average variance as explained in Section 4.3, by always setting the initial conditions of the radial mode in the

vacuum when solving the Fokker-Planck equation rather than taking into account the actual distribution of initial conditions. For a sample of values $H_I/v_a, \lambda$, we have checked this approximation numerically by solving the Fokker-Planck equation for various initial conditions and then weighting their contribution to the average variance by calculating the probability distribution for the starting positions. We have found that the approximation results in about a $10 - 20\%$ uncertainty in the critical variance, which may be smaller than the uncertainty due to $\xi_{\rm crit}$ and can similarly be absorbed in uncertainty of the value of H_I corresponding to fixed λ, $H_{\rm des}$.

- We have assumed that radiation domination is reached immediately after inflation. During a period of matter domination that lasts between the end of inflation and the end of reheating at $H_{\rm RH}$ the number of e-folds that re-entered is $N_{\rm mat} = (1/3)\log(H_I/H_{\rm RH})$, which is smaller than $N_{\rm rad} = (1/2)\log(H_I/H_{\rm RH})$ if this period was also radiation dominated as we assumed. Since the e-folds re-entered correspond to the number of e-folds of inflation over which fluctuations accumulated, we see that for a period of matter domination fluctuations enter slower, so the network will be destroyed at later times. We provide additional detail on the reheating temperature in Section 5.3, but for now we note that for the result of this Chapter to be relevant we required that PQ symmetry is not restored by a high reheating temperature. This puts a lower limit on the number of e-folds that re-entered during matter domination at $N_{\rm mat} \gtrsim 6$.

- We have assumed that the empiric relation (4.12) that we have found from simulations with massless axions still holds after the axion mass becomes relevant. We expect that to be the case in the intermediate scenario, since the network is underdense and long strings are on average many horizons apart and cannot interact, even if the domain walls are pulling them together.

- We have not derived the spectrum of domain walls emissions and instead set the energy of emitted axions to m_a. As mentioned in Section 4.5.1 the relevant momentum scales are $H < m_a$ and m_a, so this at most introduces an order 1 error in the calculation of the relic abundance. Additionally an error up to a factor of 2 in the relic abundance is due to the unknown contribution of domain walls during the network's evolution.

- In the underdense regime accessible in the simulations we have not found evidence of further dependence on $\log(m_r/H)$ in the evolution of the network, other than the fact the variance increases with the number of e-folds re-entered. However we cannot fully exclude additional log dependence at late times.

- We ignored friction between strings and the plasma. This is typically a reasonable assumption [272–276] in the post-inflationary scenario, and even more so in the intermediate scenario, in which the relevant dynamics happen at lower temperature.

- The statistical error when fitting the data in Figure 4.7 is comparatively low, at about 1%.

4.6 Comparison with recent papers on related scenario

Very recently a couple of papers have considered a similar scenario with late strings/domain walls [130, 131]. Both of these works consider the possibility that symmetry breaking happens at some time during the last $N_{\rm tot} \sim 60$ e-folds of inflation such that the strings and domain walls produced only re-enter the horizon after the time the axion field starts oscillating. The mechanisms mentioned that could achieve this are a coupling between the PQ field and the inflaton, a coupling between the PQ field and the scalar curvature, and multiple stages of inflation, all of which are considered in more detail in Chapter 5. Meanwhile the intermediate scenario we discussed so far was concerned with the case of strings formed by quantum fluctuations, whose size is set by the value of H_I. Thus the size of H_I controls the evolution of the strings after the end of inflation, and there must exist values of H_I for which the strings become sufficiently dense only late.

In any case, various mechanisms that realise late strings/domain walls re-entry have in common that the domain walls contribution dominates that of strings and misalignment, and is larger the later walls re-enter, which can easily saturate the DM bound even for low values of f_a. More specifically, the calculation of the relic abundance proceeds in the same way as already discussed in Section 4.5.1 and this puts a limit (4.30) on how late the network can be destroyed, which in the case of [130, 131] is an upper limit on the number of e-folds of inflation that have passed after PQ symmetry breaking. Similarly [129] considers a period of supercooling that lasts close to the QCD phase transition characteristic to strongly coupled theories at TeV scale, which would result in the intermediate scenario if otherwise the PQ symmetry was restored in the early Universe, and discusses the consequences for the axion relic abundance.

Let us start by comparing our estimate for the axion abundance in the intermediate scenario and comment on the differences. In [130] the axion abundance is written as[12]:

$$\Omega_{\rm DW} = \Omega_{\rm mis} e^{(N_{\rm des} - N_{\rm err})}\,, \tag{4.42}$$

where $N_{\rm err}$ roughly corresponds to $N_\star$ since at that time the energy in domain walls is similar to that in misalignment and absorbs all other sources of uncertainty, such as the exact time the network is destroyed compared to the time the PQ breaking scales re-enter, the density and shape of domain walls at this time and the spectrum of emissions. They estimate $N_{\rm err}$ in a fairly large interval to correspond to the range of f_a allowed by astrophysical constraints and the various uncertainties.

[12] A minus sign in the exponential comes from the fact that we denote by $N_{\rm des}$ the number of e-folds that re-enter before the network is destroyed.

On the other hand in [131] the axion abundance is expressed in a form very similar to ours:

$$\rho_{\rm DW} = \frac{27}{4} f_a^2 m_a(T_{\rm des}) H_{\rm des}\,, \tag{4.43}$$

which would be the same as our estimate (4.29) if $\mathcal{A}(t_{\rm des}) = 3/8$. This checks out, as they assume one flat domain wall of area $\pi/H_{\rm des}^2$ per horizon at the time the network is destroyed, which indeed corresponds to $\mathcal{A}(t_{\rm des}) = 3/8$ from eq. (4.15).

Additionally [131] discusses typical properties of the axion miniclusters produced in the intermediate scenario. They point out that there are multiple mechanisms which allow axions to account for all of DM for axion masses larger than that in the post-inflationary scenario for $N_{\rm DW} = 1$. In the case of a detection of an axion of such mass, the spectrum of potentially observable miniclusters could be used to differentiate between the intermediate scenario and other such mechanisms, with the exception of the post-inflationary scenario with $N_{\rm DW} > 1$, which could be tested if the precision of Strong CP phase measurement is improved and possibly requires fine tuning of the additional explicit symmetry breaking required to collapse the domain walls. Our estimation for the mass of the miniclusters eq.(4.38) corresponds to theirs, again we if we set $\mathcal{A}(t_{\rm des}) = 3/8$.

Meanwhile [130] considers isocurvature constraints on axions produced by quantum fluctuations, which in the intermediate scenario may have higher density than the misalignment population. Similarly to the constraints detailed Section 4.5.2, these are weaker than the DM abundance bound for a QCD axion.

4.7 Conclusions

For a long time two axion inflationary scenarios have been recognised, pre- and post-inflationary, each associated with vastly different predictions for the QCD axion mass such that the axion constitutes the entirety of DM. The typical condition separating the two scenarios in the literature was whether the quantum fluctuations in the angular direction during inflation are sufficiently large to randomise the field over an order 1 number of e-folds. We have studied the conditions for string formation in more detail in order to find a more precise condition separating pre- and post-inflationary axion scenarios.

We intuitively expected that the density of strings that form after the end of inflation is correlated to the probability that the radial mode has passed over the top of the potential during inflation due to quantum fluctuations. We have checked this assumption via numerical simulations of the strings evolution in a theory with the simplest $U(1)$ symmetric potential (2.29) starting from realistic initial conditions for the PQ field, i.e. that were obtained by an approximate realisation of the Langevin equation (3.19) which describes the evolution of the field under the effect of quantum fluctuations. The precise relation between the string density and the probability of the field going over the top of the potential is represented in Figure 4.7 and is fit well by eq. (4.12), where the

variance of the radial mode distribution is used as a measure of the probability. The main point is that when the string density ξ is plotted against the variance of the radial mode distribution over regions that have re-entered the horizon, the evolution of the strings over various simulations corresponding to different $H_I/v_a, \lambda$ overlap and align as shown in Figure 4.7. The variance is directly related to the probability to pass over the top of the potential in the limit $\lambda = 0$ and the overlap between $\lambda = 0$ and $\lambda > 0$ simulations suggest that is is a good measure even for $\lambda > 0$.

We explained how the time at which the strings/domain walls network is destroyed can be used to characterise the inflationary scenario: if it happens as soon as the axion mass becomes relevant and domain walls form we have the post-inflationary scenario, while if the network would re-enter and be destroyed significantly later than today we have the pre-inflationary scenario, since topological defects would give a negligible contribution to axion density compared to that of misalignment. The time the network is destroyed is expected to be connected to the string density, since strings on both ends of large domain walls must have re-entered each other's horizon before they can be destroyed, implying a minimum string density at network destruction $\xi_{\text{crit}} \sim \mathcal{O}(1)$. For a given value of the network density necessary for the strings/domain walls network to collapse ξ_{crit} as well as fixed H_I, f_a, λ, the relation (4.12) can be extrapolated to find the number of e-folds that have re-entered until the network becomes dense enough to be destroyed and correspondingly the relevant inflationary scenario. This signals the existence of an additional scenario, one for which the network is destroyed somewhat later than the time the axion mass becomes relevant, but before today. We have found that in this scenario which interpolates between the post- and pre-inflationary, the contribution of domain walls to axion density ends up dominating over that of strings if the network is destroyed sufficiently late. Additionally, the axion abundance will depend on the time the network is destroyed, which allows the axion to account for all of the DM for values of the axion mass higher than what would be possible in both the pre- and post-inflationary scenario with $N_{\text{DW}} = 1$, up to the maximum mass allowed by supernova 1987a bounds. We give an example in Figure 4.9 of the parameter space corresponding to this intermediate scenario by assuming that the network requires $\xi_{\text{crit}} = 1$ to be destroyed.

While we expect that our approach of considering the probability the radial mode passes the top of the potential would hold for more complex potentials than that in (2.29), the situation could be more complicated. First of all for more complex potentials it could be that the distribution deviates from Gaussianity significantly more than for the simple potential we considered, and thus the variance may no longer be a good measure of the probability the radial mode has been pushed over the top of the potential. This would require to fit the string density as a function of the actual probability of the field passing the top of the potential. Unfortunately we cannot exclude that the quantitative details of the relation between the string density and the probability the field was pushed over the top of the potential are model dependent in a currently unknown way. Therefore more complex models could require dedicated simulations, which would be interesting to investigate further.

On the other hand, we have seen that the axion abundance in the intermediate scenario is very sensitive to the moment the network is destroyed, the exact details of which are unknown. We have limited to assuming that the condition for the network to be destroyed is simply that the strings are dense enough $\xi_{\text{crit}} \simeq \mathcal{O}(1)$. A more precise determination would require a quantitative understanding of requirements for domain walls collapse, which would likely involve simulations of underdense networks with the mass of the axion turned on at various values of the string density. This is also a potentially interesting future direction to consider.

Chapter 5

Alternative ways to restore PQ symmetry

Having considered the case of quantum fluctuations, we now move to alternative ways that lead to PQ symmetry restoration. We explore various mechanisms that can achieve this and discuss when they lead to the post-inflationary scenario, or the intermediate scenario introduced previously corresponding to strings re-entering late. All of these have been previously considered in the literature in various contexts, and we apply these to the case of axions and discuss phenomenological implications.

5.1 Coupling between PQ field and inflaton

One interesting possibility which was initially considered in [277] is that of a direct coupling between the PQ field ϕ and the inflaton φ, for example of the form $(1/2)g\varphi^2 |\phi|^2$. This interaction contributes to the potential of the PQ field (2.29), resulting in a single minimum at $\phi = 0$ if:

$$g\varphi^2 > m_r^2 = 2\lambda v_a^2 \,. \tag{5.1}$$

If we work with a model where the inflaton during inflation is slowly rolling towards a minimum at $\varphi = 0$, then eventually we have $\varphi \lesssim \varphi_c = m_r/\sqrt{g}$ and symmetry would be spontaneously broken, with the value of the axion field being fully randomised after this time. Let us denote the number of e-folds after spontaneous symmetry breaking and until the end of inflation by $N_{\rm ent}$. Then when these $N_{\rm ent}$ e-folds have re-entered the horizon after the end of inflation the field would have large inhomogeneities corresponding to long strings re-entering each other's horizon. Let us denote the value of the Hubble when that happens by $H_{\rm ent}$, which in a radiation dominated Universe after inflation is given by:

$$H_{\rm ent} = H_I e^{-2N_{\rm ent}} \,. \tag{5.2}$$

Again we distinguish the same scenarios as before: the standard post-inflationary scenario corresponds to $H_{\rm ent} > H_\star$, while for $H_{\rm ent} < H_\star$ the strings and domain walls re-enter late. This is very similar to the the intermediate scenario discussed in Section 4.5, the network is expected to collapse approximately when the strings re-enter $H_{\rm des} \simeq H_{\rm ent}$, although we do not provide an exact quantitative condition and it is possible the network collapses some time before. For a given $H_{\rm des}$ the axion abundance is calculated in the same way as in Section 4.5.1. The strings and domain walls must re-enter before the time corresponding to $H_{\rm min}$ of eq. (4.30), or otherwise the domain walls contribution to axion abundance would exceed the total DM abundance. Alternatively, spontaneous symmetry breaking could have happened before the last $N_{\rm tot}$ e-folds of "visible" inflation, in which case the strings have not re-entered until today, which corresponds to the standard pre-inflationary scenario.

Another possibility is that this coupling restores PQ symmetry even at the end of inflation, i.e. $\varphi_{\rm end} \gtrsim \varphi_c$. This corresponds to the standard post-inflationary scenario as spontaneous symmetry breaking happens during the reheating era as the inflaton decays.

Meanwhile the interaction term also affects the potential of the inflaton and modifies the slow-roll conditions, in particular making slow-roll easier to achieve. While symmetry is restored in this way and ϕ is kept in the minimum at $\phi = 0$ it contributes a constant $V_\phi(0) = \lambda v_a^4/4$ to the total energy density, while the condition for inflation to continue is

$$\frac{\left|\dot{H}_I\right|}{H_I^2} \lesssim 1\,. \tag{5.3}$$

Once symmetry breaking happens the PQ field will settle into the new minimum and lose its extra energy. Of course it is possible that slow-roll did not rely on this extra contribution and inflation will ultimately end by the inflaton potential alone, and in this case the post-inflationary and intermediate scenario are certainly possible, depending on the number of e-folds of inflation that happen after symmetry breaking. However, the post-inflationary scenario is more naturally achieved in hybrid models in which inflation relies on the extra contribution to the potential, since in this case inflation is expected to end relatively soon after spontaneous symmetry breaking. Let us consider this type of models in more detail.

5.1.1 Hybrid Inflation

Hybrid inflation models were initially introduced in [277, 278] and in particular have the advantage that inflation happens for relatively small field values and correspondingly small Hubble parameter H_I. The idea in hybrid inflation is that there is an additional field other than the inflaton (we take this to be the PQ field), which is kept in a false vacuum through its interaction with the inflaton as explained above. Characteristic to hybrid models is that the constant contribution to the potential due to this additional field being in the false vacuum is substantial and it maintains inflation for

lower values of the inflaton than the potential V_φ would allow alone, by dominating the energy density near the end of inflation. This means that once the PQ field starts rolling toward its true vacuum, inflation can only continue for a limited amount of time. In particular, as we show below, inflation will end by the time the effective mass of the radial mode becomes of order $\mathcal{O}(H_I)$ [279].

To see this we can estimate the change in the inflaton field ΔN e-folds after symmetry breaking as $\delta\varphi = (\dot{\varphi}\Delta N)/H$ where $\dot{\varphi} = -\left(V'_\varphi(\varphi_c)\right)/(3H)$ is taken at symmetry breaking. The number of e-folds until the effective mass of the radial mode $m^2_{\rm eff} = m_r^2 - g\varphi^2$ becomes at least of order $\mathcal{O}(H_I)$ is then:

$$\Delta N = \frac{\lambda v_a^6 \varphi_c}{64 M_P^4 V'_\varphi(\varphi_c)}\,. \tag{5.4}$$

Once the PQ field starts oscillations ΔN e-folds after symmetry breaking it will soon track the position of its instantaneous minimum:

$$|\phi_m|^2 = \frac{v_a^2}{2} - \frac{g}{4\lambda}\varphi^2\,. \tag{5.5}$$

This allows us to replace ϕ in terms of φ in the potential and thus calculate the effective slow-roll parameters as if inflation was single field:

$$\epsilon = \frac{M_P^2 V'^2}{2V^2} \simeq \frac{M_P^2 (V'_\varphi + 4g\lambda v_a^2 \delta\varphi)^2}{2V^2}\,, \tag{5.6}$$

$$\eta = \left|\frac{M_P^2 (V''_\varphi - g v_a^2)}{V}\right|\,, \tag{5.7}$$

at lowest order in $\delta\varphi$.

It is easy to see that after ΔN e-folds the slow-roll condition $\eta \ll 1$ generally fails, since:

$$\frac{g v_a^2 M_P^2}{V} \simeq \frac{4 g v_a^2}{\lambda v_a^4} = \frac{8 M_P^2}{\varphi_c^2} \gg 1\,, \tag{5.8}$$

in most hybrid inflation models.

Therefore an upper bound on the number of e-folds between PQ symmetry breaking and the end of inflation, which we also use as an estimate for the number of e-folds that need to re-enter before the string interaction become efficient in order to destroy the network:

$$N_{\rm ent} \lesssim \Delta N \simeq \frac{\lambda v_a^6 \varphi_c}{64 M_P^4 V'_\varphi(\varphi_c)}\,. \tag{5.9}$$

Additional constraints on hybrid inflation are coming from the CMB for example the amplitude

of the spectrum of density perturbation gives [280]:

$$\frac{V^{3/2}}{M_P^3 V'} = \frac{\lambda^{3/2} v_a^6}{8 M_P^3 V'_\varphi(\varphi_{\rm CMB})} = 5 \times 10^{-4} \,, \tag{5.10}$$

since at the time CMB scales exit the horizon symmetry will be restored in the intermediate and post-inflationary scenarios. This can be deduced from the equation (1.25) by replacing H_I and ϵ from equation (1.19) in terms of the potential, i.e.:

$$A_s = \frac{1}{2\epsilon}\left(\frac{H_I}{2\pi M_P}\right)^2 = \frac{V^3}{12\pi^2 M_P^6 (V')^2} = 2.1 \times 10^{-9} \,, \tag{5.11}$$

where

$$3 H_I^2 M_P^2 = V \,, \tag{5.12}$$

$$\epsilon = \frac{M_P^2}{2}\left(\frac{V'}{V}\right) . \tag{5.13}$$

The conditions (5.10) leads to:

$$N_{\rm ent} \lesssim \frac{5 \times 10^{-4} v_a}{4 M_P \sqrt{2g}} \,. \tag{5.14}$$

Given the upper limit $f_a \lesssim 10^{10}\,\text{GeV}$ for the QCD axion in the post-inflationary and intermediate scenarios, we find that indeed the post-inflationary scenario is naturally achieved in hybrid models. The condition that the vacuum energy of the PQ field dominates at the end of inflation also sets the H_I:

$$H_I \simeq \sqrt{\frac{\lambda}{12}} \frac{v_a^2}{M_P} \,, \tag{5.15}$$

clearly much smaller than v_a. Therefore hybrid models require much smaller H_I to achieve the post-inflationary scenario than the case of quantum fluctuations. On the other hand in order to achieve late strings $H_{\rm ent} < H_\star$ the coupling g must be very small $g \lesssim \mathcal{O}\left(10^{-28}\right)$ and correspondingly $\lambda \lesssim 10^{-12}$ and $H_I \lesssim 20\,\text{keV}$.

We have not yet specified the potential of the inflaton V_φ. At the time the CMB scales exit the horizon the inflaton will contribute to the slow-roll parameters through V'_φ and V''_φ and so it will be responsible for meeting the CMB constraints.

We conclude that, while it should be possible to achieve the intermediate scenario through hybrid inflation, it requires substantial fine tuning of the couplings of the PQ field, both its self-coupling λ and its coupling to the inflaton g. Hybrid inflation most naturally results in the post-inflationary scenario, even for low values of H_I and reheating temperature that would otherwise correspond to the pre-inflationary scenario. Indeed, the absolute maximum temperature achievable in the early Universe is parametrically $\sqrt{H_I M_P}$, even for instant inflaton decay and thermalisation. Meanwhile in hybrid models PQ symmetry is restored at a scale $v_a \sim \sqrt{H_I M_P}/\lambda^{1/4}$, even for

$\lambda \simeq \mathcal{O}(1)$ the Hubble during hybrid inflation is $H_I \sim \mathcal{O}(f_a^2/M_P) \ll f_a$. As we show later in Section 5.4, hybrid inflation is also more efficient at restoring the PQ symmetry than non-perturbative energy transfer from the inflaton to the PQ field during preheating, in the sense that is requires smaller coupling between the inflaton and the PQ field.

5.2 Coupling to scalar curvature

So far we have considered minimal coupling to gravity. We could add the lowest order non-minimal coupling between the PQ field and scalar curvature $\mathcal{R}$, of the form $\mathcal{L} \supset \epsilon\mathcal{R}\,|\phi|^2$ where during inflation $\mathcal{R} \simeq -12H_I^2$. Similarly to the case with a coupling to the inflaton the modified potential:

$$V = V_\phi - \epsilon\mathcal{R}\,|\phi|^2 = \lambda\left(|\phi|^2 - \frac{v_a^2}{2}\right)^2 + 12H_I^2\,|\phi|^2\ , \tag{5.16}$$

has a single minimum at $\phi = 0$ if $\epsilon > \lambda/(12(H_I^2/v_a^2))$, which means PQ symmetry is restored. This would be mostly interesting for values $H_I/v_a \lesssim \mathcal{O}(1)$ for which symmetry is not restored by the quantum fluctuations already.

If the PQ symmetry is restored in this way at the end of inflation, it will eventually be broken as the Universe reheats to become radiation dominated, resulting in the standard post-inflationary scenario.

5.3 Symmetry restoration by finite temperature

After inflation the Universe must transition from a stage of matter domination by the inflaton field to a stage of radiation domination through the decay of the inflaton and subsequent thermalisation of its decay products, which requires thermal and chemical equilibrium to be reached. This is of course incredibly complicated to analyse in full detail and involves many unknowns, so we limit to considering consequences for the QCD axion and more generally ALPs in relatively simple models, with the particular assumption that thermalisation happens nearly instantaneously after the decay of the inflaton and thus the temperature is the highest it could be. Efficient thermalisation indeed occurs for some couplings and matter content (e.g. if this happens through interactions with massless gauge bosons, see [281, 282]), in which case temperatures close to the estimates in this Section are achieved.

If we denote the maximum radiation temperature during the early Universe by $T_{\rm max}$ and the sector that gives rise to the axion is sufficiently close to thermal equilibrium at this time, then the PQ field would receive finite temperature corrections to its effective potential $\Delta V \sim \lambda T_{\rm max}^2\phi^2$ which restores the PQ symmetry if $T_{\rm max} > \mathcal{O}(v_a)$. This is generally the case for many choices of

matter content and potentials (including eq. (2.29)) [283–285].[1] In this case, the PQ symmetry spontaneously breaks when the temperature subsequently drops below $\mathcal{O}(v_a)$ and a string network forms [172–174]. Notice that this restoration mechanism cannot result in a situation where strings and domain walls form late, which would be similar to the intermediate scenario discussed in Section 4.5, since that would require symmetry restoration to happen at a temperature $T_{\max} \lesssim T_\star$, much lower than the symmetry breaking scale v_a.

There exist a standard estimate in the literature for the reheating temperature $T_{\rm RH}$ [287–289], which is defined as the effective temperature when the Hubble is equal to the inflaton decay rate $H_{\rm RH} = \Gamma_{\rm RH}$. The inflaton rapidly decays after this point, and assuming thermalisation happens instantly the Universe enters radiation domination at a temperature:

$$T_{\rm RH} \simeq \left(\frac{90}{g_\star(T_{\rm RH})\pi^2}\right)^{1/4} \sqrt{M_P \Gamma_\varphi}\,. \tag{5.17}$$

We see that there exist the possibility that $T_{\rm RH} \gg v_a \gg H_I$, so that symmetry is restored by thermal fluctuation but not by quantum fluctuations during inflation. Additionally, at earlier times the total energy density is much larger than it would eventually be at reheating, so it is possible that, even if the inflaton has only partially decayed to radiation, the temperature is larger than $T_{\rm RH}$. This has been studied in [290] where the maximum temperature has been estimated, again assuming instant thermalisation:

$$T_{\max} \simeq 0.30 M_P^{\frac{1}{4}} H_I^{\frac{1}{4}} T_{\rm RH}^{\frac{1}{2}} \simeq 0.22 M_P^{\frac{1}{2}} H_I^{\frac{1}{4}} \Gamma_\varphi^{\frac{1}{4}}\,, \tag{5.18}$$

which is parametrically larger than the reheating temperature $T_{\rm RH}$.

In this estimate it was assumed that the perturbative decay rate Γ_φ is constant. However, the inflaton can also lose it's energy via scatterings such as $\varphi + \varphi \to \chi + \chi$ where χ is an effectively massless scalar field (compared to the inflaton) and the corresponding interaction term in the Lagrangian giving rise to this scattering is $\mathcal{L} \supset -g_{\varphi\chi}\varphi^2\chi^2$. The interaction rate of such scattering (at the perturbative level) is proportional to the square of the amplitude of inflaton oscillations [291]:

$$\Gamma_{2\to 2} = \mathcal{O}(1)\frac{g_{\varphi\chi}^2 \varphi^2}{4\pi m_\varphi}\,. \tag{5.19}$$

If right after inflation we have $\varphi_{\rm end} \gg m_\varphi$ these scatterings will dominate the energy loss of the inflaton in the early Universe when only a small fraction of the inflaton has decayed, which is the rate relevant in the calculation of $T_{\max}$. Meanwhile at completion of reheating the amplitude of the inflaton oscillations will have decreased substantially and thus the decay rate at reheating will be dominated by different decay channels, such as those resulting from trilinear couplings to

[1] High temperature does not restore symmetries in all theories, and the relevance of this to the formation of topological defects has been studied in [286].

bosons or fermions, whose decay rate is non-zero in the limit of very small amplitude of inflaton oscillations. Overall we can modify (5.18) to:

$$T_{\rm max} \simeq 0.22 M_P^{1/4} H_I^{1/4} T_{\rm RH}^{1/2} \left(\frac{\Gamma_I}{\Gamma_{\rm RH}}\right)^{1/4}, \tag{5.20}$$

where $\Gamma_I, \Gamma_{\rm RH}$ are the decay rates at the end of inflation and end of reheating respectively.

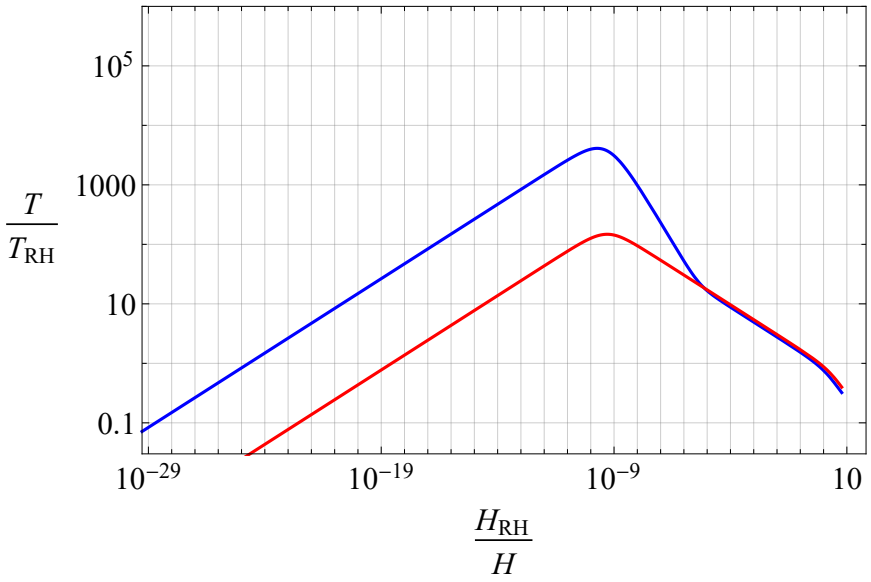

Figure 5.1: Example of the evolution of the temperature of radiation assuming instant thermalisation. Red line corresponds to constant decay rate of the inflaton, while blue corresponds to an initially larger energy loss rate due to 2 to 2 scatterings which decreases down to the decay rate at reheating which is dominated by 1 to 2 decays. The time the maximum temperature is achieved is not substantially modified by including scatterings.

5.4 Preheating

Another possibility is that the inflaton decays through non-perturbative processes, rapidly transferring its energy to other scalar fields. This is sometimes called preheating and it is enhanced by exponentially growing occupation numbers of the modes the inflaton decays into. There are two ways this could result in PQ symmetry restoration: firstly the effective decay rate for such processes increases exponentially while they are efficient, meaning a correspondingly large $T_{\rm max}$ which could restore PQ symmetry through thermal fluctuations. Secondly, the fluctuations in the daughter field at the end of preheating are potentially huge even outside of thermal equilibrium and correspond to an equivalent temperature $T_{\rm eff}^2 \sim \langle \phi^2 \rangle$ which could exceed the maximum temperature in the Universe $T_{\rm max}$. The possibility that these fluctuations restore symmetry for a daughter field with symmetry breaking potential has been considered before [292–297].

We start by considering a general scalar field Ψ coupled to the inflaton through a term $\frac{1}{2}g\Psi^2\varphi^2$. We follow [298] and write the equation of motion for the fluctuations of Ψ in momentum space:

$$\ddot{\Psi}_k + 3H\dot{\Psi}_k + \left(\frac{k^2}{R(t)^2} + m_\Psi^2 + g\tilde{\varphi}^2\sin^2(\omega_\varphi t)\right)\Psi_k = 0 \ , \tag{5.21}$$

where by Ψ_k we denoted the momentum modes of Ψ, ω_φ is the frequency of inflaton oscillations around the minimum of its potential and $\tilde{\varphi}$ is the amplitude of inflaton oscillations. If the dominant term of the inflaton potential around the minimum is quadratic, which is generally the case, then the frequency of the inflaton oscillations is simply the mass of the inflaton $\omega_\varphi = m_\varphi$.

This is usually recast in the form of the Mathieu equation:

$$\Psi_k'' + [A_k - 2q\cos(2z)]\Psi_k = 0 \ , \tag{5.22}$$

by replacing $q = g\tilde{\varphi}^2/(4m_\varphi^2)$; $A_k = ((k/R)^2 + m_\Psi^2)/m_\varphi^2 + 2q$; $z = m_\varphi t$ and differentiating with respect to the re-scaled time z. In the usual Mathieu equation the parameters q, A_k, m_φ would be constant in time, which corresponds to no expansion of the Universe and no decay of the inflaton. The Mathieu equation has been studied extensively, see [299] for a review, and solutions have resonance bands which depend on the parameters q, A_k and are centered at integer multiples of the inflaton frequency ω_φ. Modes whose momentum correspond to parameters inside this band are exponentially amplified in time $\Psi_k \sim e^{\alpha z}$ with $\mathrm{Re}(\alpha) > 0$.

However, the expansion of the Universe results in a redshifting of modes momentum, meaning that modes inside resonance bands exit it while modes of higher momentum enter the bands. Meanwhile as energy is transferred from the inflaton to the daughter field Ψ the parameter q which control the width of the resonance bands will decrease and the mass of the inflaton will receive a contribution, which at tree level has the form:

$$\Delta m_\varphi^2 = g\left\langle\Psi^2\right\rangle \ , \tag{5.23}$$

so the frequency of oscillations increases and the position of bands changes. The complications due to the expansion of the Universe and backreaction due to the inflaton decay have been considered in [298]. The result is a so-called stochastic resonance inside a broad, continuous band at relatively low frequency. This resonance is different to the simple resonance bands of the Mathieu equation is the sense that a mode inside the broad resonance is not actually continuously amplified, instead it rapidly shifts into and out of multiple different Mathieu resonance bands, meaning it is exponentially amplified for only a portion of the time. Nevertheless, on average modes inside the broad band grow exponentially in time provided that the amplitude of inflaton oscillations is sufficiently large, $q \gtrsim \frac{1}{3}$ [298]. Therefore, preheating is eventually terminated either by the inflaton losing its energy to Hubble friction or by the backreaction of the created particles, both of which reduce the value

of q. For simplicity we will assume that modes inside the broad resonance continuously grow exponentially with some average exponent[2] $\alpha \simeq 0.1$, which on average replicates the effect of the stochastic resonance on the occupation numbers.

More specifically, modes will be amplified inside a broad band $\omega \in (0, \omega_{\rm max})$ where we denote $\omega \equiv \frac{k^2}{R^2} + m_\Psi^2$ and $\omega_{\rm max}$ is given by:

$$\omega_{\rm max} = \sqrt{\frac{g^{1/2}\tilde{\varphi} m_\varphi}{2}}\,, \tag{5.24}$$

which means efficient preheating can only last while $\omega_{\rm max} > m_\Psi$.

5.4.1 Direct preheating of the PQ field

Here we consider the idea that preheating happens directly to the radial mode of the PQ field, which could result in large non-thermal fluctuations $\langle \phi^2 \rangle \gtrsim \mathcal{O}(v_a^2)$ and restore the PQ symmetry.

For this we replace the generic field Ψ to be the radial mode of the PQ field and remember that for $g\tilde{\varphi}^2_{\rm end} > m_r^2$ the PQ symmetry is already restored at the end of inflation by the contribution of the interaction term to the PQ potential as discussed in Section 5.1, so there is no point to further consider restoration through preheating. However if we simultaneously impose $g\tilde{\varphi}^2_{\rm end} < m_r^2$ and $\omega_{\rm max} > m_r$ we find $q < \frac{1}{16}$, which does not correspond to the broad resonance case according to [298] so preheating directly to the PQ field is not efficient through a broad resonance unless the PQ symmetry was already restored by the large inflaton Vev.

The situation for the PQ field as the daughter field is thus more appropriate to be studied as a narrow resonance band than a broad resonance. Narrow resonance bands have been studied for example in [291] for quadratic and quartic inflaton potentials. Modes are exponentially amplified inside a resonance band centered on the inflaton frequency, $\omega_\varphi = m_\varphi$ for a quadratic inflaton potential, with a width:

$$\delta\omega \simeq \frac{g\tilde{\varphi}^2}{4\omega_\varphi} = \frac{g\tilde{\varphi}^2}{4m_\varphi}\,, \tag{5.25}$$

and an exponent that is at most:

$$\alpha \lesssim \frac{g\tilde{\varphi}^2}{8m_\varphi}\,, \tag{5.26}$$

The modes quickly scan the narrow resonance band due to the expansion of the Universe, which reduces their momentum, while the width of the resonance band continuously decreases as the inflaton is losing its energy. For values of g and $\tilde{\varphi}$ such that $g\tilde{\varphi}^2 < m_r$ so that the PQ symmetry was not already restored by the coupling during inflation and $m_r < m_\varphi$ so that the resonance is energetic enough to produce the radial mode, initial fluctuations of the radial mode are amplified by at most a small factor $e^{\frac{1}{8}} \simeq 1.1$.

[2]The actual exponent varies with q between $0.1 \div 0.2$, see the table in [298] for more detail.

The analysis is a bit different if preheating happens while the inflaton is effectively massless with a potential $V_\varphi = (\lambda_\varphi/4)\varphi^4$, since in this case the frequency of inflaton oscillations $\omega_\varphi \sim \sqrt{\lambda_\varphi}\tilde{\varphi}$ redshifts at the same rate as comoving momentum i.e. as the inverse scale factor $1/R$. Because of this the resonance would be expected to last longer even for narrow resonance bands, as modes have to be taken out of the resonance by backreaction or scattering.

The narrow resonance band[3] is again centered around the frequency of inflaton oscillations [291]:

$$\omega_\varphi \simeq 0.85\sqrt{\lambda_\varphi}\tilde{\varphi}\,, \tag{5.27}$$

and has a width

$$\delta\omega \simeq \frac{g\tilde{\varphi}^2}{4\omega_\varphi}\,. \tag{5.28}$$

Assuming modes for which $k/R \simeq \omega_\varphi \gg m_r$, their frequency redshifts at the same rate as the narrow band, i.e. as $1/R$, so modes that started inside the band remain there and their occupation numbers are exponentially amplified. However the amplitude and frequency of the inflaton oscillations decrease slightly faster than pure redshift due to energy transfer to the PQ field. When the difference is larger than the width of the narrow band, the modes leave the band and are no longer amplified.

Let $\tilde{\varphi}_{\rm red}(t) = \tilde{\varphi}_{\rm end}R_I/R(t)$ be the amplitude of inflaton oscillations in the absence of energy transfer to the PQ field, where $\tilde{\varphi}_{\rm end}$ is the amplitude of inflaton's oscillation at the end of inflation Then the resonance ends at a time t_f when the inflaton amplitude is:

$$\tilde{\varphi}_f = \tilde{\varphi}_{\rm red}(t_f) - \frac{\delta\omega}{0.85\sqrt{\lambda_\varphi}}\,. \tag{5.29}$$

Meanwhile, the energy transferred to the PQ field until this time can be written:

$$\rho_{\rm PQ} = \frac{\lambda_\varphi}{4}\left(\tilde{\varphi}_{\rm red}(t_f)^4 - \tilde{\varphi}_f^4\right) \simeq \frac{g\tilde{\varphi}_{\rm red}(t_f)^4}{1.7^2}\,, \tag{5.30}$$

since $\delta\omega \ll \omega_\varphi$.

On the other hand the energy transferred can be written in terms of the amplification of the occupation numbers:

$$\rho_{\rm PQ} = \int_{k_f-\delta\omega}^{k_f} \frac{k^2}{2}\,|\phi_{k,\rm end}|^2\, e^{2\alpha(t_f-t_{\rm end})}dk\,. \tag{5.31}$$

In the equation above $k_f = 0.85\sqrt{\lambda_\varphi}\tilde{\varphi}_{\rm red}(t_f)$ denotes the momentum of modes that started in the centre of the band at the end of inflation, $\phi_{k,\rm end}$ are the modes functions inside the resonance band at the end of inflation which are exponentially amplified and $\alpha \sim g\tilde{\varphi}^2/(8\omega_\varphi)$ is the coefficient that

[3]The conditions for an efficient stochastic resonance in the case of a quartic inflaton potential were studied in [300]. Similarly to the quadratic inflaton potential the relevant situation to PQ symmetry restoration is that of a narrow resonance.

parametrises the exponential amplification of modes inside the resonance band.

It is possible to replace the parameters in equations (5.30, 5.31) in terms of $H_I, M_P, g, \lambda_\varphi, H_f$ and thus estimate $\rho_{\rm PQ}$. This is sufficient to restore PQ symmetry if $\rho_{\rm PQ} \gg \mathcal{O}(m_r^2 f_a^2)$ which parametrically requires:

$$\frac{g^2 M_P^2}{\lambda_\varphi^2} \gg f_a^2 \,. \tag{5.32}$$

We conclude that non-perturabative inflaton decay to the radial mode does not open any additional parameter space to restore PQ symmetry if the inflaton potential around the vacuum is approximately quadratic, since it would require values of the coupling g for which PQ symmetry was already restored during inflation in the way discussed in Section 5.1. On the other hand preheating is more efficient if the inflaton potential around the vacuum is approximately quartic and could restore the PQ symmetry even for lower coupling g which corresponds to it being broken at the end of inflation, however it would be challenging for such an inflaton potential to correspond to a viable inflationary model.

5.4.2 Indirect preheating of the PQ field

As we have shown the PQ symmetry is not restored by broad resonance preheating directly to the radial mode, unless the coupling to the inflaton is so large that symmetry was already restored at the end of inflation, or the inflaton potential around its vacuum is quartic rather than quadratic. This however is not an issue if preheating first happens to a new, light, scalar and this then transfers energy to the sector that gives rise to the axion. This way the coupling between the inflaton and PQ field could be small enough so that PQ symmetry is broken at the end of inflation while the coupling between the daughter field and the inflaton is sufficiently large to support the broad resonance. As an example in which this happens we consider a theory where the energy transfer to the axion sector happens through an interaction of the form $g_{\Psi\phi}\Psi^2|\phi|^2$, where Ψ is a real scalar that is preheated as before and to maximize the efficiency of preheating we take it to be effectively massless.

Calculating the effective temperatures Ψ and ϕ reach after this process is complex due to the non-perturbative and out of equilibrium nature of the dynamics. We therefore take a simplified approach in which we analyse the distribution of energy in Ψ after preheating and use this to approximate the scattering rate Γ of $\Psi + \Psi \to \phi + \phi$. We will compare this to the Hubble parameter H at the time when the energy density transferred into Ψ and the energy density remaining in the inflaton are equal. Earlier than this, the energy density in Ψ will be significantly lower, leading to a lower effective temperature in the axion sector. However, if preheating lasts beyond this time, then backreaction will play an important role in the evolution, which makes the dynamics more complicated and is expected to slow down energy transfer from the inflaton to Ψ. Assuming preheating ends when half the energy is transferred is enough for an order of magnitude estimate of the maximum effective temperature achievable (indeed, even if the entire energy density of the

inflaton is subsequently transferred into Ψ, this will be at most a factor of 2 higher than that at the moment of equality).

We denote the amplitude of the inflaton oscillations at the point where the energy density of the inflaton and of Ψ are equal by $\tilde{\varphi}_{\rm eq}$. To estimate the typical occupation numbers n_k of Ψ_k modes that are inside the resonance band $k \in (0, \omega_{\rm max})$ we equate the energy density in Ψ at this moment

$$\rho_\Psi \approx \frac{2\pi}{3} n_k \omega_{\rm max}^4 = \frac{\pi}{6} n_k g \tilde{\varphi}_{\rm eq}^2 m_\varphi^2 \,, \tag{5.33}$$

to the energy density in the inflaton $\frac{1}{2}\tilde{\varphi}_{\rm eq}^2 m_\varphi^2$, so $n_k \simeq 3/(\pi g)$ inside the resonance band. Meanwhile, modes outside the resonance band $k > \omega_{\rm max}$ have not been exponentially amplified, so their occupation numbers are negligible.

To transfer energy to ϕ efficiently there must be Ψ modes that are energetic enough for $\Psi + \Psi \to \phi + \phi$ to occur, which requires $\omega_{\rm max} \gg m_r$. This puts a lower bound on g:

$$g \gtrsim \frac{4 m_r^4}{\tilde{\varphi}^2 m_\varphi^2} \,. \tag{5.34}$$

Given the momentum distribution described above, the scattering rate $\Gamma = n \langle \sigma_{\Psi\phi} v \rangle$ can be calculated, where $\sigma_{\Psi\phi}$ is the interaction cross section: [4]

$$\sigma_{\Psi\phi} = \frac{g_{\Psi\phi}^2 \sqrt{k^2 - m_r^2}}{128\pi k^3} \,, \tag{5.35}$$

leading to

$$\Gamma = \frac{3 g_{\Psi\phi}^2 m_\varphi^{1/2} \tilde{\varphi}_{\rm eq}^{1/2}}{32\sqrt{2}\pi g^{3/4}} = \frac{3^{5/4} g_{\Psi\phi}^2 H_{\rm eq}^{1/2}}{32\sqrt{2}\pi g^{3/4}} \,. \tag{5.36}$$

If this scattering rate is larger than the Hubble at that time preheating ends $\Gamma \gtrsim H_{\rm eq}$ then Ψ and ϕ will reach equilibrium at an effective temperature $T_{\rm eq} \sim \sqrt{H_{\rm eq} M_{\rm P}}$. Both Γ and $H_{\rm eq}$ depend on the values of m_φ and $\tilde{\varphi}_{\rm end}$ i.e. on the details of the inflationary model. For example in the simplest chaotic inflation model the potential is purely quadratic[5] which sets $\tilde{\varphi}_{\rm end} = \sqrt{2} M_P$ and $m_\varphi = \sqrt{3} H_I$. In this model preheating lasts for approximately 20 inflaton oscillations until a significant fraction of the inflaton energy has been transferred, provided that preheating lasts until this point, which requires $g \gtrsim 10^{-6}$ [298, 301]. In this case the Hubble at the end of preheating can be estimated $H_{\rm eq} \simeq 0.025 H_I$. Meanwhile, if $\Gamma \ll H$ immediately after preheating the energy transferred to the axion sector through this process is not sufficient to restore the PQ symmetry, since the rate of energy transfer by $\Psi + \Psi \to \phi + \phi$ will decrease faster than the Hubble parameter.

Let us check if this type of non-perturbative decay of the inflaton actually restores PQ symmetry in situations where the temperature that would otherwise be achieved perturbatively does not.

[4] See for example [8] for a review of the calculation of interaction rates.

[5] Such model is ruled out by Planck data, and is only shown here as a simple example.

In [290] the scale factor when the maximum temperature is reached is calculated, and thus we can estimate $\tilde{\varphi}_{\rm max} \simeq 0.5\tilde{\varphi}_{\rm end}$ at this time and the perturbative decay rate associated with the coupling between the inflaton an Ψ:

$$\Gamma_{\rm pert} = \frac{g^2\tilde{\varphi}^2_{\rm max}}{4\pi m_\varphi}\,. \tag{5.37}$$

It is interesting to see when $T_{\rm eq} \gtrsim T_{\rm max}$ corresponding to this decay rate, plugging everything in and replacing g for the lower bound (5.34) a necessary condition is:

$$H_I^3 M_P^2 m_\varphi^3 \gtrsim 10 m_r^8\,, \tag{5.38}$$

where in typical models of inflation one would expect $H_I \gtrsim m_\varphi/\sqrt{3}$ to keep the second slow-roll parameter small. For the QCD axion even for strong self-coupling $m_r \simeq f_a > H_I$ it is possible for this mechanism to be the more efficient at restoring the symmetry than both thermal and quantum fluctuations. For ALPs with much larger f_a, this mechanism still might be more efficient than a large temperature if $\lambda \ll 1$.

5.5 Roller-coaster inflation

So far we have assumed that the Hubble during inflation remains roughly constant over the last $\mathcal{O}(60)$ e-folds of inflation, which correspond to scales exiting the horizon that are now the size of our Universe. Here we consider the converse, where inflation is broken into multiple separate stages, briefly interrupted by periods of radiation or matter domination. Such a possibility has been considered in [302] (see also references therein). The idea is that in order to solve the typical problems, such as the horizon and flatness problems, inflation only requires a total number of e-folds $\mathcal{O}(60)$, but not that they all happen in one go. Meanwhile, if the last $\mathcal{O}(15)$ e-folds to re-enter happened in one go (which correspond to the first $\mathcal{O}(15)$ out of the last $\mathcal{O}(60)$ e-folds of inflation) and the periods of decelerated expansion between successive stages of inflation are comparatively short, then the modes corresponding to scales that are currently probed by the CMB have all exited inside the same stage of inflation and have remained frozen, and thus there will be no observable difference in the CMB between one stage of continuous inflation or multiple.

There are many ways in which multiple stages of inflation can lead to a situation similar to the intermediate scenario discussed in Section 4.5. For example the PQ symmetry could be restored inside some of the earlier stages of inflation by a coupling to the (respective) inflaton or to the scalar curvature, but not during the later ones. Alternatively, the PQ symmetry could be restored by the temperature achieved during stages of radiation domination between consecutive stages of inflation. Then subsequent stages of inflation during which the PQ symmetry is not restored could result in late strings and domain walls re-entry $H_{\rm min} < H_{\rm ent} < H_\star$.

Finally, it is possible that some of the earlier stages of inflation had $H_I \gg f_a$ corresponding to quantum fluctuations that easily produce strings, while the final stages of inflation have $H_I \ll f_a$

and have diluted the strings. In Figure 4.9 we showed the value H_I/v_a necessary for strings to become relevant at relatively late times after the axion field starts oscillating, which is the intermediate scenario. We see that the intermediate scenario happens for H_I in a relatively narrow interval since an order $\mathcal{O}(1)$ increase of H_I would move us into the post-inflationary scenario while an $\mathcal{O}(1)$ decrease into the pre-inflationary scenario, or in a region that is ruled out by DM overabundance[6]. This means that, if the last $\mathcal{O}(N_\star)$ e-folds of inflation happened in a stage with a value $H_{I,2}$ that corresponds to the pre-inflationary scenario and before that there was a stage with $H_{I,1}$ which corresponds to the post-inflationary scenario, then late strings could be achieved while the required separation between $H_{I,1}$ and $H_{I,2}$, which corresponds to the duration of the stage of decelerated expansion between these two stages of inflation, need not be too large.[7] This is just a simple example, as discussed in Chapter 4 the string density is connected to the variance of the distribution of the radial mode, which accumulates with the number of e-folds. With multiple stages of inflation there exist many possibilities to accumulate the required variance $\sigma^2_{\rm crit}$ corresponding to network destruction over a number of e-folds larger than $N_\star$.

5.6 Symmetry Restoration with a Light Radial Mode

Here we show that if the radial mode (and additional PQ quarks) are light, the PQ phase transition happens at temperatures that are lower than f_a. Consequently, PQ symmetry restoration happens for reheating temperatures lower than if the mass of the radial mode is around f_a (which as discussed, typically requires temperatures $\gtrsim f_a$).

As an example we consider the Lagrangian in eqs. (2.28, 2.29), with a quartic $\lambda = m_r^2/(2f_a^2) \ll 1$, with the radial mode coupled to fermions ψ (such interactions are present e.g. in the KSVZ QCD axion model).

Although it will turn out not to restore the PQ symmetry for $T \ll f_a$ it is useful to first consider the finite temperature contribution from ϕ to its own thermal potential. In the high temperature limit $T \gg m_r$ this is given by

$$V_T \simeq \frac{1}{24} m_r^2\left(\phi\right) T^2 \simeq \frac{1}{16}\frac{m_r^2}{f_a^2}|\phi|^2 T^2 \ , \tag{5.39}$$

where $m_r\left(\phi\right)^2 \sim \lambda|\phi|^2$ is the mass of the radial mode on the background of its own expectation value (and in the second equality we have dropped a ϕ independent term). Comparing eqs. (2.29) and (5.39), we immediately see that eq. (5.39) can only restore the symmetry for $T \gtrsim f_a$ (i.e.

[6] In Figure 4.9 we have assumed a specific value for $\xi_{\rm crit} = 1$. While the exact $\xi_{\rm crit}$ is not known it is still true that the region between pre- and post-inflationary scenario corresponds to a relatively narrow interval of H_I.

[7] In fact, one of the examples considered in [302] consists in two stages of accelerated expansion each 25 e-folds long separated by a stage of radiation domination for 3 e-folds and is compatible with cosmological constraints. In this case $H_{I,1}/H_{I,2} = e^6 \simeq 400$, which is enough difference to allow $H_{I,1}$ to correspond to the post-inflationary scenario while $H_{I,2}$ to the pre-inflationary scenario, which could overall result in the intermediate scenario.

$T \gtrsim m_r$ is not sufficient). It is straightforward to show that the conclusion is unchanged if the full thermal potential is used rather than eq. (5.39) [285, 303].

However, the complex scalar could also couple to new fermions. In a QCD axion model these might be the fermions that generate the QCD-PQ anomaly in KSVZ models, but more generally the new fermions need not be charged under the SM gauge group.[8] We consider an interaction of the form

$$\mathcal{L} \supset g\phi\psi^c\psi + \text{h.c.} \ , \tag{5.40}$$

where ψ and ψ^c are Weyl fermions that are massless in the absence of a ϕ expectation value (and h.c. denotes the Hermitian conjugate).[9] The dependence of the mass of ψ on ϕ's expectation value leads to finite temperature contribution to ϕ's potential [303, 304]

$$V_T = \frac{-n_f T^4}{2\pi^2} \int_0^\infty q^2 \log\left(1 + e^{-\sqrt{q^2 + g^2|\phi|^2/T^2}}\right) \, dq \ , \tag{5.41}$$

where $n_f = 4$ if there are a single pair of fermions. In the high temperature limit $T \gg m_\psi = g\langle\phi\rangle$ eq. (5.41) is approximately

$$V_T \simeq \frac{1}{24} g^2 \phi^2 T^2 \ . \tag{5.42}$$

Consequently $\langle\phi\rangle = 0$ is a local minimum of the potential for any temperature $T \gtrsim m_r/g$. However, we impose a stronger condition, which is that the thermal potential ensures that the system reaches $\langle\phi\rangle = 0$ regardless of the initial conditions.[10] This is not automatic given eq. (5.42), because this is only valid for $T \gg g\langle\phi\rangle$, which is not satisfied around $\langle\phi\rangle \sim f_a$ if $T \lesssim g f_a$. Instead, for $T \ll g f_a$ the thermal potential of eq. 5.41 is exponentially suppressed at $\langle\phi\rangle \sim f_a$. Physically, this happens because ψ decouples from the thermal bath when its mass is greater than the temperature. Therefore, there is a local minimum close to the zero temperature minimum for temperatures in this range.

Combining the preceding conditions, the lowest temperature at which the PQ symmetry is restored regardless of the initial condition is parametrically given by:

$$T_{\text{min}} \simeq \text{Max}\left(\frac{m_r}{g}, g f_a\right) \ , \tag{5.43}$$

which is lower than the temperature required for the ϕ contribution to its own potential to restore PQ symmetry if $m_r \lesssim g f_a$. Precise results for the minimum temperature for a given model can easily be obtained by evaluating eq. (5.41) numerically. In Figure 5.2 we plot the results for the

[8] Indeed to avoid a too large axion mass for the parameter space that we are interested in, they must not lead to a QCD induced axion mass.

[9] Unless g is tiny radiative corrections induced by this term typically require that ϕ's mass is fine tuned. We do not worry about this issue, which could be avoided for example if the axion and new fermion sector is supersymmetric.

[10] We could e.g. consider models of inflation such that $\langle\phi\rangle = 0$ initially, in which case $T \gtrsim m_r/g$ would keep the system at this point. However, in such a theory strings will form anyway, so the thermal potential is not required for this.

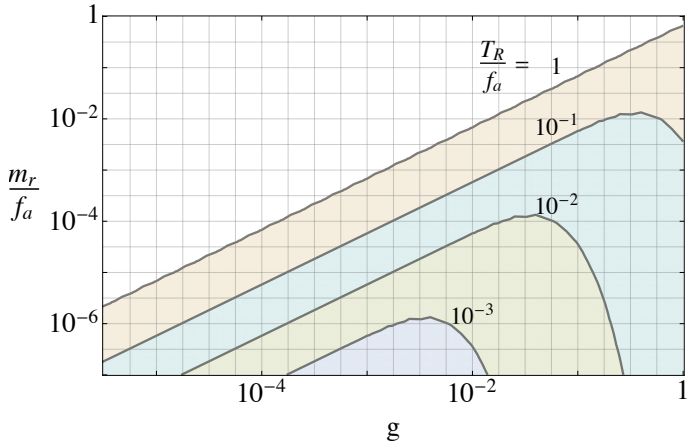

Figure 5.2: The minimum reheating temperature required to restore the axion PQ symmetry (regardless of the system's initial conditions) in theories such that the radial mode of the complex scalar ϕ that gives rise to the axion has a mass m_r that is significantly smaller than the axion decay constant f_a, and ϕ has an interaction with fermions with coupling constant g as in eq. (5.40).

simple model of eq. (2.28) with a single pair of fermions ψ ψ^c as a function of m_r/f_a and the coupling g. It can be seen that eq. (5.43) is quite accurate (although the condition $T > gf_a$ is slightly too strong since the fermions do not decouple from the thermal bath immediately when this condition is violated). If an axion arises from a more complex theory the minimum temperature required will change by order 1 factors, but the main parametric dependence will remain fixed.

Finally note that the typical interaction rate of the fermions ψ with the thermal bath is of the order g^2T, which has to be larger than the Hubble in order for the fermions to be in thermal equilibrium and our analysis using the thermal potential to be valid. Parametrically this requires $gM_P \gtrsim f_a$ and $g^3M_P \gtrsim m_r$.

Chapter 6

ALP detection via gravitational waves

6.1 Introduction

Gravitational waves can provide valuable insight into high energy physics and in particular evidence for various extensions of the Standard Model or alternatively constraints on them. As such it would be interesting to know if ALP models predict a background of gravitational waves and whether these are observable by proposed GWs detectors. For this reason we have considered the spectrum of gravitational waves resulting from a network of scaling axion strings which are characteristic to the post-inflationary scenario reviewed in Section 2.4.3.[1]

The crucial ingredients needed to determine the resulting spectrum are: 1) the energy emitted instantaneously from the string network in GWs as a function of time, and 2) the momentum distribution with which this energy is emitted. In fact, we will be able to derive these quantities (up to order one coefficients) analytically from energy conservation and the Nambu–Goto effective theory with the Kalb–Ramond term, which describes strings coupled to the axion field in the limit of small string thickness (and captures the logarithmic dependence of the tension mentioned above). We will then see that these predictions are reproduced remarkably well by first principles numerical simulations of the physical system, which confirm the validity of the theoretical assumptions and allow us to extract the unknown coefficients. As will be clear in what follows, numerical simulations can only access a relatively narrow time range, and it is impossible to directly extract the GW energy and its momentum distribution at the physically relevant time, so a careful extrapolation is essential. However, the existence of the scaling solution, in combination with our analytic understanding on the GW emission, makes this extrapolation reliable.

We will show that the energy emitted in GWs at later times during the scaling regime is logarithmically enhanced, primarily as a result of the logarithmic increase of the string tension,

[1] Other papers have considered the case of GWs sourced by ALP domain walls [191, 305], which can dominate the contribution of strings if domain walls survive later than the time the ALP field starts oscillating. This can happen because in the post-inflationary scenario with $N_{\rm DW} > 1$ domain walls are stable until additional energy bias becomes relevant.

and the energy is always produced with a momentum distribution localised at frequencies of order the Hubble scale. When the emission from the entire scaling regime is taken into account, this leads to logarithmic deviations from a scale invariant GW spectrum, which increase the amplitude of the spectrum at low frequencies (indeed, these frequencies are emitted the latest, when the enhancement is largest). As we will show in Section 6.2, the deviation can be approximated by a spectrum $d\Omega_{\rm gw}/d\log f \propto \log^4(f_a/H_f)$, where f_a is the axion decay constant and $H_f \propto f^2$ is the Hubble parameter at the time when GWs of present day frequency f are emitted. Given the large value of this logarithm (up to 10^2 for the relevant axion masses), the deviation from scale invariance is substantial and means that axions with $f_a \gtrsim 10^{14}$ GeV lead to GW spectra that are observable in multiple upcoming experiments.

To better understand the range of decay constants and masses that could be discovered via GW observations, in Section 6.3 we study additional properties of the post-inflationary scenario, which give constraints on the axion parameter space. In particular, we derive a lower bound on the relic abundance of axions from strings. We also calculate the spectrum of density perturbations in the axion field, which leads to isocurvature perturbations measurable for instance in the cosmic microwave background (CMB) that are potentially in conflict with observations. Finally, we discuss how the axions emitted during the scaling regime contribute to dark radiation, which is constrained by big bang nucleosynthesis (BBN) and CMB measurements.

We will see there is a significant region of allowed and observable masses and decay constants for ultralight axions, i.e. with a mass $\lesssim 10^{-17}$ eV. However, the GWs from QCD axion strings are not observable due to the bound $f_a \lesssim 10^{10}$ GeV from DM overproduction in this case [188]. GW searches are particularly useful since they are complementary to other approaches, such as astrophysical observations and DM direct detection experiments, with their sensitivity strongest for large decay constants for which the axion couplings are typically suppressed. Our work will enable limits from GW observations, or even possible future discoveries, to be related to physics at energy scales far beyond any that could be explored directly. It will also allow complementary progress (e.g. potential improvements in searches for isocurvature perturbations and of the measurement of $N_{\rm eff}$) to be interpreted in terms of the post-inflationary scenario.

6.2 Gravitational Waves from Strings

During the scaling regime the motion and interactions of the strings act as a continual source of GWs. In this Section we study the resulting spectrum by combining the effective theory of global strings, and field theory simulations of the physical system described by the PQ Lagrangian in eqs. (2.28, 2.29) for $N_{\rm DW} = 1$, so $v_a = f_a$. In particular, in Section 6.2.1 we use the Nambu–Goto effective theory coupled to the axion field via the Kalb–Ramond term, which captures the dynamics of the parts of the network with small curvature. Both the effective theory and numerical simulations will show that the GWs can be self-consistently treated as a perturbation of the string

network if $G\mu^2/f_a^2 \ll 1$, which will be satisfied for all f_a and m_a of interest. In this case, the fact that GWs are produced does not significantly influence the evolution of the network, which follows the previously described attractor.[2]

For $G\mu^2/f_a^2 \ll 1$ energy conservation and the scaling regime fix the time dependence of the energy emitted into axions Γ_a, via eq. (2.53). However, this cannot be directly used to infer the emissions to GWs Γ_g, which accounts for only a small fraction of the energy released. Nevertheless, in this Section we will show that we can still make use of eq. (2.53) thanks to a convenient relation between the rate of energy emission into GWs and that into axions. We will argue for this relation theoretically using the Nambu–Goto effective theory, and confirm it with numerical simulations of the physical system in the scaling regime. This will allow us to have analytic control of Γ_g at all times, except for an order one coefficient that will be directly extracted from the simulations. In combination with the momentum distribution of the instantaneous GW emission, whose general form can be easily guessed and will be confirmed in simulations, this will allow us to determine the total GW spectrum produced by the network up to $H = H_\star$ when it is destroyed. After being produced the GWs propagate freely, redshifting as the universe expands, so today they make up an irreducible contribution to the stochastic background. As we will see in Section 6.2.4, during the scaling regime the GWs at the observable frequencies are emitted when $\log \gg 1$, and therefore in the following we will often refer to the large log limit, where we define $\log \equiv \log(m_r/H)$.

6.2.1 Theoretical Derivation of GW Emission

The required relation between Γ_g and Γ_a can be argued for via the low energy limit of the action in eqs. (2.28, 2.29), which is the effective theory of Nambu–Goto strings coupled to the axion field [306] by the Kalb–Ramond action [307]. In particular, this effective theory can be obtained from eq. (2.28) on the background of a string and at energies smaller than m_r (i.e. integrating out the radial mode, see [308] for the explicit derivation). It describes the evolution of an infinitely thin string, with a trajectory identified by the space-time coordinate $X^\mu(\tau, \sigma)$, where τ, σ are worldsheet coordinates. The string is coupled to the axion field, described by its (dual) antisymmetric tensor $A_{\mu\nu}$. The corresponding action is

$$S = -\mu \int d\tau d\sigma \sqrt{-\gamma} - \frac{1}{6}\int d^4x F^{\mu\nu\rho}F_{\mu\nu\rho} - g\int d\tau d\sigma \epsilon^{ab}\partial_a X^\mu \partial_b X^\nu A_{\mu\nu}(X) \ , \tag{6.1}$$

where $F_{\mu\nu\rho} = \partial_\mu A_{\nu\rho} + \partial_\nu A_{\rho\mu} + \partial_\rho A_{\mu\nu}$ and γ is the determinant of the induced metric on the worldsheet $\gamma_{ab} = \partial_a X^\mu \partial_b X_\mu$, with $a, b = \tau, \sigma$. The coupling g defines the axion-string interaction, while μ is the string energy per unit length (this is easily seen from the first component of the energy momentum tensor, see eq. (6.4)). As we will see in the following, μ accounts for the energy in the axion gradients, as well as that localised in the core. The axion is related to the only degree

[2] If instead $G\mu^2/f_a^2 \gtrsim 1$ gravity dramatically changes the evolution of the system, and affects the scaling regime in a way that is not known.

of freedom of $A_{\mu\nu}$ by $F^{\mu\nu\rho} = \epsilon^{\mu\nu\rho\sigma}\partial_\sigma a/\sqrt{2}$.[3]

Since a changes by multiples of $2\pi f_a$ around a string, the coupling g is quantised in terms of f_a as $g = 2\pi n f_a/\sqrt{2}$, with n integer.[4] The gauge invariance $A_{\mu\nu} \to A_{\mu\nu} + \partial_\mu\Lambda_\nu + \partial_\nu\Lambda_\mu$ and worldsheet reparametrisation invariance of eq. (6.1) can be fixed by choosing the gauge $\partial_\mu A^{\mu\nu} = 0$ and $\dot{X}\cdot X' = \dot{X}^2 + X'^2 = 0$ where $\dot{X}^\mu \equiv \partial_\tau X^\mu$ and $X'^\mu \equiv \partial_\sigma X^\mu$. In the frame $\tau = t$, the equations of motion for a string with winding $n = 1$ are

$$\mu(\ddot{X}^\mu - X''^\mu) = 2\sqrt{2}\pi f_a F^{\mu\nu\rho}\dot{X}_\nu X'_\rho \,, \tag{6.2}$$

$$\partial_\alpha\partial^\alpha A^{\mu\nu} = \sqrt{2}\pi f_a \int d\sigma \left(\dot{X}^\mu X'^\nu - \dot{X}^\nu X'^\mu\right)\delta^3(\vec{x} - \vec{X}) \,. \tag{6.3}$$

This system of coupled equations determines the evolution of the string and the axion field. The axion is sourced from a moving string via eq. (6.3), whose motion is itself influenced by the axion via eq. (6.2).

Before proceeding, let us clarify a subtlety of this theory. As discussed in [306, 309] the action in eq. (6.1) is strictly speaking ill defined, since the solution of the equations of motion for $A_{\mu\nu}$ in eq. (6.3) is divergent as x^μ approaches X^μ. This makes the interaction term in eq. (6.1) (logarithmically) divergent when evaluated on such solutions. This UV divergence can be regularized and completely reabsorbed in the redefinition of the (bare) string tension μ. After reabsorbing the divergence, the equations of motion will have the same form as eqs. (6.2) and (6.3), but (just like in the renormalization of quantum field theories) with finite $\mu(\Delta)$ and $A_{\mu\nu}(\Delta)$ depending on a new (unphysical) length scale Δ, which can be interpreted as the length at which one probes the string core. In particular, under the change of this scale to Δ', $\mu(\Delta') = \mu(\Delta) + (g^2/2\pi)\log(\Delta'/\Delta) = \mu(\Delta) + \pi f_a^2 \log(\Delta'/\Delta)$.[5] As this scale is not physical, it can be chosen arbitrarily. If Δ is chosen as $m_r^{-1} \ll \Delta \lesssim L$, where L is the IR cutoff ($\simeq H^{-1}$ for long strings), the interpretation of $\mu(\Delta)$ will be that of an effective tension that includes the energy in the axiostatic gradient (up to the IR cutoff Δ), while $A_{\mu\nu}(\Delta)$ will include mostly the axion radiation.[6] In the following we will tacitly assume that the preceding regularization and subtraction has been performed, and that Δ has been always chosen in this way, so that $\mu(\Delta)$ (which we will call μ for simplicity) corresponds to the total energy per unit length, including the gradient energy (see [309] for a more complete treatment). From eq. (6.2) it follows that the effective coupling of the axion to the string is determined by

[3] The normalisation is fixed by equating the energy momentum tensor of the second term in eq. (6.1) to that of a free axion.

[4] This is a consequence of the fact that the commutator $[\partial_i, \partial_j]a$ is non-zero (and quantized) around a string [308] and is easily seen by imposing $2\pi n f_a = \oint_C dx^\mu \partial_\mu a$ where C is a loop surrounding the string, and evaluating the right hand side of this equation via Gauss' theorem and using the equations of motion $\partial_\mu F^{\mu\nu\rho} = -g\int d\tau d\sigma \epsilon^{ab}\partial_a X^\nu \partial_b X^\rho \delta^4(x - X)$.

[5] The same running has been studied in a generalisation of the theory we consider in the context of the effective string description of vortices in superfluids [310].

[6] The fact that changing Δ does not change the equations of motion implies that, as far as the dynamics of the string at small curvature is concerned, it does not matter whether the energy is localised in the string core or in the axion gradient.

$f_a^2/\mu \propto 1/\log$.

Notice that the preceding discussion does not hold when the inverse core-size m_r^{-1} is of the order of the IR cutoff L. Consequently, this effective theory describes the dynamics of the physical system in the parts of the network where the finite string thickness is smaller than the inverse string curvature, but it will break down when strings intersect and reconnect, or when loops shrink (such processes are sensitive to the details of the structure of the potential of the field ϕ and will therefore need the full theory in eq. (2.29)).

In the presence of gravity a moving string sources gravitational radiation, which can be determined by linearising Einstein's equations giving e.g. in the harmonic gauge $\partial^\mu h_{\mu\nu} = \frac{1}{2}\partial_\nu h$

$$\partial_\alpha \partial^\alpha h^{\mu\nu} = 16\pi G \left(T_s^{\mu\nu} - \frac{1}{2}\eta^{\mu\nu} T_{s\,\lambda}^{\lambda} \right), \quad T_s^{\mu\nu} = \mu \int d\sigma \left(\dot{X}^\mu \dot{X}^\nu - X'^\mu X'^\nu \right) \delta^3(\vec{x} - \vec{X}) \,, \tag{6.4}$$

where $g_{\mu\nu} = \eta_{\mu\nu} + h_{\mu\nu}$ is the metric, $h \equiv h^\mu_{\ \mu}$ and $T_s^{\mu\nu}$ is the energy momentum tensor of the string from the first term of eq. (6.1). It is straightforward to show that the energies radiated at infinity per unit time in axions and GWs from a string trajectory X^μ are respectively

$$\frac{dE_a}{dt} = r_a[X]\, f_a^2 \ , \qquad \frac{dE_g}{dt} = r_g[X]\, G\mu^2 \ , \tag{6.5}$$

where $r_a[X]$ and $r_g[X]$ are dimensionless functionals of the shape of the string trajectory (but independent of the string length). In more detail, for any string trajectory X^μ that is a solution of eqs. (6.2) and (6.3), the axion and GW fields are determined by eqs. (6.3) and (6.4). These are wave-like equations of the form $\partial_\alpha \partial^\alpha B = j$, with solution $B = \int d^3y j(t - |\vec{x} - \vec{y}|, \vec{y})/(4\pi|\vec{x} - \vec{y}|)$, and therefore $A_{\mu\nu} \propto f_a$ and $h_{\mu\nu} \propto G\mu$. The emitted energy is $dE/dt \equiv -\int d^3x \dot{T}^{00}$, where for the axion $T_a^{\mu\nu} \sim (\partial A)^2$ and for the GWs $T_g^{\mu\nu} \sim G^{-1}(\partial h)^2$. This fixes the dependence on f_a^2 and $G\mu^2$ of eq. (6.5), while the remaining factors (called r_a and r_g) must be dimensionless functionals of the string trajectory only.

The main conclusion from eq. (6.5) is that GWs are emitted proportionally to the (square of) the string tension, since they are sourced by the energy momentum tensor. Conversely, the axion coupling to the string is fixed by f_a and the axion energy is proportional to f_a^2 only. We stress that eq. (6.5) is valid for any trajectory that is a solution of eqs. (6.2) and (6.3), irrespective of the ratio f_a^2/μ, i.e. regardless of the magnitude of the axion-string coupling. Therefore eq. (6.5) is expected to capture the energy emission from the pieces of the string network for which the string thickness can be neglected at all values of the log, including those accessible in simulations (related previous analysis in the literature has been carried out in the limit of zero coupling [311, 312]).

Since we will not need the functional form of $r_a[X]$ and $r_g[X]$, we give their expressions in Appendix D.1, where we also give further details of the derivation of eq. (6.5). From eqs. (D.6) in Appendix D.1 it can be seen explicitly that (as expected given that they are dimensionless) $r_a[X]$ and $r_g[X]$ are invariant under the rescaling of the length of the trajectory and of time, and therefore

depend only on the shape of the trajectory. We note that the coefficients $r_a[X]$ and $r_g[X]$ have been calculated in [312] for particular trajectories in the limit of zero coupling.

Finally, we observe that, as mentioned, this effective field theory predicts that the GWs do not significantly influence the motion of the strings provided $G\mu^2/f_a^2 \ll 1$. Indeed, the inclusion of gravitational backreaction modifies eq. (6.2) by introducing, on the right hand side, the term $-\mu\Gamma^\mu_{\nu\rho}(\dot{X}^\nu\dot{X}^\rho + X'^\nu X'^\rho)$, where $\Gamma^\mu_{\nu\rho}$ are the Christoffel symbols (this was first studied in [313,314]). Since $\Gamma^\mu_{\nu\rho} \sim \partial h$, and h is of order $G\mu$, this term is suppressed by $G\mu^2/f_a^2$ with respect to the one already present in eq. (6.2). Similarly, the energy emitted in GWs from eq. (6.5) is suppressed with respect to that into axions by the same factor.

6.2.2 GW Spectrum during the Scaling Regime

We now apply the results of Section 6.2.1 to the evolution of the scaling network reviewed in Section 2.4.3 to extract information on the emission of GWs during the scaling regime. As outlined, we use an approach that avoids having to calculate the GW emission directly from eq. (6.5), which would require understanding the form of the trajectories X_s^μ of long strings and loops during scaling.

Given that eq. (6.5) holds for a generic string trajectory, the energy densities Γ_a and Γ_g emitted per unit time during the scaling regime are related by $rG\mu_{\rm eff}^2/f_a^2$, where $r \equiv r_g[X_s]/r_a[X_s]$. We can therefore use our knowledge of Γ_a from energy conservation (i.e. eq. (2.53)) to infer the energy density emitted per unit time in GWs during the scaling regime. This reads

$$\Gamma_g = r\,\frac{G\mu_{\rm eff}^2}{f_a^2}\Gamma_a \quad \overset{\log\gg 1}{\longrightarrow} \quad 8\xi r H^3 \frac{G\mu_{\rm eff}^3}{f_a^2}\ , \tag{6.6}$$

where the second relation holds in the large log limit, and in that case $\Gamma_g \simeq 8\pi^3 r G f_a^4 H^3 \xi \log^3$. In eq. (6.6) the dimensionless coefficient r is a functional of the average shape of the string network (and expected to be of order 1). The average shape of the strings is preserved throughout the scaling regime, and therefore we expect r to be time-independent, or at most have a weak log dependence. The coefficient r can be interpreted as a form factor of the string network that encodes how efficiently the string trajectories during scaling emit GWs compared to axions. In particular it parametrises the string dynamics that are responsible for the GW emission (long strings, small loops, string reconnection, etc.).

The validity of eq. (6.6) with a constant r relies solely on energy conservation during the scaling regime and on the Nambu–Goto effective theory. While the latter must break down when strings reconnect and loops shrink, it is possible that most of the axion and GW energy is emitted in the regime where the effective theory is valid. Indeed, we will see in Section 6.2.3 that eq. (6.6) is reproduced remarkably well with a constant r in first principles field theory simulations, which will allow us to also directly extract its value (instead of calculating it from its definition). We will also see that $\mu_{\rm eff}$, which we defined in terms of the string energy, is well matched by the theoretical form

eq. (2.49). Given this, we will assume that eq. (6.6) holds in the remainder of our present analysis.[7] In particular, assuming the growth of ξ as in eq. (2.47), this implies that Γ_g is proportional to $H^3 \log^4$ at large log.

Since GWs redshift freely, we can straightforwardly obtain the GW energy density ρ_g at a generic time during the scaling regime from $\dot{\rho}_g + 4H\rho_g = \Gamma_g + \dots$, where the dots stand for possible additional GW sources, which we subsequently neglect. It immediately follows that $\rho_g(t) = \int_{t_1}^{t} dt'(R(t')/R(t))^4\Gamma_g(t')$, where t_1 is the time when the scaling regime starts. The remaining ingredient required to calculate the GW spectrum is the momentum distribution of Γ_g. It is convenient to write Γ_g as a function of the differential emission rate $\partial\Gamma_g/\partial k$ and to further express this in terms of the instantaneous emission spectrum F_g, i.e.

$$\Gamma_g(t) = \int dk \frac{\partial\Gamma_g}{\partial k}[k,t] \ , \qquad \frac{\partial\Gamma_g}{\partial k}[k,t] = \frac{\Gamma_g(t)}{H(t)} F_g\left[\frac{k}{H}, \frac{m_r}{H}\right] . \tag{6.7}$$

The function $F_g[x,y]$ fully captures the momentum dependence of the instantaneous emission via the variable $x = k/H$ and its possible time dependence via the variable m_r/H, and is normalised to one by definition, $\int dx F_g[x,y] = 1$. Plugging eq. (6.7) into $\rho_g(t)$ we obtain the total GW energy density spectrum, defined by $\rho_g = \int dk \partial\rho_g/\partial k$,

$$\frac{\partial\rho_g}{\partial k}[k,t] = \int_{t_1}^{t} dt' \frac{\Gamma_g'}{H'} \left(\frac{R'}{R}\right)^3 F_g\left[\frac{k'}{H'}, \frac{m_r}{H'}\right] , \tag{6.8}$$

where $k' = kR/R'$ is the redshifted momentum and all other primed quantities are evaluated at t'. Eq. (6.8) is just the superposition of all the spectra emitted from t_1 to t, properly redshifted.

Given the existence of a scaling solution, we have some theoretical expectations for the form of the instantaneous GW spectrum F_g, which closely resembles the analogous axion spectrum studied in [188]. First, since strings typically have a curvature of order Hubble, the spectrum of GWs emitted at each instant should be peaked at momenta of order the Hubble parameter at that time. Meanwhile, production of GWs with momentum below Hubble or above the string core scale is expected to be strongly suppressed. The absence of any scale between H and m_r suggests that between these two (IR and UV) cutoffs the spectrum follows a single power law $F_g \propto 1/x^q$. It is also expected from the Nambu–Goto description that most of the GW energy Γ_g is contained in (IR) momenta of order Hubble, as opposed to (UV) momenta of order m_r (see [309]), which corresponds to $q > 1$.

We will show in the next Section that all of the properties above are verified in numerical simulations of the scaling regime, where we will provide the exact form of F_g. To get a general picture of the resulting total GW spectrum, it is sufficient to approximate the instantaneous emission with

[7] Eq. (6.6) must break down when $\log \sim M_{\rm P}/f_a$. In Section 6.3 we will see that the values of f_a allowed by existing constraints are always small enough for this to be true (for all m_a). With an abuse of language, we will therefore use the phrasing 'large log' to indicate $\log \lesssim M_{\rm P}/f_a$.

sharp IR and UV cutoffs at momenta $x_0 H$ and m_r, i.e. $F_g[x,y] \propto 1/x^q$ for $x \in [x_0, y]$, and zero elsewhere. Inserting this F_g into eq. (6.8) we obtain the GW spectrum. At a generic time during the scaling regime with $\log \gg 1$, in the momentum range $k \gtrsim x_0 H$ but $k \lesssim x_0\sqrt{H H_1}$ (where $H_1 = 1/2t_1$ is the Hubble parameter at the start of the scaling regime) this is given by

$$\frac{\partial \rho_g}{\partial \log k}[k,t] = 8\pi^3 c_1 r G f_a^4 H^2 \log^4\left[\frac{m_r}{H}\left(\frac{x_0 H}{k}\right)^2\right] , \quad \text{for } x_0 H \lesssim k \lesssim x_0\sqrt{H H_1} , \tag{6.9}$$

where c_1 defined in eq. (2.47) determines the growth rate of ξ, and we omitted terms proportional to additional inverse powers of log, which are negligible in the regime we are considering. The full expression for the spectrum is given in Appendix D.2.

We observe that the spectrum is (approximately) scale invariant between the IR and UV momenta $x_0 H$ and $x_0\sqrt{H H_1}$, so the total GW energy is spread over a wide range of frequencies. This is because the rate at which energy in previously emitted GWs redshifts and the main decrease in $\Gamma_g \propto H^3$ in a radiation dominated universe combine to give $\partial\rho_g/\partial k \propto 1/k$. Such a spectrum accumulates only between the two extremes $x_0 H$ and $x_0\sqrt{H H_1}$, which correspond to the peaks of the instantaneous emission at H and at H_1 respectively (redshifted until H).

However, as time progresses the GW emission is enhanced due to the (increasing) $\log^4$ factor in Γ_g. This leads to a violation of the spectrum's scale invariance, which consequently has larger values at smaller k. This is captured by the logarithmic factor in eq. (6.9), which ranges from $\log^4(m_r/H) = \log^4$ at $k \simeq x_0 H$ to $\log^4(m_r/H_1)$ at $k \simeq x_0\sqrt{H H_1}$. One $\log^2$ factor is due to the increase in the energy stored in the network (from ξ and $\mu_{\rm eff}$), and the additional $\log^2$ factor to the efficiency at which this energy can be emitted in GWs, proportional to coupling of the GWs to the string $G\mu^2$. Although a single power of log relies on the extrapolation of the log growth of ξ observed in simulations, the other three powers are inevitable. Since at the end of the scaling regime $\log \simeq 100$, the violation of scale invariance is substantial and – as we discuss in Section 6.2.4 – it could make the low frequencies of an otherwise invisible signal detectable. It is also clear that it is essential to extrapolate to large log to make any sensible physical predictions, and results directly extracted from simulations, which can reach only $\log \lesssim 8$, are guaranteed to be off by many orders of magnitude.

There are several other features of the GW spectrum from scaling that are worth noting. First, the dependence of the spectrum in eq. (6.9) on x_0 is only logarithmic, and the dependence on q only comes in (neglected) terms proportional to $(q-1)^{-1}\log^{-1}$ (i.e. together with inverse powers of log, see eq. (D.11) in Appendix D.2). Thus, as long as $q-1$ is definitely larger than $1/\log$ the dependence on q is negligible for modes with $k > x_0 H$. This means that even an approximate determination of x_0 and q from simulations will be sufficient to understand the spectrum in the momentum region of eq. (6.9). Moreover, a possible dependence of x_0 and q on log – as long as it keeps $q > 1$ – would not significantly change the spectrum.

Second, if the effective number of degrees of freedom in thermal equilibrium g is not constant,

the scale factor away from particle thresholds is $R \propto t^{1/2} g^{-1/12}$ where g is evaluated at the temperature corresponding to the time t. The spectrum in eq. (6.9) at time t gets the (k-dependent) multiplicative correction $(g(t)/g(t_k))^{1/3}$. Here, t_k is defined by $x_0 H(t_k) \equiv kR(t)/R(t_k)$, and is the time when most of the GWs that have momentum k at time t are emitted. We refer to Appendix D.2 for the explicit derivation. As we will see in more detail in Section 6.2.4, the change in g distorts the $\log^4$ dependence at the momenta corresponding to the temperature when the degrees of freedom decouple from the thermal bath.

Finally, as explained in Appendix D.2, at UV momenta $k \gtrsim x_0\sqrt{HH_1}$ the spectrum $\partial\rho_a/\partial \log k$ is suppressed as $1/k^{q-1}$ and rapidly falls. The critical Hubble $\sqrt{HH_1}$ is model dependent, since it depends on when the scaling regime began (and so when and how the string network forms). Meanwhile, at IR momenta $k \lesssim x_0 H$ the spectrum is also power law suppressed and follows the same behaviour as F_g for $x \lesssim x_0$. Contrary to the simplified case discussed above, we will see that $F_g[x, y] \propto x^3$ for $x \lesssim x_0$ and this implies $\partial\rho_g/\partial k \propto k^3$ at $k \lesssim x_0 H$. This last part of the spectrum is produced at the time when domain walls form, so will also get a contribution from domain walls, which is expected to change it by at least an order one amount (we discuss this contribution briefly in Appendix G).

We also note that in the large log limit the total energy in GWs emitted from t_1 to t, i.e. $\rho_g = \int_{t_1}^{t} dt' \Gamma'_g (R'/R)^4$, is $\rho_g = (4/5) H^2 G \mu_{\rm th}^3 \xi \log / f_a^2 \propto H^2 \log^5$. The additional log factor is related to the fact that this energy gets equal contributions from all the times from t_1 to t on a logarithmic scale. It is straightforward to see that the approximately scale invariant spectrum in eq. (6.9) reproduces this formula.

6.2.3 Comparison with Numerical Simulations

We now show that results from numerical simulations match the preceding analysis extremely well. This confirms our theoretical assumptions (i.e. that the Nambu–Goto EFT is valid at least for determining the relative emission into axions and GWs, and the general shape of the instantaneous emission spectrum) and allows us to extract the values of the parameters r, x_0 and q.

In the simulations we evolve the complex scalar ϕ by numerically integrating the equations of motion that follow from eqs. (2.28, 2.29) on a discrete lattice. The simulation code was written by my collaborators, Dr Marco Gorghetto and Dr Edward Hardy in C++ and it was not made publicly available. More details of their implementation can be found in Appendix E as well as the Appendices of their previous papers [186, 188]. Starting from suitable initial conditions, a network of strings forms and evolves, and is driven to the attractor. Due to the competing requirements that the grid must contain at least a few Hubble patches (to capture the infinite-volume properties of the network), and must have at least a few lattice points per string core (to reproduce the string interactions correctly), such simulations can only access values of $\log \lesssim 8$.[8] This is the origin of the

[8] In more detail, the maximum log is limited to $\sim \log N$, where N is the number of gridpoints in the box side. Here

previously mentioned required extrapolations (in our approach, we need to extrapolate r, x_0 and q, as well as ξ).

As well as the physical system of eq. (2.29), we also simulate the so-called 'fat' string system, which is defined by the same potential as eq. (2.29) but with $m_r \propto R^{-1}$ decreasing with time. In this way the string core size remains constant in comoving coordinates. In this system the same hierarchy in log corresponds to a larger ratio between final and initial cosmic times, and the string network therefore flows to the attractor faster, leading to cleaner results. Although the qualitative features are expected to be reproduced, the quantitative parameters of the scaling solution could differ from those of the physical string system (which we therefore use to extract the numerical values). For both systems we set the initial conditions as close as possible to the scaling solution, on which ξ grows logarithmically (the evolution of ξ is plotted in Figure F.1 in Appendix F.1, where we give more details). It is straightforward to evaluate the energy in axions and radial modes in simulations, and therefore the emission rates Γ_a and Γ_r.

The GWs produced during the evolution are obtained by numerically solving the linearised Einstein equations

$$\ddot{h}_{ij} + 3H\dot{h}_{ij} - R^{-2}\nabla^2 h_{ij} = 16\pi G T^{\rm TT}_{\phi,ij} \,, \tag{6.10}$$

where $T^{\rm TT}_{\phi,\mu\nu}$ is the transverse-traceless part of the energy momentum tensor of eq. (2.28).[9] At a generic time the energy density in GWs is $\rho_g \equiv T^{00}_g$, where $T^{\mu\nu}_g = (32\pi G R^2)^{-1}\langle \partial^\mu h_{\alpha\beta} \partial^\nu h^{\alpha\beta}\rangle$ is their energy momentum tensor and the brackets stand for the spatial average. From ρ_g the emission rate of GWs can be calculated using $\Gamma_g = R^{-4}\frac{d}{dt}(R^4\rho_g)$. Further details concerning our numerical implementation can be found in Appendix E. In Appendix E.1 we analyse the systematic uncertainties in simulations, e.g. from the finite lattice spacing, and the results we show are with parameter choices such that these are negligible.

The gravitational backreaction (in the weak gravity regime) is represented in the equations of motion of the Lagrangian in eq. (2.28) by the addition of a term $R^{-2}h^{ij}\partial_i\partial_j\phi$. By carrying out simulations with this term included, in Appendix F.2 we show that – as expected – the (evolving) effective parameter that controls the gravitational backreaction during the scaling regime is $G\mu^2_{\rm eff}/f_a^2$. This is shown in Figure F.9 of Appendix F.2, where the deviations in ξ and ρ_a due to the backreaction depend only on $G\mu^2_{\rm eff}/f_a^2$ for different choices of $f_a/M_{\rm P}$. In particular, provided $G\mu^2_{\rm eff}/f_a^2 \lesssim 0.5$, corresponding to $\log \lesssim M_{\rm P}/f_a$: (1) gravity is self-consistently in the weak regime and (2) it does not alter the dynamics of the string network.[10] The decay constants (and logs) of interest, studied in Section 6.2.4, are all safely within this limit, so we do not include backreaction in the remainder of our simulations.

we used grids of size to $N^3 \sim 2500^3$ (as opposed to 4500^3 in my collaborators' previous work) given the additional computational cost in the evolution of the GWs. The resulting maximum $\log \sim 7.5$ is still sufficient for the properties and trends in the attractor solution to be reliably identified.

[9] Here h is in the transverse-traceless gauge, which is convenient in the FRW background.

[10] This is expected, since the backreaction term is negligible with respect to the gradient term $-R^{-2}\nabla^2\phi$ for such f_a, as $h \sim G f_a^2$ from the linearised Einstein equations.

We now turn to our main results from simulations. We first observe that the total energy emitted per unit time from the network $(\Gamma_a + \Gamma_r)$ in simulations should match the theoretical formula for Γ in eq. (2.53) with the theoretically expected form of the tension $\mu_{\rm th}$ given by eq. (2.49). In more detail, although eq. (2.49) determines uniquely $\mu_{\rm th}$ at large log, at the small log relevant in the simulations $\mu_{\rm th}$ (and consequently Γ) is sensitive to the (only) free parameter η. We extract the value of η by fitting the data such that $(\Gamma_a+\Gamma_r)/\Gamma$ is constant in the range $\log > 4$, for the simplest model in which η is constant as a function of time, where as mentioned $(\Gamma_a+\Gamma_r)$ is measured in the simulations and Γ is given by (2.53). However there an additional complication since Γ of equation (2.53) strictly applies to long strings only and this energy does not fully go into radiation directly, since some short loops are also emitted at first which eventually also decay into radiation. We give additional detail in Appendix F.1, where we explain that this complication can be accounted for due to the fact that the fraction of string length in long strings is constant in the scaling regime. For the fat string system this fraction was determined to be $f_{\rm L,\ fat} = 0.84$ in [186] and we can directly fit the data for the value of η to find $\eta_{\rm fat} \simeq 0.95/\sqrt{4\pi} \simeq 0.27$, which is close to the value it would have if the long strings were straight and parallel to each other $1/\sqrt{4\pi}$. In the case of physical strings however we add the ratio $f_{\rm L,\ phys}$ as an additional free parameter to the fit. The best fit values in the physical string system are found to be $f_{\rm L,phys} = 0.9$ and $\eta_{\rm phys} \simeq 0.7/\sqrt{4\pi} \simeq 0.2$. We show in Figure 6.1 the ratio $(\Gamma_a + \Gamma_r)/\Gamma$ for fat strings, with the corresponding $\eta = 0.27$ set to its best fit value and $f_L = 0.84$. The fact that the ratio $(\Gamma_a + \Gamma_r)/\Gamma$ is close to unity at all times for such time-independent choice of η is a non-trivial check that eq. (2.53) captures the emission rate at the logs accessible in simulations. This also (indirectly) shows that $\mu_{\rm eff}$ is well reproduced by the theoretical expectation $\mu_{\rm th}$ of eq. (2.49) and is growing logarithmically as expected, so we can use the latter expression in the analysis that follows. [11] To assign an error to η we plot the ratio $(\Gamma_a + \Gamma_r/\Gamma)$ for various values $\eta_{\rm fat}$ in Figure 6.2. Additionally, in Figure F.3 of Appendix F.1 we plot the same ratio for fat and physical strings, for data collected for a previous paper of my collaborators [188], which was taken on larger grids (4500^3 instead of 2500^3). Based on this we assign ranges $\eta_{\rm fat}\sqrt{4\pi} \in (0.8, 1.1)$ and $\eta_{\rm phys}\sqrt{4\pi} \in (0.4, 1.5)$ in order to estimate the error on the coefficient r. Inside these ranges the ratio $(\Gamma_a + \Gamma_r)/\Gamma$ is constant to within about 10% tolerance.

Having confirmed the validity of Γ and $\mu_{\rm th}$, we are ready to study the GW emission Γ_g and extract the coefficient r. As discussed, we do so using r's relation to Γ_g and Γ_a of eq. (6.6), i.e. $r = f_a^2\Gamma_g/(\Gamma_a G\mu_{\rm eff}^2)$. This leads to a small ambiguity in determination of r at small log, because the small (and decreasing) proportion of energy emitted into radial modes is by construction not captured by the Nambu–Goto description, and could be included along with Γ_a in eq. (6.6). Since the radial modes take a proportion of the energy that would otherwise go into axions, it is natural to expect that the inclusion of Γ_r leads to the quantity conserved during scaling. In the following we therefore consider $r_{\rm sim} \equiv f_a^2\Gamma_g/(\Gamma G\mu_{\rm th}^2)$, where Γ and $\mu_{\rm th}$ are calculated from

[11] As also explained in Appendix F.1, eq. (2.49) strictly speaking holds for non-relativistic strings (since there is no boost factor), but any corrections from this are absorbed in the definition of r.

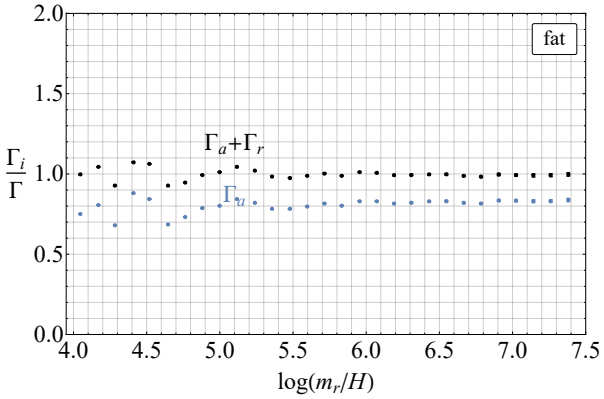

Figure 6.1: The ratio between the energy emitted by strings as measured in the simulation into axions (blue) and axions plus radial mode (black) and the energy lost by the strings for the fat strings system. The total energy lost by strings Γ is given by the energy lost by long strings eq. (2.53) multiplied by a correction factor depending on the ratio of long strings to loops, which adjusts for the fact that the energy lost by long strings does not fully go into radiation, with some of it going into short string loops which decay later. For the fat strings system we have fitted the data with a constant free parameter $\eta_{\rm fat}$ appearing in the string tension eq. (2.49) and set the fraction of length in long strings to $f_{\rm L,\ fat} = 0.84$ as found in [186]. The best fit value of $\eta_{\rm fat}$ was $\eta_{\rm fat} = 0.27$. Error bars represent the statistical errors over a set of 30 simulations on grids of size 2500^3 grid points, which we run to study the gravitational waves emissions and differ only in the random seed used to generate initial conditions.

eqs. (2.49) and (2.53) with the same constant value of η mentioned before (indeed Γ reproduces $\Gamma_a + \Gamma_r$ measured in simulations), while Γ_g is evaluated in the simulations. Note that using the theoretical Γ in the extraction of r instead of the result of $\Gamma_a+\Gamma_r$ from simulations reduces possible systematic uncertainties related to fluctuations of the last two quantities, which especially at small logs are affected by parametric resonance effects between axion and radial modes especially for the physical system.[12]

In Figure 6.3 we plot the time evolution of $r_{\rm sim}$ for the fat and the physical systems. The uncertainties on the data points represent the statistical error over a set of 30 simulations with initial conditions with the same initial string density ξ, which differ only in the random seed and are otherwise identical. In both cases $r_{\rm sim}$ is of order one and its time-independence is manifest over more than three e-foldings. This corresponds to a verification of eq. (6.6) and provides a remarkably consistent picture of the dynamics of the string system. First, it confirms the validity of the effective Nambu–Goto description at least for the emission of GWs, which therefore also allows analytic control of Γ_g beyond the range that can be simulated. The constant form of $r_{\rm sim}$ even holds well from $\log = 4$ when there is only a mild hierarchy between the string core scale and the Hubble parameter. In fact it is not unreasonable that r is constant even at such early

[12] On the other hand Γ_g fluctuates far less since the coupling of the GWs to the radial modes is much weaker.

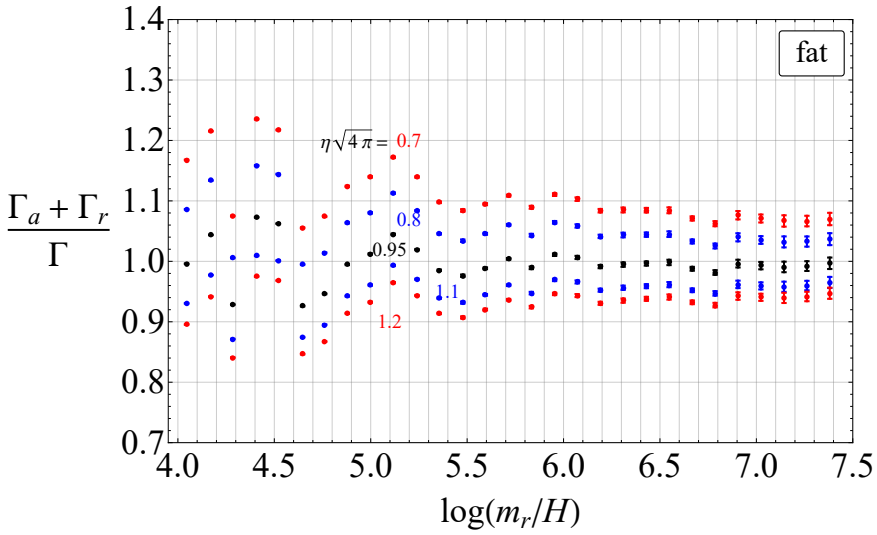

Figure 6.2: The ratio between the energy emitted by strings as measured in the simulation and the energy lost by the strings for various values of $\eta_{\rm fat}$. The blue plots correspond to the range $(0.8, 1.1)$ which we have allocated to $\sqrt{4\pi}\eta_{\rm fat}$, while the black dots correspond to the best fit value $\sqrt{4\pi}\eta_{\rm fat} = 0.95$. Inside this range the ratio $(\Gamma_a + \Gamma_r)/\Gamma$ differs by about 10% or less inside the simulation range $4 < \log < 7.4$ and this is true also for data on larger grids from [188], which reach up to $\log = 7.9$ and are represented in Figure F.3 in Appendix F.1.

times, since the theoretical expectation in eq. (6.6) does not rely on the string system being in the pure Nambu–Goto limit (namely it should hold even at small log when the strings are strongly coupled to the axion). Moreover, as anticipated in Section 6.2.2, the constant value of $r_{\rm sim}$ is strong evidence that the string configuration is self-similar. This in turn confirms that the scaling regime has been achieved in the simulation and that the logarithmic increase in ξ is a part of it.[13] Although we cannot exclude a qualitative change in the evolution of $r_{\rm sim}$ after $\log = 7.5$, both theory and simulations suggest that such a change is unlikely. The extrapolation of r after $\log = 7.5$ therefore seems robust despite the difference in log between the simulations and the physically relevant system. On the other hand, simulations can never exclude the possibility that there is a small logarithmic running of r but only bound its value, and we comment on this when discussing the uncertainties on our predictions of GW spectra in Section 6.2.4.

In Figure 6.3 we also show the fit of this observable with a constant function. For the physical system we start the fit at $\log > 4.5$, since the first few data points at small log seem to deviate slightly, as the system has not yet fully reached the scaling regime at such early times (see also the not completely linear behaviour of ξ at those log in Figure F.1).[14]

We now estimate the uncertainty on $r = f_a^2\Gamma_g/(\Gamma_a G\mu_{\rm eff}^2)$ for physical string network. A first

[13] If the logarithmic increase were a transient, we would expect the configuration not to be self-similar. This is also consistent with the observation that the fraction of ξ in strings of different lengths remains constant [186].

[14] The small disagreement of the last two data points of the fat system is likely to be due to a statistical fluctuation.

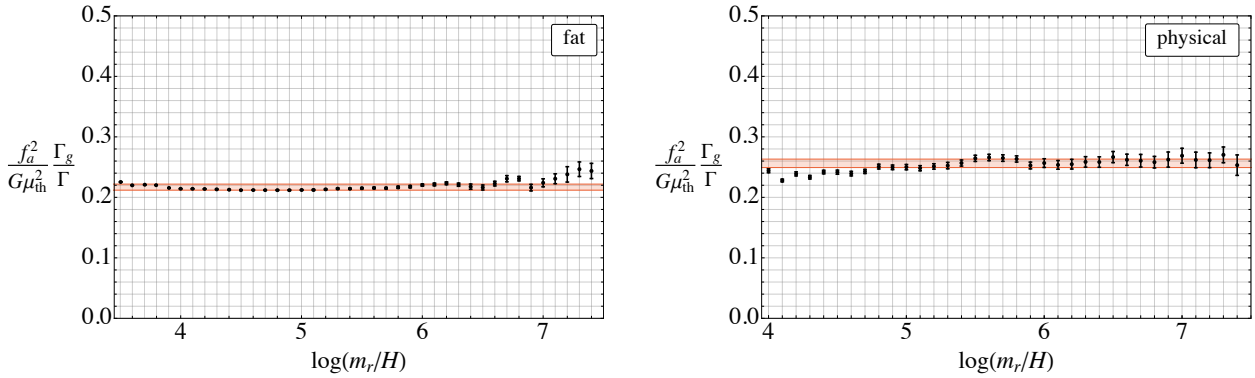

Figure 6.3: The evolution of energy density Γ_g emitted in GWs per unit time during the scaling regime normalised to $\Gamma G\mu_{\rm th}^2/f_a^2$, where Γ is the total energy emission rate and $\mu_{\rm th}$ is the theoretical expectation for the string tension, for the fat string system (left) and the physical system (right). Error bars on the data points represent the statistical error over a set of 30 simulations. The red bands are centered on the average value of r over all data points and its width is given by the standard deviation. The constant value of this ratio is in agreement with the theoretical expectation of Section 6.2.1, and indicates that the relative emission to GWs grows as $\Gamma_g/\Gamma_a \propto \log^2(m_r/H)$ at large log. This Figure was produced by my collaborators for our joint work [1].

source of uncertainty comes from the precise value of the string tension $\mu_{\rm eff}$ at small log (for which, as mentioned, the value of η is relevant), which feeds into the value of r extracted from Γ_g measured in simulations. As mentioned, $\mu_{\rm eff}$ is well reproduced by $\mu_{\rm th}$ for $\eta_{\rm phys} \simeq 0.20$. However, given the large fluctuations of $\Gamma_a + \Gamma_r$ in the physical system, values of $\eta_{\rm phys} = 0.1 \div 0.3$ still reproduce $\Gamma = \Gamma_a + \Gamma_r$ acceptably well (this range is obtained by varying η such that $(\Gamma_a + \Gamma_r)/\Gamma$ remains approximately constant, see Figure F.3 and Appendix F.1). This translates into an uncertainty on $r_{\rm sim}$ in the range $0.17 \div 0.34$ (estimated by evaluating $r_{\rm sim}$ at the final time for $\eta_{\rm phys}$ in the range $0.1 \div 0.3$, see Appendix F.1 and Figure F.4 for more details). Moreover, the previously mentioned ambiguity in using Γ or Γ_a introduces a theoretical uncertainty in the value of r (although $r_{\rm sim}$ seems to be the conserved quantity). We can conservatively quantify the associated error as about 10%, corresponding to the contribution that Γ_r provides provide to Γ at the largest simulated log of Figure 6.3. The actual statistical uncertainty on data of Γ_g is negligible with respect to the mentioned ones. As a result, we obtain a value for r with a conservative error estimate of

$$r = 0.26(11) \ . \tag{6.11}$$

Since r is of order one, as expected for $f_a \ll M_{\rm P}$ only a small fraction of energy is emitted in GWs. Moreover, as well as qualitative agreement, in Appendix F.2 we show that our value of r is quantitatively consistent with the decrease in axion energy, for a fixed $f_a/M_{\rm P}$, when backreaction is included.

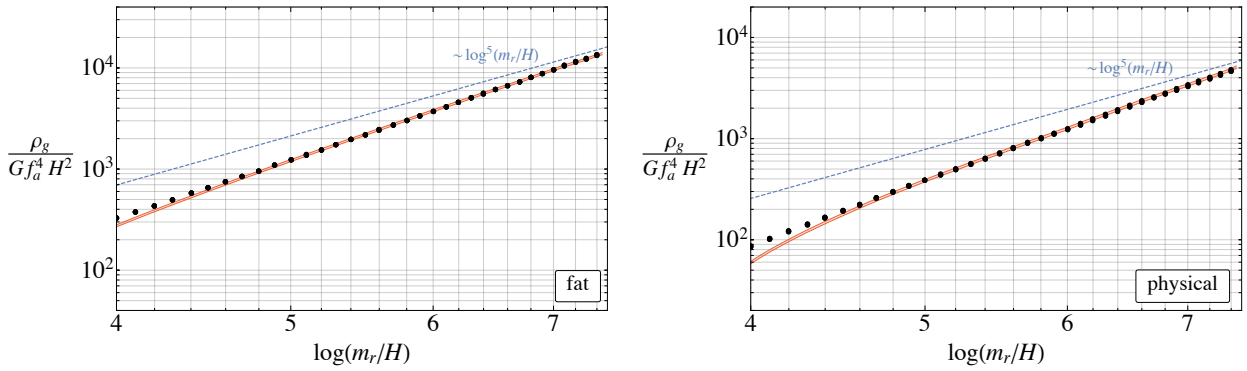

Figure 6.4: The evolution of the total energy density in GWs ρ_g (black points, with statistical errors smaller than the plotted data points), and the theoretical prediction for this quantity with the range of r extracted from Figure 6.3 (red bands). The data are in full agreement with the predictions. We also plot $\rho_g \propto H^2 \log^5$, which is valid at $\log \gg 1$, and which the prediction and data asymptote to. This Figure was produced by my collaborators for our joint work [1].

In Figure 6.4 we also show the evolution of the total GW energy density ρ_g measured in the simulations (black points). In the same plot we show the theoretical prediction for this quantity, i.e. $\rho_g = \int_{t_1}^{t} dt' \Gamma'_g (R'/R)^4$, with $\Gamma_g = r G \mu_{\rm th}^2 \Gamma / f_a^2$ where the constant r (together with its error) is extracted from Figure 6.3 and Γ is as in eq. (2.53) and is evaluated as before (in doing the integration we take t_1 such that $\log(m_r/H_1) = 3.5$). As expected given Figure 6.3, the agreement between the prediction and the data is excellent. We also note that the data approach the expected large log behaviour $\rho_g \propto H^2 \log^5$, discussed in Section 6.2.2.

The remaining input required to calculate the GW spectrum is the momentum distribution of the instantaneous GW emission F_g. It is straightforward to extract this from simulations, and results for $F_g[x, y]$ are plotted for the physical system in Figure 6.5 (left) at different times, i.e. different $y = m_r/H$ (labelled by $\log(m_r/H)$). As expected, the distribution has an IR cutoff corresponding to $x_0 \sim 2\pi$ and a UV cutoff at around the string core scale, corresponding to $x \sim m_r/(2H)$, which are the same as for the axion spectrum.[15] The spectrum has a somewhat broad peak around the IR cutoff, from $x \simeq 5$ to 20. Above this, an intermediate power law is visible and compatible with $q = 2$, which implies an IR dominated emission. Thus, the numerical results fully confirm (at least at small log) our assumptions of Section 6.2.2.

The parameters x_0 and q appear to be time-independent in the range of log accessible to simulations. This can be seen from the fact that the F_g overlap for all y (we carry out a more detailed analysis in Appendix F). It is interesting to note that, although the IR and UV cutoffs of F_g are similar to those of the corresponding axion instantaneous emission spectrum F_a, the spectral indices of the two, q and q_a respectively, are dramatically different. For the axion q_a increases with

[15] The value $k/H \simeq 2\pi$ is also motivated since for such momentum the wavelength equals the Hubble distance.

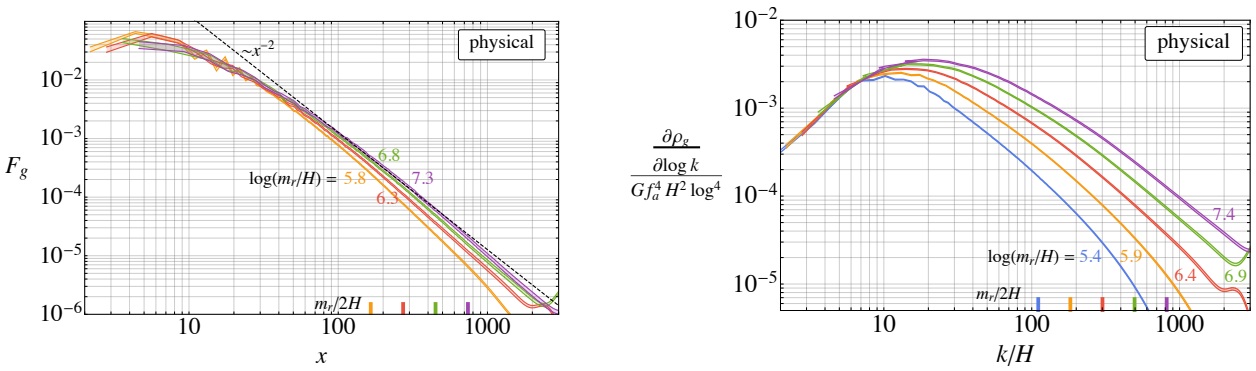

Figure 6.5: *Left:* The momentum distribution $F_g[x, y]$ of the GWs emitted instantaneously from the string network, as a function of their physical momentum normalised to Hubble, $x = k/H$. Different lines indicate different times i.e. changing $y = m_r/H$, which are labelled by $\log(m_r/H)$. At all times the distribution is dominated by (IR) momenta of order Hubble, and decays as x^{-2} at higher momenta. *Right:* The evolution of total spectrum of GWs produced by the network, plotted at different times. We factor out the expected time dependence of the amplitude of the IR peak $\propto H^2 \log^4$. This Figure was produced by my collaborators for our joint work [1].

log (from $q_a = 0.75$ to 0.95 between log = 6 and 8 indicating a UV dominated spectrum that is gradually becoming IR dominated).[16] We also note that an emission with $q = 2$ is characteristic of kink-kink collisions [315], as opposed to cusps and kinks which instead provide $q = 4/3$ and $q = 5/3$ respectively. Although this could be an indication that kink-kink collisions are the dominant source of the emission, our results do not rely on the modelling of the particular process sourcing the GWs, as the evolution of the field equations captures the full dynamics of the system.

Despite these results, we cannot exclude a slow logarithmic running of x_0 and q. However, as discussed in Section 6.2.2, a slow increase in q would have little effect on the integrated GW spectrum (and a decrease in q until $q < 1$ would be extremely surprising). Likewise, a slow change in x_0 would only have a very minor effect, so we do not analyse this possibility in detail. Consequently, we can safely assume that the form of F_g is preserved also at large log.

In Figure 6.5 (right) we also show the total GW spectrum $\partial\rho_g/\partial\log k$ at different times as a function of the physical momentum normalised to Hubble. The general features derived in Section 6.2.2 are reproduced. However, due to the small final log, the approximately scale invariant region $x_0 H \lesssim k \lesssim x_0\sqrt{HH_1}$ of eq. (6.9) corresponds only to a small portion of the spectrum. Indeed, the first nontrivial emission in the scaling regime happens around $\log(m_r/H_1) \sim 4$ and therefore eq. (6.9) holds in the restricted range $x_0 \lesssim k/H \lesssim x_0\sqrt{HH_1}/H \sim 40 \div 50$ at the final time

[16] This could be due to the fact that the coupling of the radial modes to axions is much larger than the coupling of radial modes to GWs. Therefore the radial modes which are partly emitted by the strings at small log could produce energetic axions [188], contributing to the UV part of the axion spectrum (but not to the GW one). The emission of radial modes diminishes logarithmically, and the spectrum therefore decreases in the UV.

log = 7.4.[17] Nevertheless, the key result from eq. (6.9) that at fixed $k/H \sim x_0$ the spectrum (once the leading H^2 is factored out) grows proportionally to $\log^4(m_r/H)$ is matched well in Figure 6.5 (right), which is of course consistent with the extrapolation to large log being essential (a version of the plot without the $\log^4$ factored out is given in Figure F.7 of Appendix F).[18] Finally we observe that $\partial\rho_g/\partial k \propto k^3$ for $k \lesssim x_0 H$ (this is the same behaviour as F_g at small x), while $\partial\rho_g/\partial k \propto k^{q-1}$ at momenta higher than $x_0\sqrt{HH_1}$. In Appendix E we show the results for F_g and the total spectrum for the fat string system, which are qualitatively, and even quantitatively, similar to those of the physical system.

6.2.4 The GW Spectrum Today

The present day remnant of the GW spectrum from the scaling regime can be straightforwardly computed by combining the theoretical discussion of Section 6.2.2 and the results of Section 6.2.3. For the sake of definiteness for now we assume a temperature-independent axion mass, and we discuss the temperature-dependent case later.

As mentioned, the scaling regime ends (approximately) when $H = m_a$, at which time the network is destroyed and GWs stop being produced at the rate in eq. (6.6). The GW spectrum at $H = m_a$ follows from eq. (6.8). From $H = m_a$ on the GWs redshift freely until today, and their contribution to the present day total energy density of the Universe is $\Omega_{\rm gw} \equiv \rho_g/\rho_c$, where ρ_c is the critical density.

In Figure 6.6 we plot the GW spectrum $d\Omega_{\rm gw}/d\log f$ (from a numerical integration of eq. (6.8)), where f is the frequency. We use the value of r from eq. (6.11) to evaluate Γ_g in eq. (6.6), and a functional form of F_g that fits Figure 6.5 (left) (see Appendix D.2 for more details). Results are shown for different choices of axion decay constant and mass that are not excluded by other cosmological constraints (derived in Section 6.3). For an axion that produces GWs in the detectable frequency range, these constraints require $f_a \lesssim 10^{15}\,\text{GeV}$ (from dark radiation bounds discussed in Section 6.3.2) and $10^{-28}\,\text{eV} \lesssim m_a \lesssim 10^{-17}\,\text{eV}$ (the lower limit is due to bounds on string surviving until recombination which is discussed in Section 6.3.4 and as a result the network is destroyed before matter-radiation equality, the upper limit is due to the bound on the axion relic abundance discussed in Section 6.3.1).[19] We also show $f_a = 3\times10^{15}\,\text{GeV}$, which is likely to be in tension with dark radiation bounds, see Section 6.3.2.

In this plot we assume that the Hubble parameter H_1 when the scaling regime starts is sufficiently large that the GW spectrum is in the approximately scale invariant region for the entire range of frequencies shown. Later in this Section we show that this assumption is highly plausible. We also assume a standard cosmological history with radiation domination up to high temperatures

[17] H_1 corresponds to when the UV and IR cutoffs of the spectrum $x_0 H$ and $m_r/2$ coincide.

[18] At small log, $\partial\rho_a/\partial\log k$ actually grows faster than $\log^4$ due to the subleading log corrections of Γ_g in eq. (6.6), and indeed at $k/H \sim x_0$ the spectrum in Figure 6.5 (right) shows a slight increase.

[19] This confirms that the condition for gravitational backreaction to be negligible $G\mu_{\rm eff}/f_a^2 \ll 1$ is satisfied.

and only the particle content of the SM plus the axion, and that $m_r = f_a$. We describe the errors that we include on the GW spectra and other sources of uncertainty in detail at the end of this Section.

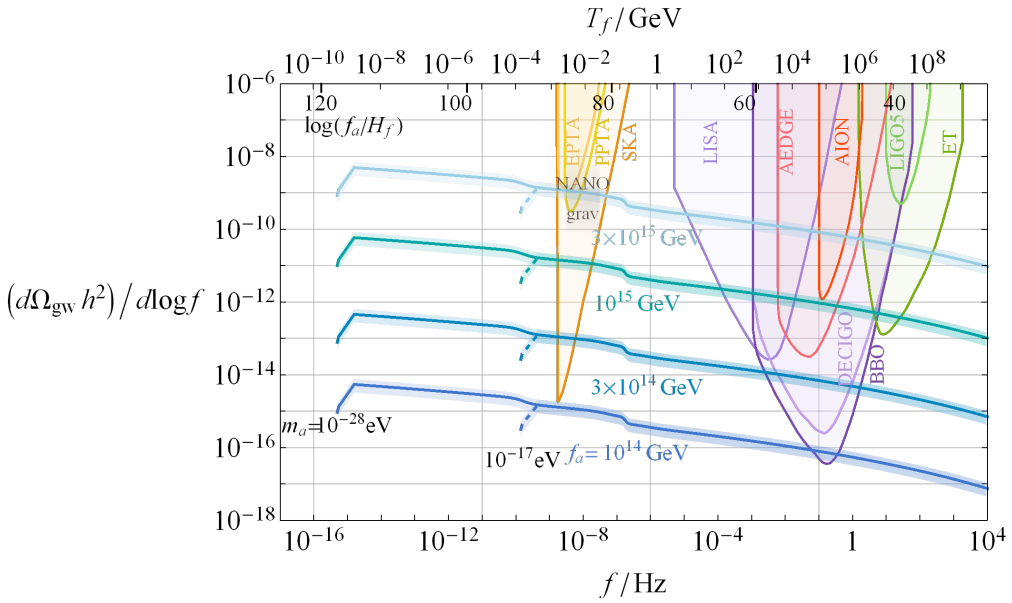

Figure 6.6: The contribution to the energy density of the Universe today from the GWs emitted by axion strings during the scaling regime, as a function of their present day frequency f. To produce this figure the parameters x_0 and q which describe the instantaneous emissions spectrum F_g discussed above were set to $x_0 = 5$ and $q = 2$. Different lines correspond to different values of the axion decay constant f_a and mass m_a. We plot values of m_a that are compatible with current constraints on the post-inflationary scenario. Values of $f_a \lesssim 10^{15}\,\text{GeV}$ are possible, while larger values are in tension with isocurvature and dark radiation bounds. GWs with higher frequencies are produced at earlier times, and we indicate the temperature of the Universe when GWs of a particular frequency are dominantly produced, T_f, as well as the corresponding value of the log at this time $\log(m_r/H_f)$. All the GWs are emitted in radiation domination and the network decays before matter-radiation equality. We also indicate the range of masses allowed for symmetry breaking scales $f_a \gtrsim 10^{14}\,\text{GeV}$ which are detectable by gravitational waves. For this range of masses the frequencies at which detectors are sensitive are always larger than the value corresponding to the IR peak of the emissions spectrum, and as mentioned are lower than the value corresponding to the and UV peak for $H_I \gg$ keV.

A useful (and for most purposes accurate) analytic approximation for $\Omega_{\rm gw}$ in the $\log \gg 1$ limit is derived from eq. (6.9) in Appendix D.2 (see eq. (D.13)) and reads

$$\frac{d\Omega_{\rm gw}h^2}{d\log f} \simeq 0.80\times 10^{-15}\left(\frac{c_1}{0.24}\right)\left(\frac{r}{0.26}\right)\left(\frac{f_a}{10^{14}{\rm GeV}}\right)^4\left(\frac{10}{g_f}\right)^{\frac{1}{3}}\left\{1+0.012\log\left[\left(\frac{m_r}{10^{14}{\rm GeV}}\right)\left(\frac{10^{-8}{\rm Hz}}{f}\right)^2\right]\right\}^4, \tag{6.12}$$

where g_f is the effective number of degrees of freedom in thermal equilibrium at the temperature T_f, when most of the GWs with today's frequency f are emitted.[20] Eq. (6.12) holds in the frequency range $3\times 10^{-12}(m_a/10^{-20}{\rm eV})^{1/2} \lesssim f/{\rm Hz} \lesssim 10^3(H_1/\,{\rm GeV})^{1/2}$. This corresponds to the extremes in eq. (6.9) evaluated at $H = m_a$, redshifted to today. As stressed in Section 6.2.2, at lower and higher frequencies than these IR and UV cutoffs, $d\Omega_{\rm gw}/d\log k$ is suppressed as f^3 and f^{q-1} respectively.[21]

Several comments are in order. First, we observe that f_a controls the overall amplitude of the spectrum, since it ultimately determines both the energy density of the string network and also the efficiency at which this is emitted into GWs. Conversely, m_a only affects the position of the IR-cutoff $\propto m_a^{1/2}$ of the approximately scale-invariant part of $\Omega_{\rm gw}$ (which is m_a independent). This is not surprising given that m_a is unimportant during scaling, and its only role is in determining when the network is destroyed. The resulting IR cutoff is visible in Figure 6.6.

The $\log^4$ dependence of the frequency is evident in Figure 6.6 and eq. (6.12). In Figure 6.6, we indicated the value of the log when most of the GWs with frequency f are emitted, $\log_f \equiv \log(m_r/H_f)$. Since this varies by more than a factor of 2 over the frequencies of observational interest (in the range $\log_f = 30 \div 90$), there is a substantial effect on the spectral shape as well as the amplitude. We also note that the GWs in most of the observable range are emitted when $\xi = 10 \div 20$ from eq. (2.47). As expected, the spectral shape is also modified by the changes in number of relativistic degrees of freedom in the Universe. In particular, this has an effect at frequencies that are dominantly emitted at temperatures T_f (shown on the upper axis) at which such changes occur (the largest effect is around $T \simeq 100\,{\rm MeV}$ when a large number of the degrees of freedom decouple). As a result the spectrum at higher frequencies is suppressed by more that the $\log^4$ factor, since these are emitted at earlier times when g_f is larger leading to increased expansion of the Universe. However, such effects are fairly weak, as $\Omega_{\rm gw}$ depends only on $g_f^{1/3}$.

In Figure 6.6 we also show the projected sensitivity curves for ongoing and proposed GW searches (EPTA [126], PPT [127], SKA [128], LISA [122], DECIGO/BBO [123], AEDGE [124], AION [125], LIGO [119], and ET [120, 121]), as well as an extremely tentative possible signal by NANOgrav [317], which we comment on in the Conclusions. In particular, we plot the power-law-integrated sensitivity curves [318–320] as derived in [321]. Partly due to the enhancement of the signal at low frequencies, the near future detection prospects are best at Pulsar-Timing Arrays such as SKA, which scan the lowest frequencies and could be sensitive to all $f_a \gtrsim 10^{14}$ GeV. Detection is also possible at space-based interferometers: although LISA could be sensitive only

[20] More precisely, this temperature is defined by $x_0 H(T_f) \equiv f R(T_0)/R(T_f)$.

[21] The dependence on f^3 of the super-horizon modes is fixed by causality after such modes starts oscillating [316].

to $f_a \gtrsim 5 \times 10^{14}$ GeV, its proposed successors could explore lower values of f_a. The wide range of axion masses and decay constants that lead to a measurable GW signal motivates the effort to develop such experiments.

As mentioned, complementary constraints require $m_a \lesssim 10^{-17}\,\text{eV}$, and therefore in case of a detection the actual value of m_a will not be inferred. This is because, for this mass range, all the detectable frequencies are emitted deep inside the scaling regime, so the IR cutoff of $\Omega_{\rm gw}$ is unobservable. Additionally, any temperature-dependence of the mass – as long as is monotonically decreasing – does not affect the detectable GWs, as it can only modify lower frequencies, emitted when the mass is relevant. We note that if the string network is destroyed before $T \simeq 10^6$ GeV (e.g. for a heavy axion mass, $m_a \gtrsim$ MeV, which is still allowed by the observational constraints in Section 6.3), the IR cutoff frequency is so large that the spectrum does not extend down to observable frequencies.

Although neglected in this discussion, after $H = m_a$ additional GWs will be emitted by domain walls, which will supplement those from the scaling regime. As discussed in Appendix G, one calculable contribution to these GWs has frequencies (and amplitude) of the same order as that from the last e-folding of the scaling regime. Therefore, although it will modify the shape of the IR-cutoff of the GW spectrum from the scaling regime, this contribution at least will not be observationally relevant.

Uncertainties on the Spectrum

Given its experimental importance, an understanding of the possible sources of uncertainty on the GW prediction is crucial. The error bands on the GW spectra plotted in Figure 6.6 are obtained by combining the uncertainties on the coefficient of the growth of ξ (i.e. c_1 of eq. (2.47)), on r, and by varying x_0 in the range $5 \div 10$ (which only has a visible effect on the location of the IR cutoff). We do not think it would be fair to associate a sharp numerical uncertainty to the extrapolations necessary to reconstruct the scaling regime at large log. Instead, we now summarise the assumptions needed to obtain eq. (6.12) and Figure 6.6, and the corresponding possible uncertainties. In all cases we have made the most conservative extrapolations possible, and taken together a deviation of more than a factor of $2 \div 4$ from our predictions would be surprising.

- We assumed that ξ continues to grow logarithmically as in eq. (2.47) during the scaling regime beyond the range of simulations. While such an increase has not yet found a mathematical proof, it has been numerically demonstrated in simulations at $\log \lesssim 8$, providing the best fit of the data (which disfavours any function that saturates soon after $\log = 8$, as observed in [186, 188] and evident in Figure F.1 of Appendix F).[22] Such a growth is theoretically

[22]This behaviour has been confirmed independently [182, 184, 185, 187]. An enhanced value of ξ is also suggested by Nambu–Goto string simulations [177, 178, 322], and in a system where the tension of the strings is increased via additional degrees of freedom, [323, 324].

plausible given the logarithmic sensitivity of the system to m_r/H, and given the excellent fit over the range of logs that can be simulated it is the most conservative assumption for the late time behaviour of ξ. The resulting string densities at the times relevant to the emission of observable GWs are $\xi = 10 \div 20$. This is a factor of 10 larger than is reached in simulations, correspondingly increasing the energy emitted into GWs, on top of the (much larger) enhancement from μ_{eff}.

Nevertheless, we cannot exclude the possibility that ξ saturates (or its growth accelerates) at log far beyond the reach of simulations. In these cases, the emission would be damped (or increased) proportionally to the value of ξ. In particular, a different value of ξ would modify the amplitude in Figure 6.6 at the frequency f by the factor $\sim \xi/(c_1 \log_f)$. Therefore, as long as ξ does not saturate at a value smaller than 5 (which seems highly unlikely given that such values are obtained in simulations that partly reproduce the dynamics of the system at large log by boosting the string tension [324]), in the case of a saturation the amplitude of Ω_{gw} would only decrease by a factor of two at LISA frequencies and a factor of four at SKA frequencies. Consequently the uncertainty on ξ does not qualitative change the prospects of detection, strengthening the robustness of our results (e.g. $f_a \gtrsim 10^{14}\,\text{GeV}$ remains just about detectable by SKA).

- We assumed that the energy emission rate into GWs continues to follow the prediction in eq. (6.6) based on the Nambu–Goto strings effective theory, with r constant, throughout the scaling regime. Numerical simulations confirmed this result for $\log \lesssim 7.5$ with fixed $r = 0.26(11)$, as in eq. (6.11). As mentioned, we cannot exclude a small logarithmic dependence in r (for instance, due to a change in the average shape of the string trajectories). However such a running is bounded by Figure 6.3 and (if present) would most likely give Γ_g a log dependence that is subleading to that from ξ. This possibility therefore only makes a small contribution to the overall uncertainty on Ω_{gw}.

- We assumed that the form of the instantaneous emission spectrum of GWs F_g of Figure 6.5 is preserved during the whole scaling regime, also after $\log \simeq 7.5$. This assumption is motivated by the existence of the scaling regime (and F_g is seen to be preserved during the whole simulation range). As noted in Section 6.2.2, as long as the IR cutoff x_0 does not change exponentially and q does not decreased below 1 (both of which are unlikely), the uncertainties on Ω_{gw} from these quantities are negligible.

As well as those from our reconstruction of the scaling regime, there are also uncertainties on Ω_{gw} due to unknown features of the early Universe.

- In obtaining Figure 6.6 we have taken the Hubble parameter H_1 when the scaling regime starts sufficiently large that the GWs in the observable frequency range are in the approximately scale invariant part of the spectrum. This is actually a mild assumption requiring just that

$H_1 \gtrsim$ keV (corresponding to a temperature of the order of 100 TeV), so the UV cutoff of the spectrum is at frequencies $f \gtrsim$ Hz. Values of H_1 much larger than this are expected in all of the models that lead to symmetry restoration at the relevant f_a, which we discuss in Section 6.4. It is also expected that there is sufficient time for the string network to reach the attractor prior to the Universe dropping to the temperature 10^7 GeV when the first GWs in the observable frequency range are emitted. Moreover, friction on the string due to interactions with the thermal bath, which is relevant at high temperatures if the axion couples to standard model particles (but we do not include in our analysis of the scaling regime), will be negligible by this point for axion decay constants that lead to observable signals. In particular, the friction is expected to be irrelevant for temperatures $\lesssim 10^{11}\,\mathrm{GeV}(f_a/10^{14}\,\mathrm{GeV})^2$ [273], which is safely far above those corresponding to observable frequencies (further analysis would be required to determine the temperature at which friction becomes irrelevant precisely, see also [272, 274–276]).

In contrast, the UV part of the spectrum $f \gtrsim (H_1/\,\mathrm{keV})^{1/2}$ Hz depends on how (and when) the network formed and reached the scaling regime, and possibly gets additional contributions e.g. from the U(1) phase transition. However, in practice this is not detectable in any motivated model.

- In our derivation we also assumed that the Universe is in radiation domination up to high temperatures (say, 10^8 GeV, as show in Figure 6.6). Different cosmological scenarios, e.g. matter domination or kination, would drastically modify the spectrum's shape. Indeed, it is easy to show from eq. (6.8) that, if $R \propto t^\alpha$, $\partial\rho_g/\partial \log k$ is proportional to a negative (positive) power of k depending on $\alpha > 1/2$ ($\alpha < 1/2$) [325–328]. An accurate determination of the spectrum in such scenarios would require recalculating ξ and r from simulations with such α.

- Finally, we assumed only SM degrees of freedom. If additional degrees of freedom are present the prediction will be modified as in eq. (6.12). Indeed, as pointed out in [329], a precise measurement of the spectrum could in principle provide information about g at high temperatures (it is plausible that a significant number of beyond SM degrees of freedom could enter at energies $\gtrsim$ TeV, and the possibility this could be detected by analysing the GW spectrum from strings has been considered in [327]). However, given the uncertainties discussed above and the weak dependence of Ω_{gw} on g_f, extracting the number of degrees of freedom would appear to be very challenging.[23]

[23] Strictly speaking, our results for ξ and r have been obtained from numerical simulations with $R \propto t^{1/2}$, that do not account for the change in the number of degrees of freedom. We expect however a very minimal change in such observables when one takes into account the time-dependence on R from g.

6.3 Constraints on the Axion Mass and Decay Constant

Having shown that post-inflationary axions lead to GWs with amplitude and frequency that could be accessible to proposed experiments, we now analyse some other phenomenological features of this scenario. These provide direct and indirect constraints on f_a and m_a, completing our understanding of the axions that could be discovered via GWs, and also giving complementary observational signatures.

In the following we will consider a single axion with a temperature-independent mass m_a.[24] Axions with $f_a \gtrsim 10^{14}$ and $m_a \lesssim$ MeV are cosmologically stable regardless of the details of their couplings to the SM [330]. In Section 6.3.1 we will see that, given this stability, only ultralight axions are not ruled out by dark matter overproduction for the relevant values of f_a, so we focus on this mass range (as described in Appendix J, axions with $m_a \gtrsim$ MeV can decay, but, as mentioned, for such values the scaling regime ends before observable GWs are produced). In Appendix J we show that only the ultra-light mass range is allowed for large f_a also in the case of a temperature-dependent axion mass.

In Figure 6.7 we summarise the constraints, which we detail in the remainder of this Section. Given their stability, axions form a component of dark matter (potentially overproducing the observed abundance) and those that are relativistic at the time of BBN or decoupling act as dark radiation. The resulting limits are shown in red and blue respectively. DM axions from strings and domain walls have isocurvature perturbations, which are constrained by CMB and Lyman-α observations. As explained in Section 6.3.3, it is challenging to determine the resulting limits precisely, however we will derive reasonable conservative bounds (which should still be treated with caution), shown in purple. We also show bounds on the fraction of dark matter that can be ultralight from Lyman-α observations (Lα). Finally, if m_a is small enough, axion strings persist at the epoch of CMB decoupling, and are constrained by CMB observations. In Appendix H we summarise other constraints that are less strong than those shown, e.g. from from black hole superradiance.

Even though these limits are fairly restrictive and become stronger for larger f_a (exactly when the GWs become detectable), there is about one order of magnitude of allowed values of f_a and many orders of magnitude of m_a that provide observable GW signals from strings. We note that these constraints do not depend on the possible axion couplings to the SM (which we did not specify). Moreover, although we considered a model with a single axion, the bounds are not expected to significantly change if additional light fields are included and coupled to the axion, so our conclusions apply to generic axion models in the post-inflationary scenario.[25]

[24] Although we remain agnostic on how the mass is generated, we observe that this mass could arise from explicit breaking of the axion's shift symmetry in the ultra-violet (UV) theory.

[25] Some models with unusual features (such as the clockwork mechanism) might avoid these constraints.

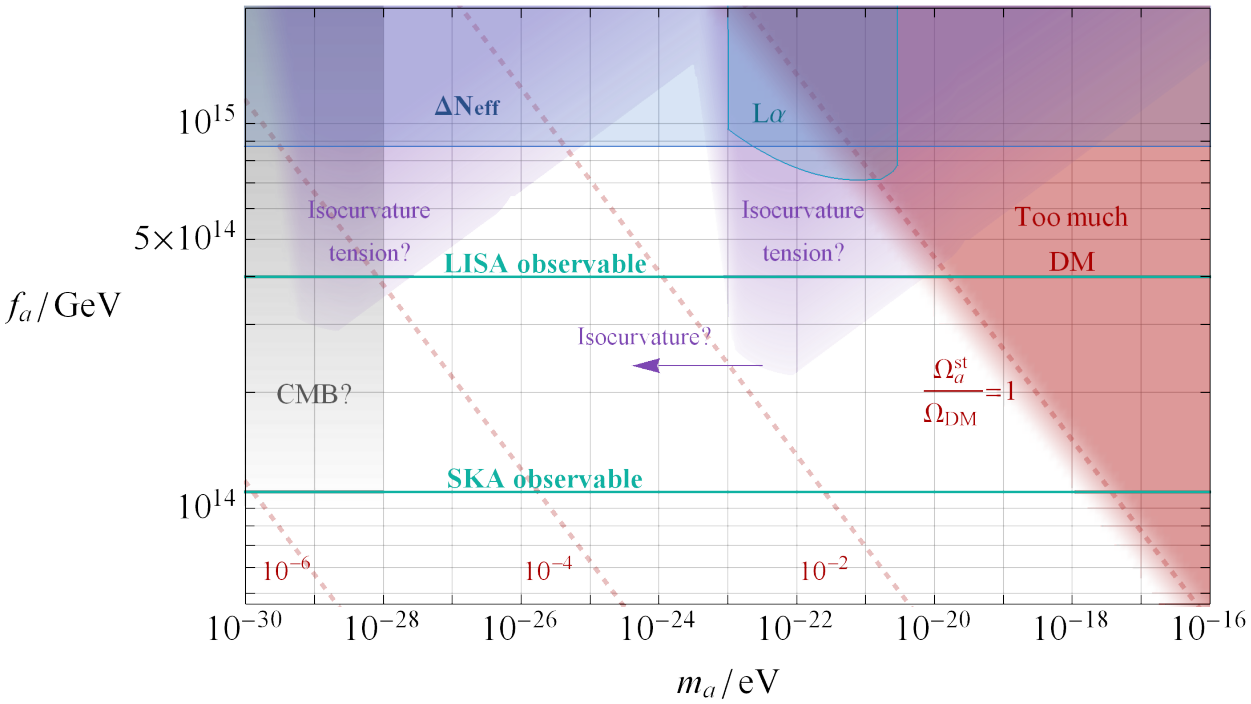

Figure 6.7: Constraints on axion mass and decay constant in the post-inflationary scenario, with a temperature independent axion mass. Limits from dark matter overproduction and dark radiation are shown in red and blue respectively. The bound from isocurvature perturbations is conservative but is still particularly uncertain (see the main text for details), and it based on the assumption that the spectrum of isocurvature perturbations is very strongly suppressed beyond the peak at $k_\star = H_\star R_\star / R_0$. In particular in the region $m_a \lesssim 10^{-22}$ eV marked by the purple arrow a complete reanalysis is required to obtain fully reliable bounds, using the full details of the spectrum of isocurvature perturbations which are difficult to extract. In case such bounds could be obtained they are potentially stronger than those plotted. A similar analysis would be required to extract the exact bounds in the region $m_a \lesssim 10^{-28}\,$GeV, however in this region there are already strong constraints. Specifically, direct CMB observations rule out extremely light axions with large f_a (in grey), since strings persist at the time of decoupling causing anisotropies. There are also constraints on the fraction of DM that ultra light ALPs can make up, for example from Lyman-α forest observations which we plotted in light blue. Additionally the CMB also constraints the fraction of DM that ALPs with masses $10^{-33}\,{\rm eV} \lesssim m_a \lesssim 10^{-22}\,{\rm eV}$ make up [331,332], which we have not plotted since they are weaker than the dark radiation bounds. We mention further constraints that are less strong than those plotted in Appendix H. We also identify the parts of parameter space in which axion strings produce a GW spectrum that is detectable by SKA and LISA, and the fraction of DM that axions from the scaling regime comprise (red dotted lines). This Figure was produced by my collaborators for our joint work [1], which I have slightly modified to include the purple arrow pointing to the region with uncertain isocurvature limits.

6.3.1 Dark Matter

As discussed in Section 2.4.3, during the scaling regime energy is continuously radiated into axions at the rate Γ_a. Such axions are relativistic during the scaling regime (since $m_a \ll H$), and most of them become non-relativistic soon after the axion potential V becomes relevant, when $H \simeq m_a$. Since these axions are stable they form a component of dark matter.

The number density of axions during the scaling regime can be obtained following a similar approach as for GWs in Section 6.2.2. As mentioned, the momentum distribution of Γ_a has the same form as that of Γ_g in Figure 6.5. However, the spectral index q_a for the axion emission changes in time and, although $q_a < 1$ for $\log \lesssim 8$, its extrapolation indicates that $q_a > 1$ at $\log \gtrsim 9$, which we will assume in the following (see [186, 188] for more details). Once $q_a > 1$, the axion number density during the scaling regime $n_a^{\rm st} \equiv \int dk/\omega_k \partial\rho_a/\partial k$ is approximately $8H\xi\mu_{\rm eff}/x_{0,a}$ (here $\omega_k^2 \equiv k^2 + m_a^2$; $\partial\rho_a/\partial k$ is the axion energy density spectrum, defined in the same way as the GW one in eq. (6.8); and $x_{0,a}$ is the IR cutoff of the instantaneous axion emission spectrum). Consequently, the number density $n_{a,\star}^{\rm st}$ at $H = H_\star$ is enhanced by a factor of $\xi_\star \log_\star \gg 1$ with respect to that in the pre-inflationary scenario, which is of order $\theta_0^2 H_\star f_a^2$ at this time [163] (the subscript '$\star$' refers to quantities evaluated at $H = H_\star \equiv m_a$).

We can obtain a conservative lower bound on the final axion abundance by considering only the axion waves emitted during the scaling regime up to $H_\star$ (i.e. $n_{a,\star}^{\rm st}$ only), which can be reliably determined (following the logic applied to QCD axion strings in [188]). Additional axions will be produced during the destruction of the string network, however a reliable calculation of this component appears challenging as the system of strings and domain walls cannot be simulated at the physical value of m_a/m_r.[26]

As shown in [188], the waves emitted during the scaling regime redshift relativistically for some time even after $H_\star$, since their kinetic energy a factor of $\xi_\star \log_\star \gg 1$ larger than their potential energy (bounded by $V \lesssim m_a^2 f_a^2$), which is therefore negligible.[27] The relativistic redshift ends when the potential and kinetic energies become comparable. At this time, the waves experience a nonlinear transient (the main features of which can be understood analytically, up to order 1 coefficients that need to be obtained from numerical simulations). Soon after this most of the axions from the scaling regime become non-relativistic and their number density per comoving volume is conserved. The net effect of the relativistic redshift and the nonlinear transient is a non-conservation of the comoving axion number density between $H_\star$ and the end of the transient. However, unlike the case of a temperature dependent mass, this only amounts to an up to $O(20\%)$ effect for a temperature-independent mass with $\xi_\star \log_\star = 3 \times 10^3$ or smaller (see Appendix F.3 for the derivation). Given the much larger uncertainties involved, in what follows we will therefore make the approximation that $n_a^{\rm st}$ is conserved.

[26] The final number density of axions arising from the axions emitted by the scaling regime is not expected to be affected by more than an order one factor by the presence of domain walls connected to strings [188].

[27] The relevant kinetic energy is the one is IR modes, approximately given by $8\pi\xi_\star \log_\star H_\star^2 f_a^2 \gg m_a^2 f_a^2$ at $H_\star$.

Number density conservation from $H_\star$ leads to the (non-relativistic) axion energy density today $\rho_a^0 = m_a (R_\star/R_0)^3 n_{a,\star}^{\rm st}$, and the relic abundance of axions from strings during the scaling regime $\Omega_a^{\rm st} \equiv \rho_a^0/\rho_c$ is

$$\Omega_a^{\rm st} \simeq 0.1 \left(\frac{\xi_\star \log_\star}{3\times 10^3}\right) \left(\frac{f_a}{10^{14}\,{\rm GeV}}\right)^2 \left(\frac{m_a}{10^{-18}\,{\rm eV}}\right)^{\frac{1}{2}} \left(\frac{10}{x_{0,a}}\right) \left(\frac{3.5}{g_\star(T_\star)}\right)^{\frac{1}{4}} , \tag{6.13}$$

for $\xi_\star \log_\star \lesssim 10^3$. For larger values of $\xi_\star \log_\star$, eq. (6.13) must be changed to take into account the non-conservation of the number density. For a temperature independent axion mass, this results in $\Omega_a^{\rm st} \propto (\xi_\star \log_\star)^{3/4}$ up to logarithmic corrections (see Appendix F.3). Note that, unlike the QCD axion, in eq. (6.13) f_a and m_a can vary independently and, for a fixed f_a, smaller values of m_a give smaller $\Omega_a^{\rm st}$.

As expected, for $\xi_\star \log_\star$ small enough that the transient is negligible, the relic density of axions from strings is a factor of $\xi_\star \log_\star$ larger than that from misalignment in the pre-inflationary scenario (with $\mathcal{O}(1)$ misalignment angle) [333], with the same leading parametric dependence on f_a and m_a. For ultralight axions $\log_\star = \log(m_r/m_a) \simeq 10^2$ and, as discussed in Section 6.2.4, the extrapolation of ξ suggests that $\xi_\star = c_1 \log_\star \simeq 25$. Therefore, the relic density leads to severe constraints for $f_a \gtrsim 10^{14}\,{\rm GeV}$, forcing $m_a \lesssim 10^{-17}\,{\rm eV}$. We show the bound $\Omega_a^{\rm st} < \Omega_{\rm DM}$ in Figure 6.7 assuming that the IR cutoff of the spectrum is $x_{0,a} = 10$ also at large log, and that the growth of ξ in eq. (2.47) continues (we also fix that the network persists until $3H = m_a$, as suggested by simulation results for a temperature independent axion mass in Appendix F.3, which leads to a constraint that is stronger by a factor of $\sqrt{3}$).

Eq. (6.13) is expected to hold at best up to an order one coefficient that encodes the effect of the system of strings and domain walls on the axion waves produced during the scaling regime. We finally note that eq. (6.13) only provides a lower bound on the axion dark matter abundance, as it misses the unknown part from string-domain wall collapse. In any case, as shown in Figure 6.7, even if this contribution to the axion relic abundance is a few orders of magnitude larger than $\Omega_a^{\rm st}$, a wide range of axion masses are still allowed for $f_a \gtrsim 10^{14}\,{\rm GeV}$ (thanks to the dependence of $\Omega_a^{\rm st}$ on m_a and f_a).

As mentioned, we obtained eq. (6.13) by assuming that at large log the axion spectrum becomes IR dominated, with $q_a > 1$, as suggested by extrapolations of simulation results [188]. If this is not the case the number density of axions from strings will be negligible with respect to that predicted by the misalignment mechanism with an effective initial misalignment angle $\langle \theta_0^2 \rangle \simeq 2.15^2$. The resulting relic abundance is a factor of $\xi_\star \log_\star$ smaller than eq. (6.13), and the correspondingly weakened bound from dark matter in Figure 6.7 can be straightforwardly obtained. We also note that Lyman-α observations limit the fraction of the dark matter that can have a mass below $\sim 10^{-20}$ eV [334, 335]. We plot the resulting constraints in Figure 6.7, labelled Lα. Even though they are weaker than those from isocurvature that we study later, these bounds have the advantage

of not depending on the (uncertain) details of the axion density power spectrum.[28]

6.3.2 Dark Radiation

For the ultra-light axion masses allowed by the relic abundance constraint in eq. (6.13) (plotted in Figure 6.7), the scaling regime ends when the Universe's temperature is less than an MeV (see also the upper axis of Figure 6.6). Consequently all the axions emitted during the scaling regime up to that point are relativistic at the time of BBN. Additionally, due to the approximately scale-invariant form of the axion energy density spectrum $\partial\rho_a/\partial k$ (see eq. (F.6) in Appendix F.3), an order one fraction of the axion energy is in modes that are relativistic at CMB decoupling even if the string network is destroyed prior to this. Constraints from current limits on dark radiation at these times, usually expressed in terms of the effective number of neutrinos $N_{\rm eff}$, are therefore potentially relevant.[29]

Similarly to gravitational waves, during the scaling regime the energy density in axions is $\rho_a(t) = \int_{t_1}^{t} dt'(R'/R)^4\Gamma'_a$, where Γ_a takes the form in eq. (2.53). As a result, up to $1/\log$ corrections and neglecting changes in the number of relativistic degrees of freedom g, and assuming $\xi = c_1 \log$ as in eq. (2.47),

$$\rho_a = \frac{4}{3}H^2 c_1 \pi f_a^2 \left(\log^3 - \log_1^3\right) \ , \tag{6.14}$$

where $\log_1 \equiv \log(m_r/H_1)$ is the value of the log when the scaling regime starts. From eq. (6.14) we see that the energy in axions could be sizeable as it is enhanced by a $\log^3$ factor, which ultimately comes from the fact that the axion spectrum deviates from scale invariance by a $\log^2$ correction. Moreover, the dependence on the initial condition, which sets $\log_1$, is not important as long as $\log_1 \ll \log$ (in the following we therefore neglect $\log_1$, and the resulting bound is barely affected by varying this in its plausible range).

The axion energy corresponds to an effective number of neutrinos $\Delta N_{\rm eff} \equiv (8/7)(11/4)^{4/3}\rho_a/\rho_\gamma$ where ρ_γ is the energy density in photons.[30] At a temperature of 1 MeV eq. (6.14) leads to

$$\Delta N_{\rm eff} = 0.6 \left(\frac{c_1}{0.24}\right)\left(\frac{f_a}{10^{15}\ \text{GeV}}\right)^2 \left(\frac{\log}{90}\right)^3 \ , \tag{6.15}$$

where $\log(m_r/H_{\rm BBN}) \simeq 90$ if $m_r = 10^{14} \div 10^{15}$ GeV. To determine the overall coefficient in eq. (6.15) precisely, we improved the calculation of ρ_a in eq. (6.14) by numerically integrating Γ_a to account for the changing number of relativistic degrees of freedom. Owing to the increased expansion of

[28] There is an additional constraint from Lyman-α [336] observations, not plotted, which requires $m_a > 2\times10^{-20}$ eV in the case the axion makes up the entirety of the dark matter. While this excludes some values of m_a and f_a such that the axion makes up the whole DM abundance, the extension of this bound to the case of an axion that makes up a fraction of the total DM is currently unknown.

[29] For larger axion masses a fraction of ρ_a is in modes that are relativistic at BBN, but constraints from dark matter overproduction are stronger in this case.

[30] The effective number of neutrinos is defined by $N_{\rm eff} \equiv (8/7)(11/4)^{4/3}(\rho_\nu + \rho_X)/\rho_a$. In principle the energy density in strings and gravitational waves also contributes to ρ_X, however this energy is much smaller than ρ_a.

the Universe this suppresses the result by about 30%.[31]

Although bounds that we will study in Section 6.3.4 require that the string network is destroyed prior to the formation of the CMB for the $f_a \gtrsim 10^{14}\,\text{GeV}$, limits on dark radiation from the CMB are still potentially relevant. In this case, the energy in relativistic axions at the time of decoupling is simply obtained by redshifting the value of eq. (6.14) from the time of the network destruction, accounting for the proportion of the axions that become non-relativistic.

We use the 95% limits from [45], which correspond to $\Delta N_{\text{eff}} < 0.46$ and 0.28 at BBN and CMB times respectively (imposing constraints derived from different analyses or the 68% limits, e.g. [337] only changes the constraint on f_a relatively mildly). As can be seen from eq. (6.15), the limits from BBN constrain $f_a \lesssim 10^{15}$ GeV as shown in Figure 6.7. Those from the CMB lead to a comparable bound, although the maximum allowed ΔN_{eff} is more uncertain given tensions between different determinations of the Hubble parameter. As we will see shortly, all such values of f_a are in tension with limits from isocurvature. However, the constraints from dark radiation are still useful since they are subject to fewer uncertainties.

We finally note that the detection of GWs from strings would predict a non-vanishing ΔN_{eff}. Conversely, given the quadratic dependence on f_a, a plausible improvement in the measurement of ΔN_{eff} to an uncertainty of $\sigma(\Delta N_{\text{eff}}) \simeq 0.02$ [338] could rule out $f_a \gtrsim 2 \times 10^{14}$, which is a large part of the range that gives GWs that could be observed in the near future.[32]

6.3.3 Isocurvature Perturbations

The main equations used to calculate constraints from isocurvature perturbations have been reviewed in Section 4.5.2 where the intermediate scenario was considered. The main difference here is that in the post-inflationary scenario the strings contribution is dominant and that the network is destroyed at the time $t_\star$. The important quantities to consider are the (dimensionless) power spectrum $\Delta_a^2(k)$ defined by eq. (4.31), which by the same causality argument also has a k^3 shape at momenta bellow the peak $H_\star R_\star / R_0$, and the fraction between isocurvature and curvature perturbations:

$$f_{\text{iso}}(k) = \frac{\Omega_a}{\Omega_{\text{DM}}} \sqrt{\frac{C k^3 R_0^3}{A_s H_\star^3 R_\star^3}}\,. \tag{6.16}$$

Given the highly nonlinear dynamics of the scaling regime and the destruction of the string network, the only way to determine Δ_a^2 accurately would be to numerically simulate the system until the strings and domain walls have all vanished. Unfortunately, as discussed, it is extremely hard to study the network's destruction reliably. Despite this, similarly to the dark matter abundance, we can obtain a conservative isocurvature constraint by considering only the axion waves produced during the scaling regime up to $H_\star$. Provided the presence of domain walls does not affect these

[31] In particular, the contribution to ρ_a from earlier times, already suppressed by $\log^3$, is further suppressed by $g^{1/3}$.

[32] Additionally, the possibility that the background of relativistic axions left over today could be directly detected (for axion-to-photon coupling $g_{a\gamma\gamma}$ larger than f_a^{-1}) has recently been studied [339].

waves by more than an order one amount, the axions from the scaling regime can be approximated as a separate component of DM (distinct from that produced by domain walls) with its own power spectrum and a relic abundance given by eq. (6.13). Neglecting the effects of domain walls, we will be able to determine the power spectrum for this component and in doing so obtain an isocurvature bound. The DM axions from domain walls will also have density perturbations so are expected to only strengthen the constraint.[33] Finally, the power spectrum at $k \gtrsim H_\star$ depends on the details of the destruction of strings and domain walls, and it could be affected by oscillons [184], and is beyond the scope of our present work.

To determine Δ_a^2, we solve the equations of motion $\ddot{a} + 3H\dot{a} - R^{-2}\nabla^2 a + V'(a) = 0$ (with $V = m_a^2 f_a^2(1-\cos(a/f_a))$ and m_a temperature independent as before) numerically. As discussed in Appendix F.4 we expect very similar results from any other potential bounded to be $\lesssim m_a^2 f_a^2$. We start at $H = H_\star$ with initial conditions given by a superposition of waves with the energy density spectrum $\partial\rho_a/\partial k$ predicted by the scaling regime at $\xi_\star \log_\star = 10^3$ (see Appendix F.4 and [188] for more details). As mentioned in Section 6.3.1, the field undergoes a period of relativistic redshift and a nonlinear transient, after which the non-relativistic regime is rapidly reached with (at least the IR part of) Δ_a^2 constant.[34]

In Figure F.12 (left) of Appendix F.4 we plot the resulting Δ_a^2, defined as in eq. (4.31), as a function of the momentum and time. As expected, the spectrum reaches an order one value at momenta corresponding to the scale $H_\star$. The peak is somewhat above $H_\star$ since $x_{0,a} \simeq 10$ and correlations at smaller scales are likely since the average axion momentum is larger than x_0 (see [188]). At smaller momenta the expected k^3 behaviour is reproduced, with a constant coefficient $C \approx 2 \times 10^{-5}$ (the nonlinearities turn out to be important, as this coefficient is about a factor of 4 smaller than if the evolution of these waves were linear, i.e. with $V = 1/2 m_a^2 a^2$, see the green line in Figure F.12 (left) of Appendix F.4). In the following we will derive constraints assuming Δ_a^2 and $\Omega_a^{\rm st}$ as described above. To get a feel for how much the DM axions from domain walls might potentially strengthen the constraint, in Appendix F.4 we also plot and discuss results for the power spectrum obtained after the destruction of the full string-domain wall network at the unphysical value $\log_\star = 5$.

Isocurvature constraints from the CMB and Lyman-α

For axion masses $m_a \gtrsim 10^{-22}$ eV such that the modes constrained by Lyman-α observations $k_{\rm L\alpha} \sim 10\ {\rm Mpc}^{-1}$ are in the k^3 part of Δ_a^2, we can be immediately apply the results in [260,261] to obtain a bound on f_a, which can be written in term on $f_{\rm iso}(k_{\rm CMB})$ in (6.17) bellow, i.e. $f_{\rm iso}\,(k_{\rm CMB}) < 0.004$. For sufficiently small masses, $m_a \lesssim 10^{-22}$ eV, such modes are not in the k^3 region however.

[33] A large weakening of the bound would require that the domain walls absorb a large fraction of low momentum axion waves emitted during scaling and homogeneously remit them as high momentum modes.

[34] Unlike simulations of the string network, the axion only simulations do not need to probe length scales f_a^{-1} (since it is the IR part of the axion spectrum that contains the majority of the axion number density so is relevant to the constraint), therefore the physical dynamics are reproduced directly.

Consequently the results of [260] cannot be applied since they rely on the specific k^3 shape of the spectrum, and instead a complete reanalysis is needed, which would take into consideration the full shape of the spectrum, including momenta higher than the peak. We do not attempt this in our present work, and instead we discuss conservative constraints coming from the CMB alone. We stress however that given the density power spectrum remains of order 1 up to $k/H \sim 100$ and drops relatively slowly above this, a full reanalysis of the Lyman-α constraints in this mass region is likely to result in stronger bounds than the those discussed bellow in the region $m_a \lesssim 10^{-22}$ eV.

For 10^{-28} eV $\lesssim m_a \lesssim 10^{-22}$ eV, $k_{\rm CMB}$ is inside the k^3 part of $\Delta_a^2(k)$ while $k_{\rm L\alpha}$ is not. In this mass region we directly apply the CMB limit $f_{\rm iso} < 0.64$ obtained in [259] for a k^3 shape of the spectrum of isocurvature perturbations, which gives conservative isocurvature constraints. In general the axions from scaling only comprise a fraction of the total dark matter, so there is a factor of $\Omega_a^{\rm st}/\Omega_{\rm DM}$ in their contribution to $f_{\rm iso}$. Consequently, assuming there are no isocurvature fluctuations in the remainder of the DM, at $k = k_{\rm CMB}$

$$\begin{aligned} f_{\rm iso}\left(k_{\rm CMB}\right) &= \frac{\Omega_a^{\rm st}}{\Omega_{\rm DM}} \sqrt{\frac{C\, k_{\rm CMB}^3}{A_s k_\star^3}} \\ &\simeq 0.2 \left(\frac{\xi_\star \log_\star}{3\times 10^3}\right) \left(\frac{f_a}{5\times 10^{14}\ \text{GeV}}\right)^2 \left(\frac{m_a}{10^{-28}\ \text{eV}}\right)^{-1/4} \left(\frac{C}{2\times 10^{-5}}\right)^{1/2} , \end{aligned} \tag{6.17}$$

where $A_s = 2.1 \times 10^{-9}$, and $k_\star \equiv H_\star R_\star / R_0$ is the comoving momentum corresponding to H at $H = H_\star = m_a$ redshifted to today. As discussed, we expect eq. (6.17) to give a lower bound on $f_{\rm iso}$, and to be valid up to an order one factor. We note that the isocurvature constraint is potentially important even when the axions produced by the scaling regime make up a small fraction of the abundance. This is because, for sufficiently light axions, the relative density fluctuations reach values close to one at the observationally constrained scales.

Finally, for masses $m_a \lesssim 10^{-28}$ eV the limit in [259] can no longer be applied as $k_{\rm CMB}$ is not in the k^3 part of $\Delta_a^2(k)$. However in this region we expect strong constraints due to the fact that strings survive until the time of recombination, which are discussed in Section 6.3.4.

Impact on the allowed axion masses and decay constants

The bounds on the axion mass and decay constant from CMB and Lyman-α isocurvature constraints are plotted in Figure 6.7. The limits at higher axion masses come from Lyman-α observations, while those at lower masses are due to the CMB observations. As discussed, we do not give bounds from Lyman-α for axion masses smaller than about 10^{-22} eV.

Although we expect the domain walls not to affect the power spectrum associated to pre-existing axions waves by more than an order one factor, we blur the resulting constraints in Figure 6.7 to reflect this uncertainty. Moreover, the constraints from isocurvature would strengthen if the axions from domain walls have large density perturbations, i.e. if their density power spectrum corresponds

to a larger coefficient C, if their relic abundance is comparable to that of the axions from scaling (though the bound on f_a would increase only proportionally to $C^{1/4}$). The bounds would also strengthen if the domain walls produced more DM axions than the scaling regime, even if they have the same density power spectrum as those from scaling, because $f_{\rm iso}$ includes a factor of $\Omega_a/\Omega_{\rm DM}$, as in eq. (6.17). We also note that there are other possible constraints on isocurvature from spatial scales between the CMB and Lyman-α observations (e.g. from structure formation and galaxy clusters [261]), which could matter for intermediate axion masses $\sim 10^{-25}$ eV. However, these are more sensitive to astrophysical details, and would require a dedicated analysis.

We note that it is clear from eq. (6.17) that the isocurvature constraints are not relevant for the QCD axion in the post-inflationary scenario. Indeed, for the QCD axion $H_\star$ corresponds to the Hubble parameter shortly before the QCD crossover, which is much larger than that for ultralight axions, and so $k_\star$ is larger and $f_{\rm iso}$ more suppressed. Finally, for both the QCD axion and ultralight axions, isocurvature perturbations sourced during inflation (if the axion was present at this point) are averaged out by the dynamics of the strings and are simply incorporated into the coefficient C of the white noise spectrum.

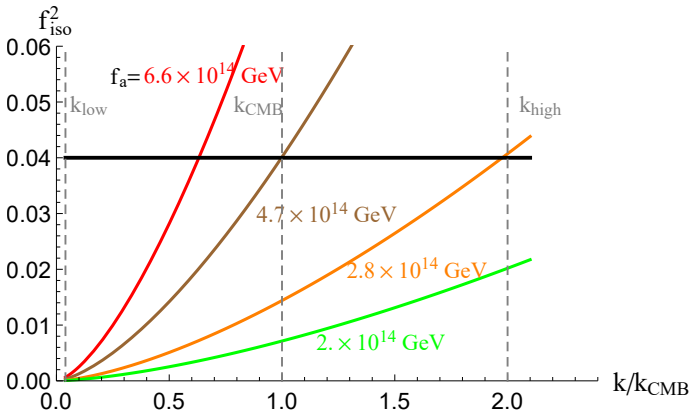

Figure 6.8: Comparison between the fraction of isocurvature perturbations produced by strings relative to curvature perturbation as defined in equation (6.16) for various values of the symmetry breaking scale (colored lines), and the scale invariant isocurvature fraction constrained by the CMB [205] (black line). The various isocurvature fractions are represented as functions of momentum in units of $k_{\rm CMB} = 0.05\,{\rm Mpc}^{-1}$ and the ALP mass was set at $m_a = 10^{-26}$ eV. We have also plotted the values of $k_{\rm low} = 0.002\,{\rm Mpc}^{-1}$ and $k_{\rm high} = 0.1\,{\rm Mpc}^{-1}$ at which the CMB limits on the isocurvature fraction are reported in [205]. Due to the k^3 momentum dependence of Δ_a^2 and $f_{\rm iso}^2$, if the CMB limits are satisfied at the highest momentum $k_{\rm high}$, they are automatically satisfied at lower momentum. However, strictly the CMB limits should be derived by taking the shape of the isocurature perturbations spectrum into account, which is k^3 rather than scale invariant, and for this reason we rely on the analysis in [259] which considers this spectral shape for the plot in Figure 6.7. At higher ALP masses stronger constraints come from Lyman-α forest observation, which are sensitive to higher momentum scales $k_{\rm L\alpha} \simeq 10\,{\rm Mpc}^{-1}$. For definiteness we have also set the normalisation of the isocurvature spectrum in equation (6.16) to $C = 2 \times 10^{-5}$.

6.3.4 Strings and CMB anisotropies

If strings are present at the time of decoupling their gravitational interactions introduce additional anisotropies in the CMB [340, 341]. In particular, a long string induces a 'deficit angle' $\delta = 8\pi G\mu$ in the locally flat metric around it, giving the metric a global conical structure. As a result, two particles moving towards the string in parallel acquire a nonzero relative velocity as they pass the string, and eventually collide.[35] If this is applied to an observer and a source of photons, the observer will see a discontinuous Doppler shift of the photons as the string is passed. Consequently, strings lead to discontinuous temperature fluctuations, of order $\delta T/T \propto G\mu$, in the CMB photons around them [342]. Moreover, a string that moves in the primordial plasma produces a wake behind it by pure gravitational interactions, and therefore additional density perturbations, which are again potentially measurable in the CMB. Since the strings act as a random source, such perturbations are not coherent and do not result in the observed acoustic oscillations [343–345]. Consequently they can contribute, at most, a relatively small fraction of the total anisotropy (see e.g. [110–113]).

A statistical analysis comparing the effects mentioned above with CMB observations gives an upper limit on the string tension μ and consequently on the allowed f_a for an axion network that is not destroyed prior to decoupling. These constraints are therefore relevant for axion masses $m_a \lesssim 10^{-28}$ eV. As for the GW spectrum and axion DM abundance, it is challenging to determine the string induced anisotropy spectrum at the relevant time, which cannot be studied directly in simulations. Reliable constraints can only be obtained by fully accounting for the effects of scaling violations on the string induced anisotropy spectrum, and we do not attempt this in our present work.[36] Instead, we simply note that, based on the previous literature (e.g. [346–348] for local strings and [349] for global strings), a bound very roughly in the range of $G\mu \lesssim 10^{-7}$ is plausible, corresponding to $f_a \lesssim 2\times 10^{14}$ GeV. This is in possible tension with any axion with $m_a \lesssim 10^{-28}$ eV and f_a large enough for observable GWs. We however stress that there is significant uncertainty remaining and blur the bound in Figure 6.7 to indicate this. In particular, if the bound on $G\mu$ turns out to be significantly weaker than the quoted limit, observable GWs from axion strings would be allowed for arbitrarily small axion masses.

6.3.5 The case $N_{\mathrm{DW}} > 1$

In the previous Sections of this Chapter we have performed our analysis assuming that the U(1) breaking scale v_a equals the axion decay constant f_a. Our results are however easily generalised when $N_{\mathrm{DW}} = v_a/f_a > 1$. In this case additional explicit breaking of the remaining discrete symmetry must be present to avoid the domain walls over-closing the Universe [191], and this

[35] On the other hand, loops are expected to oscillate many times before disappearing and at large distances the gravitational field averaged over one oscillation is the usual Newtonian potential, which affects the motion of bodies like conventional matter.

[36] It would be particularly challenging to accurately determine constraints around $m_a \sim 10^{-28}$ eV, given that the string network is being destroyed by domain walls around the time of decoupling in this case.

breaking must be sufficiently large that axion emission from domain walls does not produce a too large dark matter abundance (as previously, our constraints from the dark matter abundance considering emission from the string network are conservative).

First we observe that the calculation of the axion and GW emission from the strings depends on v_a, which enters in eq. (2.29) and therefore determines the string tension in eq. (2.49) and the emission rates Γ_a and Γ_g. Thus, the GW spectrum in eq. (6.12) and Figure 6.6 is valid for a generic v_a with the substitution $f_a \to v_a$. Similarly, the bounds from dark radiation and CMB anisotropies in Sections 6.3.2 and 6.3.4 and Figure 6.7 apply to v_a.

On the other hand, since the decay constant f_a determines the axion potential $V \propto m_a^2 f_a^2$, a $v_a \neq f_a$ affects the dark matter abundance and isocurvature perturbations discussed in Sections 6.3.1 and 6.3.3. In all our calculations in those Sections the scale v_a enters only through the inputted axion energy density spectrum from the scaling regime, and it appears together with $\xi_\star \log_\star$ (in particular, $\partial\rho_a/\partial k \propto v_a^2 \xi_\star \log_\star$). The dark matter abundance in eq. (6.13) is therefore easily generalised by substituting $\xi_\star \log_\star \to N^2 \xi_\star \log_\star$. However, as discussed in Section 6.3.1, if $N_{\rm DW} \gg 1$ one needs to account for the number density non-conservation. This is done by multiplying eq. (6.13) by the suppression factor in eq. (F.3), which makes $\Omega_a^{\rm st} \propto (N_{\rm DW}^2 \xi_\star \log_\star)^{3/4}$ (instead of a quadratic dependence on $N_{\rm DW}$). A similar change occurs in eq. (6.17) via the DM abundance (notice that C depends on $\xi_\star \log_\star$, and needs to be recomputed).

The overall effect of $N_{\rm DW} > 1$ can therefore be summarised by substituting $f_a \to v_a$ in Figures 6.6 and 6.7, but with a stronger constraint from dark matter overproduction (by a factor $\mathcal{O}(N^{3/2})$ on the vertical axis of Figure 6.7).

6.4 Peccei-Quinn Restoration in the Early Universe

The post-inflationary scenario occurs if the U(1) symmetry has ever been restored after inflation. In this Section we apply the mechanisms considered in Chapters 4, 5 to see which of them could lead to symmetry restoration for the relatively large symmetry breaking scales $f_a \gtrsim 10^{14}\,\text{GeV}$ required for observable gravitational waves.

- Quantum fluctuations during inflation induce perturbations in any effectively massless scalar field present at this time. As mentioned before, the rough condition often considered in the literature for the post-inflationary scenario is simply $H_I/2\pi \gtrsim f_a$ [197,251]. Given the results presented in Figure 4.9 it is likely that the actual condition is of the order $H_I/f_a \gtrsim 2$. The current bound on H_I from the non-observation of tensor modes is [205]

$$\frac{H_I}{2\pi} < 9.6 \times 10^{12}\ \text{GeV}\ . \tag{6.18}$$

  Consequently such fluctuations do not lead to the post-inflationary scenario for values of f_a that give observable GWs, even if we relax the condition for restoration as suggested by our

analysis in Chapter 4.

- The PQ symmetry can be restored if the maximum temperature $T_{\max}$ during reheating is greater than $\mathcal{O}(f_a)$ and the sector that gives rise to the axion is sufficiently close to thermal equilibrium at this time. As explained in Section 5.3 the maximum temperature of the Universe can be estimated [290]:

$$T_{\max} \simeq 0.30 M_P^{\frac{1}{4}} H_I^{\frac{1}{4}} T_{\rm RH}^{\frac{1}{2}} \simeq 0.22 M_P^{\frac{1}{2}} H_I^{\frac{1}{4}} \Gamma_\varphi^{\frac{1}{4}} \,. \tag{6.19}$$

  With H_I close to the maximum allowed value, symmetry restoration for $f_a \sim 10^{14} \div 10^{15}\,\text{GeV}$ requires that the inflaton decay rate is of the order $\Gamma_\varphi \sim 10^8 \div 10^{12}\,\text{GeV}$. For a mass of the inflaton $m_\varphi \sim H_I$ and a decay to fermions through a coupling $\mathcal{L} \supset g\varphi\overline{\psi}\psi$ for example, $g \sim 10^{-3} \div 0.1$ would be required. We conclude that this is possible, albeit a bit tight for $f_a \simeq 10^{15}\,\text{GeV}$, especially since in achieving this maximum temperature instant thermalisation of the inflaton decay products is also required.

- Additionally, for many types of interaction, the inflaton expectation value during inflaton restores the PQ symmetry if it couples to the PQ sector, provided the coupling is large enough [350–353]. Depending on the details of the theory, the PQ symmetry might then break during inflation (as the inflaton evolves towards its final expectation value), or during reheating (once the inflaton is settling down e.g. to $\langle\varphi\rangle = 0$). In many theories the inflaton expectation value is large compared to other scales, so this restores a PQ symmetry with large f_a even if the inflaton only has relatively weak couplings. This was considered in detail in Section 5.1 and the particular case of hybrid inflation in Section 5.1.1. The attractive feature of hybrid inflation is that, for values of λ that are not very small, slow-roll inflation ends within a very short time after PQ symmetry breaking, which naturally results in the post-inflationary scenario. Additionally the value of H_I is relatively small in this case:

$$H_I \simeq \sqrt{\frac{\lambda}{12}} \frac{f_a^2}{M_P} \lesssim 10^{11}\,\text{GeV}\,, \tag{6.20}$$

  which is significantly below the CMB constraint even for $\lambda \sim \mathcal{O}(1)$ and $f_a \simeq 10^{15}\,\text{GeV}$. We see that this mechanism is very efficient at restoring the PQ symmetry, which happens for maximum temperatures significantly smaller than f_a.

  For an inflaton coupling of the type

$$V_{\rm int} = \frac{1}{2} g\varphi^2 |\phi|^2 \,, \tag{6.21}$$

the condition for PQ symmetry to be restored during inflation is

$$g\left\langle\varphi^2\right\rangle > m_r^2 \,, \tag{6.22}$$

which is possible for couplings $g \lesssim \mathcal{O}(1)$ if the inflaton assumes a large value $\langle\varphi^2\rangle \gtrsim f_a^2$.

- Similarly a non-minimal coupling of the PQ field to scalar curvature $\mathcal{L} \supset \epsilon\mathcal{R}\left|\phi\right|^2$ could restore symmetry for $\epsilon > \frac{\lambda f_a^2}{12H_I^2}$. However this would require either $\lambda \ll 1$ or H_I close to the maximum limit in eq. (6.18) so that the coupling $\epsilon \lesssim 1$.

- We discussed in Section 5.4 that the PQ symmetry could be restored by non-perturbative decay of the inflaton. We have considered two cases: that the inflaton couples directly to the PQ field, where we found that the size of the coupling necessary for efficient preheating would have restored the PQ symmetry already during inflation; and that the inflaton preheats an intermediate massless scalar which then heats up the PQ field. The indirect preheating is considered in more detail in Section 5.4.2 where the condition that it could restore symmetry for parameter values for which $T_{\max}$ could not is found:

$$H_I^3 m_\varphi^3 M_P^2 > 10 m_r^8 \,. \tag{6.23}$$

  For large values of the self-coupling λ such that $m_r \simeq f_a \simeq 10^{15}\,\text{GeV}$ this is not significantly more efficient than restoration via the maximum temperature $T_{\max}$, although it could be for somewhat smaller λ.

- In Section 5.6 we discussed the possibility to restore PQ symmetry at a lower reheating temperature, if the radial mode is light and is coupled to light fermions as $\mathcal{L} \supset g\phi\psi^c\psi$. The minimum temperature needed to restore PQ symmetry in this situation is parametrically:

$$T_{\min} \simeq \text{Max}\left(\frac{m_r}{g}, g f_a\right) \,. \tag{6.24}$$

  Additionally $g^2 T_{\min} > H$ is required for the fermions to be in thermal equilibrium and the treatment of Section 5.6 to be valid. Overall the simultaneous requirements that PQ symmetry can be restored in this way and that the treatment is consistent translate to $g^2 M_P \gtrsim T_{\min} \gtrsim g f_a$ and $g^3 M_P \gtrsim g T_{\min} \gtrsim m_r$ up to order 1 factors. Given the maximum temperature discussed above and the parameter space of interest $10^{14}\,\text{GeV} \lesssim f_a \lesssim 10^{15}\,\text{GeV}$ this is possible for $g \lesssim 10^{-3}$ and sufficiently light radial mode $m_r \lesssim 10^9\,\text{GeV}$.

  So far in this Chapter we assumed $m_r \simeq f_a$, however the GW signal emitted by such a network will be largely unaffected by the small m_r, i.e. it will approximately match the predictions of Section 6.2. This is because the GW energy depends on the string tension, which is set by f_a not m_r, and the GW spectrum is IR dominated so it is unaffected by the UV cutoff

at m_r being much smaller than f_a. The only effect on the GW spectrum will be through the value of $\log(m_r/H)$ being slightly reduced.[37] This will feed into ξ and the ratio $\Gamma_{\rm GW}/\Gamma_a$ as well as the tension. However, the change is not too dramatic as long as m_r is not too small. For example, taking $m_r = 5 \times 10^8$ GeV and $f_a = 5 \times 10^{14}$ GeV (so that, from Figure 5.2, the symmetry can be restored for temperatures $\sim 5 \times 10^{11}$ GeV), the value of the log when the GW emission is relevant to SKA is $\log \sim 60$, as opposed to $\log \sim 75$ if $m_r \sim f_a$. The amplitude of the resulting GW signal is reduced by roughly 50% relative to that plotted in Figure 6.6, but it remains detectable by SKA.

6.5 Summary and Conclusions

Gravitational wave observations can only be used to learn about physics beyond the Standard Model if we understand the spectrum expected in motivated theories. Here we have made a step towards such a goal by studying the GWs emitted by the network of global strings that forms in the early Universe in a generic axion model if the U(1) symmetry has been ever restored after inflation.

During the subsequent scaling regime GWs are produced by the motion and interactions of strings. Calculating the resulting spectrum directly from numerical simulations is impossible, as these only have access to a small range of early times. However, in Section 6.2.1 we have shown that the Nambu–Goto effective theory with the Kalb–Ramond term – which describes the parts of the string network for which the string thickness can be neglected – gives us analytic control of the GW emission Γ_g at all times, up to an (order one) constant coefficient r related to shape of the string trajectories during scaling. In particular, $\Gamma_g/\Gamma_a = rG\mu^2/f_a^2$, where Γ_a is the emission rate into axions and is fixed by energy conservation. As shown in Section 6.2.3, this result is reproduced spectacularly well by first principles numerical simulations of the string network (at the accessible small values of $\log(m_r/H)$), from which we have extracted the value of r together with the momentum distribution of Γ_g (this is peaked at momenta of order Hubble and falls off at higher momenta as $\propto 1/k^2$). The existence of the attractor solution then allowed us to reconstruct the GW spectrum from the entire scaling regime, and our results are shown in Section 6.2.4. Due to the logarithmic increase of μ (and of ξ), the spectrum has substantial deviations from scale invariance. This enhances its amplitude at low frequencies, and makes it observable by multiple planned experiments for $f_a \gtrsim 10^{14}$ GeV. Importantly, the detection prospects are not significantly altered by the remaining uncertainties. We note that similar scaling violations have previously been predicted in the GW spectrum from global strings, using models aiming to capture the emission from small loops, and we discuss the relation of our work to the existing literature in Appendix I.

In passing, we noted the remarkably self-consistent picture of the scaling regime arising from numerical simulations. In particular, the logarithmic scaling violations of many of the observables seem to be a part of the scaling regime (for instance ξ and the power law q_a of the instantaneous

[37] Since the divergence in the energy of the string is cut of by the physical string core size m_r^{-1} rather than f_a^{-1}.

emission spectrum of axions $\propto 1/k^{q_a}$ both increase logarithmically with time). This is particularly convincing because the energy emitted in axions and radial modes in the simulations is reproduced precisely by the energy emission rate in eq. (2.53) with the ξ in eq. (2.47) and string tension in eq. (2.49), see Appendix 6.2.3. Moreover, the theoretical expectation that $\Gamma_g/\Gamma_a \propto G\mu^2/f_a^2$ (for trajectories with a fixed shape) is matched in the numerical simulations of the scaling regime, which suggests that the scaling solution in which ξ increases logarithmically is self-similar (showing that this increase is not a transient). Additionally, the GW spectrum shows the similar features as the axion spectrum, but with $q > 1$. This suggests that indeed our extrapolation of the axion spectrum is correct and that $q_a > 1$ at large log (when the axion will be more weakly coupled to the string cores, like the GWs are).[38]

In Section 6.3 we studied other general properties of axions in the post-inflationary scenario (including their dark matter abundance, contribution to dark radiation, and isocurvature perturbations), which led to complementary constraint on the axion mass and decay constant. This analysis shows that for all masses in the range 10^{-28} eV $\lesssim m_a \lesssim 10^{-17}$ eV ultralight axions can have decay constants large enough ($f_a \gtrsim 10^{14}$ GeV) to lead to observable GWs. The upper limit on m_a comes from dark matter overproduction, while the lower limit comes from CMB observations (see Figure 6.7). As discussed in Section 6.3.4, this last limit is particularly uncertain and a revised analysis of $G\mu$ from CMB anisotropies could make it irrelevant by weakening the lower bound on f_a for $m_a \lesssim 10^{-28}$ eV. In particular, our results exclude the possibility that GWs from QCD axion strings during scaling are observable, assuming a standard cosmological history, since the dark matter bound in this case requires $f_a \lesssim 10^{10}$ GeV.[39]

As well as constraints, the phenomenological features discussed in Section 6.3 also lead to complementary observational signals of ultralight axions in the post-inflationary scenario, including $\Delta N_{\rm eff}$ and isocurvature perturbations. For values of f_a that lead to observable GWs these are close to current bounds, and within reach of future improvements. Moreover, a PQ symmetry with large f_a is most easily restored in the early Universe for large Hubble during inflation, so tensor modes with an amplitude close to the current observational upper bound might be present if GWs from strings are discovered. We also see that any interpretation of the recent possible GW signal by the pulsar timing experiment NANOgrav as being from global strings of an ultralight axion is in tension with cosmological observations. Although we do not attempt a detailed analysis of the possible signal, from Figure 6.6 a GW signal of the observed magnitude (with a standard cosmology) requires $f_a \gtrsim 10^{15}$ GeV, which from Figure 6.7 is in conflict with bounds on $\Delta N_{\rm eff}$ from BBN.[40]

We also note that the small axion masses mentioned above are theoretically plausible, see

[38] It would be useful to reach large enough log to directly see $q_a > 1$, possibly employing adaptive mesh refinement approaches such as the one used in [354].

[39] We cannot exclude signals from the subsequent dynamics of domain walls.

[40] The power law of the spectrum extracted by NANOgrav might also suggest that the signal is not approximately scale invariant as is predicted by global strings. GWs from QCD axion strings in non-standard cosmologies has been recently considered in [328], which modelled the GW emission from loops and suggested that the NANOgrav result could be interpreted as the emission from QCD axion strings if the equation of state is $w < 1/3$ [355].

e.g. [356] and references therein. It appears inevitable that quantum gravity will explicitly break all global symmetries [146, 147, 269], including the PQ one. The resulting breaking is often exponentially suppressed (e.g. in the ratio $f_a/M_{\rm P}$ [148, 357]) and could therefore lead to the required ultra-light masses.

Finally we consider the remaining open questions and directions for future work. From a theoretical direction, it would be valuable to understand further which classes of axion models cosmic strings can form in. In particular, we have focused on axions that arise as the PNBG of a symmetry that is realised in four dimensional Lagrangian (e.g. from a scalar with a symmetry breaking potential or a new sector that runs into strong coupling, i.e. a composite axion model). Such axions can appear in string theory models from the closed string sector [358]. However, in string theory compactifications axions often come from the open string sector. Although the conventional picture is that cosmic strings cannot form in this case, given the uncertainties surrounding early Universe cosmology and de Sitter vacua in string theory we believe this merits further study.

Another direction in which to extend our work is the study of local strings, which arise from a spontaneously broken gauged U(1) symmetry. In a system of local strings all the degrees of freedom are massive, and, when the Hubble parameter is much smaller than the UV physics scale, the energy might be radiated only in GWs. However, the emission of heavy modes is efficient at small values of $\log(m_r/H)$ (where m_r is the mass of the heavy modes). Consequently, extrapolation will be essential to determine the GW spectrum at observable frequencies.[41]

We also note that the GW signals from axion strings are fairly close to the maximum reach of proposed detectors. Consequently, continued detailed analysis of astrophysical foregrounds will be essential if such signals are to be identified.[42] Although challenging, subtraction of e.g. the foreground from neutron star and black hole binaries in the BBO frequency range appears feasible [361]. A careful study of the impact of the foregrounds on the prospects of the detecting GW signals from strings in different frequency ranges would be worthwhile in the the future.

[41] Indeed, at small log the system of local strings seems to resemble the global string one in many ways.

[42] Note also that, if an ultralight axion makes up an order one percentage of the observed DM, the oscillations in its gravitational field lead to signals at pulsar timing array frequencies that are of the same order as the stochastic GW background from black hole binaries [359]. Axion miniclusters that appear in the post-inflationary scenario could also leave imprints in pulsar timing arrays through their gravitational interactions [360], though there are still large uncertainties on the properties of these objects.

Chapter 7

Conclusions

The Standard Model of Particle Physics encapsulates our current understanding of matter in the Universe, while the ΛCDM model of cosmology explains the history of the evolution of the Universe under the effect of gravity and is consistent with most of the cosmological data. However, both these models have associated open questions. In particular, one of the major questions which concerns both particle physics and cosmology is that of dark matter, which is required to explain many astrophysical and cosmological observations such as the CMB, structure formation, galaxy rotation curves and gravitational lensing observations, while having no explanation inside the Standard Model of Particle Physics.

A leading candidate for cold dark matter is the QCD axion, which is a pseudo Nambu-Goldstone boson associated with the spontaneously broken $U(1)$ Peccei-Quinn symmetry introduced to solve the Strong CP problem of the Standard Model. The axion's couplings and mass are proportional to the inverse of the symmetry breaking scale of the associated Peccei-Quinn symmetry, meaning that the axion's interactions could be small enough for it to behave like dark matter and remain stable over times longer than the age of the Universe. Meanwhile, the main production mechanisms for the axion are non-thermal, meaning that axions are primarily created with relatively low momentum, allowing them to evade bounds on hot dark matter otherwise relevant for particles so light. Additionally, on top of the Strong CP and dark matter puzzles the QCD axion plays a role in more complex models which seek to solve further open questions of particle physics and cosmology, such as the hierarchy problem, the matter/antimatter asymmetry in our Universe, the smallness of neutrino masses, the flavour puzzle. For these reasons extensive theoretical and experimental efforts have been made over the past decades to understand the possible parameter space in which axions can be dark matter as well as ways to detect them.

Similarly to the QCD axion, more general axion like particles have come under consideration as viable dark matter candidates. These are pseudo Nambu-Goldstone bosons associated with spontaneous symmetry breaking of global $U(1)$ symmetries, which appear in many extensions of the Standard Model such as grand unified theories, theories of leptogenesis and neutrino masses,

as well as in string theory constructions. They behave in a similar manner as the QCD axion, with the exception that their mass is not fixed by their symmetry breaking scale due to an anomalous coupling to QCD.

It is standard lore that there are two inflationary scenarios for axion like particles, related to whether spontaneous symmetry breaking of their associated $U(1)$ symmetry last occurred before or after the end of inflation. These scenarios have very different consequences for the parameters of axions which are allowed and which can produce the expected dark matter abundance, mainly because they are associated with vastly different densities of topological defects. More specifically, the post-inflationary scenario involves a large density of axion strings and later of domain walls, which reach a scaling solution whose properties could in principle be extracted from numerical simulations. On the other hand the pre-inflationary scenario involves effectively no strings or domain walls. A rough condition separating these two scenarios is usually written in terms of the approximately constant Hubble parameter during inflation and the axion's symmetry breaking scale. One of the objectives of this thesis was to revisit the conditions separating these two scenarios in more detail, and I have done so in Chapter 4 by showing empirical evidence in Figure 4.7 for the relation (4.12) between the density of axion strings and the probability that the radial mode of the complex scalar field that gives rise to the axion is pushed over the top of its potential by quantum fluctuations. Assuming the validity of this relation, the density of strings can be calculated at different times after the end of inflation for given values of the relevant parameters, which are the axion symmetry breaking scale, the Hubble parameter during inflation and the quartic coupling of the radial mode's potential. The post-inflationary scenario is then relevant if the string density at the time the axion begins oscillating is close to the scaling value, while the pre-inflationary scenario when the density today would be small and topological defects have negligible contribution to the energy density. There exist a small intermediate region of the parameter space where strings and domain walls become dense enough to decay only much later than the time the axion begins oscillating around its potential, but before today. A representation of this intermediate scenario can be seen in Figure 4.9, which is an example for a specific value of the string density required for the network to decay. Despite the lower density of topological defects the axion abundance is actually enhanced in this intermediate scenario, owing to the lower dilution of the energy stored in domain walls due to the expansion of the Universe than is the case of radiation or matter. Thus this intermediate scenario predicts an even higher axion abundance than the post-inflationary scenario, which is interesting as it allows the QCD axion to be all of dark matter for any value of its mass that is otherwise allowed by astrophysical bounds.

Alternatively, the post-inflationary scenario and the intermediate scenario could be achieved by mechanisms that restore the $U(1)$ symmetry associated to the axion other than quantum fluctuations during inflation. Chapter 5 is dedicated to various such possibilities for symmetry restoration. The mechanisms considered are a coupling between inflaton and PQ field restoring the symmetry during inflation, non-perturbative decay of the inflaton generating large non-thermal fluctuations

of the PQ field and a large temperature in the early Universe restoring the symmetry through thermal fluctuations. Additionally, I discussed the possibility of multiple stages of inflation and found that the intermediate scenario can also be achieved in this way.

Additionally, Chapter 6 considered the spectrum of gravitational waves that would be emitted by an evolving network of axion strings for a general axion like particle in the post-inflationary scenario. This was done by showing that the effective Nambu–Goto theory with a Kalb–Ramond term predicts a simple relation between the energy that the strings emit into axions and gravitational waves respectively, up to order 1 factors that parametrise the average shape of the strings during their evolution. This relation insures analytic control over the gravitational waves emissions at all times and allows us to conclude that the backreation of the gravitational waves should have negligible effects on the strings evolution while the scale of $U(1)$ symmetry breaking is much smaller than the Planck mass. Numerical simulations confirm that the factor related to the shape of the strings is constant for a scaling network, at least over the range of $\log(m_r/H)$ accessible in simulations, and were used to extract its value. It was found that the gravitational waves spectrum deviates substantially from scale invariance, and in particular is enhanced at lower frequencies, which could be probed by future gravitational waves detectors if the symmetry breaking scale is sufficiently large $f_a \gtrsim 10^{14}\,\text{GeV}$, as can be seen in Figure 6.6. This is particularly interesting since gravitational detectors are more sensitive to axion like particles with largest symmetry breaking scales, which otherwise are those with the lowest coupling to light or matter, meaning most other detection methods are least sensitive to them. Various constraints applicable to axion like particles detectable in this way were considered and the resulting range of masses and symmetry breaking scales allowed is shown in Figure 6.7. In particular, constraints on additional number of relativistic degrees of freedom put an upper limit on the symmetry breaking scale $f_a \lesssim 10^{15}\,\text{GeV}$ while the requirements that axions emitted by the scaling network do not overproduce dark matter and that the network is destroyed prior to recombination limit the axion masses to the range $10^{-28}\,\text{eV} \lesssim m_a \lesssim 10^{-17}\,\text{eV}$, with parts of this parameter space also being ruled out by isocurvature constraints. Finally, we discuss the possibilities that lead to the post-inflationary scenario for large symmetry breaking scales that result in detectable gravitational waves. We see that indeed a future observation of gravitational waves with a spectrum consistent with the emissions of a scaling network of axion strings can provide insights into our Universe, including the nature of dark matter, the size of the reheating temperature or the energy scale of inflation.

Appendix A

Checks of the numeric solution to the Fokker-Planck equation

In this Appendix we show various consistency checks related to the numeric solution of the Fokker-Planck equation we implemented, as discussed in Section 4.3.1. In particular we have checked that the solution does not depend on the limits for $\tilde{r}$ between which we have chosen to solve the equation, shown in Figure A.1, or on the parameter "MaxStepSize", shown in Figure A.2.

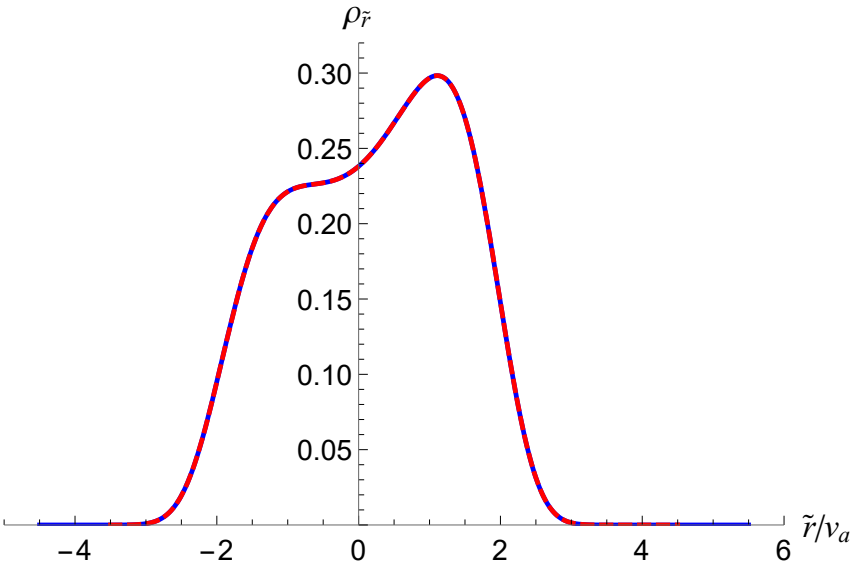

Figure A.1: Comparison between the solution to the Fokker-Planck equation (3.33) for the probability distribution of $\tilde{r}$ for the box size $\tilde{r} \in (-3.5v_a, 4.5v_a)$ that we have used to obtain the results of Chapter 4 (red), and a larger box size $\tilde{r} \in (-4.5v_a, 5.5v_a)$ (blue). For definiteness both solutions are for $H_I/v_a = 2.5$, $\lambda = 0.5$ and $N = 40$ e-folds.

Additionally, in Figure A.3 we compare the one field Fokker-Planck solution for the distribution

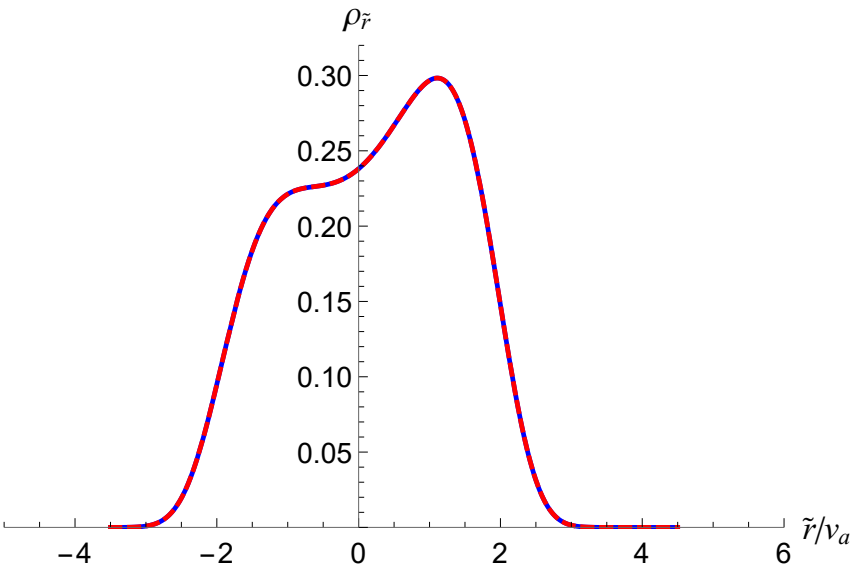

Figure A.2: Comparison between the solution to the Fokker-Planck equation (3.33) for the probability distribution of $\tilde{r}$ for "MaxStepSize= 0.1" that we have used to obtain the results of Chapter 4 (red), and a smaller "MaxStepsize= 0.01" (blue). For definiteness both solutions are for $H_I/v_a = 2.5$, $\lambda = 0.5$ and $N = 40$ e-folds.

of $\tilde{r}$ with a potential (4.9) to the solution for one of the components of the complex PQ field after solving the two field Fokker-Planck equations, which are the coupled partial differential equations:

$$\frac{\partial \rho_\phi(\phi_1,\phi_2,N)}{\partial N} = \frac{1}{3H_I^2}\frac{\partial}{\partial \phi_i}\left(\lambda\phi_i(\phi_1^2+\phi_2^2-v_a^2)\rho_\phi(\phi_1,\phi_2,N)\right) + \frac{H_I^2}{8\pi^2}\frac{\partial^2\rho_\phi(\phi_1,\phi_2,N)}{\partial\phi_i^2}\,, \qquad \text{(A.1)}$$

where ϕ_i stands for either ϕ_1 or ϕ_2, $\phi = (\phi_1+\phi_2)/\sqrt{2}$ and the initial conditions are $\rho_\phi(\phi_1,\phi_2,0) \sim \text{sech}^2(100\ (\phi_1/v_a - 1)) \times \text{sech}^2(100\ \phi_2/v_a)$ (a sharp distribution around $\phi_1 = v_a$, $\phi_2 = 0$). We similarly solve equations (A.1) in Mathematica [254] using "NDSolve", method "BDF" with a "MaxStepSize"= 0.1, inside a box $\phi_{1,2} \in (-3.5v_a, 4.5v_a)$. We then integrate for the probability distribution of ϕ_1, which we compare with the probability distribution of $\tilde{r}$ obtained from the one field Fokker-Planck equation.

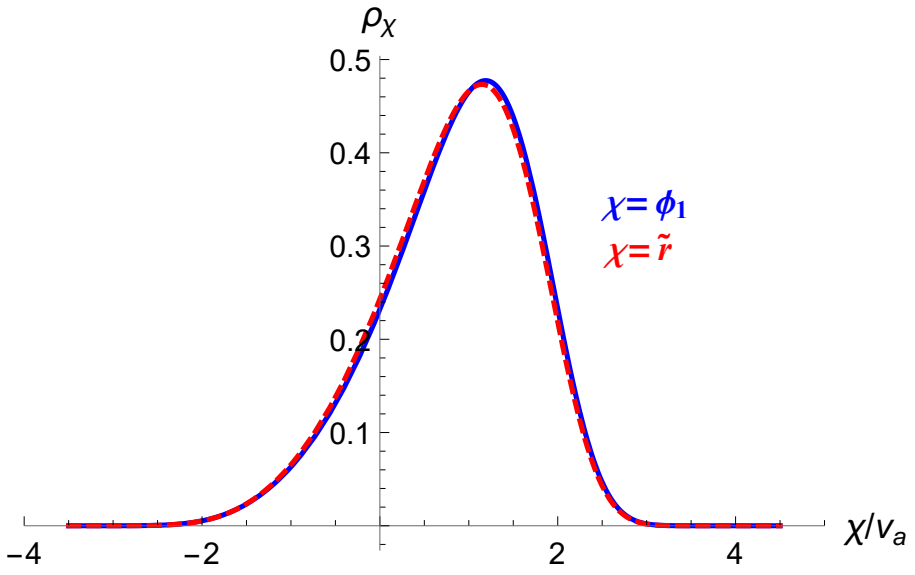

Figure A.3: Comparison between the probability distribution of $\tilde{r}$ (red) found by solving the Fokker-Planck equation (3.33) replacing the potential by (4.9) and the probability distribution of the ϕ_1 component of the complex PQ field (blue) which is found by solving the coupled equations (A.1). The initial conditions for both $\tilde{r}$ and ϕ_1 are the same i.e. $\tilde{r} = v_a$ and $\phi_1 = v_a$ at the initial time $N = 0$. For definiteness we have plotted for $H_I/v_a = 2.5$, $\lambda = 0.5$, $N = 7$.

Appendix B

Consistency of generating initial conditions by the Langevin equation

In Section 3.4 we have introduced a procedure to approximately simulate the Langevin eq. (3.19), which we later used to generate initial conditions for our numerical simulations detailed in Section 4.4. The procedure involves kicking the value in each coarse graining patch of size $1/(\epsilon H_I)$ at each time step by a random number K distributed by a Gaussian with mean 0 and variance $\Delta N H_I^2/(4\pi^2)$ where ΔN is the size of the time step measured in number of e-folds. We then evolve the value of the field in each patch between time steps with the noise turned off. Here we show that this procedure indeed approximately reproduces the effect of Langevin equation if the potential is not too steep. Let us start by breaking the time step ΔN into a large number of infinitesimally small steps δN, $\Delta N = n\,\delta N$ with n a large integer.

Over each of these smaller time steps the field experiences a random kick $\delta\overline{\Psi}$ which are random numbers distributed according to an unknown distribution with mean 0 and variance $\delta N H_I^2/(4\pi^2)$, which can be derived from equations (3.27, 3.26). The kick over the larger time step is then the sum of these smaller kicks:

$$K = \sum_{i=1}^{n} \delta\overline{\Psi}_i \,, \tag{B.1}$$

which as mentioned in Section 3.4 can now be approximately taken as a Gaussian distributed quantity with mean and variance as above due to the Central Limit Theorem.

Denote the value of the field inside an arbitrary patch at the start of an arbitrary time step before receiving the corresponding kick by $\overline{\Psi}_0$. Then after one time step the value of the field in our approximate procedure is:

$$\overline{\Psi}_{\rm app} = \overline{\Psi}_0 + K - \frac{1}{3H_I^2}\int_0^{\Delta N} \frac{\partial V(\overline{\Psi}(N))}{\partial\overline{\Psi}} dN \,. \tag{B.2}$$

Meanwhile the exact value of the field inside the same patch at the end of the time step is:

$$\overline{\Psi}_{\rm ex} = \overline{\Psi}_0 + \sum_{i=1}^{n} \left(\delta\overline{\Psi}_i - \frac{1}{3H_I^2} \int_{(i-1)\delta N}^{i+\delta N} \frac{\partial V(\overline{\Psi}(N))}{\partial \overline{\Psi}} dN \right) , \tag{B.3}$$

in the limit of infinitesimally small δN, i.e. $n \to \infty$.

Our approximation works if $\left|\overline{\Psi}_{\rm ex} - \overline{\Psi}_{\rm app}\right| \ll \left|\overline{\Psi}_{\rm ex} - \overline{\Psi}_0\right|$ or equivalently $\left|\overline{\Psi}_{\rm ex} - \overline{\Psi}_{\rm app}\right| \ll \left|\overline{\Psi}_{\rm app} - \overline{\Psi}_0\right|$ since then the difference between the distance the field traveled in our approximate procedure and the distance it actually traveled is small. We have

$$\left|\overline{\Psi}_{\rm ex} - \overline{\Psi}_{\rm app}\right| < \frac{1}{3H_I^2} \left(\left| \sum_{i=1}^{n} \int_{i\delta N}^{(i+1)\delta N} \frac{\partial V(\overline{\Psi}(N))}{\partial \overline{\Psi}} dN \right| + \left| \int_0^{\Delta N} \frac{\partial V(\overline{\Psi}(N))}{\partial \overline{\Psi}} dN \right| \right) , \tag{B.4}$$

which is further bounded up

$$\left|\overline{\Psi}_{\rm ex} - \overline{\Psi}_{\rm app}\right| < \frac{2\Delta N \max(V')}{3H_I^2} , \tag{B.5}$$

where $\max(V')$ is the maximum absolute value the gradient of the potential achieves over the path of the field. This is a very rough upper bound, since the two integrals are expected to have the same sign and cancel each other to some degree.

Similarly a lower bound on $\left|\overline{\Psi}_{\rm app} - \overline{\Psi}_0\right|$ is:

$$\left|\overline{\Psi}_{\rm app} - \overline{\Psi}_0\right| > |K| - \frac{\Delta N \max(V')}{3H_I^2} . \tag{B.6}$$

Now for the approximation to be correct it is sufficient:

$$\frac{\Delta N \max(V')}{H_I^2} \ll |K| . \tag{B.7}$$

Upon replacing $|K|$ by its typical value which is of the order $\sqrt{\Delta N} H_I/(2\pi)$, this translates into a condition for the gradient of the potential:

$$\max(V') \ll \frac{H_I^3}{2\pi\sqrt{\Delta N}} . \tag{B.8}$$

Given that we use the procedure discussed is used to generate initial condition starting from one grid point in the vacuum as we explain in Section 4.4, the relevant gradient of the potential is in the region between the top of the potential and the vacuum. For the potential (2.29), then $\max(V')$ is $4\lambda f_a^3/(3\sqrt{6})$, and given the values of H_I/f_a and λ we used in simulations represented in Figure 4.7 (i.e. $H_I/f_a \simeq 2.5 \div 2.8$ for $\lambda = 0.25$, $H_I/f_a \simeq 3$ for $\lambda = 0.5$, $H_I/f_a \simeq 3.25$ for $\lambda = 0.75$ and $H_I/f_a \simeq 3.4$ for $\lambda = 1$), we see that indeed the approximation of applying a cumulative kick K and then allow the field to relax for $\Delta N = \log(2)$ works well, which is the time it takes for the

scale factor to double during inflation.

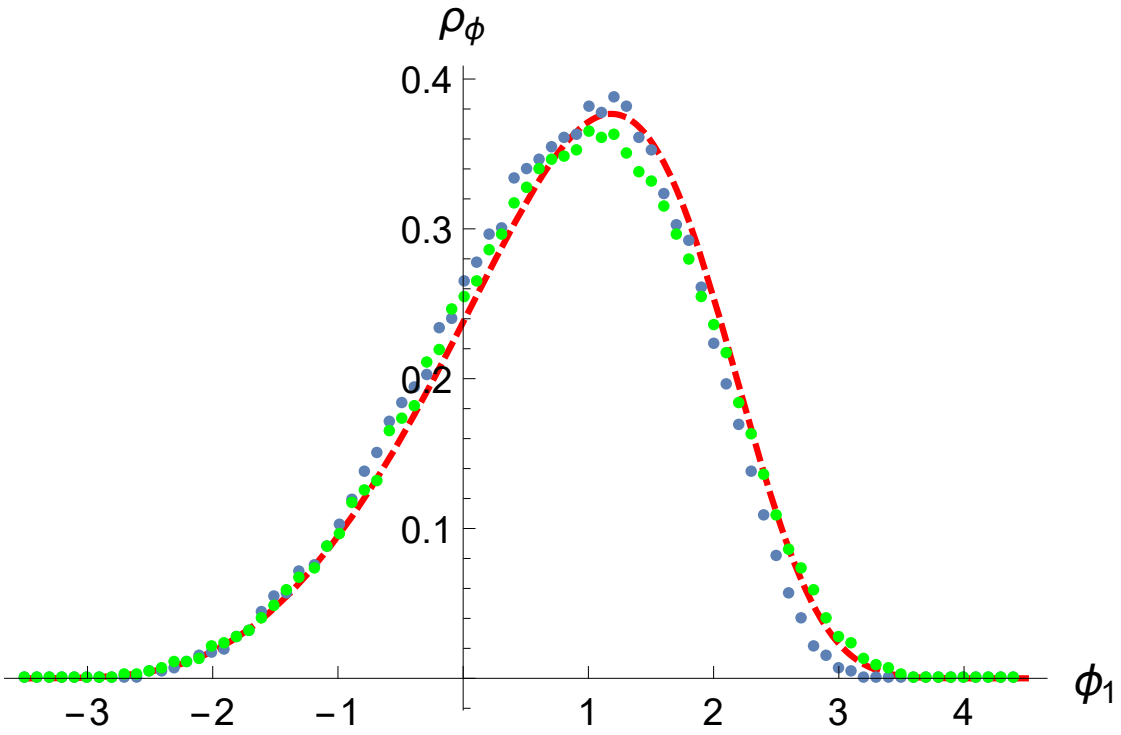

Figure B.1: Comparison between the probability distribution of the field ϕ_1 when generated with the Langevin procedure with kicks applied every time the network doubles in size $\Delta N = \log(2)$ (blue dots) as was done for the numerical simulations, distribution generated with the Langevin procedure with kicks applied twice as often $\Delta N = 0.5\log(2)$ (green dots), and the prediction from the Fokker-Planck equation (A.1) (red dashed line). We plotted for $\lambda = 0.5$ and $H_I/v_a = 3$, which is one pair of values of H_I, λ used in the simulations, see Figure 4.7.

Appendix C

Large initial radial mode displacement

The conclusions in Chapter 4 have been based on the situation when the average of the radial mode inside causal patches during inflation is close to the vacuum. Here we consider the opposite case in which the radial mode inside many causal patches during inflation takes a large value. This could happen either because the radial mode has been pushed to very large values by quantum fluctuations, or because the potential of the radial mode during inflation is modified in a way that maintains the radial mode at large values, for example by a coupling to the inflaton or scalar curvature.

Let us start with an unspecified distribution of the average value of the radial mode over the causal regions at the end of inflation that will re-enter the horizon until today. We assume only that the mean of this distribution is $r_m \gg v_a$ and that after the end of inflation the relevant radial mode potential is the one in eq. (2.29). As in Chapter 4 we replace the radial mode by $\tilde{r}$ with potential (4.9). Eventually the field $\tilde{r}$ in each of the patches at the end of inflation will lose its energy to Hubble friction and will end up in one of the minimums of the potential after passing the top of the potential a number of times. We define a set of positions r_n such that if the field in some patch started at $\tilde{r} \in (r_n, r_{n+1})$ it has passed n times over the top of the potential before relaxing to the vacuum. The point is that if the probability distribution at the end of inflation is such that there is substantial probability for the $\tilde{r}$ to be in two or more such consecutive intervals, then there would be many such patches that will settle on each side of the top of the potential. We expect this results in strings similarly to the case where quantum fluctuations push the radial mode over the top of the potential during inflation.

Therefore, if the mean of the distribution of $\tilde{r}$ at the end of inflation is $r_m \in (r_{n-1}, r_n)$ and the variance is comparable to $\min(r_m - r_{n-1}, r_n - r_m)$ strings would be expected to form. The positions r_n can be found by solving the equation of motion after the end of inflation:

$$\frac{\partial^2 \tilde{r}}{\partial t^2} + \frac{2}{t}\frac{\partial \tilde{r}}{\partial t} + \lambda \tilde{r}(\tilde{r}^2 - v_a^2) = 0\,, \tag{C.1}$$

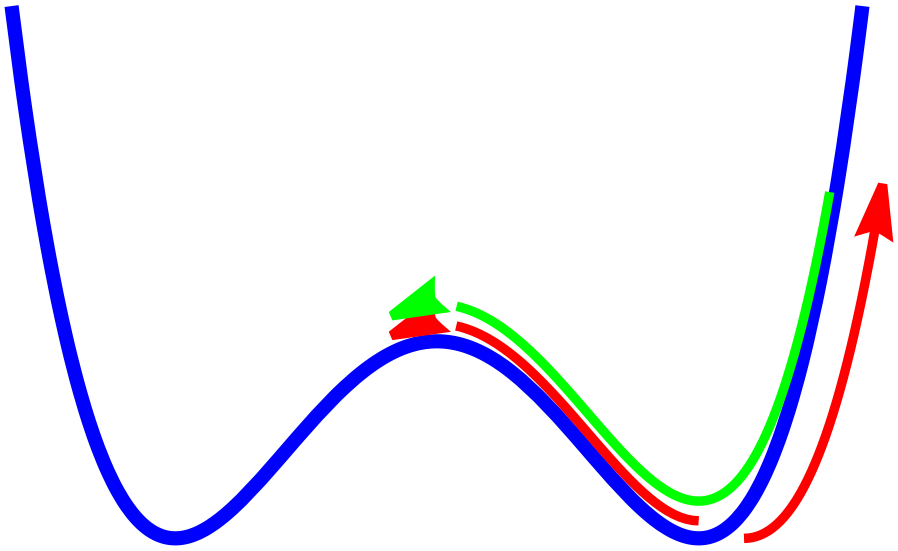

Figure C.1: Schematic representation of the second way quantum fluctuations can result in strings, which is most relevant to the situation where the value of the radial mode at the end of inflation is displaced away from the minimum. While quantum fluctuations represented by red arrows can push the radial mode over the top of the potential to produce strings, they can also result in the radial mode reaching higher potential energy than at the local maximum at $\phi = 0$ (or $\tilde{r} = 0$). When that happens the field will pass over the top of the potential after the end of inflation and during the matter domination period prior to thermalisation, represented by the green arrows. The radial mode in each causal patch will pass over the top of the potential a number of times depending on its value inside the patch. This means that calculating the probability that the radial mode passed over the top of the potential by integrating the probability distribution is not fully accurate, and for the full result one must add the contribution from regions in the field space that pass over the top of the potential an odd number of times while oscillating.

for various values initial values of $\tilde{r}$, which we did numerically using Mathematica "NDSolve" [254]. In general the positions r_n are sensitive to the coupling λ as well as the evolution of the scale factor after the end of inflation, which in the equation (C.1) above we assumed it behaves as in matter domination. We argue that the interesting situation is when the field oscillations happen during a period of matter domination before the end of reheating, since otherwise the reheating temperature exceed v_a and the PQ symmetry is already restored by thermal fluctuations as explained in Section 5.3. To see this parametrically notice that the field starts oscillating at a time when $m_r \sim \sqrt{\lambda} v_a \gtrsim H$ and if the Universe is radiation dominated at this point we can write $H \sim T^2/M_P$ so $\sqrt{\lambda} v_a M_P \sim T^2$. But $T \lesssim v_a$ if the PQ symmetry is not restored thermally, meaning $\sqrt{\lambda} M_P \lesssim v_a$, which is only possible for very small $\lambda \lesssim 10^{-16}$. Meanwhile the variance of the probability distribution can be found by solving the Fokker-Planck equation (3.33) for $\tilde{r}$ in the same way as we did in Chapter 4, but with different initial conditions. An example of the various turning points r_n can be seen in Figure C.2.

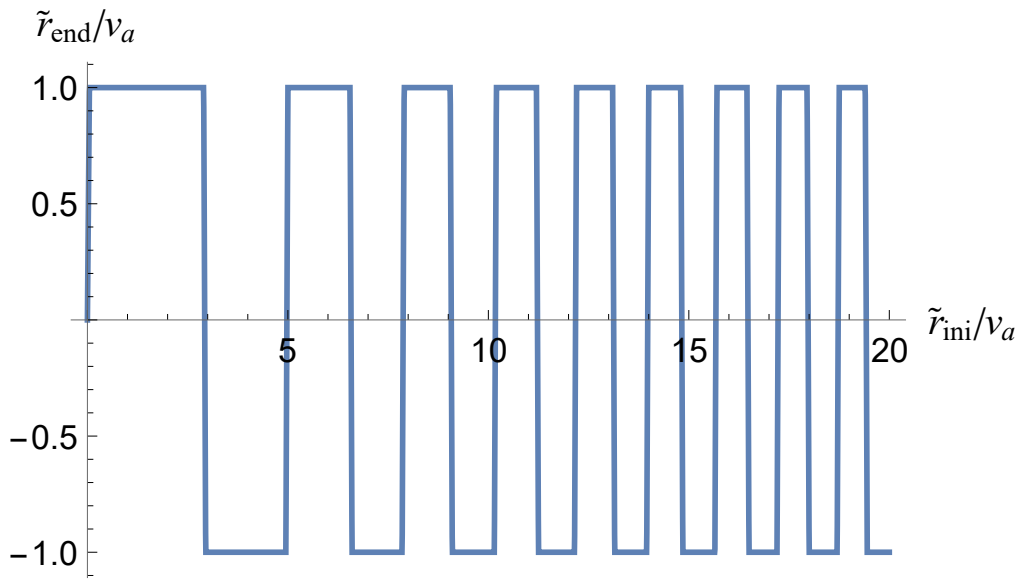

Figure C.2: The final position of the field $\tilde{r}$ as a function of the initial position $\tilde{r}_{\rm ini}$. This is found by solving (C.1) for $\lambda = 1$ and under the assumption that the field oscillates and losses its energy matter domination, which as explained is required if we want the PQ symmetry not to be restored by a large reheating temperature.

We remark that, if the reason the radial mode takes such large values is the effect quantum fluctuations alone without any modification to the potential (2.29) during inflation, then the equilibrium distribution of the radial mode must be sufficiently spread, which requires parametrically $H_I^4 \gg \lambda f_a^4$. In this case fluctuations starting from a delta function configuration initially accumulate as if the potential is negligible, i.e. the variance grows as $NH_I^2/(4\pi^2)$ with the number of e-folds. Thus variance large enough for the post-inflationary scenario is likely to be achieved regardless if the radial mode initially started close to the vacuum or at large values[1].

On the other hand if the radial mode potential is modified during inflation such that the radial mode is stuck at large values the situation is more complicated. Finding the relevant axion scenario in this case would require solving the Fokker-Planck equation (3.33) for the new potential to find the distribution at the end of inflation.

[1]This is even without taking into account potential parametric self-resonance effects that would significantly enhance the fluctuations of the PQ field when the initial displacement is large, see [89].

Appendix D

More Details on GWs from Strings

In this Appendix we give more details on the analytic derivations of Section 6.2. In particular, we will discuss the GW emission from Nambu–Goto strings in Appendix D.1 and from the whole scaling regime in Appendix D.2.

D.1 Axions and Gravitational Waves from Nambu–Goto Strings

In this Appendix we derive eq. (6.5) in detail and compute the coefficients $r_a[X]$ and $r_g[X]$, showing that they are invariant under rescaling of the string trajectory.

Eq. (6.4) can be rewritten in terms of the transverse metric fluctuation $H^{\mu\nu} \equiv h^{\mu\nu} - \frac{1}{2}\eta^{\mu\nu}h$ and reads $\partial_\alpha\partial^\alpha H^{\mu\nu} = 16\pi G T_s^{\mu\nu}$. At large distance $r \equiv |\vec{x}|$ from the region where the trajectory $\vec{X}$ is localised, eq. (6.3) and this last equation provide the axion and gravitational wave field

$$A^{\mu\nu} = \frac{f_a}{2\sqrt{2}r}\int d\sigma \left(\dot{X}^\mu X'^\nu - X'^\mu \dot{X}^\nu\right), \tag{D.1}$$

$$H^{\mu\nu} = \frac{4G\mu}{r}\int d\sigma \left(\dot{X}^\mu \dot{X}^\nu - X'^\mu X'^\nu\right), \tag{D.2}$$

where we neglected terms that decay faster than $1/r$. The right hand sides of eqs. (D.1) and (D.2) are evaluated at the retarded time $t' = t - |\vec{x} - \vec{X}|$, which at this order in $1/r$ reads $t' = t - r + \vec{X}\cdot\vec{n}$ with $\vec{n} \equiv \vec{x}/r$. Clearly eqs. (D.1) and (D.2) verify the wave relations $\partial_\alpha H^{\mu\nu} = n_\alpha \dot{H}^{\mu\nu}$ with $n^0 \equiv 1$ (so that $n^2 = 0$) up to $1/r^2$ terms. The harmonic gauge condition is rewritten as $\partial_\mu H^{\mu\nu} = 0$ which implies the relation $n_\mu \dot{H}^{\mu\nu} = 0$ for the solutions of eqs. (D.1) and (D.2).

The axion and gravitational wave energy radiated per unit time at infinity is given by $dE/dt \equiv -\int d^3x \dot{T}^{00}$, where $T^{\mu\nu}$ is the energy momentum tensor of the axion (from the second term in

eq. (6.1)) or the gravitational waves, which are respectively

$$T_a^{\mu\nu} = F^{\mu\alpha\beta}F^{\nu}{}_{\alpha\beta} - \frac{1}{6}\eta^{\mu\nu}F^{\alpha\beta\gamma}F_{\alpha\beta\gamma}, \tag{D.3}$$

$$T_g^{\mu\nu} = \frac{1}{32\pi G}\left(\partial_\mu H^{\alpha\beta}\partial_\nu H_{\alpha\beta} - \frac{1}{2}\eta^{\mu\nu}\partial_\alpha H\partial^\alpha H\right) , \tag{D.4}$$

with $H = H^\alpha_\alpha$. We can use the conservation of $T^{\mu\nu}$ and Gauss theorem to rewrite $dE/dt = \int d^3x\partial_j T^{j0} = \int d\Sigma^j T^{j0}$ where the last integral is done on the sphere at spatial infinity. So,

$$\frac{dE}{dt} = \lim_{r\to\infty} r^2 \int d\Omega\, n^j T^{j0} . \tag{D.5}$$

Plugging eqs. (D.1) and (D.2) into eqs. (D.3) and (D.4), and then plugging these in eq. (D.5), the whole (neglected) subleading dependence on $1/r$ vanishes in the limit and we obtain eq. (6.5). For instance, the coefficient for the gravitational wave emission is

$$r_g[X] = \int \frac{d\Omega}{2\pi}\left\{\left[\int d\sigma\partial_t(\dot{X}^\mu\dot{X}^\nu - X'^\mu X'^\nu)\right]^2 - \left[\frac{1}{2}\int d\sigma\partial_t(\dot{X}^2 - X'^2)\right]^2\right\} , \tag{D.6}$$

where again the right hand side is evaluated in $t' = t - r + \vec{X}\cdot\vec{n}$. A similar equation holds for the axion emission. The parameter σ can be taken to parametrise the string trajectory at a fixed time, and in this case it runs in the interval $[0, L]$ where L is the length of the string trajectory. As initially claimed, eq. (D.6) is invariant under the rescaling $t \to \alpha t$ and $L \to \alpha L$ (and $\vec{x} \to \vec{x}$). This can be easily seen by noticing that[1] $X^\mu(\alpha t, \sigma) = \alpha X^\mu(t, \sigma/\alpha)$ and making the change of variable $\sigma \to \alpha\sigma$.

Note that in the non-relativistic limit the dependence on $\vec{n}$ in t' is subleading and one can perform the angular integral in eq. (D.6) exactly. The result is the well-known quadrupole approximation

$$r_a[X] = \frac{2\pi}{3}\left[\int d\sigma\partial_t(\dot{X}^i X'^j - \dot{X}^j X'^i)\right]^2 , \tag{D.7}$$

$$r_g[X] = \frac{1}{5}\left\{\left[\int d\sigma\partial_t^3(\dot{X}^i\dot{X}^j)\right]^2 - \frac{1}{3}\left[\int d\sigma\partial_t^3(\dot{X}^i\dot{X}^i)\right]^2\right\} . \tag{D.8}$$

D.2 GW Spectrum during the Scaling Regime

In this Appendix we give more details on the derivation of the GW spectrum in eqs. (6.9) and (6.12). We perform in eq. (6.8) the change of variable $x = k'/H(t')$ with $k' \equiv kR/R'$, and use eqs. (6.6)

[1] This is because, by dimensional analysis, $X^\mu(t, \sigma)$ must be proportional to σ times a dimensionless function of all the other parameters on which X^μ depends, i.e. t/σ, L/σ and t/L, etc.. Such a function is therefore left invariant by the mentioned rescaling.

and (2.47). As a result, for $R \propto t^{1/2}$ and in the large log limit

$$\frac{\partial \rho_g}{\partial \log k}[k,t] = 8\pi^3 c_1 r G f_a^4 H^2 \int_{\max\left[x_0, \frac{k}{\sqrt{HH_1}}\right]}^{k/H} dx\, F_g[x,y] \log^4\left(x^2 \frac{m_r H}{k^2}\right) , \tag{D.9}$$

where $y \equiv m_r k^2/(Hx^2)$ and, as mentioned in Section 6.2.2, we approximated the momentum distribution to be $F_g[x,y] = 0$ for $x < x_0$. For $k < x_0\sqrt{HH_1}$, the lower extreme of the integral in eq. (D.9) is just x_0. Approximating the momentum distribution with a single power law, i.e.

$$F_g[x,y] = \begin{cases} \frac{(q-1)x_0^{q-1}}{x^q} & x \in [x_0, y] \\ 0 & x \notin [x_0, y] \end{cases} , \tag{D.10}$$

eq. (D.9) for $k < x_0\sqrt{HH_1}$ leads to

$$\frac{\partial \rho_g}{\partial \log k}[k,t] = 8\pi^3 c_1 r G f_a^4 H^2 \log^4\left(\frac{m_r}{H}\right) \left\{ \left(1 - 2\frac{\log(k/k_0)}{\log}\right)^4 - \left(\frac{k_0}{k}\right)^{q-1} + \right.$$
$$\left. + \frac{8}{(q-1)\log}\left[\left(1 - 2\frac{\log(k/k_0)}{\log}\right)^3 - \left(\frac{k_0}{k}\right)^{q-1}\right] + \frac{48}{(q-1)^2\log^2}\left[\left(1 - 2\frac{\log(k/k_0)}{\log}\right)^2 - \left(\frac{k_0}{k}\right)^{q-1}\right] + \cdots \right\}, \tag{D.11}$$

where $k_0 \equiv x_0 H$ and the dots stand for terms proportional to further inverse powers of $(q-1)\log$ (up to $(q-1)^{-4}\log^{-4}$). In the large log limit and as long as $q-1$ remains definitely larger than $1/\log$, only the first two terms in eq. (D.11) survive (see also the discussion in Section 6.2.2). The second term in eq. (D.11) is negligible for $k \gtrsim x_0 H$,[2] and the first terms indeed corresponds to the full eq. (6.9). For higher momenta, $k > x_0\sqrt{HH_1}$, the lower extreme in eq. (D.9) is $k/\sqrt{HH_1}$ and the integration gives

$$\frac{\partial \rho_g}{\partial \log k}[k,t] = 8\pi^3 c_1 r G f_a^4 H^2 \log^4\left(\frac{m_r}{H}\right) \left[\frac{x_0\sqrt{HH_1}}{k}\right]^{q-1} \left[1 - \left(\frac{H}{H_1}\right)^{\frac{q-1}{2}} + \cdots\right], \tag{D.12}$$

which gives the dependence on $1/k^{q-1}$ mentioned in Section 6.2.2 (the dots stand again for subdominant $(q-1)^{-1}\log^{-1}$ corrections).

Note that if the effective number of degrees of freedom in thermal equilibrium g is not constant, entropy conservation ($gR^3T^3 = \text{const}$) and the Friedmann equations ($H^2 = 1/(2t)^2 \propto gT^4$, valid away from particle thresholds) imply $R \propto g^{-1/12}t^{1/2}$. In this case, neglecting time derivatives of g, the same change of variable as before provides the overall factor $(g(t_k)/g(t))^{1/3}$ in eqs. (D.9), (D.11) and (D.12), plus a change in the argument of the logarithms of a factor $(g(t_k)/g(t))^{1/6}$, which is negligible. Finally, we observe that the spectrum in eq. (D.11) is has a very similar form as the

[2] This term encodes the IR profile of $\partial\rho_g/\partial\log k$, and as visible in Figure 6.5 is not well resembled by the simple assumption of a hard IR cutoff for $F_g[x,y]$.

axion spectrum in Appendix E.1 of [188], with however two more powers of log since $\Gamma_g/\Gamma_a \propto \log^2$ at large log.

From the end of the scaling regime (when $H = H_\star$) to today the GWs redshifts freely, i.e. $\frac{d\rho_g}{d\log k}[t_0, k] = (R_\star/R_0)^4 \frac{d\rho_g}{d\log k}[t_\star, kR_\star/R_0]$. From eq. (6.9) and conservation of entropy density, we get the spectrum today in the $\log \gg 1$ limit

$$\frac{d\Omega_{\rm gw}}{d\log k} = \frac{c_1 \pi^4 r f_a^4}{90 M_{\rm P}^4} \frac{g_0 T_0^4}{\rho_c} \left(\frac{g_0}{g_k}\right)^{1/3} \log^4 \left[\frac{\pi x_0^2 g_0^{2/3} m_r T_0^2}{3\sqrt{10} g_\star (T_\star)^{5/6} M_{\rm P} k^2}\right], \tag{D.13}$$

where T_0 and g_0 are the temperature of photons and the effective number of relativistic degrees of freedom today, and g_k is the effective number of relativistic degrees of freedom at time t_k, defined by $x_0 H(t_k) \equiv kR(t)/R(t_k)$, which is the time when most of the GWs that have momentum k at time t are emitted. Eq. (6.12) is the numerical evaluation of eq. (D.13) and is valid in the momentum range $x_0 H_\star (R_\star/R_0) < k < x_0 \sqrt{H_\star H_1}(R_\star/R_0)$. Although eq. (D.13) is a very good approximation of the spectrum at large log, as mentioned in Section 6.2.4 to obtain the lines in Figure 6.6 we integrated numerically eq. (6.8), accounting for the smooth change in g and using a double power-law form for $F_g[x]$ (this resembles well the simulation results of Figure 6.5). In particular we used $F_g[x] \propto x^3$ for $x \lesssim x_0$ and $F_g[x] \propto 1/x^2$ for $x \gtrsim x_0$, as in eq. (38) of [186] with $x_2 \to \infty$.

Appendix E

Details of Simulations

In Chapter 4 numerical simulations were used to explore underdense string networks, while in Chapter 6 they were used to explore gravitational waves emissions of scaling string networks. In this Appendix we give more detail about these simulations.

Both the simulations in Chapters 4 and 6 proceed in two phases. Phase one is the generation of initial conditions, which is responsible for producing a field configuration for the two components ϕ_1, ϕ_2 of the complex PQ field ϕ, which are defined as:

$$\phi = \frac{1}{\sqrt{2}}(\phi_1 + i\phi_2)\,. \tag{E.1}$$

This phase is different whether we are interested in studying underdense networks or scaling networks. For underdense networks I have implemented a procedure that mimics the evolution of the fields ϕ_1, ϕ_2 during inflation, which is formally described by the Langevin equation (3.19). This procedure was introduced in Section 4.4. For the scaling networks my collaborators have implemented a different procedure to generate initial conditions, which has the purpose of reaching the scaling solution as quickly as possible. This procedure is best described later, after we first consider the second phase which is simulating the formation and the evolution of the strings.

The second phase is that of the evolution of strings, starting from the respective initial conditions for the components of the PQ field. This phase is nearly identical between simulations considering underdense and scaling networks, with the exception of the calculation of the gravitational waves emissions and of the backreaction of gravitational waves for the scaling networks, as well as the choice of the time step in the evolution of the equations of motion, all of which we discuss bellow. The code that performs this phase was written by my collaborators, Dr Marco Gorghetto and Dr Edward Hardy and it has been previously used to obtain the results in their papers [186, 188]. The code was written in C++ and makes use of the fftw library [362] for Fourier transforms. It runs in parallel on multiple cluster nodes using OpenMP [363] and Open MPI [364] for the parallelisation. To perform the simulations presented in Chapter 6 we have used the Marconi Skylake partition,

for which we thank the collaboration between both SISSA and CINECA, and ICTP and CINECA; the Ulysses HPC Linux Cluster, for which we thank SISSA and ICTP; as well as the University of Liverpool Barkla HPC cluster. Simulations presented in Chapter 4 have used the University of Liverpool Barkla HPC cluster exclusively.

The second phase involves evolving the equations of motion resulting from the Lagrangian in (2.28, 2.29). It is most convenient to work with the re-scaled PQ field defined as $\psi = R(t)\phi/v_a$ and conformal time defined as:

$$\tau(t) = \int_0^t \frac{dt'}{R(t')} \,. \tag{E.2}$$

We also write the equation of motion in terms of dimensionless time and distance variables, which are $m_r\tau$ and $m_r x$ respectively, where m_r is the mass of the radial mode. Assuming radiation domination in a spatially flat background, the equation motion is then:

$$\psi'' - \nabla_x^2\psi + u(\tau)\psi\left(|\psi|^2 - \frac{R^2}{2}\right) = 0\,, \tag{E.3}$$

where prime denotes differentiation with respect to the dimensionless time and ∇_x with respect to dimensionless distance as defined above, and $u(\tau)$ is a function that depends on the model, either physical strings $u(\tau) = 1$ or fat strings $u(\tau) = \tau_{\rm ini}/\tau$, where $\tau_{\rm ini}$ is the conformal time at the start of the phase of the evolution of strings. We also set $\lambda = 1$ for the physical strings model or $\lambda_{\rm ini} = 1$ at the start of the phase of the evolution of strings in the case of the fat string model. The fat string model involves replacing the constant mass of the radial mode m_r with a time dependant mass:

$$m_r(\tau) = m_{\rm r,ini}\frac{R_{\rm ini}}{R(\tau)} = m_{\rm r,ini}\frac{\tau_{\rm ini}}{\tau} \,. \tag{E.4}$$

This has two advantages: 1) it takes a longer physical time for the maximum log to be reached, and 2) the string core scale changes with time at the same rate as the momentum redshifts, which means that axion waves emitted at the string core scale remain in the UV part of the spectrum (this leads to a cleaner spectrum in the physically relevant region $k < m_r/2$, as discussed in [188]).

We discretise the space on a three dimensional cubic lattice containing $N_{\rm grid}^3$ uniformly distributed grid points (so $N_{\rm grid}$ points on each side) with periodic boundary condition. For the results presented in Chapter 6 the grid size was set to $N_{\rm grid} = 2500$ points. Meanwhile for the simulations presented in Chapter 4 the grid size was required to be a power of two due to the way we generated initial conditions as explained in Section 4.4, and it was thus set to $N_{\rm grid} = 2048$ points. In both cases the maximum number of grid points was limited by the available memory.

We then numerically integrate the equation of motion (E.3) following a standard central-difference Leapfrog algorithm for wave-like PDEs [365], discretising the time in equal intervals of dimensionless conformal time $m_r\Delta\tau$. Meanwhile the physical distance between grid points $\Delta(\tau)$ grows with time as $\Delta(\tau) = \Delta(\tau_{\rm ini})\ \tau/\tau_{\rm ini} = \Delta(\tau_{\rm ini})\sqrt{H_{\rm ini}/H}$ given that we assume radiation

domination and where $H_{\rm ini}$ denotes the Hubble at the start of the phase of evolution of strings. To ensure convergence of the algorithm a maximum ratio between the size of the time step and distance between grid points is allowed. A necessary condition is the Courant–Friedrichs–Lewy condition [366] $\Delta\tau/\Delta(\tau_{\rm ini}) < 1$, however for a sufficient condition a numerical analysis has to be performed. For the case of scaling networks studied in Chapter 6 a sufficient condition has been found to be $\Delta\tau/\Delta(\tau_{\rm ini}) \lesssim 1/3$ in [186] (for more detail see Appendix B.2 and Figure 16 of this reference), and we subsequently set the time step size to $\Delta\tau = \Delta(\tau_{\rm ini})/3$. Meanwhile, for the different initial conditions that result in the underdense networks studied in Chapter 4 we have found that convergence of the algorithm requires a stronger condition $\Delta\tau/\Delta(\tau_{\rm ini}) \lesssim 1/6$, see Section E.1 and Figure E.4.

It is essential that systematic uncertainties from simulations are under control if their results are to be reliable. The most important sources of systematic errors come from the lattice spacing $m_r\Delta(\tau)$, the time spacing $\Delta\tau$ and the number of Hubble lengths in a box HL, where $L = N_{\rm grid}\Delta(\tau)$ is the physical box length. We discuss these in further detail in Section E.1 bellow.

In order to calculate the string density inside the simulation it is important to have a procedure to identify strings. We do so by adopting the algorithm proposed in the Appendices of [182] involving counting plaquettes that are pierced by a string, which are those around which the value of the complex field crosses the real axis twice with the same handedness. This allows us to flag grid points that are close to the string cores, the number of which is related to the string length which can be computed by using a statistical correction factor, under the assumption that strings are equally distributed in all directions. This algorithm has also been implemented by my collaborators.

Now that we have explained the phase of the simulations that follows the evolution of strings we can also discuss the procedure to generate initial conditions that reach scaling as quickly as possible, in order to show the properties of the scaling regime as clearly and accurately as possible. To achieve this, we start with random initial conditions and follow the evolution of the network as explained above until the string length inside the box is close to some fixed string length to within a 10% tolerance. We use the resulting configuration as the initial condition for the phase of the evolution of strings after resetting the value of the Hubble parameter and the size of the box. The desired string length at which the generation of initial conditions stops is chosen such that the initial string density at the start of the phase of strings evolution is small, $\xi_{\rm ini} = 0.01$. For the fat string system the second phase of the simulation, that of formation and evolution of strings, starts at $\log(m_r(t_{\rm ini})/H_{\rm ini}) = 0$, while for the physical string system the results have been found to be cleaner for $\log(m_r/H_{\rm ini}) = 2$. Additional details as well as extensive further discussion can be found in [186, 188].

We calculate the GWs emission following the method developed in [367], to which we refer for the details. In this approach, six independent fields u_{ij}, with $u_{ij} = u_{ji}$, are evolved according to eq. (6.10), but sourced by the total energy momentum tensor (rather than its TT part). The

Fourier Transform (FT) of the GW field, $h_{ij}(t,\vec{k})$, is then obtained by projecting the FT of u_{ij} as

$$h_{ij}(t,\vec{k}) = \left(P_{il}(\hat{k})P_{jm}(\hat{k}) - \frac{1}{2}P_{ij}(\hat{k})P_{lm}(\hat{k})\right) u_{lm}(t,\vec{k}) \ , \tag{E.5}$$

where $P_{lm}(\hat{k}) \equiv \delta_{ij} - k_i k_j/|\vec{k}|^2$ (it is indeed easy to see that h_{ij} solves eq. (6.10) if and only if u_{ij} solves the same equation sourced by the total energy momentum tensor).[1] This procedure avoids the need to obtain the TT part of the energy momentum tensor at every simulation timestep, which greatly reduces the computational cost. Instead FTs are only required at particular timeshots when the h_{ij} are needed to evaluate the GW energy and spectrum. We use the same approach when evaluating the GW emission at the time of the axion mass turn on in axion only simulations, as studied in Appendix G, simply by substituting the appropriate energy momentum tensor.

As mentioned in Section 6.2.3, numerical simulations including the GW backreaction (analysed in Appendix F.2) require that eq. (E.3) is evolved with the additional term $R^{-2}h_{ij}\partial_i\partial_j\phi$ on the left hand side, and thus the expression of h_{ij} needs to be known at every timestep. For such simulations we calculate h_{ij} from u_{ij} via eq. (E.5) at all time steps (by carrying out all of the required FTs and anti-FTs). Given the computational cost, we limit ourselves to grids of size 800^3 for this analysis, which allows $\log \simeq 6$ to be reached. Such a log is sufficient for the system to be in scaling and emitting axions with a momentum distribution with a gap between the IR peak and UV scale for an interval $\Delta \log \simeq 2$, enough to extract the time-dependence of the relevant physical observables. For our main simulations, which are much less computationally demanding, we use larger grids, with 2500^3 lattice points.

E.1 Analysis of Systematics

In [186, 188] it was shown that $HL \geq 1.5$ and $m_r\Delta \geq 1$ are accurate for ξ and most observables relevant to the axion emission in the scalling regime. Here we will show that the same values of HL and Δ are accurate for the GW observables of interest as well, and we therefore use these for our main simulations. We fix the time step to be $\Delta\tau = \Delta(\tau)/3$ where $\Delta\tau$, Δ are the comoving time and space steps respectively, which is small enough to introduce a negligible error in all quantities for the scalling network as discussed in [186].

In particular, we analyse the effect of $m_r\Delta$ and HL on two of the most important observables: the fraction of energy going into GWs, defined by $r_{\rm sim}$, and the instantaneous GW emission spectrum, F_g. The latter is more sensitive to finite box size systematics than the total GW spectrum, which, even at the end of simulations when HL is small, includes emission from earlier times when HL was larger. In combination with the analysis of the effects on the axion observables described in [188], this assures us that the effects of systematics on the results in the main text are negligible.

[1] See [368] for an analysis demonstrating that the lattice version of the projector does not introduce systematic errors.

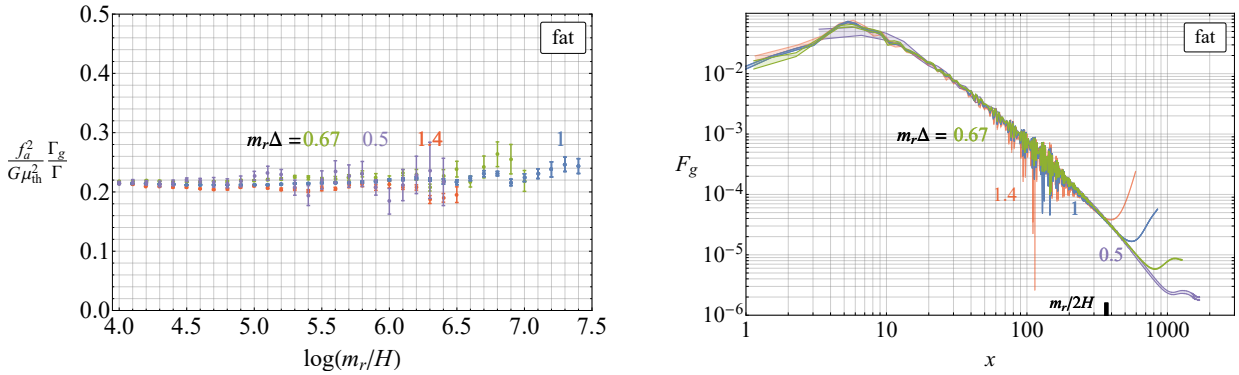

Figure E.1: The dependence on the lattice spacing $m_r\Delta$ of the energy emission rate into GWs (left), and of the GW instantaneous emission spectrum, plotted at log = 5.4 (right). Data is shown for $m_r\Delta = 1$ (blue) which was used for the main simulations, and also for finer lattices with $m_r\Delta = 0.67$ (green) and $m_r\Delta = 0.5$ (purple), as well as a less fine lattice with $m_r\Delta = 1.4$ (orange). The agreement between these data sets indicates that $m_r\Delta = 1$ does not introduce significant systematic uncertainties (in particular, they are smaller than the statistical fluctuations in our main data set, while networks with lower resolution than the main simulations still give similar results). For this test we have used averaged over 10 simulation runs that differ only in the random seed used to generate initial conditions. We have used smaller grids i.e. $N_{\rm grid} = 1500$ for the green data and $N_{\rm grid} = 1024$ for the orange and purple data. We performed this test for the fat string system since in this case the resolution of the strings $m_r\Delta$ remains constant during the simulation. For the physical system however the resolution decreases (i.e. $m_r\Delta$ increases) during the simulation, so setting the final resolution for the physical system to be the same as the one in the fat system can only result in finer resolution throughout the simulation.

In Figure E.1 we plot $r_{\rm sim} \equiv f_a^2\Gamma_g/(G\mu_{\rm th}^2\Gamma)$ and F_g for $m_r\Delta = 1$, for the finer lattice spacing $m_r\Delta = 2/3$ and $m_r\Delta = 1/2$, as well as a less fine lattice spacing $m_r\Delta = 1.4$, all for the fat string system (the results are averaged over 10 simulations). The only deviations between $r_{\rm sim}$ the data sets are small statistical fluctuations at late times (when the number of independent Hubble patches is indeed smallest), and the form of F_g is consistent in all cases (as for the axion instantaneous spectrum F_a, a finer lattice spacing reduces the energy going into modes with momentum $k > m_r$, however it has no effect on the part of F_g from which we extract the spectral index q).

Similarly, in Figure E.2 we study the HL systematics. To do so we carried out a set of simulations on small grids, of size 800^3, with smaller value of HL (but with otherwise identical properties as the main simulations, e.g. identical initial string density and also with $m_r\Delta = 1$). At a log such that $HL \simeq 1$ on the small grids, HL is safely $\gg 1$ on the large grid, enabling the finite volume effects to be easily identified. From Figure E.2 it is clear that $HL \gtrsim 1.5$ has no visible effect on the result for $r_{\rm sim}$. For smaller values of HL, the IR part of F_g starts being distorted, but the momentum range of interest for extracting the spectral index q (i.e. $k/H \gtrsim 10$) is unchanged.

For the scaling networks the maximum time $\log(m_r/H)$ for which the simulation lasts is limited

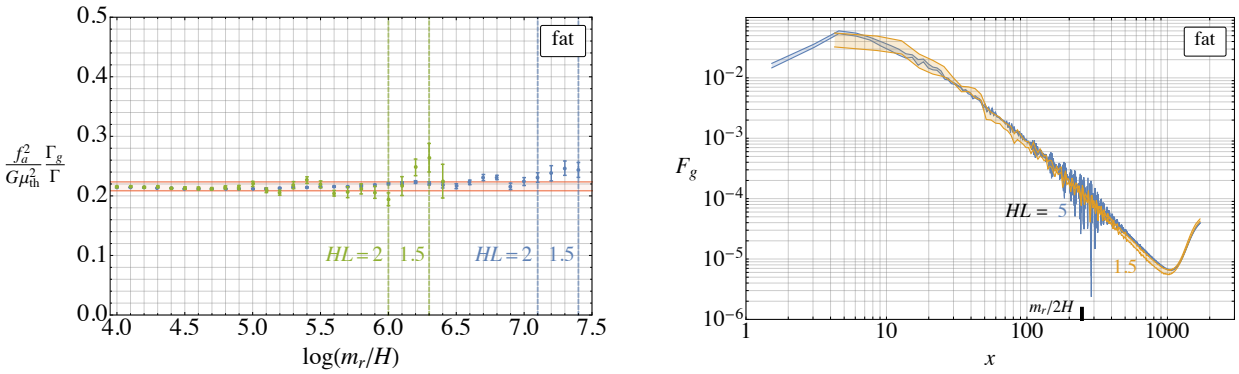

Figure E.2: The effect of the finite box size L on the fraction of energy going into GWs, left, and the normalised GW instantaneous emission spectrum (plotted at log = 6.2), right. The two data sets are from simulations on different sized grids. The smaller grids reach $HL \simeq 1$ earlier, when there are many Hubble patches left in the larger simulations. The agreement between these two data sets up to when the smaller grid has $HL = 1.5$ indicates that $HL \geq 1.5$ does not lead to large systematic uncertainties in these quantities. This Figure was produced by my collaborators for our joint work [1].

by two requirement: that systematic errors from the finite lattice resolution as well as finite box size are not too large. The former requires that there is at least order one lattice point per string core in order to resolve the string $m_r\Delta(t) \lesssim \mathcal{O}(1)$ as seen in Figure E.1, while the latter translates into a lower bound on $N_{\rm grid}\Delta(t)H \gtrsim 1.5 \div 2$ as seen in Figure E.2, i.e. there are at least some minimum number of causal patches inside the simulation box at any time. In the case of underdense networks however there is an additional requirement that the statistical errors towards the end of the simulation are not too large. In more detail, since we selected initial conditions specifically to keep networks underdense, a side effect is that there are few (if any) simulations containing strings sufficiently long to be larger than the size of the horizon by the time when finite size systematic errors mentioned above become relevant. In principle such issue could be resolved by averaging over a large number of simulations, however in practice it would take a very long amount of time to gather sufficient simulations for each pair of parameters $(H_I/v_a, \lambda)$ that we represent in Figure 4.7 to have reasonable statistical errors all the way up to the time when finite size systematic errors become relevant. Instead for each pair $(H_I/v_a, \lambda)$ we averaged for a number of 4 simulations which differ only in the random seed used to generate the initial conditions. Then we directly inspect the results of the numerical simulations averaging ξ over these outputs for each pair of parameters. We cut the points where there is a large jump in the size of statistical errors, see Figure E.3 for an example. Sometimes, but not always, this large jump directly corresponds to the moment when ξ starts decreasing, which is an indication that there are no more strings longer than the horizon inside any of the simulation boxes that we average over. Then for pairs of parameter where only a small number of points remain uncut we add additional simulations to gather more data, until

a satisfactory number of good data points (we choose 6 points minimum to plot) is left and we plot those in Figure 4.7. We stopped at a maximum number of 20 simulations for a given pair $(H_I/v_a, \lambda)$, and for this reason we did not plot result of simulations with $H_I/v_a < 1.78$ in Figure 4.7.

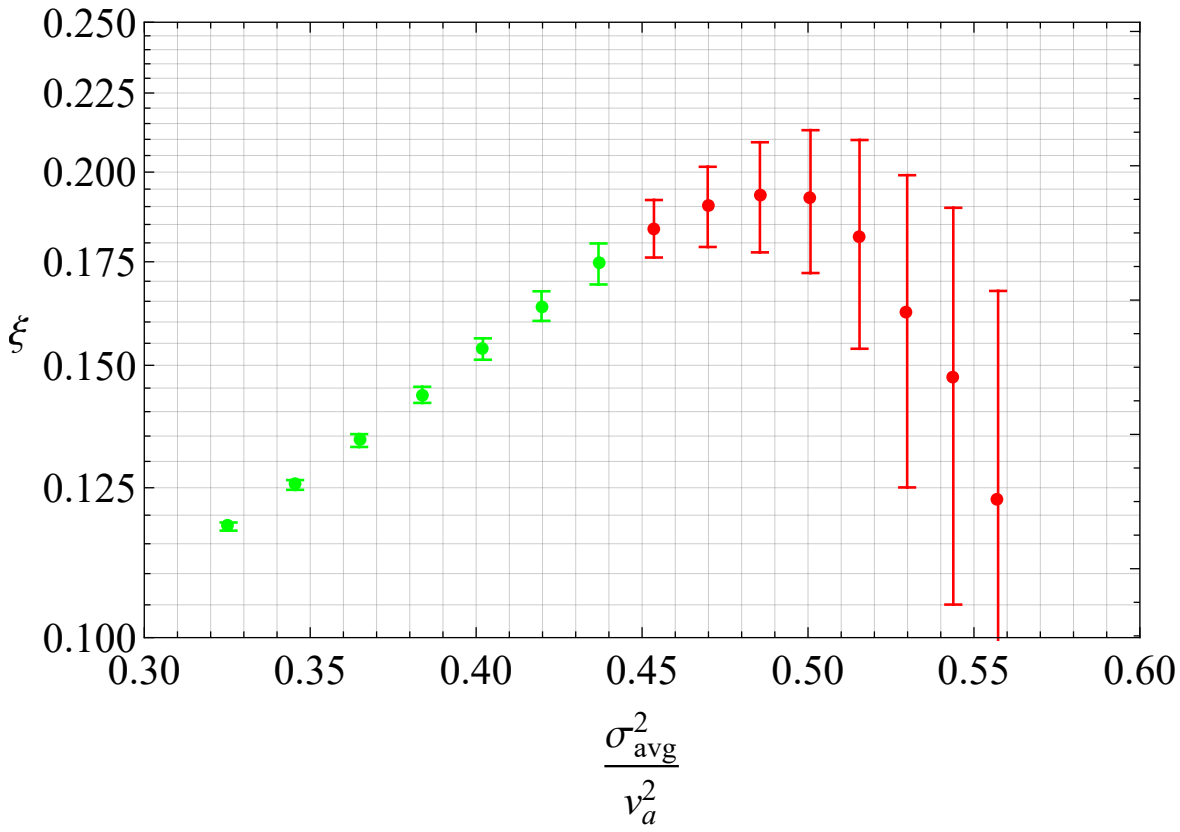

Figure E.3: The string density of an underdense network as a function of the average variance of the distribution of the radial mode over regions the size of the horizon. Initial conditions were generated by the procedure introduced in Section 4.4, which mimics the evolution of the Langevin equation (3.19), for $H_I/v_a = 2.55$, $\lambda = 0.25$. The red data points have been cut due to large statistical errors, which appear because toward the end of the simulations only few, if any of the underdense networks still contain a string longer than the size of the horizon (this is also visible by the drop of ξ over the final few data points). For each pair of parameters $H_I/v_a, \lambda$ we have cut the data by directly inspecting when the statistical errors have a large jump.

In the case of underdense networks the generation of initial conditions also results in more dramatic differences between the field at neighbouring grid points, which as a result requires a smaller time step for the algorithm to converge. To find the size of the time step we perform simulations of underdense networks with identical initial conditions (i.e. same random seed), but different ratios of $\Delta\tau/\Delta(\tau_{\rm ini})$ in the second phase of evolution of strings. We show results in Figure E.4, which points to the time step used to obtain the result in Chapter 4, i.e. $\Delta\tau = \Delta(\tau_{\rm ini})/6$,

being sufficiently small for the systematic errors to be bellow 1%.

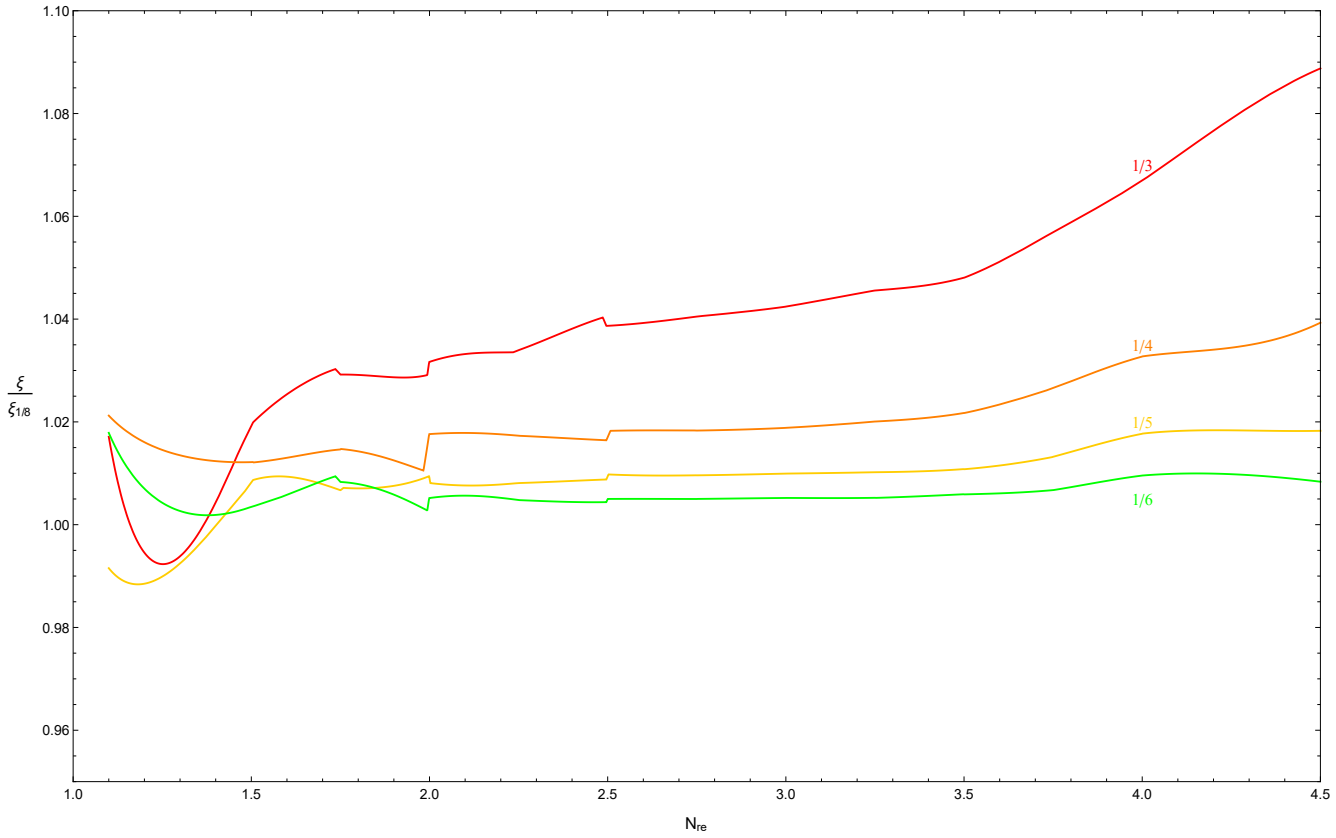

Figure E.4: The string density of underdense network as a function of the number of e-folds which re-entered the horizon for various ratios of $\Delta\tau/\Delta(\tau_{\rm ini})$, normalised by dividing by the density for the smallest ratio simulated $\Delta\tau/\Delta(\tau_{\rm ini}) = 1/8$. It can be seen that for $\Delta\tau/\Delta(\tau_{\rm ini}) = 1/6$ the errors are bellow 1%, which is the value we have set for simulations of underdense networks. For each ratio $\Delta\tau/\Delta(\tau_{\rm ini})$ we have averaged over a set 20 simulations on smaller grids of size $N_{\rm grid} = 512$, and use the same random seeds to generate initial conditions over all ratios $\Delta\tau/\Delta(\tau_{\rm ini})$.

Additionally let us discuss potential systematic errors introduced by the lattice spacing in the case of underdense networks. One would expect that the required strings resolution in this case should not be different than that in the case of scaling network, however this is difficult to test exactly due to the fact that different lattice spacing result in different sizes of fluctuations inside the string cores at early times when $m_r \simeq H$. We show in Figure E.5 the evolution of strings in simulations with identical H_I/v_a and λ but with different lattice spacing $m_r\Delta \in \{0.5, 1, 2\}$ respectively. It can be seen that the errors for the lattice spacing $m_r\Delta = 1$ that we used in the main simulations are not very large, about 10% when compared to the highest resolution. Unfortunately even higher resolution would be difficult to test for available grid sizes, since that would result in finite volume systematic errors due to the lower number of Hubble patches inside the simulation. We also point out that the higher resolution also results in larger fluctuations

inside the string core at the start of the simulation, which is similar to the situation with large values of H_I/v_a where we have found that the subsequent evolution suffers from systematic error, as discussed in Section E.2 bellow. It is possible that the difference we see between the evolution for $m_r\Delta = 1$ and the higher resolution $m_r\Delta = 0.5$ is partially (or totally) due to this effect.

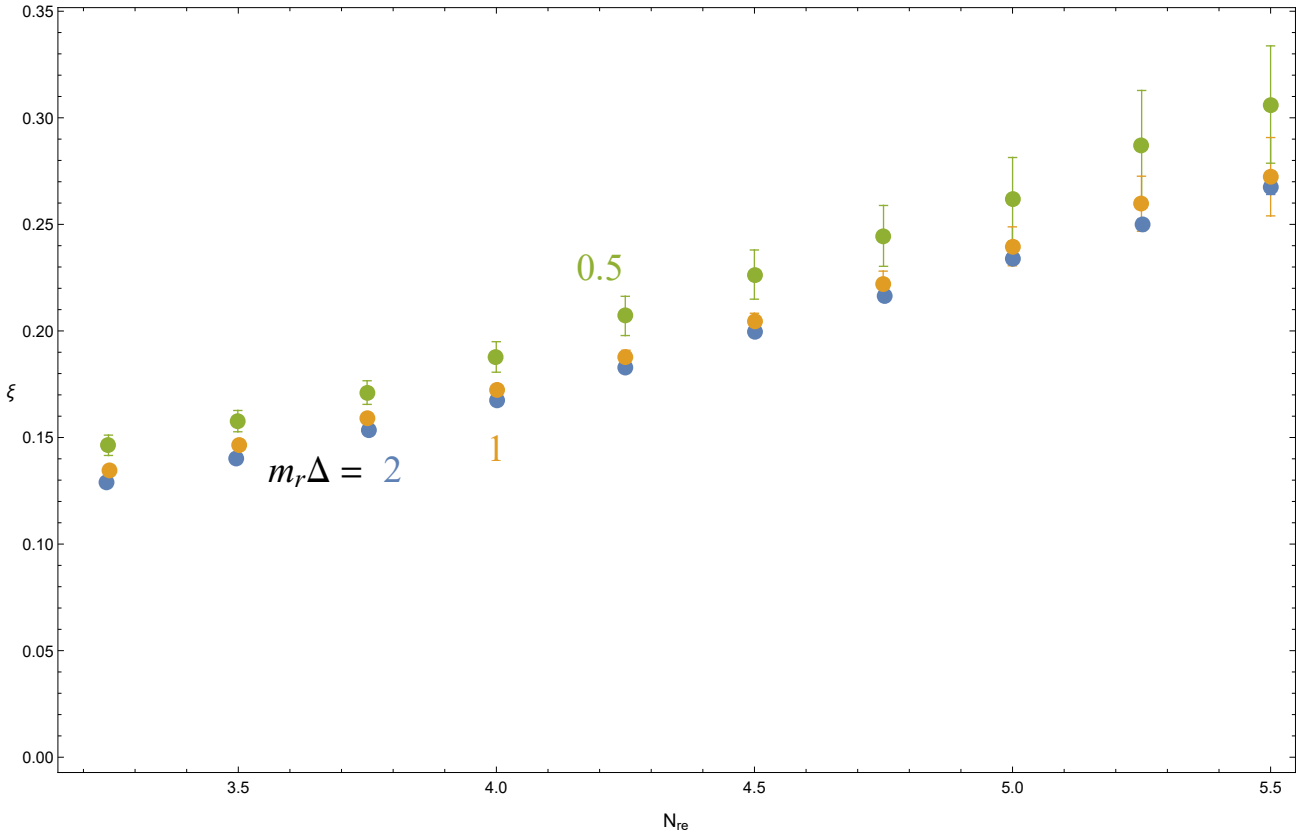

Figure E.5: Evolution of the string density ξ as a function of the number of e-folds which re-entered the horizon for various lattice spacing. Orange data points correspond to one grid point per string core, which is the resolution we have used for the main simulations, while blue and green points correspond to lower and higher resolution respectively. For each lattice spacing we have averaged over 10 simulation with the same $H_I/v_a = 3.2$ and $\lambda = 0.25$ with grid size $N_{\text{grid}} = 1024$.

E.2 Initial conditions with large H_I

Simulations that we have represented in Figure 4.7 of Chapter 4 have in common that they remain well in the underdense regime for the time window being simulated. The reason is that we are interested in obtaining a way to describe the evolution of the network towards scaling without having to worry about additional complications introduced by the interactions between strings as the network becomes dense. However, we run into complications if we wish to perform simulations with the same way to generate initial conditions, i.e. by evolving a discretised Langevin equation,

but with a larger H_I. The issue is that if we increase the value of H_I above some threshold depending on λ, the subsequent growth of ξ is slower than it is for lower H_I, which makes no sense physically.

We suspect that the reason for this behaviour is that for large H_I the fluctuations between neighbouring grid points, which at early times are inside (or close to) the string cores since, $m_r = H$ at the start of the simulation. To solve this we have employed a trick of "skipping" the kicks, i.e. in the final few e-folds of generating the initial conditions we only expand the grid, without modifying the values of the field at each grid point by a random kick. With this change the behaviour of simulations approaching the scaling regime is more in line with expectation, in the sense that the growth of ξ is again faster for larger H_I. We used this trick to obtain the black line labeled "scaling" in Figure 4.8, which corresponds to $H_I/v_a = 16.9$. The asymptotic behaviour of scaling simulations obtained with this procedure also matches the one observed in [186, 188] quantitatively, which is evidence that our "skipping" trick works as intended.

Appendix F

Further Results from Simulations

In this Appendix we provide further results from the numerical simulations of the string system. In particular, in Appendix F.1 we give more details on the scaling regime and the emission of radiation from long stings. In Appendix F.2 we discuss the effect of the backreaction of the GWs on the string network. In Appendix F.3 and F.4 we describe the end of the scaling regime for a temperature-independent mass and the power spectrum of axion overdensities after the string network is destroyed. Finally in Appendix F.5 we show the distribution of loop lengths for an underdense network resulting from initial condition as explained in Section 4.4 and compare to that for a scaling network.

F.1 The Scaling Regime

In Figure F.1 we show the evolution of the number of strings per Hubble volume ξ, where the logarithmic increase mentioned in Section 2.4.3 is evident. The black points correspond to the simulations used in this work, while for comparison we also show data from [186,188] starting from different initial conditions and reaching larger log.[1] As discussed in [186, 188], the data clearly rules out any behaviour that saturates soon after log = 8. Moreover, for the most overdense initial conditions, ξ first drops and then starts rising again, suggesting that the logarithmic growth is not a transient but a part of the attractor solution.

As shown in [186], the logarithmic growth affects both long strings (defined to be the strings with length much larger than H^{-1}) and loops (which are all the other strings). In particular, ξ restricted only to long strings – which we call ξ_L – is at any time during the scaling regime a fixed fraction of ξ, i.e. $\xi_L = f_L\xi$ with $f_L \simeq 0.814$ for the fat string system (this can be extracted from the jump of the cumulative distribution of ξ in Figure 4 of [186]; this jump makes the distinction between long strings and loops sharp). As a result, the fraction of strings in loops is also constant.

[1] As mentioned, in our present simulations, evolving the fields u_{ij} adds to the computational cost, so to gain sufficient statistics we use slightly smaller grids.

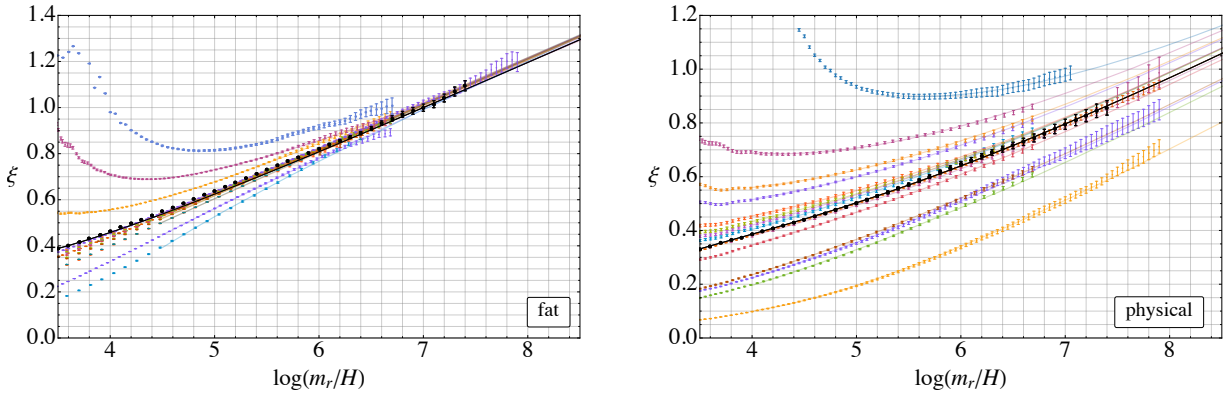

Figure F.1: The number of strings per Hubble volume ξ for the fat (left) and physical (right) string systems. The initial conditions that we use for the GW analysis, starting close to the attractor, are plotted in black. The evolution of the system starting from other initial conditions (studied in [186, 188]) is shown for comparison. This Figure was produced by my collaborators for our joint work [1].

The fact that the proportion of length in long strings and loops remains the same provides another convincing evidence that the logarithmic growth is a property of the scaling solution.

Energy Emission Rate and Long Strings

As mentioned in Section 2.4.3, in order to maintain the scaling regime the energy that needs to be released from the string system is $\Gamma = \dot{\rho}_s^{\rm free} - \dot{\rho}_s$. We derived such a quantity in eq. (2.53) assuming that $\rho_s^{\rm free} \propto R^{-2}$ (see [186] for the details). However, this derivation, strictly speaking, applies only to the part of the string network whose energy decreases proportionally to R^{-2} in the free limit, which are only the long strings.[2] For the sake of a completely consistent treatment, we therefore split the energy density in strings as $\rho_s = \rho_s^L + \rho_s^{\rm loops}$, where $\rho_s^L = \xi_L \mu_L / t^2$ is the energy in long strings and $\rho_s^{\rm loops}$ the energy in loops. The tension of long strings μ_L is expected to take the form $\mu_{\rm th}$ in eq. (2.49) during the scaling regime. The total energy lost by long strings, $\Gamma = \dot{\rho}_{\rm free} - \dot{\rho}_s^L$, is then correctly given by eq. (2.53) but with ξ substituted with ξ_L, i.e.

$$\Gamma = \frac{\xi_L \mu_{\rm th}}{t^2} \left[2H - \frac{\dot{\xi}}{\xi} - \frac{\pi f_a^2}{\mu_{\rm th}} \left(H + \frac{\dot{\eta}}{\eta} - \frac{1}{2}\frac{\dot{\xi}}{\xi} \right) \right] , \tag{F.1}$$

where for convention we evaluate $\mu_{\rm th}$ with ξ (rather than ξ_L: the difference is a constant reabsorbed in η) and in the square bracket we can use ξ instead of ξ_L given that they are proportional.

The energy Γ lost by long strings is either directly converted into axion and radial mode radiation ($\Gamma^{\rm rad}$), or lost by the formation of string loops ($\Gamma^{\rm loops}$), which continually arise from the intersection

[2] Sub-horizon loops redshift as non-relativistic matter in the free limit.

of long strings and then decay into radiation. Therefore $\Gamma = \Gamma^{\rm rad} + \Gamma^{\rm loops}$. The total emission rate into axions and radial modes $\Gamma_a + \Gamma_r$ from the network is the sum of the energy emitted into radiation directly from long strings ($\Gamma^{\rm rad}$) and the one from loops. If such loops decay into radiation efficiently, this last quantity also equals the energy lost by long strings by the formation of loops, $\Gamma^{\rm loops}$. As a result, we expect $\Gamma = \Gamma_a + \Gamma_r$. In the following we will show that numerical simulations reproduce this expectation remarkably well.

We stress that in this picture the energy emitted into radiation $\Gamma_a + \Gamma_r$ originally comes from long strings. However a part of it comes *directly* from long strings ($\Gamma^{\rm rad}$), and the other *via* loops that decay ($\Gamma^{\rm loops}$), which thus act as an efficient mean dissipation of the energy that is originally in long strings. So, although fixed by Γ in eq. (F.1), the eventual emission into axions happens through both long strings and loops, which is why in Section 6.2.1 we studied a *generic* trajectory, which includes long strings and loops. Similarly, the total emission into GWs, which for a trajectory with a fixed shape is proportional to the one into axions (see Section 6.2.1), depends on both long strings and loops, but we will refer to Γ_g as the sum of the two (Γ_g will have a contribution from long strings and another from loops, which we will not distinguish, as we cannot distinguish them in simulations). In the following, by proving that $\Gamma = \Gamma_a + \Gamma_r$, we will see that this picture agrees with the evolution of the physical system at least at small log. We will comment on the possible changes of this picture if the energy is not emitted efficiently from the decay of loops at large log.

Similarly to [186,188], during the evolution of the field we extract the energy densities in axions ρ_a and radial modes ρ_r (that are present at a generic time) from the kinetic energies $\langle \dot{a}^2 \rangle$ and $\langle \dot{r}^2 \rangle$, where the averages are done over spatial points away from the string cores (to avoid the contribution from the strings). The emission rates are then calculated as the time variation of these energies, namely $\Gamma_a = R^{-4} \frac{d}{dt}(R^4 \rho_a)$ and $\Gamma_r = R^{-z} \frac{d}{dt}(R^z \rho_r)$ where $z = 4$ for the fat strings.[3] For the physical system the redshift factor is $3 < z < 4$, and can be calculated as $\int dk z[k/m_r] \partial \rho_r / \partial k$ where $z[k/m_r] \equiv 3 + (k/m_r)^2/((k/m_r)^2 + 1)$ is the redshift factor of one mode with momentum k (the spectrum of radial modes $\partial \rho_r / \partial k$ can be found in [188]).[4]

In Figure F.2 we show the numerical results for Γ_a and $\Gamma_a + \Gamma_r$ for the fat and physical systems using the data from the larger 4500^3 grids of [188], reaching log = 7.9 (we did the same for the data that we collected in simulations including gravitational waves emissions in Figure 6.1 of the main text). To allow the direct comparison with the previous discussion, the results are normalised to the theoretical expectation in eq. (F.1) for the total emission rate Γ. In this last equation we fit the data for the simplest model in which the only free parameter η is kept constant, and in such a way that $(\Gamma_a + \Gamma_r)/\Gamma$ equals unity. The fact that Γ reproduces $\Gamma_a + \Gamma_r$ over more than four e-foldings in time (especially clearly for the fat system) is a remarkable confirmation of the

[3] Irrespectively of whether they are relativistic or not, free radial modes in the fat string system have energy $\sqrt{k^2 + m^2}$ that redshifts as R^{-1}, given that $m_r \propto R^{-1}$ (so the energy density redshift as R^{-4} assuming comoving number density conservation).

[4] This is easily seen by calculating $d \log E / d \log R$ where the energy E is $E = n_{\rm com}(R_0/R)^3 \sqrt{m_r^2 + k_{\rm com}^2 (R_0/R)^2}$ and assuming comoving number density conservation $dn_{\rm com}/dR = 0$ and using $dk_{\rm com}/dR = 0$.

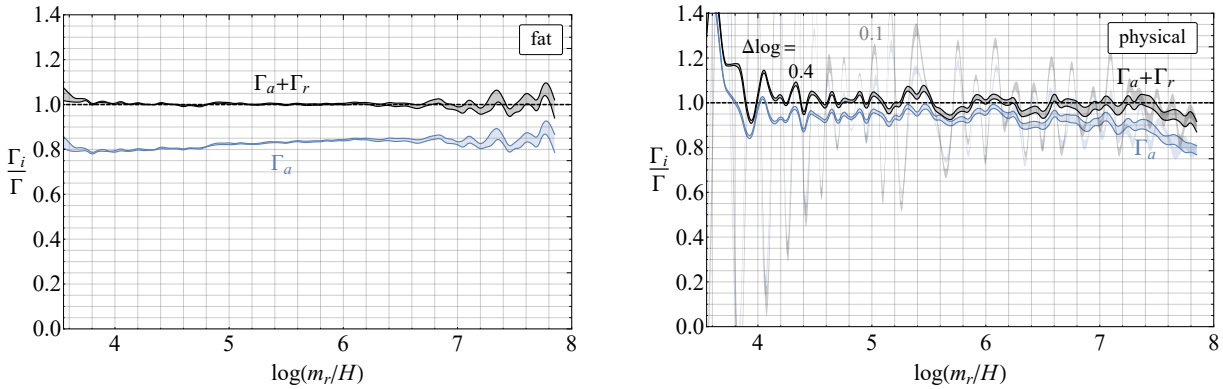

Figure F.2: The energy density emitted in axions and radial modes, Γ_a and Γ_r, during the scaling regime calculated in the simulation, normalised to the theoretical expectation of the total emission rate from (long) strings Γ in eq. (2.53) after fitting the (constant) value η, defined in eq. (2.49). The fact that $\Gamma_a + \Gamma_r$ coincides with the theoretical expectation Γ is a confirmation that the emission rate is described by eq. (2.53) and that the string tension is reproduced by $\mu_{\rm th}$ in eq. (2.49) for a fixed value of η. For the fat strings the time derivatives in eq. (2.53) are done averaging over $\Delta \log = 0.2$, while for the physical system for $\Delta \log = 0.4$ and $\Delta \log = 0.1$ respectively, as labeled. To produce this figure the data from my collaborators' previous paper [188] has been used, which was collected on larger grids $N_{\rm grid} = 4500$. This Figure was produced by my collaborators for our joint work [1].

theoretical picture described above. In particular this shows that the form eq. (2.53) captures the total emission rate during scaling when ξ is restricted to the only long strings, that such emission happens either directly or via loops, and that eq. (2.49) reproduces the effective string tension μ_L even at small log for a fixed choice of η.[5]

We now discuss the details for fat and physical strings separately. For the fat string system, shown in Figure F.2 (left), the agreement between Γ and $\Gamma_a + \Gamma_r$ is excellent and η is fixed precisely. The value of η selected by the fit (in which we consider only $\log > 4$ data and, as mentioned, we evaluate Γ using $f_L = 0.84$), is $\sqrt{4\pi}\eta \simeq 0.95$. This is close to $1/\sqrt{4\pi}$, which is the value this parameter would get if all the long strings were straight and parallel to each other.[6] Although such η reproduces the emission, we assign to it a conservative 15% uncertainty, i.e $\sqrt{4\pi}\eta_{\rm fat} = 0.95(15)$. This uncertainty is estimated by looking at how much the ratio $(\Gamma_a + \Gamma_r)/\Gamma$ varies with log for different choices of η: as shown in Figure F.3, if $\sqrt{4\pi}\eta$ is outside the range $0.8 \div 1.1$ the ratio is not constant (to assign this range we have chosen values of η that result in a maximum change of the ratio $(\Gamma_a + \Gamma_r)/\Gamma$ of 10%), suggesting that the choice of this parameter outside this range is not

[5] Another approach to measure the string tension would be by subtracting the energy in waves, as was done in [188], which leads to compatible results.

[6] This is seen requiring that the argument of the log in eq. (2.49) equals the inter-string distance in units of m_r^{-1}.

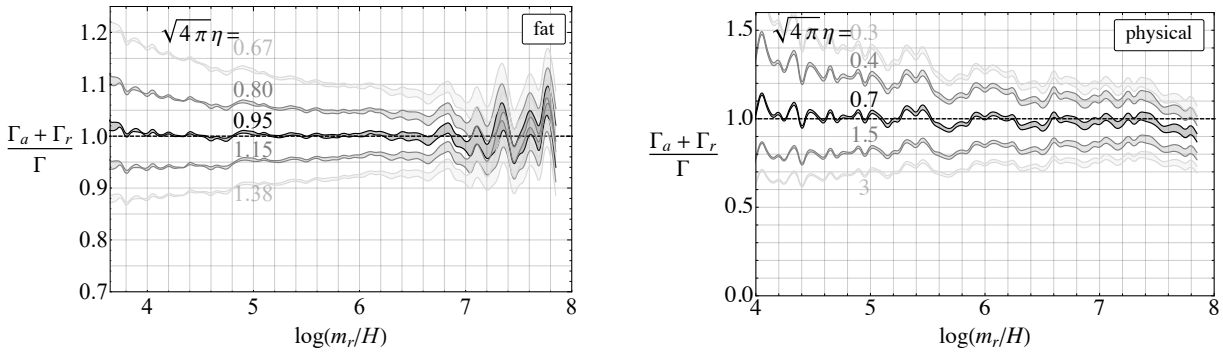

Figure F.3: The dependence of the ratio $(\Gamma_a + \Gamma_r)/\Gamma$ on the choice of the parameter η. Values of η outside the intervals $0.8 \div 1.1$ and $0.4 \div 1.5$ for the fat and physical strings respectively (shown in light grey) do not lead to a constant ratio, signalling that they are not able to reproduce the emission and therefore the string tension (for this purpose we considered the ratio to be constant if it does not differ by more than 10% throughout the range $4 < \log(m_r/H) < 7.9$). This Figure was produced by my collaborators for our joint work [1] and uses data collected for their previous paper [188].

appropriate to describe the emission.[7][8] Notice that the agreement between Γ and $\Gamma_a + \Gamma_r$ for the value of $f_L = 0.84$ extracted from the jump of loop distribution is remarkable, and is a particularly convincing confirmation of the theoretical discussion above. Even more remarkably, leaving both η and f_L as free parameters in the fit $(\Gamma_a + \Gamma_r)/\Gamma = 1$ provides a similar value of η and a value of f_L that differs by less than 1% from the one extracted from the loop distribution. Notice also that as shown in detail in [188], radial modes are still produced (i.e. $\Gamma_r \neq 0$), though increasingly less with respect to axions (i.e. Γ_r/Γ_a diminishes), and it is indeed the sum $\Gamma_a + \Gamma_r$ that reproduces Γ.

The results for the physical system are shown in Figure F.2 (right), where we calculate the derivative averaging over $\Delta \log = 0.1$ (shaded lines) and over $\Delta \log = 0.4$ (solid lines). For such a system some fluctuations are visible, and are particularly evident at early times and with the smaller time averaging. As already noted in [188], these are related to parametric resonance effects between the axion and radial modes, and possibly to the emission from excited string cores due to imperfect initial conditions.[9] As the value of f_L is not known for physical strings, in the fit $(\Gamma_a + \Gamma_r)/\Gamma = 1$ (done for $\log > 4.5$) both the parameters η and f_L are allowed to vary. The best fit values correspond to $f_L \simeq 0.9$ and $\sqrt{4\pi}\eta \simeq 0.7$, which are those for which we evaluate Γ in Figure F.2 (right). As expected, the fit selects $f_L < 1$, and the parameters f_L and η turn out to be remarkably very close to the fat string values. As shown in Figure F.2 (right), despite the fluctuations, for such values of η and f_L the ratio $(\Gamma_a + \Gamma_r)/\Gamma$ is in average close to unity at

[7] Note that indeed the definition of long strings is not completely fixed (and so f_L), so in principle one can just require the ratio to be a constant close to one rather than exactly one.

[8] For the fat string time derivatives are done averaging over $\Delta \log = 0.2$.

[9] These effects are clearly visible in the axion instantaneous emission spectrum as studied in [188], which has large oscillations at around the string core scale.

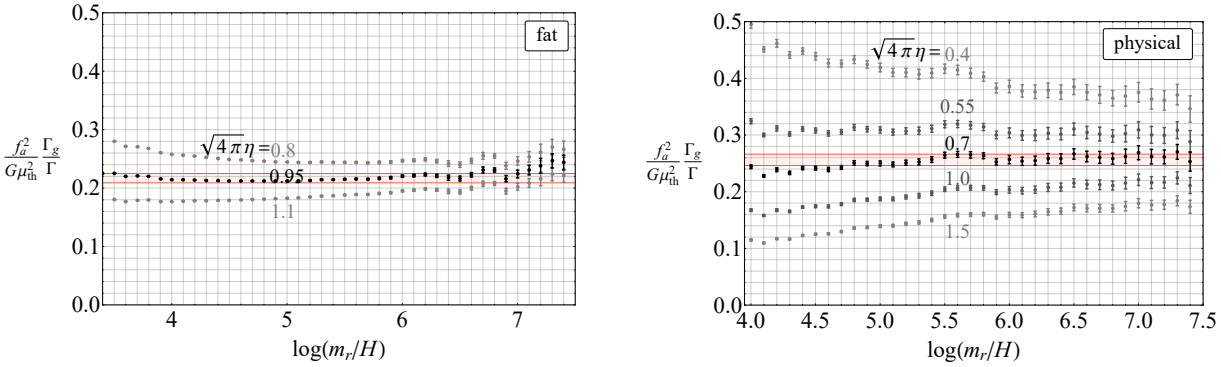

Figure F.4: The dependence of $r = f_a^2\Gamma_g/(G\mu_{\rm th}^2\Gamma)$ on the parameter η, which enters the string tension $\mu_{\rm th}$ for the fat (left) and physical (right) string systems. We plot results for the range of η compatible with the measured instantaneous energy emitted to axions and radial modes of Figure F.3. For the value of η across this range, the plotted ratio approaches a constant value, as is expected from the theoretical analysis in Section 6.2.1.The red bands are centered on the average value of r over all data points and its width is given by the standard deviation. This Figure was produced by my collaborators for our joint work [1].

all times. The large fluctuations however lead to a greater uncertainty on the actual value of η that reproduces the emission. Similarly to the fat string system, we estimate this uncertainty by varying η and looking at the impact on Γ. As is clear from Figure F.3 (right), all the η's in the range $0.4 \div 1.5$ give an approximately constant ratio, while if they are outside this range the ratio starts tilting. We can take this range as a conservative estimate for $\eta_{\rm phys}$.

As in the fat system, the production of radial modes is non-negligible. However the fluctuations make the time evolution of Γ_r/Γ_a more unclear than in the fat string system. Notice that such radial modes are mildly relativistic (in particular, $z \simeq 3.3$ in the whole time range; this turns out to be an essential information for getting a $\Gamma_r \neq 0$ from $R^{-z}\frac{d}{dt}(R^z\rho_r)$).

Let us now discuss the GW emission Γ_g and r, defined in eq. (6.6). As mentioned in Section 6.2.3, the uncertainty on η translates into an uncertainty on the string tension $\mu_{\rm eff}$ (more precisely on μ_L; we discuss later the contribution of $\rho_s^{\rm loops}$ to ρ_s). This uncertainty also affects the value of $\mu_{\rm th}$ to be used in the calculation of $r_{\rm sim} \equiv f_a^2\Gamma_g/(G\mu_{\rm th}^2\Gamma)$ defined in Section 6.2.3.[10] In Figure F.3 we show the value of $r_{\rm sim}$ from different η's chosen in the ranges mentioned above (note that η enters both in $\mu_{\rm th}$ and in Γ). Remarkably, the best fit value of η selected by the above discussion leads a constant $r_{\rm sim}$. As described in the main text, this matches the expectation from the Nambu–Goto effective theory, further confirms that the value of η reproduces the string tension and ensures the energy emitted into GWs can safely be extrapolated to large log. As expected, larger (smaller) values of η lead to an increasing (decreasing) $r_{\rm sim}$, and the results are compatible with $r_{\rm sim}$ evolving asymptotically to

[10] As in the main text, Γ_g is calculated by averaging the time derivative of ρ_g over $\Delta\log = 0.2$, which is already consistent with the continuum limit.

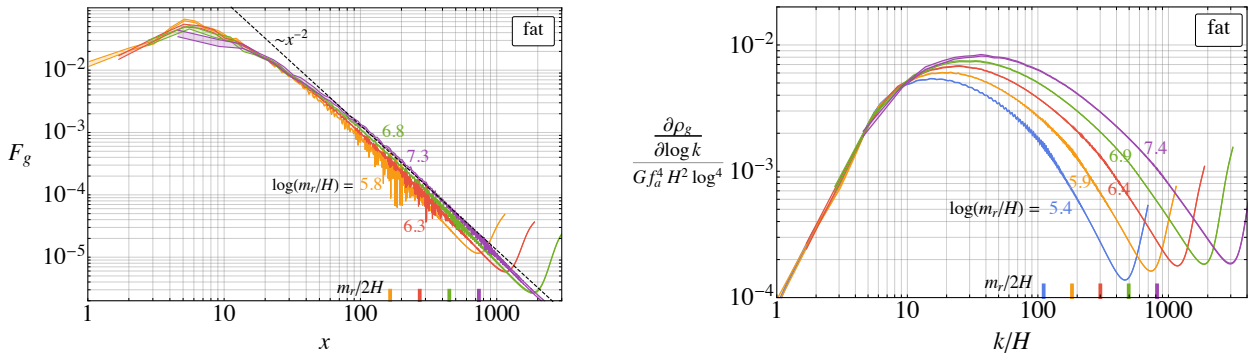

Figure F.5: The normalised instantaneous emission spectrum (left) and the total spectrum of GWs in simulations (right) for the fat string system. The key features match those of the physical system plotted in Figure 6.5. This Figure was produced by my collaborators for our joint work [1].

the same constant regardless of the value of η. Although the best fit values of η lead to a constant $r_{\rm sim}$, we conservatively estimate the uncertainty on r from the one on η by varying $\eta_{\rm fat}$ and $\eta_{\rm phys}$ in the intervals mentioned before for which $(\Gamma_a + \Gamma_r)/\Gamma$ is constant, and considering the range in which $r_{\rm sim}$ varies at the largest available $\log = 7.4$ for such η's. For instance, $r_{\rm phys}$ ranges in the interval $0.17 \div 0.34$.[11]

The discussion above confirms that the tension of long strings μ_L is reproduced by $\mu_{\rm th}$, i.e. $\rho_s^L = \xi_L \mu_{\rm th}/t^2$, with the η fixed as before. As mentioned at the beginning, the energy density in strings $\rho_s = \rho_s^L + \rho_s^{\rm loops}$ however contains also the contribution from loops $\rho_s^{\rm loops}$. This in principle changes ρ_s and therefore could make the effective string tension $\mu_{\rm eff}$ not match $\mu_{\rm th}$ anymore for the same value of η (note that $\mu_{\rm eff}$ – and not μ_L – is the one determining the GW emission, as GWs are emitted both from long strings and from loops, and therefore should be the one that leads to a constant $r = f_a^2 \Gamma_g/(G\mu^2 \Gamma_a)$, since Γ_g is the *total* GW emission rate).

First, we expect a possible overall (constant, see [188]) factor on the total string tension $\mu_{\rm eff}$ due to the non-trivial boost factor of loops but, as mentioned in footnote 11 in Section 6.2.3, this gives an overall correction to $\mu_{\rm th}$ and could be simply reabsorbed in the definition of r. In particular, Γ_g defined in eq. (6.6) with r extracted from Figure 6.3 still provides the correct large log behaviour of the emission.

Moreover, the fact that η predicted by long strings works well in providing a constant r suggests that even the time dependence of $\mu_{\rm eff}$ is close to that of $\mu_{\rm th}$ with the same value of η (or that, alternatively, most of the GW emission is from long strings).[12][13]

[11] Notice that strictly speaking $\Gamma_a = \xi_L \mu_{\rm th}/t^3$ at large log (rather than $\Gamma_a = \xi \mu_{\rm th}/t^3$). This makes the extraction of the numerical value of r from $r_{\rm sim}$ a factor of f_L^{-1} larger and Γ_a a factor of f_L smaller than what mentioned in the main text, leaving in any case the GW emission rate Γ_g in eq. (6.6) invariant.

[12] The fact that the effective tension of the strings is close to $\mu_{\rm th}$ with $\eta \approx 1/\sqrt{4\pi}$ is also suggested by the direct measurement of the string tension in [188].

[13] During the scaling regime, the loop distribution is scale invariant, i.e. contains a fixed number of loops per

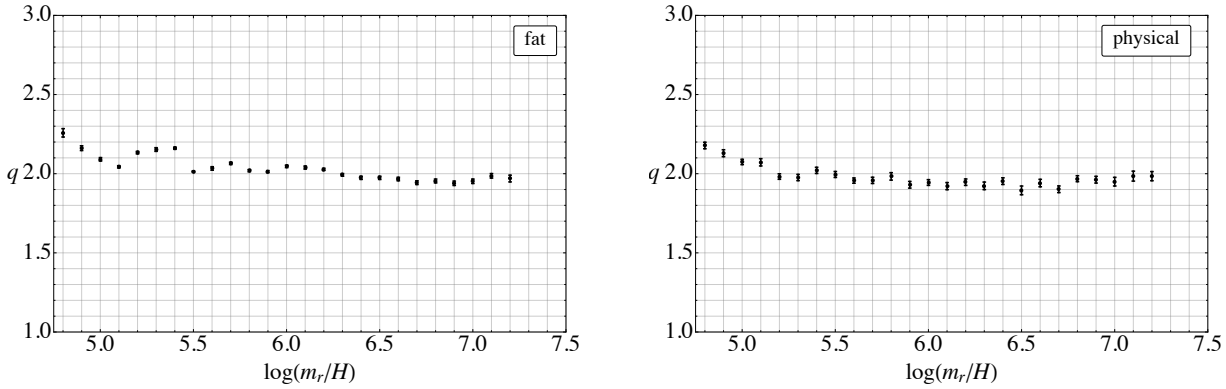

Figure F.6: The time-evolution of the power-law q of the instantaneous GW spectrum $F_g[x, y] \propto 1/x^q$ for the fat (left) and physical (right) string systems. In both cases after log = 5 the values are approximately constant (and compatible with 2). For smaller times the GW spectrum fluctuates and has no definite power law. This Figure was produced by my collaborators for our joint work [1].

We finally comment on the validity of this picture at larger values of log. If the loops become very long lived, the energy could be radiated less efficiently from loops into radiation, therefore the total emission rate will be enhanced with respect to the energy lost by long strings in eq. (F.1) (i.e. $\Gamma_a + \Gamma_r > \Gamma$). Indeed, the string loops oscillate under the effect of their tension, and in the limit of infinite oscillations the loop energy density will redshift as R^{-3}, which diminishes slower than R^{-4}, which is the rate at which the energy would decrease if it were immediately radiated into axions. Although we do not see a sign of this in the simulation between log = 4 and log = 8, we cannot exclude this possibility at very large log. If this is the case, this would enhance most likely the axion and GW emission, and our predictions would still be reliable lower bounds.

The GW Spectrum

Finally, we give more details on the GW spectrum $\partial\rho_g/\partial k$. To extract $\partial\rho_g/\partial k$ in the simulation we used its explicit expression in terms of $\dot{u}_{ij}(\vec{k})$ defined in eq. (E.5), easily derived from its definition $\int dk \partial\rho_g/\partial k \equiv T_g^{00} = (32\pi G)^{-1}\langle \dot{h}_{ij}\dot{h}_{ij}\rangle$, see e.g. eq. (29) in [367]. From $\partial\rho_g/\partial k$ we calculate the instantaneous emission spectrum F_g defined in eq. (6.7) as (we calculate the time derivatives

decade of loop length, for lengths between the IR and UV cutoffs $\simeq H^{-1}$ and $\simeq m_r^{-1}$ (see [188] for more details). For such a distribution the energy takes the form $(\xi - \xi_L)\pi f_a^2 \log(m_r/H\eta')/t^2$, where η' is a (possibly time-dependent) parameter that depends on the precise location of the cut-offs in units of H^{-1} and m_r^{-1}. [To show this, notice that for such a distribution the number of loops per unit length and unit volume is $dn_\ell/d\ell = 4H^3(\xi - \xi_L)/\ell$ and the energy of a loop of length ℓ is $E_\ell = \pi f_a^2 \log(m_r \ell)$. The mentioned energy density follows from $\int_{m_r^{-1}}^{H^{-1}} d\ell\, E_\ell\, dn_\ell/d\ell$ in the limit $m_r \gg H$.] This formula implies $\rho_s^{\rm loops} \approx (\xi - \xi_L)\mu_{\rm th}/t^2$ (except for the value of η'), which justifies why $\mu_{\rm eff}$ in eq. (2.48) is approximated by $\mu_{\rm th}$, at least at large log. We stress in any case that the precise form of $\rho_s^{\rm loops}$ is still uncertain as loops could become longer lived at late time, meaning we do not know the full details of the cutoffs of the loop distribution and of the boost factors of the loops, which could change the formula above.

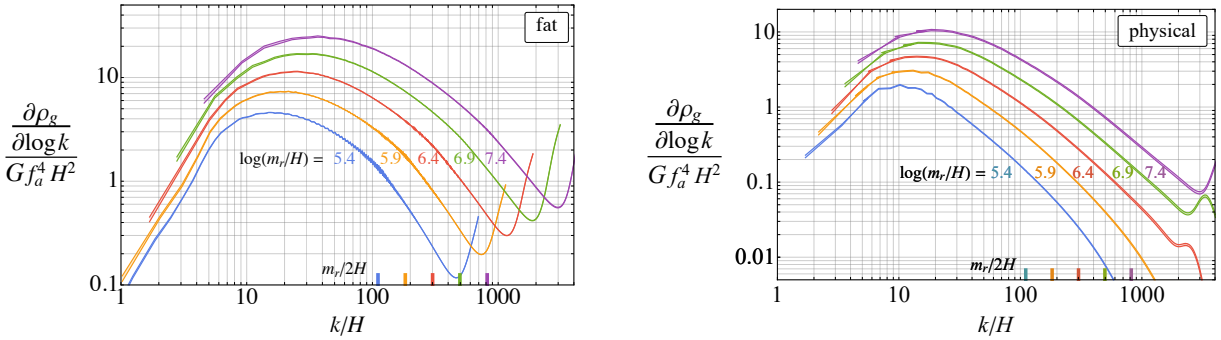

Figure F.7: The total GW spectrum for the fat (left) and physical (right) string networks. The results are identical to those in Figures 6.5 and F.5 except without the $\log^4$ normalisation. The growth of the spectrum is clear in both cases. This Figure was produced by my collaborators for our joint work [1].

numerically considering $\Delta\log = 0.2$)

$$F_g\left[\frac{k}{H},\frac{m_r}{H}\right] = \frac{H/\Gamma_g}{R^3}\frac{\partial}{\partial t}\left(R^3\frac{\partial\rho_g}{\partial k}\right) \ . \tag{F.2}$$

In Figure F.5 we plot $\partial\rho_g/\partial k$ and $F_g[x,y]$ for the fat string system. Both these observables have similar features to the physical system, shown in Figure 6.5. In particular, the approximate power law $q \simeq 2$ is reproduced and is time-independent. As a further study, in Figure F.6 we show the best best fit value for the slope of F_g in the momentum range $30H < k < m_r/4$. As mentioned in Section 6.2.3, given that q is safely above 1 (and appears constant), we do not analyse further its time-dependence and the possible dependence of the fitted value of the slope on the momentum range.[14] Although already clear from the previous plots, to show explicitly the time-dependence of the spectrum we also plot the total GW spectrum without the $\log^4$ normalisation in Figure F.7 for the fat and physical system.

F.2 GW Backreaction on the Strings

In this Appendix we discuss the GW backreaction on the string network in the physical system of eq. (2.28) by solving the coupled eqs. (6.10) and (E.3) (including the backreaction term $R^{-2}h_{ij}\partial_i\partial_j\phi$ in the left hand side of this last equation). As mentioned in Appendix E, this is numerically expensive as requires to perform FT and anti-FT every time step, and we therefore limit ourselves to small 800^3 grids that can explore values of $\log < 6$.[15]

[14] Such detail is more important for the power law of the axion instantaneous spectrum since it changes with the log.

[15] Similarly to the simulations in the main text, this corresponds to the time when $HL = 1.5$ for $m_r\Delta = 1$.

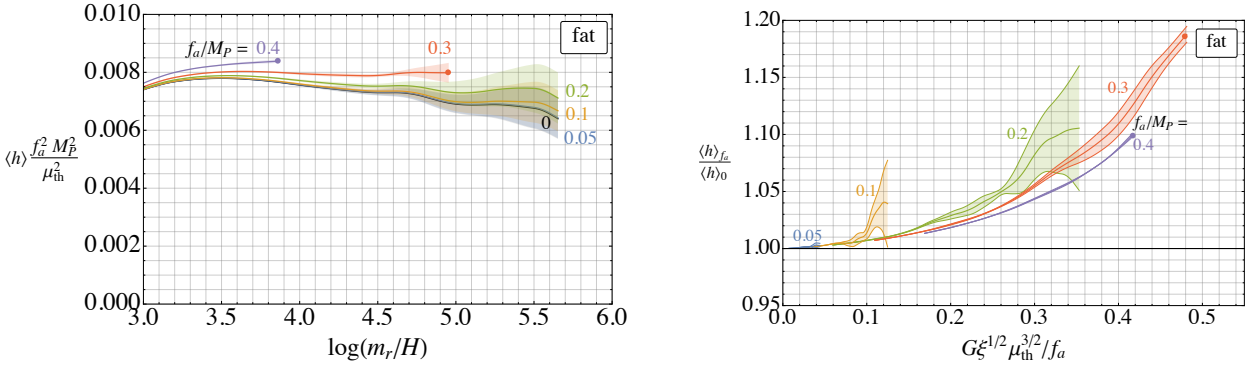

Figure F.8: The evolution of the average square value of the GW field $\langle h \rangle \equiv \langle h_{ij} h_{ij} \rangle^{1/2}$ for different values of $f_a/M_{\rm P}$, and in the limit $f_a/M_P \to 0$ normalised to the theoretical expectation for the string tension squared $\mu_{\rm th}^2$ (left). We also show the relative deviation of $\langle h \rangle$ for different non-zero $f_a/M_{\rm P}$ from its value for $f_a/M_P \to 0$ (right). On the x-axis we plot $G\xi^{1/2}\mu_{\rm th}^{3/2}/f_a$, which is the parameter expected to control the deviation of $\langle h \rangle$. This Figure was produced by my collaborators for our joint work [1].

The theoretical discussion of Section 6.2 suggests that the (evolving) effective parameter controlling the relevance of the GW backreaction on the string network during scaling is $G\mu^2/f_a^2 = \pi/8(f_a \log/M_{\rm P})^2$ (as in the main text, $M_{\rm P} = 1/\sqrt{8\pi G}$). Numerical simulations will confirm this expectation. In particular we will see that, as long as $G\mu^2/f_a^2 \lesssim 0.5$ (corresponding to $f_a \lesssim M_{\rm P}/\log$), (a) gravity is always in the perturbative regime and (b) the effects of the GWs on the properties of the string network (e.g. ξ and ρ_a) is smaller than few percent. Therefore the backreaction is relevant only for $f_a \gtrsim M_{\rm P}/\log$ which is well beyond the region allowed by the bounds in Figure 6.7. A detailed analysis of the impact of the backreaction is therefore not necessary (and, as mentioned, we did not include the backreaction in the simulations presented the main text).

First, notice that the equations of motion (6.10) and (E.3) depend only on the dimensionless ratio $f_a/M_{\rm P}$.[16] We evolve these equations for fat strings and different values of $f_a/M_{\rm P} = 0.05, 0.1, 0.2, 0.3, 0.4$, for the same set of initial conditions (similar to those in Figure F.1), as well as in the limit $f_a/M_{\rm P} \to 0$, i.e. not taking into account the backreaction term in eq. (E.3). In Figure F.8 (left) we show the evolution of the average square value of the GW field $\langle h \rangle \equiv \langle h_{ij} h_{ij} \rangle^{1/2}$ in the limit $f_a/M_{\rm P} \to 0$. As expected from the form of the instantaneous GW emission in eq. (6.6) and of the energy density in GWs, $\langle h \rangle$ is of order $f_a^2/M_{\rm P}^2$ for $\log = \mathcal{O}(1)$ and increases proportionally to $\log^2$ (up to subleading corrections).

Figure F.8 (right) and Figure F.9 show the effect of a finite value of $f_a/M_{\rm P}$ on $\langle h \rangle$, ξ and ρ_a by plotting the time evolution of these observables for different values of $f_a/M_{\rm P}$, normalised to their value in the absence of backreaction. To make the role of the effective parameter $G\mu^2/f_a^2$ manifest,

[16] This can be seen by redefining $\phi \to \phi f_a$ and $h_{ij} \to h_{ij} f_a^2/M_{\rm P}^2$ in such equations.

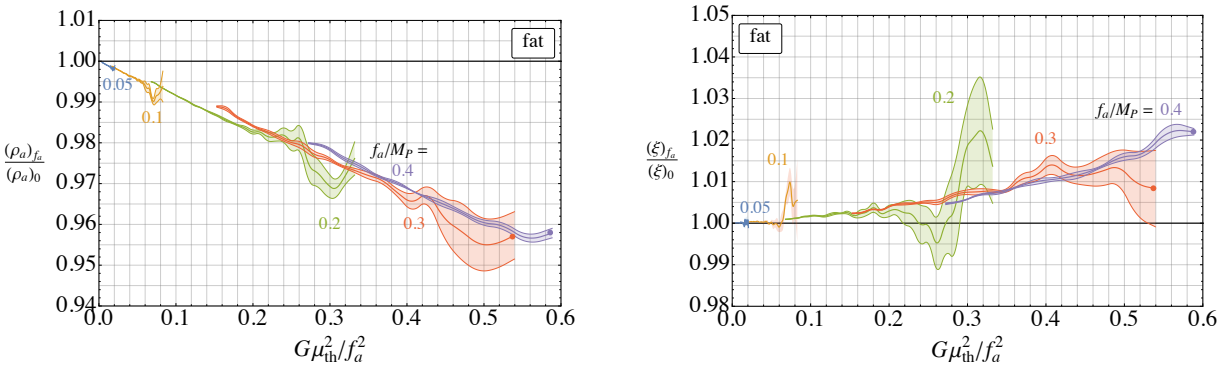

Figure F.9: The evolution of ξ and ρ_a for different values of $f_a/M_{\rm P}$, normalised to their value in the limit $f_a/M_{\rm P} \to 0$ (i.e. without GW backreaction, as in the main Sections). We plot $G\mu^2_{\rm th}/f_a^2$ rather than $\log(m_r/H)$ on the x-axis to highlight that the deviations of these observables from GW backreaction depend on the effective (evolving) parameter $G\mu^2_{\rm eff}/f_a^2$. The filled circles correspond to the time when the numerical evolution of the linear approximation of the Einstein equations breaks down, and at this point $G\mu^2_{\rm eff}/f_a^2 \simeq 0.5$. For smaller values of this parameter, the linear approximation is valid and the observables deviate by less than few percent from their value in the $f_a/M_{\rm P} \to 0$ limit. This Figure was produced by my collaborators for our joint work [1].

we trade $\log(m_r/H)$ with $G\mu^2_{\rm th}/f_a^2 = \pi/8 f_a^2/M_{\rm P}^2 \log^2(m_r/H\eta/\sqrt{\xi})$ in the x-axis.[17] For a non-zero value of $f_a/M_{\rm P}$, the quantities $\langle h\rangle/(f_a^2/M_{\rm P}^2)$ and ξ increase with respect to their value in the limit $f_a/M_{\rm P} \to 0$, while ρ_a decreases. Indeed, as expected, more energy is transferred to GWs rather than to axions, making h_{ij} larger and ρ_a smaller. Crucially, the deviation of these observables from their value at $f_a/M_{\rm P} \to 0$ is controlled by the combination $G\mu^2_{\rm th}/f_a^2$, rather than by log and $f_a/M_{\rm P}$ separately. Indeed, simulations with different value of $f_a/M_{\rm P}$ present the same deviation at a different value of log but at the same $G\mu^2_{\rm th}/f_a^2$, as suggested by the fact that the lines overlap in Figure F.9.

When $G\mu^2_{\rm th}/f_a^2 \simeq 0.5$ the numerical evolution of the equations of motion breaks down for all $f_a/M_{\rm P}$.[18] This can mean either a numerical issue that results in the simulation not reproducing the continuum limit of the equations of motion we used, or it is signalling that the linear approximation of the Einstein equations is no longer valid, which corresponds to higher order terms being relevant in the equations of motion. We therefore show the results for $\langle h\rangle$, ξ and ρ_a until the evolution makes sense, with a filled circle at the time when the numerical evolution breaks. From Figure F.8, it is easy to see that this value of $G\mu^2_{\rm th}/f_a^2$ corresponds to $\langle h\rangle \simeq 0.1$ (the local value of h_{ij} will be larger than this). Moreover, at this value of $G\mu^2_{\rm th}/f_a^2$, the observables ξ and ρ_a have changed only of a few percent with respect to their value in the absence of backreaction. Given that the numerical breakdown happens at a specific value of $G\mu^2_{\rm th}/f_a^2 \simeq \mathcal{O}(1)$ which is the same for $f_a/M_P = 0.3$ and

[17] We fix the same value of η as in the main text.

[18] This is seen by the non-convergence of the numerical algorithm that integrates eqs. (6.10) and (E.3).

$f_a/M_P = 0.4$, and that the corresponding value of h_{ij} at breakdown also approaches order one, this suggests that the cause could be indeed that the linear approximation of the Einstein equation is no longer sufficient. The dramatic change of the evolution of the network beyond this point can be only captured by the full general relativity description of the system.

The decrease in energy in axions seen for non-zero $f_a/M_{\rm P}$ in Figure F.9 left is quantitatively consistent with the energy that is found to be in gravitational waves, and therefore the value of r obtained in Section 6.2.3 (there is a small increase in the sum of the energy in all components as f_a increases, which is expected since the effect of backreaction is to slightly increase ξ, as seen in Figure F.9, right).

We observe that, while the dependence on the parameter $G\mu_{\rm th}^2/f_a^2$ has only been tested for small logs and relatively large values of $f_a/M_{\rm P}$, the theoretical discussion in Section 6.2 allows to extrapolate the results of Figure F.8 and F.9 also at large logs (and smaller $f_a/M_{\rm P}$), in particular ensuring that the GW backreaction is negligible for all f_a in Figure 6.7, despite the large log. Finally notice that, as the evolution of the system is not known for $f_a \gtrsim M_{\rm P}/\log$, there are in principle two orders of magnitude of f_a below $M_{\rm P}$ for which the bounds in Figure 6.7 do not apply, and a complete general relativity reanalysis would be needed.

F.3 The End of the Scaling Regime and Nonlinear Transient

In this Appendix we give more details on the end of the scaling regime for a temperature-independent axion mass. We will also study in more depth the non-conservation of the comoving number density of axons at $H \simeq H_\star$. Most of the discussion of this Appendix builds on the material of Section 3 of [188] and Appendices D and E of the same reference, to which we refer for a more pedagogical presentation.

End of the scaling regime

As mentioned in Section 2.4.3, the axion potential becomes relevant in the evolution of the string system only for $H \lesssim H_\star \equiv m_a$, at which time a network of domain walls forms and destroys the string system. To determine precisely the critical value of H (which we call $H_{\rm crit}$) when the scaling regime starts getting affected by the axion potential, we evolve eq. (E.3) with the same initial conditions as in the main text for the fat string system, but with the additional term $-m_a^2/(\sqrt{2}m_r^2)$, which corresponds to including the axion potential $V = m_a^2 f_a^2(1-\cos(a/f_a))$ in the Lagrangian of eq. (2.28) (see Appendix D of [188]). Notice that the dependence on m_a of the equations of motion enters only through the ratio m_a/m_r, and we therefore refer to different axion masses via the value of $\log(m_r/m_a) = \log(m_r/H_\star) \equiv \log_\star$.

In Figure F.10 (left) we show the time-evolution of ξ for different values of $\log_\star$, plotted as a function of $H_\star/H$, together with the evolution of the equations for $m_a = 0$ (dashed lines). In Figure F.10 (right) we also show the time-evolution of the axion spectrum $\partial\rho_a/\partial k$ for $\log_\star = 5$. It

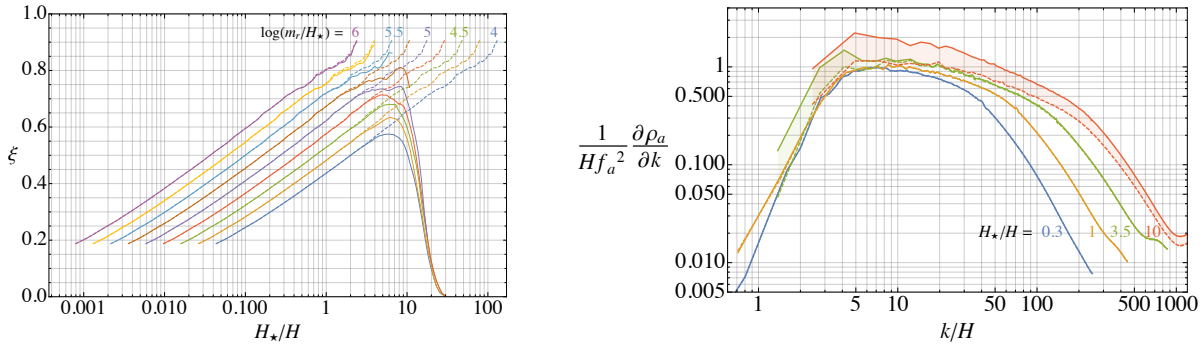

Figure F.10: Left: The evolution of ξ for a non-zero constant axion mass at different $\log_\star \equiv \log(m_r/m_a)$ (solid lines), and for $m_a = 0$ throughout with the same initial condition (dashed lines). Independently of $\log_\star$, ξ is unaffected by the mass before $H = H_{\rm crit} \equiv H_\star/3$. Right: The axion spectrum in the presence of the axion mass with $\log_\star = 5$ (upper lines) at different times labelled by $H_\star/H$, and for vanishing axion mass (lower lines, dashed). Before $H = H_{\rm crit}$ the effect of the non-zero axion mass has on the spectrum is negligible. This Figure was produced by my collaborators for our joint work [1].

can be easily seen that for values of H larger than $H_{\rm crit} \equiv H_\star/3$ both ξ and the axion spectrum are not significantly affected by the axion potential, as they closely follow the evolution for $m_a = 0$. For smaller values of H, ξ diminishes (as the network starts being destroyed) and the spectrum gets affected, starting from its IR part. Although the value of $H_{\rm crit}$ can be numerically studied only at small values of $\log_\star$, it is reasonable to expect that it will not change at larger $\log_\star$.

Nonlinear evolution of the axions waves

As mentioned in Section 6.3.1, and explained in detail Section 3 of [188], the axion waves produced up until $H_\star$ have kinetic energy much larger than the potential energy at $H = H_\star$ (we momentarily assume that $H_{\rm crit} = H_\star$, and discuss to the modification to a generic $H_{\rm crit}$ later).[19] This results in a period of relativistic redshift and a nonlinear transient, which implies a partial non-conservation of the comoving number density. However we now show that the number density non-conservation is small for the value of $\xi_\star \log_\star$ discussed in Section 6.3.1 for a temperature-independent mass.

The number density after the nonlinear transient follows the analytic description and eq. (36) of [188] (evaluated for a constant axion mass, i.e. $\alpha = 0$). The corresponding number density

[19] Recently it has been claimed that this cannot be true because the compactness of the axion field bounds the energy that can be stored in low momentum modes [369]. In fact, the periodicity of the axion only affects the zero-mode: all the other modes can be populated by arbitrarily large amplitudes.

non-conservation reads

$$\frac{n_a^{\rm st}}{n_a^{\rm st}|_{\rm linear}} = \frac{c_n c_V}{\frac{8\pi\xi_\star \log_\star}{x_{0,a}}} \left[\frac{W_{-1}\left(-\frac{c_V}{2\pi\xi_\star \log_\star} \left(\frac{x_{0,a}}{c_m}\right)^4 \right)}{-\frac{c_V}{2\pi\xi_\star \log_\star}} \right]^{\frac{3}{4}} \tag{F.3}$$

$$\simeq \frac{c_n c_V}{\frac{8\pi\xi_\star \log_\star}{x_{0,a}}} \left[2\pi\xi_\star \log_\star \log\left(\frac{2\pi\xi_\star \log_\star}{c_V} \left(\frac{c_m}{x_{0,a}}\right)^4 \right) \right]^{\frac{3}{4}} , \tag{F.4}$$

where W_k is the Lambert W-function evaluated on the k-th Riemann sheet and in the second line we expanded W_{-1} for large negative values of its argument. The coefficients $c_m,\ c_V,\ c_n$ have been extracted in [188] by fitting eq. (F.3) with the number density obtained from the numerical evolution of

$$\ddot{a} + 3H\dot{a} - R^{-2}\nabla^2 a + m_a^2 f_a \sin(a/f_a) = 0 \ , \tag{F.5}$$

with $m_a = H_\star (H_\star/H)^{\alpha/4}$ and $\alpha = 4, 6, 8$, with initial conditions (at $H = H_\star$) given by a superposition of axion waves with energy density spectrum $\partial\rho_a/\partial k$ from the (reconstructed) scaling regime at $H = H_\star$ (see [188] and the following eq. (F.6) for the explicit expression of the initial conditions). Note that such simulations (that include only the axion field) can study directly the physical point (i.e. without extrapolation, unlike simulations of the physical system in (2.28), which must include modes with $k \simeq m_r$).[20]

Let us now discuss what changes if $H_{\rm crit} < H_\star$. In this case the number density at $H = H_{\rm crit}$ is approximately $n_a = 8\pi\xi_\star \log_\star H_{\rm crit} f_a^2/x_{0,a}$.[21] If this number density is thought as coming from an axion field at $H = H_\star$ (which redshifts relativistically from $H_\star$ to $H_{\rm crit}$), such a field has the same energy density spectrum $\partial\rho_a/\partial k|_\star$ but with $x_{0,a} \to x_{0,a}(H_{\rm crit}/H_\star)^{1/2} = x_{0,a}/\sqrt{3}$ (i.e. an IR cutoff smaller by $\sqrt{3}$).[22] To evaluate the suppression of the number density for $H_{\rm crit} < H_\star$ we can therefore use eq. (F.3) with $x_{0,a} \to x_{0,a}/\sqrt{3}$, which gives a 20% non-conservation of the comoving number density for $\xi_\star \log_\star = 3000$ (and $x_{0,a} = 10$).[23]

In support of this, in Figure F.11 we also show the evolution of the comoving number density for different values of $\xi_\star \log_\star$ from the numerical evolution of the equation of motion (F.5). The set up of the simulations is explained in [188], to which we refer for the details. As in [188], we

[20] The coefficients read $c_m = 2.40,\ c_V = 0.12,\ c_n = 1.20$ and $c_m = 2.08,\ c_V = 0.13,\ c_n = 1.35$, respectively for an initial axion energy density spectrum given by the convolution of F_a sharp IR cutoff at $x = x_{0,a}$ and a more physical form as described in [188] (in both cases with $q_a = 5$).

[21] As defined in Section 6.3.1, the number density is $n_a^{\rm st} \equiv \int dk \partial\rho_a/\partial k$, and can be approximated with $\rho_{\rm IR}/(x_{0,a}H)$ during the scaling regime (up until $H_{\rm crit}$), where $\rho_{\rm IR} = 8\pi f_a^2 \xi \log H^2$ is the energy density in IR modes. The difference $\xi_\star \log_\star$ from $\xi_{\rm crit} \log_{\rm crit}$ is insignificant with respect to the change in H.

[22] In particular, at $H = H_\star$ its (relativistic) number density will be enhanced by a factor $\sqrt{3}$ with respect to $8\pi\xi_\star \log_\star H_\star f_a^2/x_{0,a}$.

[23] In doing this estimate we used a c_V that is $(1 - 1/q_a)^{-1} = 5/4$ larger than what mentioned before, in order to account for the fact that the coefficients have been extracted for $q_a = 5$ instead of $q \to \infty$ (which is the limit in which $n_a = 8\pi\xi \log /x_{0,a} f_a^2 H$ is valid.)

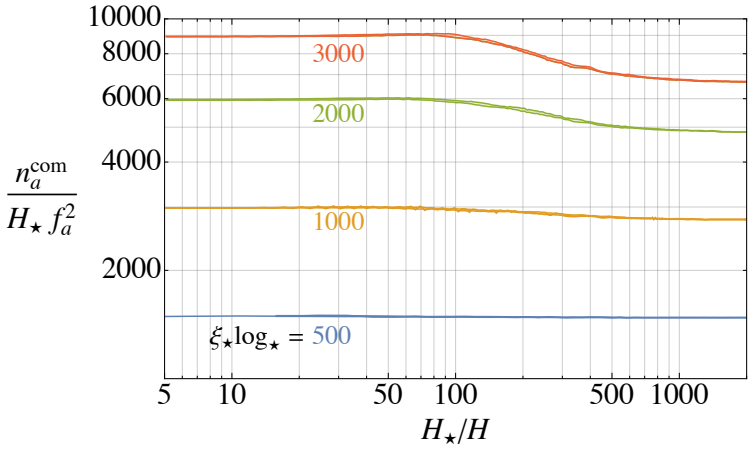

Figure F.11: The evolution of the comoving number density of the axions (produced during the scaling regime) through the nonlinear transient that occurs when the axion potential becomes cosmologically relevant. The initial conditions are set at $H = H_{\rm crit} = H_\star/3$ to be a superposition of axion waves with the energy density spectrum $\partial\rho_a/\partial k$ from the (reconstructed) scaling regime at $H = H_{\rm crit}$ (see [188]). For $\xi_\star \log_\star \lesssim 3000$ (which are the relevant values for ultralight axions) the number density non-conservation is at most 20%, and was therefore neglected in the derivation of $\Omega_a^{\rm st}$ of Section 6.3.1. This Figure was produced by my collaborators for our joint work [1].

start from $H = H_{\rm crit} = H_\star/3$ with initial conditions given by an axion field made of a random superposition of waves with the energy density spectrum of the scaling regime at $H = H_{\rm crit}$, i.e. (for $k > k_0 \equiv x_{0,a} H_{\rm crit}$)

$$\begin{aligned}\frac{\partial\rho_a}{\partial k}(t_{\rm crit},k) =& \frac{8\xi_\star\mu_\star H_{\rm crit}^2}{k}\left[\left(1-2\frac{\log(k/k_0)}{\log_\star}\right)^2-\left(\frac{k_0}{k}\right)^{q_a-1}\right.\\ &\left.+4\frac{1-2\frac{\log(k/k_0)}{\log_\star}-\left(\frac{k_0}{k}\right)^{q_a-1}}{(q_a-1)\log_\star}+8\frac{1-\left(\frac{k_0}{k}\right)^{q_a-1}}{(q_a-1)^2\log_\star^2}\right],\end{aligned} \tag{F.6}$$

which follows from eq. (6.8) with Γ_g replaced with Γ_a and F_g with F_a, and we assume $F_a \propto 1/x^{q_a}$ for $x > x_{0,a}$ and $q_a > 1$ (and $F_a = 0$ for $x < x_{0,a}$).[24] Notice from Figure F.11 that for values of $\xi_\star \log_\star = \mathcal{O}(10^3)$ the suppression is the predicted one, and for smaller values the conservation of the number density is even more accurate (and eq. (F.3) breaks). Finally, for larger (not relevant, unless $N > 1$, see Section 6.3.5) values of $\xi_\star \log_\star$ the non-conservation of the number density becomes substantial, and the relic density in eq. (6.13) must be multiplied by the suppression factor in eq. (F.3). In particular, as mentioned in the main text, $\Omega_a^{\rm st} \propto (\xi_\star \log_\star)^{3/4}$.

[24] We used $q_a = 5$ and as mentioned $x_{0,a} = 10$.

F.4 The Density Power Spectrum

In this Appendix we give more details on the determination of the power spectrum of axion overdensities $\Delta_a^2(k)$ defined in eq. (4.31), and discuss the uncertainties on this.

As described in Section 6.3.3 and Appendix F.3, we consider only the axion radiation emitted during the scaling regime up to $H = H_{\rm crit} = H_\star/3$. In particular, we neglect the strings and the domain walls that are present in the field at this time. The evolution of such radiation follows the axion equations of motion (F.5). Similarly to Appendix F.3, we start at $H = H_{\rm crit}$ with initial conditions given by a superposition of waves with the axion spectrum $\partial\rho_a/\partial k$ from the extrapolated scaling solution (with $\xi_\star \log_\star = 2000$) in eq. (F.6).[25] As discussed in Appendix F.3, the axion number density (and in general the dynamics of the IR part of this radiation) can be directly studied at the physical value of $\log_\star$ in these simulations without the need of extrapolations (thanks to the absence of strings).

Such simulations capture the dynamics of axion field up the momentum mode $k_{\rm UV} \simeq N_{\rm grid} H_\star/(H_\star L_\star)$ at $H_\star$, where $N_{\rm grid}$ is the number of lattice points and $H_\star L_\star$ is the number of Hubble lengths in the box at this time. While most of the energy density of the field is not included in the simulations due to the almost scale invariant form of the energy density spectrum $\partial\rho_a/\partial k$ (see eq. (F.6)), the axion number density $n_a = \int dk/\omega_k \partial\rho_a/\partial k$ dominantly comes from IR modes, which are included (at $k > m_a$ the contribution to the number density from the mode k is proportional to k^{-2}). Consequently, the IR modes of the field also dominantly determine the axion dark matter power spectrum $\Delta_a^2(k)$ at least at IR momenta.[26]

Since we are primarily interested in the coefficient of the k^3 IR part of the density power spectrum, the simulations are carried out starting with $HL = 20$ at $H_{\rm crit}$ so that modes with momentum down to $k/H_\star \simeq 0.2$ are included, giving a large enough momentum range for the k^3 slope to be present and C to be fit. Moreover, we set $N_{\rm grid} = 1300$, which is large enough that modes with $k/H_\star \simeq 200$ are included, corresponding to 95% of the number density. During the evolution of the field, we calculate the (discretized version of the) power spectrum as $\Delta_a^2(k) = k^3/(2\pi^2 L^3)\langle\tilde{\delta}^2(\vec{k})\rangle|_{|\vec{k}|=k}$ where $\tilde{\delta}(k)$ is the Fourier Transform of $\delta(x)$ and $\langle\cdot\rangle|_{|\vec{k}|=k}$ stands for the average over the momenta with modulus $\vec{k}$.

In Figure F.12 left we show the results for $\Delta_a^2(k)$ at increasing times during the evolution of the system at $H < H_{\rm crit}$ (as the mass becomes relevant), for the input spectrum in eq. (F.6) with $x_{0,a} = 10$. As expected, $\Delta_a^2(k)$ changes, in particular growing at scales $k_{\rm com}/H_\star \simeq 10$. Thanks to

[25] Although this spectrum derives from a simplified form of F_a, we have confirmed that starting with a more realistic F_a (discussed in [188]) with the same $x_{0,a}$ but with an IR tail $F(x) \sim x^3$ for $x < x_{0,a}$ changes the fit of the constant C to the IR of Δ_k^2 by less than 20%, which is much smaller than the uncertainties we subsequently discuss.

[26] In particular, the UV modes evolve freely without affecting the dynamics of the IR modes at any point including during the previously discussed non-linear transient [188]. Subsequently, the energy in the UV modes simply redshifts away leaving a negligible contribution to the DM abundance. The fact that simulations do not include the (large fraction of the total axion) energy that is such UV modes therefore does not introduce uncertainty in the power spectrum that we extract.

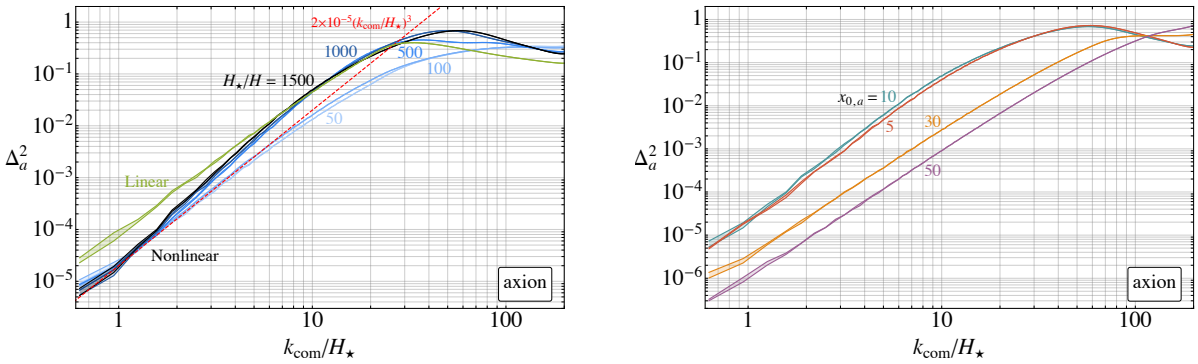

Figure F.12: *Left:* The power spectrum Δ_a^2, as a function of comoving momentum $k_{\rm com} \equiv k(R/R_\star)$, during the evolution of the axion waves (produced during the scaling regime) when the axion mass becomes cosmologically relevant (blue), and at the final simulation time (black), after the the nonlinear transient and once it has reached an approximately constant form. The simulation starts at $H = H_{\rm crit} = H_\star/3$ with waves with the energy density spectrum $\partial\rho_a/\partial k$ predicted from the scaling regime in eq. (F.6) at $\xi_\star \log_\star = 2000$ and $x_{0,a} = 10$. The green line is the result at the final time for a purely linear evolution. *Right:* The result of Δ_a^2 at the final time for different values of the IR cutoff of F_a, i.e. the parameter $x_{0,a}$, in the initial energy density spectrum. This Figure was produced by my collaborators for our joint work [1].

the relatively large $N_{\rm grid}$ used, the transient has finished and the axion energy in the simulation is redshifting non-relativistically by the end of the simulation.[27] As it is clear in Figure F.12, at this time the IR part of $\Delta_a^2(k)$ has reached a time-independent form. The UV part of $\Delta_a^2(k)$ is not fully constant, due to the presence of high momentum modes and oscillons (these contain only a small fraction of the total energy and will eventually decay into high momentum modes so will not alter the IR of the density power spectrum), and as mentioned in Section 6.3.3 its understanding is beyond our current scope.

The IR part of $\Delta_a^2(k)$ approaches the expected k^3 dependence, with coefficient $C \simeq 2 \times 10^5$ (defined in Section 6.3.3). Note that even with a linear evolution (i.e. with potential $V = 1/2m_a^2a^2$), $\Delta_a^2(k)$ would evolve simply due to modes turning non-relativistic. However the results we obtain differ from those with a linear potential due to the, previously discussed, relativistic redshift and the small non-linear transient. To understand the importance of these two effects, in Figure F.12 we also plot the Δ_a^2 that is obtained at the final simulation time evolving with a linear potential. From this is can be seen that the non-linear effects decrease $\Delta_a^2(k)$ by a factor of 4 in the IR. This is reasonable since the transient moves energy to higher momentum modes, and it is also not surprising that the effect is relatively small given that the transient only has a minor effect on the axion number density. Although we have fixed a potential of the form $V(a) = m_a^2 f_a^2(1-\cos(a/f_a))$

[27] As discussed, in reality soon after $H_\star$ a large fraction of the axion energy is in UV modes that are not captured by simulations. However, these continue to redshift until the energy they contain is negligible so the true power spectrum will eventually reach the form measured in simulations.

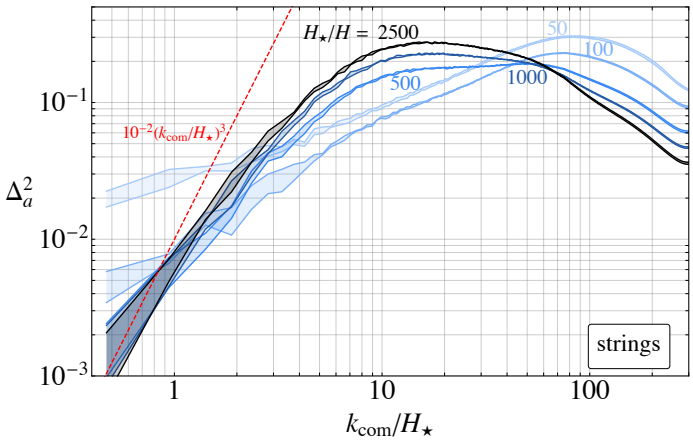

Figure F.13: The evolution of the power spectrum Δ_a^2 during the destruction of the string network at the unphysical value of $\log(m_r/H_\star) = 5$. See Figure F.10 for the corresponding evolution of ξ and the axion energy density spectrum at these times. This Figure was produced by my collaborators for our joint work [1].

we expect any other bounded potential to lead to a similar $\Delta_a^2(k)$ (since the main effect of the non-linear potential on $\Delta_a^2(k)$ comes from the extra era of relativistic redshifting).

Let us discuss the possible uncertainties in C. One uncertainty comes from the value of the IR cutoff $x_{0,a}$ of F_a. As mentioned, at $\log \simeq 7 \div 8$ the value of $x_{0,a} = 10$ (as we have used) fits well the simulation results [188], with no evidence for a strong log dependence. Nevertheless, we cannot exclude that $x_{0,a}$ has a log dependence that is smaller than would be visible with current simulations (for instance the growth of ξ might increase $x_{0,a}$). In Figure F.12 (right) we plot $\Delta_a^2(k)$ with $x_{0,a}$ between 5 and 50, from which it can be seen that $x_{0,a} > 10$ decreases $\Delta_a^2(k)$ in the IR leading to a smaller C and a weaker limit via eq. (6.17). Decreasing $x_{0,a}$ below 10 actually barely affected the fitted C, since the non-linear transient has a greater effect in this case, removing energy from IR modes. For $x_{0,a}$ between 5 and 30, which we take as a plausible range, C varies by a factor of 20. For a fixed $f_{\rm iso}$, the bound on $f_a \sim C^{1/4}$, so this leads to a 100% uncertainty on the limit on f_a. In Figure 6.7, we correspondingly blur the limit above a lower edge corresponding to the constraint for $x_{0,a} = 10$ to reflect this uncertainty. Together these uncertainties mean that the isocurvature bounds that we plot should be treated with substantial caution as discussed in the main text.

Finally, as discussed in Section 6.3.3, our analysis of density perturbations in DM axions from the scaling regime gives a conservative isocurvature bound, since it misses the DM axions produced by the network of strings and domain walls formed when the mass becomes cosmologically relevant. To get an idea of how much these could strengthen the bound, we also calculate Δ_a^2 from simulations of the string network through the mass turn on until its destruction at a small (unphysical) value

of $\log_\star$, by numerically solving eq. (2.28) with an additional mass term, as in Appendix F.3. Of course, such simulations are at small scale separations (i.e. small tension) and have no hope of accurately reproducing the dynamics of the system at the physical point, and our results are solely to give an indication of the possible magnitudes of effects. The various competing requirements in such simulations discussed in Appendix F of [188] dramatically limit the value of $\log_\star$, and the results we show are for $\log_\star = 5$.[28]

The results for Δ_a^2 are shown in Figure F.13 at increasing times until the network is destroyed (see Figure F.10 for the behaviour of ξ and the axion energy density spectrum at the corresponding times). Given the more challenging simulations, the minimum values of $k_{\rm com}/H_\star$ (where $k_{\rm com} = k(R/R_\star) = k(H_\star/H)^{1/2}$ is the comoving momentum) are larger than in simulations in which only the axion field is evolved. Nevertheless, the expected k^3 IR power law is reproduced and in this momentum region Δ_a^2 is time independent after the network disappears. The coefficient $C \simeq 5 \times 10^{-2}$ is much larger than in the axion only simulations (this is perhaps not surprising, since at $H = H_{\rm crit}$ most of the string length is in long strings, which are expected to lead to fluctuations on Hubble scales).[29] Similar results have been observed in analogous simulations where the axion mass has nontrivial temperature-dependence. This has been studied for the first time in [184], where a detailed analysis of the power spectrum (at all momenta) has been carried out at small $\log_\star$ for the QCD axion.[30]

It is plausible that the slope of the k^3 tail may be similar at large values of $\log_\star$, and if the relic abundance of axions from the destruction of the network is comparable to (or larger than) that from scaling, the isocurvature constraint would be significantly strengthened. For instance, assuming equal DM abundance from the waves produced during the scaling regime and from the destruction of the network, and $C \simeq 5 \times 10^{-2}$, using eq. (6.17) for a fixed m_a the bound on f_a Figure 6.7 would strengthen by a factor of 7, ruling out large parts of the ranges of f_a and m_a that could be detected at SKA. As mentioned in the main text, even if the true C from the destruction of the network at large tension is small, if the DM abundance is larger than that produced during scaling the isocurvature limit can also strengthen, owing to the DM abundance factor in eq. (6.17).

F.5 Distribution of loops in the underdense regime

As explained in Section 4.4, the evolution of the string density ξ in the underdense regime is empirically described by eq. (4.12). In the limit $\lambda = 0$ this corresponds to a power law $\xi \sim t^\gamma$ with $\gamma = (\alpha H_I^2)/(8\pi^2 v_a^2)$ and $\alpha \simeq 3.7$ was extracted numerically. For values of H_I/v_a that correspond

[28] These requirements include, in particular, the lattice spacing $\lesssim m_r^{-1}$, a large enough hierarchy between axion and radial model mass, and that HL is sufficiently large that the k^3 IR part of the density power spectrum can be fit once Δ_a^2 has reached a constant form in the IR part.

[29] The UV part of Δ_a^2 is still evolving at the final simulation time, but the overall energy density is mostly in IR modes so the IR part of the density power spectrum will not change dramatically.

[30] In particular, the power spectrum is also characterized by a peak related to the presence of oscillons.

to the underdense regime γ is roughly smaller than 0.2. Compared to the evolution of a network of exclusively long, non-interacting strings for which $\xi \sim t$ the network in the underdense regime grows slower. The expectation is thus that a substantial fraction of the string length is in relatively shorter loops. We have followed the distribution of loop lengths in Figure F.5 which we compare to Figure 4 of [186].

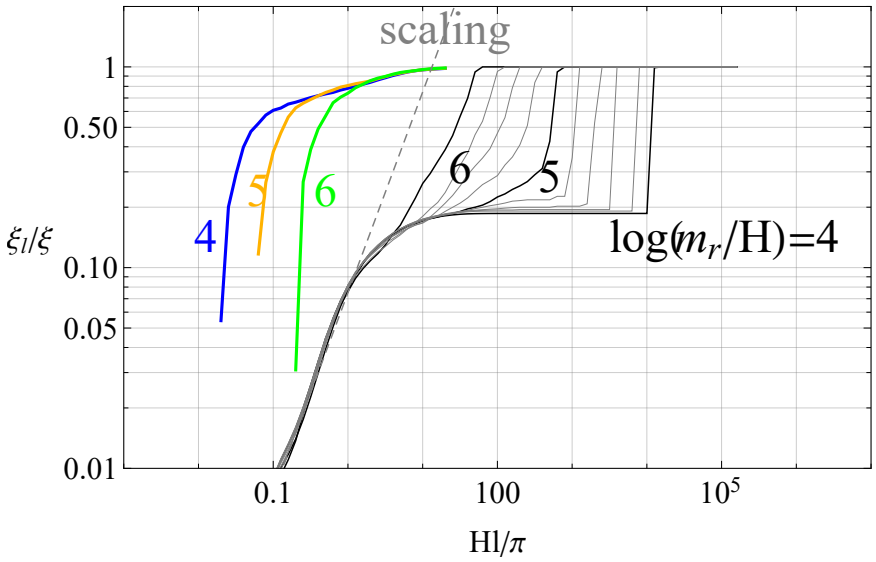

Figure F.14: Comparison of the evolution of the distribution of loops for an underdense network starting from initial conditions as explained in Section 4.4 (colored lines) and an overdense network shown in [186] (black lines). This shows that the underdense network has a higher proportion of short loops as compared to the distribution in the scaling regime.

It is not surprising that the underdense network contains many small loops, since the radial mode is most likely to fluctuate over the top of the potential towards the end of inflation, since it had to longest time to get close to the top. Meanwhile, fluctuations over the top at late times are likely to lead to small loops, as the length of the strings is least stretched by inflation.

Appendix G

GWs from the Nonlinear Transient and Oscillons

As mentioned, we refrain from attempting to calculate the contribution to the GW background from the collapse of the system of strings and domain walls at $H \simeq m_a$, since the dynamics of this system is yet not fully understood. One contribution to the GW spectrum from this collapse is expected to lie at frequencies and amplitudes of the same order as the last e-folding of the scaling regime, as already pointed out in [191] (where numerical simulations at small scale separations have been carried out). As described in Section 6.2.4, such a contribution has a too low frequency for ultralight axions (for the masses that are not excluded by DM overproduction) and a too small amplitude for the QCD axion, for which $f_a \lesssim 10^{10}$ GeV (but in principle at frequencies that are under investigation) to be observed.

As we will now explain, there could be an additional source of observable GWs in this system. As discussed in Section 6.3.1 and in more detail in [188], the axion waves (accumulated during the scaling regime) experience a period of relativistic redshift after at $H \simeq m_a$ and a small nonlinear transient. During the nonlinear transient, the field is a superposition of waves containing (topologically trivial) domain walls that decay rapidly into axions. After the transient, the axion field is mostly in the linear regime (settling down to $a = 0$), except in small regions called oscillons where it oscillates with an amplitude of order f_a. If the evolution of the axion waves were purely linear, the axion waves would not produce GWs [370]. However, the existence of a small nonlinear regime provides a possible source of GWs. Unfortunately, this contribution is again in amplitude and frequency of the same order as the last e-folding of the scaling regime, and therefore not observationally relevant both for ultralight axions and for the QCD axion.

This conclusion can be easily drawn by estimating the parametric dependence on f_a and $H_\star$ of this contribution via quadrupole formula (valid in the non-relativistic limit) applied to the topologically trivial domain walls. In any case, in Figure G.1 we show the full spectrum of GWs from the numerical evolution of the axion waves during the nonlinear regime, discussed in Appendix E

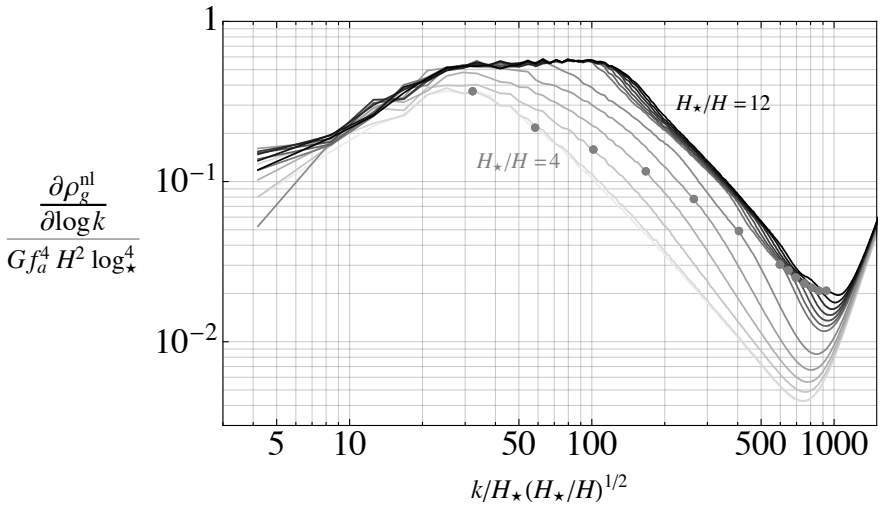

Figure G.1: The evolution of the GW spectrum generated during the nonlinear transient that the axion waves (emitted during the scaling regime) experience at the time $H \lesssim H_\star$, as a function of the (comoving) momentum. Increasing times are labelled by different values of $H_\star/H$. We show with a grey point the momentum corresponding to the axion mass. The overall redshift of the waves has been factored out in the plot by dividing the spectrum by H^2. This Figure was produced by my collaborators for our joint work [1].

of [188]. We start with a configuration of waves with the energy density spectrum from the scaling regime for $\log_\star = 65$, and we assume $m_a = R^{\alpha/2}$ with $\alpha = 8$, which is the case for the QCD axion (see Section 3.2 in [188] for more details on the details of the evolution of these waves). It is immediate to see that the spectrum in Figure G.1 is peaked at momenta a few times larger than $k \simeq x_0 H_\star$ and is of the same order as the spectrum in eq. (6.9) evaluated at $H = H_\star$ (and $k = x_0 H_\star$). Moreover, most of the GWs are produced around the time $H/H_\ell \simeq 6$, when the potential energy equals the kinetic energy and the system becomes completely nonlinear (see [188]). At the final times the field is in the linear regime except for the presence of oscillons. Being spherical, oscillons do not contribute significantly to the GWs. Indeed, the GWs stop being produced after the nonlinear regime ends (at around $H_\star/H \simeq 10$), and are not produced during the subsequent times when oscillons are present.

Finally notice that the for a temperature-independent mass, the nonlinear regime is much milder, and the contribution to the GW spectrum is smaller (and, as mentioned, outside the detectable frequency range). Given the experimental irrelevance of the GWs from the nonlinear transient, we refrain from a more detailed analytical study.

Appendix H

Other bounds

Black hole superradiance Weakly interacting light particles can spontaneously draw energy out of black holes through the phenomenon of superradiance. The observation of spinning black hole that have not had their angular momentum removed by superradiance therefore constrains the axion parameter space [233, 235, 237]. Currently, axions in the mass range $10^{-16} \div 10^{-18}$ eV are in tension with observations, however sufficiently large self-interactions prevent superradiance so the constraints only apply to $f_a \gtrsim 10^{15}$ GeV, see [238] for a detailed analysis. In the post-inflationary scenario that we consider these limits are less important than that from the axion relic abundance.

Other CMB bounds Dark matter axions with masses $\sim 10^{-25}$ eV are constrained by their effect on CMB observables independently of the presence of strings [331] (we note that bounds on such ultra light axions from neutral hydrogen intensity mapping could strengthen substantially in the future [371]). In the post-inflationary scenario these bounds are subdominant to dark energy bounds, which in some parts of the parameter space are weaker than the isocurvature constraints even with our most conservative assumption for the power spectrum of density perturbations. Additionally, a new approach to detecting strings that exist beyond the time of decoupling and are associated to an axion that interacts with photons has recently been proposed [372]. This is probably not relevant for strings that give the observable GW signals, since such long lived strings are likely to be in conflict with CMB anisotropy constraints for $f_a \gtrsim 10^{14}$ GeV.

Appendix I

Comparison to the Literature

In this Appendix we first comment on the difference between our approach and previous works on GWs from global strings from the scaling regime.[1]

- Refs. [375] and [321,376] utilise a particular model of the string evolution (also known as one-scale velocity-dependent model) and the expressions for the rate of energy emission to GWs and axions (in the zero coupling limit, derived in [311, 312]) to calculate the GW spectrum from the loops produced during the scaling regime. Such references correctly reproduce the logarithmic deviation of the GW spectrum due to the logarithmic time-dependence of the tension. In particular, the resulting $\log^3$ dependence on the momentum (and the corresponding enhancement of the spectrum) has been already pointed out in [321]. However, as such a model does not seem to always reproduce the logarithmic increase in ξ, the corresponding increase in the GW spectrum has not been captured.

- Refs. [377, 378] extract the GW spectrum directly from numerical simulations of physical systems similar to that in eq. (2.28) at small log, without any extrapolation. These references claim that the GW spectrum asymptotes to an *exactly* scale invariant form. However, as is clear from Section 6.2, this is in contradiction with conservation of energy and effective field theory, and also with our simulation results. Indeed, the spectrum results in [378] appear to show a residual time increase (and not an exactly scale invariant form).

We also observe that the original analysis of isocurvature perturbation of Section 6.3.3 has been developed for the QCD axion [257] and axion-like particles in [258, 259]. However, compared to these works we differ in our expression for the relic abundance, in the power spectrum that we use (which we obtain from simulations of the string network rather than motivated by misalignment production) and in allowing the axion to comprise a subdominant fraction of the dark matter. We also apply constraints on isocurvature from Lyman-α observations. These were derived in the

[1] There has also been some work on GW signals from axions in the pre-inflationary scenario [373, 374], which can arise if there the an axion is coupled to a light hidden sector gauge boson.

context of primordial black hole dark matter models and extended to axion string scenario in [261] (our analysis differs from this work again in our calculation of the relic abundance and in the density power spectrum that we use), see also [379, 380].

Appendix J

Cosmological Stability of the Axions and Temperature Dependent Masses

In this Appendix we show that all generic axions that lead to observable GW signals and are not ruled out by the constraints of Section 6.3 are cosmologically stable, and that also a temperature-dependent mass forces the axions to be ultralight.

As discussed in Section 6.2.4 and visible in Figure 6.6, for a temperature-independent axion mass GWs in the observable frequency range are only possible for $f_a \gtrsim 10^{14}$ GeV and $m_a \lesssim 100\,\text{keV}$ so that the string network is not destroyed before $T_\star \simeq 10^7$ GeV. In this case the axion is always stable on cosmological timescales regardless of its interactions. For example, the axion might have an interaction with photons of the form [330]

$$\mathcal{L} \supset -C\frac{\alpha_{\text{EM}}}{8\pi f_a} a F_{\mu\nu}\tilde{F}^{\mu\nu} \,, \tag{J.1}$$

which allows decays, where $F_{\mu\nu}$ is the electromagnetic field strength with associated coupling constant α_{EM}, and the coefficient C is model-dependent and expected to be not much larger than order one for the theory to be perturbative. However, denoting the temperature of the universe when $H = m_a$ by $T_\star$ the corresponding lifetime

$$\Gamma^{-1}_{a\to\gamma\gamma} = \frac{1}{C^2}\left(\frac{\text{MeV}}{m_a}\right)^3\left(\frac{f_a}{10^{14}\ \text{GeV}}\right)^2 10^{21}\ \text{s} \tag{J.2}$$

$$= \frac{1}{C^2}\left(\frac{6\times 10^7\ \text{GeV}}{T_\star}\right)^6\left(\frac{f_a}{10^{14}\ \text{GeV}}\right)^2 10^{21}\ \text{s} \,, \tag{J.3}$$

exceeds the age of the Universe for all the decay constants of interest and for axion masses $m_a \lesssim$ MeV, and in particular $m_a \lesssim 100$ keV. If the axion is sufficiently heavy and has suitable interactions it could also decay to leptons or hadrons, or hidden sector particles. However, these channels (or similar decays into hidden sector states) are not expected to significantly shorten the axion lifetime

compared to that corresponding to the only photon coupling and do not change the conclusion.

As mentioned in Section 6.3, a temperature-dependent mass does not relax the constraints in Figure 6.2.4 on f_a and $m_a(0)$ that lead to observable GWs, and still force the axion to be ultralight. To see this, we assume for simplicity that the axion mass dependence on temperature is $m_a(T) \simeq \Lambda^2/f_a \equiv m_a(0)$ for $T < \Lambda$ and $m_a(T) \leq m_a(0)$ for $T > \Lambda$, where Λ is the strong coupling scale of a new sector, which happens in typical models (for $T \gg \Lambda$ the dependence is a power law but not relevant for our present argument).

As mentioned above, the conditions for the GWs to be observable are $f_a \gtrsim 10^{14}$ GeV and $T_\star \lesssim 10^7$ GeV. If $T_\star < \Lambda$, then as far as the cosmological evolution of the string network and axions are concerned the axion mass is constant and the bounds on dark matter, dark radiation and isocurvature perturbations are those discussed in Section 6.3. On the other hand, $T_\star > \Lambda$ means that $\Lambda \lesssim 10^7$ GeV, which for $f_a \gtrsim 10^{14}$ GeV requires $m_a(0) \lesssim$ GeV. If MeV $\lesssim m_a(0) \lesssim$ GeV, such values of the axion mass and decay constant are actually ruled out as the axions decay after BBN (from eq. (J.2)) and dominate the energy density of the Universe at the time of BBN (which can be easily seen redshifting back today's would be DM abundance from eq. (6.13) to $T =$ MeV). If instead $m_a(0) \lesssim$ MeV the axion is stable and only ultralight axions do not overproduce DM ($T_\star$ in this case is always smaller than the corresponding $T_\star$ if m_a did not depend on the temperature, implying in general a larger DM abundance despite the nonlinear evolution leading to a larger suppression in this case).

We finally note that in such models there are new constraints on the effective number of degrees of freedom in the hidden sector, since Λ is far below the scale of BBN for the viable masses. These require the hidden sector is cold relative to the visible sector.

Bibliography

[1] M. Gorghetto, E. Hardy, and H. Nicolaescu, "Observing invisible axions with gravitational waves," *JCAP* **06** (2021) 034, `arXiv:2101.11007 [hep-ph]`.

[2] H. Fritzsch, M. Gell-Mann, and H. Leutwyler, "Advantages of the Color Octet Gluon Picture," *Phys. Lett. B* **47** (1973) 365–368.

[3] D. J. Gross and F. Wilczek, "Ultraviolet Behavior of Nonabelian Gauge Theories," *Phys. Rev. Lett.* **30** (1973) 1343–1346.

[4] H. D. Politzer, "Reliable Perturbative Results for Strong Interactions?," *Phys. Rev. Lett.* **30** (1973) 1346–1349.

[5] S. L. Glashow, "Partial Symmetries of Weak Interactions," *Nucl. Phys.* **22** (1961) 579–588.

[6] S. Weinberg, "A Model of Leptons," *Phys. Rev. Lett.* **19** (1967) 1264–1266.

[7] A. Salam, "Weak and Electromagnetic Interactions," *Conf. Proc. C* **680519** (1968) 367–377.

[8] M. E. Peskin and D. V. Schroeder, *An Introduction to quantum field theory*. Addison-Wesley, Reading, USA, 1995.

[9] J. S. Bell, "Time reversal in field theory," *Proc. Roy. Soc. Lond. A* **231** (1955) 479–495.

[10] F. Englert and R. Brout, "Broken Symmetry and the Mass of Gauge Vector Mesons," *Phys. Rev. Lett.* **13** (1964) 321–323.

[11] P. W. Higgs, "Broken symmetries, massless particles and gauge fields," *Phys. Lett.* **12** (1964) 132–133.

[12] P. W. Higgs, "Broken Symmetries and the Masses of Gauge Bosons," *Phys. Rev. Lett.* **13** (1964) 508–509.

[13] J. H. Christenson, J. W. Cronin, V. L. Fitch, and R. Turlay, "Evidence for the 2π Decay of the K_2^0 Meson," *Phys. Rev. Lett.* **13** (1964) 138–140.

[14] **KTeV** Collaboration, A. Alavi-Harati *et al.*, "Observation of direct CP violation in $K_{S,L} \to \pi\pi$ decays," *Phys. Rev. Lett.* **83** (1999) 22–27, arXiv:hep-ex/9905060.

[15] **NA48** Collaboration, V. Fanti *et al.*, "A New measurement of direct CP violation in two pion decays of the neutral kaon," *Phys. Lett. B* **465** (1999) 335–348, arXiv:hep-ex/9909022.

[16] **BaBar** Collaboration, B. Aubert *et al.*, "Measurement of CP violating asymmetries in B^0 decays to CP eigenstates," *Phys. Rev. Lett.* **86** (2001) 2515–2522, arXiv:hep-ex/0102030.

[17] **Belle** Collaboration, K. Abe *et al.*, "Observation of large CP violation in the neutral B meson system," *Phys. Rev. Lett.* **87** (2001) 091802, arXiv:hep-ex/0107061.

[18] **LHCb** Collaboration, R. Aaij *et al.*, "First observation of CP violation in the decays of B_s^0 mesons," *Phys. Rev. Lett.* **110** no. 22, (2013) 221601, arXiv:1304.6173 [hep-ex].

[19] **Particle Data Group** Collaboration, C. Patrignani *et al.*, "Review of Particle Physics," *Chin. Phys. C* **40** no. 10, (2016) 100001.

[20] **Super-Kamiokande** Collaboration, Y. Fukuda *et al.*, "Measurements of the solar neutrino flux from Super-Kamiokande's first 300 days," *Phys. Rev. Lett.* **81** (1998) 1158–1162, arXiv:hep-ex/9805021. [Erratum: Phys.Rev.Lett. 81, 4279 (1998)].

[21] **SNO** Collaboration, A. B. McDonald *et al.*, "Direct evidence for neutrino flavor transformation from neutral-current interactions in SNO," *AIP Conf. Proc.* **646** no. 1, (2002) 43–58.

[22] P. Minkowski, "$\mu \to e\gamma$ at a Rate of One Out of 10^9 Muon Decays?," *Phys. Lett. B* **67** (1977) 421–428.

[23] R. N. Mohapatra and G. Senjanovic, "Neutrino Mass and Spontaneous Parity Nonconservation," *Phys. Rev. Lett.* **44** (1980) 912.

[24] M. Magg and C. Wetterich, "Neutrino Mass Problem and Gauge Hierarchy," *Phys. Lett. B* **94** (1980) 61–64.

[25] J. Schechter and J. W. F. Valle, "Neutrino Masses in SU(2) x U(1) Theories," *Phys. Rev. D* **22** (1980) 2227.

[26] T. P. Cheng and L.-F. Li, "Neutrino Masses, Mixings and Oscillations in SU(2) x U(1) Models of Electroweak Interactions," *Phys. Rev. D* **22** (1980) 2860.

[27] G. Lazarides, Q. Shafi, and C. Wetterich, "Proton Lifetime and Fermion Masses in an SO(10) Model," *Nucl. Phys. B* **181** (1981) 287–300.

[28] R. N. Mohapatra and G. Senjanovic, "Neutrino Masses and Mixings in Gauge Models with Spontaneous Parity Violation," *Phys. Rev. D* **23** (1981) 165.

[29] M. Roncadelli and D. Wyler, "Naturally Light Dirac Neutrinos in Gauge Theories," *Phys. Lett. B* **133** (1983) 325–329.

[30] P. Roy and O. U. Shanker, "Observable Neutrino Dirac Mass and Supergrand Unification," *Phys. Rev. Lett.* **52** (1984) 713–716. [Erratum: Phys.Rev.Lett. 52, 2190 (1984)].

[31] S. Weinberg, "The Cosmological Constant Problem," *Rev. Mod. Phys.* **61** (1989) 1–23.

[32] J. Rubio, "Higgs inflation," *Front. Astron. Space Sci.* **5** (2019) 50, `arXiv:1807.02376 [hep-ph]`.

[33] H. Georgi and S. L. Glashow, "Unity of All Elementary Particle Forces," *Phys. Rev. Lett.* **32** (1974) 438–441.

[34] H. Fritzsch and P. Minkowski, "Unified Interactions of Leptons and Hadrons," *Annals Phys.* **93** (1975) 193–266.

[35] A. Addazi *et al.*, "Quantum gravity phenomenology at the dawn of the multi-messenger era—A review," *Prog. Part. Nucl. Phys.* **125** (2022) 103948, `arXiv:2111.05659 [hep-ph]`.

[36] C. D. Froggatt and H. B. Nielsen, "Hierarchy of Quark Masses, Cabibbo Angles and CP Violation," *Nucl. Phys. B* **147** (1979) 277–298.

[37] A. D. Sakharov, "Violation of CP Invariance, C asymmetry, and baryon asymmetry of the universe," *Pisma Zh. Eksp. Teor. Fiz.* **5** (1967) 32–35.

[38] M. B. Gavela, P. Hernandez, J. Orloff, and O. Pene, "Standard model CP violation and baryon asymmetry," *Mod. Phys. Lett. A* **9** (1994) 795–810, `arXiv:hep-ph/9312215`.

[39] T. Konstandin, T. Prokopec, and M. G. Schmidt, "Axial currents from CKM matrix CP violation and electroweak baryogenesis," *Nucl. Phys. B* **679** (2004) 246–260, `arXiv:hep-ph/0309291`.

[40] H. P. Robertson, "Kinematics and World-Structure," *Astrophys. J.* **82** (1935) 284–301.

[41] H. P. Robertson, "Kinematics and World-Structure. 2," *Astrophys. J.* **83** (1935) 187–201.

[42] H. P. Robertson, "Kinematics and World-Structure. 3," *Astrophys. J.* **83** (1936) 257–271.

[43] S. M. Carroll, *Spacetime and Geometry*. Cambridge University Press, 7, 2019.

[44] W. Hu, "Lecture Notes on CMB Theory: From Nucleosynthesis to Recombination," `arXiv:0802.3688 [astro-ph]`.

[45] **Planck** Collaboration, N. Aghanim *et al.*, "Planck 2018 results. VI. Cosmological parameters," *Astron. Astrophys.* **641** (2020) A6, arXiv:1807.06209 [astro-ph.CO].

[46] T. P. Walker, G. Steigman, D. N. Schramm, K. A. Olive, and H.-S. Kang, "Primordial nucleosynthesis redux," *Astrophys. J.* **376** (1991) 51–69.

[47] S. Sarkar, "Big bang nucleosynthesis and physics beyond the standard model," *Rept. Prog. Phys.* **59** (1996) 1493–1610, arXiv:hep-ph/9602260.

[48] K. A. Olive, G. Steigman, and T. P. Walker, "Primordial nucleosynthesis: Theory and observations," *Phys. Rept.* **333** (2000) 389–407, arXiv:astro-ph/9905320.

[49] **Particle Data Group** Collaboration, K. Hagiwara *et al.*, "Review of particle physics. Particle Data Group," *Phys. Rev. D* **66** (2002) 010001.

[50] F. Zwicky, "Die Rotverschiebung von extragalaktischen Nebeln," *Helv. Phys. Acta* **6** (1933) 110–127.

[51] V. C. Rubin and W. K. Ford, Jr., "Rotation of the Andromeda Nebula from a Spectroscopic Survey of Emission Regions," *Astrophys. J.* **159** (1970) 379–403.

[52] V. C. Rubin, W. K. Ford, Jr., and N. Thonnard, "Extended rotation curves of high-luminosity spiral galaxies. IV. Systematic dynamical properties, Sa through Sc," *Astrophys. J. Lett.* **225** (1978) L107–L111.

[53] V. C. Rubin, N. Thonnard, and W. K. Ford, Jr., "Rotational properties of 21 SC galaxies with a large range of luminosities and radii, from NGC 4605 /R = 4kpc/ to UGC 2885 /R = 122 kpc/," *Astrophys. J.* **238** (1980) 471.

[54] J. A. Tyson, R. A. Wenk, and F. Valdes, "Detection of systematic gravitational lens galaxy image alignments - Mapping dark matter in galaxy clusters," *Astrophys. J. Lett.* **349** (1990) L1–L4.

[55] G. Bertone and D. Hooper, "History of dark matter," *Rev. Mod. Phys.* **90** no. 4, (2018) 045002, arXiv:1605.04909 [astro-ph.CO].

[56] P. J. E. Peebles, "Large scale background temperature and mass fluctuations due to scale invariant primeval perturbations," *Astrophys. J. Lett.* **263** (1982) L1–L5.

[57] S. D. M. White, C. S. Frenk, and M. Davis, "Clustering in a Neutrino Dominated Universe," *Astrophys. J. Lett.* **274** (1983) L1–L5.

[58] G. R. Blumenthal, S. M. Faber, J. R. Primack, and M. J. Rees, "Formation of Galaxies and Large Scale Structure with Cold Dark Matter," *Nature* **311** (1984) 517–525.

[59] J. R. Bond and A. S. Szalay, "The Collisionless Damping of Density Fluctuations in an Expanding Universe," *Astrophys. J.* **274** (1983) 443–468.

[60] V. K. Narayanan, D. N. Spergel, R. Dave, and C.-P. Ma, "Constraints on the mass of warm dark matter particles and the shape of the linear power spectrum from the Lyα forest," *Astrophys. J. Lett.* **543** (2000) L103–L106, arXiv:astro-ph/0005095.

[61] C. Weinheimer, B. Degenddag, A. Bleile, J. Bonn, L. Bornschein, O. Kazachenko, A. Kovalik, and E. W. Otten, "High precision measurement of the tritium β spectrum near its endpoint and upper limit on the neutrino mass," *Phys. Lett. B* **460** (1999) 219–226. [Erratum: Phys.Lett.B 464, 352–352 (1999)].

[62] B. W. Lee and S. Weinberg, "Cosmological Lower Bound on Heavy Neutrino Masses," *Phys. Rev. Lett.* **39** (1977) 165–168.

[63] A. B. Lahanas, "LSP as a Candidate for Dark Matter," *Lect. Notes Phys.* **720** (2007) 35–68, arXiv:hep-ph/0607301.

[64] M. E. Peskin, "Supersymmetric dark matter in the harsh light of the Large Hadron Collider," *Proc. Nat. Acad. Sci.* **112** no. 40, (2014) 12256–12263.

[65] D. Hooper and S. Profumo, "Dark Matter and Collider Phenomenology of Universal Extra Dimensions," *Phys. Rept.* **453** (2007) 29–115, arXiv:hep-ph/0701197.

[66] J. L. Feng, S.-f. Su, and F. Takayama, "SuperWIMP dark matter in supergravity with a gravitino LSP," in *12th International Conference on Supersymmetry and Unification of Fundamental Interactions (SUSY 04)*, pp. 721–724. 10, 2004. arXiv:hep-ph/0410119.

[67] G. Steigman and M. S. Turner, "Cosmological Constraints on the Properties of Weakly Interacting Massive Particles," *Nucl. Phys. B* **253** (1985) 375–386.

[68] M. Schumann, "Direct Detection of WIMP Dark Matter: Concepts and Status," *J. Phys. G* **46** no. 10, (2019) 103003, arXiv:1903.03026 [astro-ph.CO].

[69] J. L. Feng, "Naturalness and the Status of Supersymmetry," *Ann. Rev. Nucl. Part. Sci.* **63** (2013) 351–382, arXiv:1302.6587 [hep-ph].

[70] R. D. Peccei and H. R. Quinn, "CP Conservation in the Presence of Instantons," *Phys. Rev. Lett.* **38** (1977) 1440–1443.

[71] F. Wilczek, "Problem of Strong P and T Invariance in the Presence of Instantons," *Phys. Rev. Lett.* **40** (1978) 279–282.

[72] S. Weinberg, "A New Light Boson?," *Phys. Rev. Lett.* **40** (1978) 223–226.

[73] J. E. Kim, "Weak Interaction Singlet and Strong CP Invariance," *Phys. Rev. Lett.* **43** (1979) 103.

[74] M. A. Shifman, A. I. Vainshtein, and V. I. Zakharov, "Can Confinement Ensure Natural CP Invariance of Strong Interactions?," *Nucl. Phys. B* **166** (1980) 493–506.

[75] A. R. Zhitnitsky, "On Possible Suppression of the Axion Hadron Interactions. (In Russian)," *Sov. J. Nucl. Phys.* **31** (1980) 260.

[76] M. Dine, W. Fischler, and M. Srednicki, "A Simple Solution to the Strong CP Problem with a Harmless Axion," *Phys. Lett. B* **104** (1981) 199–202.

[77] E. Witten, "Some Properties of O(32) Superstrings," *Phys. Lett. B* **149** (1984) 351–356.

[78] P. Svrcek and E. Witten, "Axions In String Theory," *JHEP* **06** (2006) 051, arXiv:hep-th/0605206.

[79] A. Arvanitaki, S. Dimopoulos, S. Dubovsky, N. Kaloper, and J. March-Russell, "String Axiverse," *Phys. Rev. D* **81** (2010) 123530, arXiv:0905.4720 [hep-th].

[80] B. S. Acharya, K. Bobkov, and P. Kumar, "An M Theory Solution to the Strong CP Problem and Constraints on the Axiverse," *JHEP* **11** (2010) 105, arXiv:1004.5138 [hep-th].

[81] M. Cicoli, M. Goodsell, and A. Ringwald, "The type IIB string axiverse and its low-energy phenomenology," *JHEP* **10** (2012) 146, arXiv:1206.0819 [hep-th].

[82] A. Ringwald, "Searching for axions and ALPs from string theory," *J. Phys. Conf. Ser.* **485** (2014) 012013, arXiv:1209.2299 [hep-ph].

[83] M. Demirtas, C. Long, L. McAllister, and M. Stillman, "The Kreuzer-Skarke Axiverse," *JHEP* **04** (2020) 138, arXiv:1808.01282 [hep-th].

[84] P. W. Graham, D. E. Kaplan, and S. Rajendran, "Cosmological Relaxation of the Electroweak Scale," *Phys. Rev. Lett.* **115** no. 22, (2015) 221801, arXiv:1504.07551 [hep-ph].

[85] G. Servant, "Baryogenesis from Strong CP Violation and the QCD Axion," *Phys. Rev. Lett.* **113** no. 17, (2014) 171803, arXiv:1407.0030 [hep-ph].

[86] P. Adshead and E. I. Sfakianakis, "Leptogenesis from left-handed neutrino production during axion inflation," *Phys. Rev. Lett.* **116** no. 9, (2016) 091301, arXiv:1508.00881 [hep-ph].

[87] P.-H. Gu, "Peccei-Quinn symmetry for Dirac seesaw and leptogenesis," *JCAP* **07** (2016) 004, arXiv:1603.05070 [hep-ph].

[88] K. S. Jeong, T. H. Jung, and C. S. Shin, "Adiabatic electroweak baryogenesis driven by an axionlike particle," *Phys. Rev. D* **101** no. 3, (2020) 035009, arXiv:1811.03294 [hep-ph].

[89] G. Ballesteros, J. Redondo, A. Ringwald, and C. Tamarit, "Standard Model—axion—seesaw—Higgs portal inflation. Five problems of particle physics and cosmology solved in one stroke," *JCAP* **08** (2017) 001, arXiv:1610.01639 [hep-ph].

[90] L. Darmé, E. Nardi, and C. Smarra, "The axion flavour connection," arXiv:2211.05796 [hep-ph].

[91] A. H. Guth, "The Inflationary Universe: A Possible Solution to the Horizon and Flatness Problems," *Phys. Rev. D* **23** (1981) 347–356.

[92] A. A. Starobinsky, "A New Type of Isotropic Cosmological Models Without Singularity," *Phys. Lett. B* **91** (1980) 99–102.

[93] A. D. Linde, "A New Inflationary Universe Scenario: A Possible Solution of the Horizon, Flatness, Homogeneity, Isotropy and Primordial Monopole Problems," *Phys. Lett. B* **108** (1982) 389–393.

[94] M. C. Guzzetti, N. Bartolo, M. Liguori, and S. Matarrese, "Gravitational waves from inflation," *Riv. Nuovo Cim.* **39** no. 9, (2016) 399–495, arXiv:1605.01615 [astro-ph.CO].

[95] M. Kamionkowski, A. Kosowsky, and A. Stebbins, "A Probe of primordial gravity waves and vorticity," *Phys. Rev. Lett.* **78** (1997) 2058–2061, arXiv:astro-ph/9609132.

[96] U. Seljak and M. Zaldarriaga, "Signature of gravity waves in polarization of the microwave background," *Phys. Rev. Lett.* **78** (1997) 2054–2057, arXiv:astro-ph/9609169.

[97] U. Seljak, "Measuring polarization in cosmic microwave background," *Astrophys. J.* **482** (1997) 6, arXiv:astro-ph/9608131.

[98] **Planck** Collaboration, Y. Akrami *et al.*, "Planck 2018 results. IX. Constraints on primordial non-Gaussianity," *Astron. Astrophys.* **641** (2020) A9, arXiv:1905.05697 [astro-ph.CO].

[99] M. Tristram *et al.*, "Improved limits on the tensor-to-scalar ratio using BICEP and Planck data," *Phys. Rev. D* **105** no. 8, (2022) 083524, arXiv:2112.07961 [astro-ph.CO].

[100] G. Galloni, N. Bartolo, S. Matarrese, M. Migliaccio, A. Ricciardone, and N. Vittorio, "Updated constraints on amplitude and tilt of the tensor primordial spectrum," arXiv:2208.00188 [astro-ph.CO].

[101] T. Matsumura *et al.*, "Mission design of LiteBIRD," *J. Low Temp. Phys.* **176** (2014) 733, arXiv:1311.2847 [astro-ph.IM].

[102] D. H. Lyth and A. Riotto, "Particle physics models of inflation and the cosmological density perturbation," *Phys. Rept.* **314** (1999) 1–146, arXiv:hep-ph/9807278.

[103] A. D. Linde, "Inflationary Cosmology," *Lect. Notes Phys.* **738** (2008) 1–54, arXiv:0705.0164 [hep-th].

[104] J. Martin, C. Ringeval, and V. Vennin, "Encyclopædia Inflationaris," *Phys. Dark Univ.* **5-6** (2014) 75–235, arXiv:1303.3787 [astro-ph.CO].

[105] J. M. Cline, L. Hoi, and B. Underwood, "Dynamical Fine Tuning in Brane Inflation," *JHEP* **06** (2009) 078, arXiv:0902.0339 [hep-th].

[106] N. Itzhaki, "The Overshoot Problem and Giant Structures," *JHEP* **10** (2008) 061, arXiv:0807.3216 [hep-th].

[107] A. D. Linde, "Quantum Creation of the Inflationary Universe," *Lett. Nuovo Cim.* **39** (1984) 401–405.

[108] A. Vilenkin, "Quantum Creation of Universes," *Phys. Rev. D* **30** (1984) 509–511.

[109] A. H. Guth and S. H. H. Tye, "Phase Transitions and Magnetic Monopole Production in the Very Early Universe," *Phys. Rev. Lett.* **44** (1980) 631. [Erratum: Phys.Rev.Lett. 44, 963 (1980)].

[110] L. Pogosian, S. Tye, I. Wasserman, and M. Wyman, "Observational constraints on cosmic string production during brane inflation," *Phys. Rev. D* **68** (2003) 023506, arXiv:hep-th/0304188. [Erratum: Phys.Rev.D 73, 089904 (2006)].

[111] M. Wyman, L. Pogosian, and I. Wasserman, "Bounds on cosmic strings from WMAP and SDSS," *Phys. Rev. D* **72** (2005) 023513, arXiv:astro-ph/0503364. [Erratum: Phys.Rev.D 73, 089905 (2006)].

[112] A. A. Fraisse, "Limits on Defects Formation and Hybrid Inflationary Models with Three-Year WMAP Observations," *JCAP* **03** (2007) 008, arXiv:astro-ph/0603589.

[113] **Planck** Collaboration, P. Ade *et al.*, "Planck 2013 results. XXV. Searches for cosmic strings and other topological defects," *Astron. Astrophys.* **571** (2014) A25, arXiv:1303.5085 [astro-ph.CO].

[114] J. H. Taylor, L. A. Fowler, and P. M. McCulloch, "Measurements of general relativistic effects in the binary pulsar PSR 1913+16," *Nature* **277** (1979) 437–440.

[115] J. H. Taylor and J. M. Weisberg, "A new test of general relativity: Gravitational radiation and the binary pulsar PS R 1913+16," *Astrophys. J.* **253** (1982) 908–920.

[116] **LIGO Scientific, Virgo** Collaboration, B. Abbott *et al.*, "Observation of Gravitational Waves from a Binary Black Hole Merger," *Phys. Rev. Lett.* **116** no. 6, (2016) 061102, arXiv:1602.03837 [gr-qc].

[117] **LIGO Scientific, Virgo** Collaboration, R. Abbott *et al.*, "GW190521: A Binary Black Hole Merger with a Total Mass of 150 M⊙," *Phys. Rev. Lett.* **125** no. 10, (2020) 101102, arXiv:2009.01075 [gr-qc].

[118] **LIGO Scientific, Virgo** Collaboration, R. Abbott *et al.*, "Properties and Astrophysical Implications of the 150 $M_\odot$ Binary Black Hole Merger GW190521," *Astrophys. J.* **900** no. 1, (2020) L13, arXiv:2009.01190 [astro-ph.HE].

[119] **LIGO Scientific, VIRGO** Collaboration, J. Aasi *et al.*, "Characterization of the LIGO detectors during their sixth science run," *Class. Quant. Grav.* **32** no. 11, (2015) 115012, arXiv:1410.7764 [gr-qc].

[120] S. Hild *et al.*, "Sensitivity Studies for Third-Generation Gravitational Wave Observatories," *Class. Quant. Grav.* **28** (2011) 094013, arXiv:1012.0908 [gr-qc].

[121] M. Punturo *et al.*, "The Einstein Telescope: A third-generation gravitational wave observatory," *Class. Quant. Grav.* **27** (2010) 194002.

[122] P. Amaro-Seoane, H. Audley, S. Babak, J. Baker, E. Barausse, P. Bender, E. Berti, P. Binetruy, M. Born, D. Bortoluzzi, J. Camp, C. Caprini, V. Cardoso, M. Colpi, J. Conklin, N. Cornish, C. Cutler, K. Danzmann, R. Dolesi, L. Ferraioli, V. Ferroni, E. Fitzsimons, J. Gair, L. G. Bote, D. Giardini, F. Gibert, C. Grimani, H. Halloin, G. Heinzel, T. Hertog, M. Hewitson, K. Holley-Bockelmann, D. Hollington, M. Hueller, H. Inchauspe, P. Jetzer, N. Karnesis, C. Killow, A. Klein, B. Klipstein, N. Korsakova, S. L. Larson, J. Livas, I. Lloro, N. Man, D. Mance, J. Martino, I. Mateos, K. McKenzie, S. T. McWilliams, C. Miller, G. Mueller, G. Nardini, G. Nelemans, M. Nofrarias, A. Petiteau, P. Pivato, E. Plagnol, E. Porter, J. Reiche, D. Robertson, N. Robertson, E. Rossi, G. Russano, B. Schutz, A. Sesana, D. Shoemaker, J. Slutsky, C. F. Sopuerta, T. Sumner, N. Tamanini, I. Thorpe, M. Troebs, M. Vallisneri, A. Vecchio, D. Vetrugno, S. Vitale, M. Volonteri, G. Wanner, H. Ward, P. Wass, W. Weber, J. Ziemer, and P. Zweifel, "Laser interferometer space antenna," 2017.

[123] K. Yagi and N. Seto, "Detector configuration of DECIGO/BBO and identification of cosmological neutron-star binaries," *Phys. Rev. D* **83** (2011) 044011, arXiv:1101.3940 [astro-ph.CO]. [Erratum: Phys.Rev.D 95, 109901 (2017)].

[124] **AEDGE** Collaboration, Y. A. El-Neaj *et al.*, "AEDGE: Atomic Experiment for Dark Matter and Gravity Exploration in Space," *EPJ Quant. Technol.* **7** (2020) 6, arXiv:1908.00802 [gr-qc].

[125] L. Badurina *et al.*, "AION: An Atom Interferometer Observatory and Network," *JCAP* **05** (2020) 011, arXiv:1911.11755 [astro-ph.CO].

[126] L. Lentati *et al.*, "European Pulsar Timing Array Limits On An Isotropic Stochastic Gravitational-Wave Background," *Mon. Not. Roy. Astron. Soc.* **453** no. 3, (2015) 2576–2598, arXiv:1504.03692 [astro-ph.CO].

[127] R. Shannon *et al.*, "Gravitational waves from binary supermassive black holes missing in pulsar observations," *Science* **349** no. 6255, (2015) 1522–1525, arXiv:1509.07320 [astro-ph.CO].

[128] G. H. Janssen, G. Hobbs, M. McLaughlin, C. G. Bassa, A. T. Deller, M. Kramer, K. J. Lee, C. M. F. Mingarelli, P. A. Rosado, S. Sanidas, A. Sesana, L. Shao, I. H. Stairs, B. W. Stappers, and J. P. W. Verbiest, "Gravitational wave astronomy with the ska," 2014.

[129] P. Baratella, A. Pomarol, and F. Rompineve, "The Supercooled Universe," *JHEP* **03** (2019) 100, arXiv:1812.06996 [hep-ph].

[130] M. Redi and A. Tesi, "The meso-inflationary QCD axion," arXiv:2211.06421 [hep-ph].

[131] K. Harigaya and L.-T. Wang, "More axions from diluted domain walls," arXiv:2211.08289 [hep-ph].

[132] W. A. Bardeen, "Anomalous Currents in Gauge Field Theories," *Nucl. Phys. B* **75** (1974) 246–258.

[133] G. 't Hooft, "Symmetry Breaking Through Bell-Jackiw Anomalies," *Phys. Rev. Lett.* **37** (1976) 8–11.

[134] **MILC** Collaboration, A. Bazavov *et al.*, "MILC results for light pseudoscalars," *PoS* **CD09** (2009) 007, arXiv:0910.2966 [hep-ph].

[135] P. Di Vecchia and G. Veneziano, "Chiral Dynamics in the Large n Limit," *Nucl. Phys. B* **171** (1980) 253–272.

[136] V. Baluni, "CP Violating Effects in QCD," *Phys. Rev. D* **19** (1979) 2227–2230.

[137] R. J. Crewther, P. Di Vecchia, G. Veneziano, and E. Witten, "Chiral Estimate of the Electric Dipole Moment of the Neutron in Quantum Chromodynamics," *Phys. Lett. B* **88** (1979) 123. [Erratum: Phys.Lett.B 91, 487 (1980)].

[138] P. Cea and G. Nardulli, "A Realistic Calculation of the Electric Dipole Moment of the Neutron Induced by Strong CP Violation," *Phys. Lett. B* **144** (1984) 115–118.

[139] H. J. Schnitzer, "The Soft Pion Skyrmion Lagrangian and Strong CP Violation," *Phys. Lett. B* **139** (1984) 217–222.

[140] M. M. Musakhanov and Z. Z. Israilov, "THE ELECTRIC DIPOLE MOMENT OF THE NEUTRON IN THE CHIRAL BAG MODEL," *Phys. Lett. B* **137** (1984) 419–421.

[141] K. Kanaya and M. Kobayashi, "Strong CP Violation in the Chiral σ Model," *Prog. Theor. Phys.* **66** (1981) 2173.

[142] J. E. Kim and G. Carosi, "Axions and the Strong CP Problem," *Rev. Mod. Phys.* **82** (2010) 557–602, arXiv:0807.3125 [hep-ph]. [Erratum: Rev.Mod.Phys. 91, 049902 (2019)].

[143] J. M. Pendlebury *et al.*, "Revised experimental upper limit on the electric dipole moment of the neutron," *Phys. Rev. D* **92** no. 9, (2015) 092003, arXiv:1509.04411 [hep-ex].

[144] G. Grilli di Cortona, E. Hardy, J. Pardo Vega, and G. Villadoro, "The QCD axion, precisely," *JHEP* **01** (2016) 034, arXiv:1511.02867 [hep-ph].

[145] M. Gorghetto and G. Villadoro, "Topological Susceptibility and QCD Axion Mass: QED and NNLO corrections," *JHEP* **03** (2019) 033, arXiv:1812.01008 [hep-ph].

[146] M. Kamionkowski and J. March-Russell, "Planck scale physics and the Peccei-Quinn mechanism," *Phys. Lett. B* **282** (1992) 137–141, arXiv:hep-th/9202003.

[147] R. Holman, S. D. Hsu, T. W. Kephart, E. W. Kolb, R. Watkins, and L. M. Widrow, "Solutions to the strong CP problem in a world with gravity," *Phys. Lett. B* **282** (1992) 132–136, arXiv:hep-ph/9203206.

[148] R. Kallosh, A. D. Linde, D. A. Linde, and L. Susskind, "Gravity and global symmetries," *Phys. Rev. D* **52** (1995) 912–935, arXiv:hep-th/9502069.

[149] M. Kreuzer and H. Skarke, "Reflexive polyhedra, weights and toric Calabi-Yau fibrations," *Rev. Math. Phys.* **14** (2002) 343–374, arXiv:math/0001106.

[150] M. R. Douglas and S. Kachru, "Flux compactification," *Rev. Mod. Phys.* **79** (2007) 733–796, arXiv:hep-th/0610102.

[151] T. Banks, M. Dine, P. J. Fox, and E. Gorbatov, "On the possibility of large axion decay constants," *JCAP* **06** (2003) 001, arXiv:hep-th/0303252.

[152] P. Svrcek, "Cosmological Constant and Axions in String Theory," arXiv:hep-th/0607086.

[153] V. M. Mehta, M. Demirtas, C. Long, D. J. E. Marsh, L. McAllister, and M. J. Stott, "Superradiance in string theory," *JCAP* **07** (2021) 033, arXiv:2103.06812 [hep-th].

[154] M. B. Green and J. H. Schwarz, "Anomaly Cancellation in Supersymmetric D=10 Gauge Theory and Superstring Theory," *Phys. Lett. B* **149** (1984) 117–122.

[155] J. E. Kim, "Light Pseudoscalars, Particle Physics and Cosmology," *Phys. Rept.* **150** (1987) 1–177.

[156] M. B. Green, J. H. Schwarz, and E. Witten, *SUPERSTRING THEORY. VOL. 2: LOOP AMPLITUDES, ANOMALIES AND PHENOMENOLOGY*. 7, 1988.

[157] J. P. Conlon, "The QCD axion and moduli stabilisation," *JHEP* **05** (2006) 078, arXiv:hep-th/0602233.

[158] M. Demirtas, N. Gendler, C. Long, L. McAllister, and J. Moritz, "PQ Axiverse," arXiv:2112.04503 [hep-th].

[159] A. Salvio, A. Strumia, and W. Xue, "Thermal axion production," *JCAP* **01** (2014) 011, arXiv:1310.6982 [hep-ph].

[160] L. Hui, "Wave Dark Matter," *Ann. Rev. Astron. Astrophys.* **59** (2021) 247–289, arXiv:2101.11735 [astro-ph.CO].

[161] J. E. Kim, "Constraints on very light axions from cavity experiments," *Phys. Rev. D* **58** (1998) 055006, arXiv:hep-ph/9802220.

[162] M. Srednicki, "Axion Couplings to Matter. 1. CP Conserving Parts," *Nucl. Phys. B* **260** (1985) 689–700.

[163] J. Preskill, M. B. Wise, and F. Wilczek, "Cosmology of the Invisible Axion," *Phys. Lett. B* **120** (1983) 127–132.

[164] L. F. Abbott and P. Sikivie, "A Cosmological Bound on the Invisible Axion," *Phys. Lett. B* **120** (1983) 133–136.

[165] M. Dine and W. Fischler, "The Not So Harmless Axion," *Phys. Lett. B* **120** (1983) 137–141.

[166] P. J. Steinhardt and M. S. Turner, "Saving the Invisible Axion," *Phys. Lett. B* **129** (1983) 51.

[167] G. Lazarides, R. K. Schaefer, D. Seckel, and Q. Shafi, "Dilution of Cosmological Axions by Entropy Production," *Nucl. Phys. B* **346** (1990) 193–212.

[168] D. J. Gross, R. D. Pisarski, and L. G. Yaffe, "QCD and Instantons at Finite Temperature," *Rev. Mod. Phys.* **53** (1981) 43.

[169] P. Fox, A. Pierce, and S. D. Thomas, "Probing a QCD string axion with precision cosmological measurements," arXiv:hep-th/0409059.

[170] O. Wantz and E. P. S. Shellard, "Axion Cosmology Revisited," *Phys. Rev. D* **82** (2010) 123508, arXiv:0910.1066 [astro-ph.CO].

[171] M. S. Turner, "Cosmic and Local Mass Density of Invisible Axions," *Phys. Rev. D* **33** (1986) 889–896.

[172] T. W. B. Kibble, "Topology of Cosmic Domains and Strings," *J. Phys. A* **9** (1976) 1387–1398.

[173] T. W. B. Kibble, "Some Implications of a Cosmological Phase Transition," *Phys. Rept.* **67** (1980) 183.

[174] W. Zurek, "Cosmological Experiments in Superfluid Helium?," *Nature* **317** (1985) 505–508.

[175] A. Vilenkin, "Cosmic Strings," *Phys. Rev. D* **24** (1981) 2082–2089.

[176] A. Albrecht and N. Turok, "Evolution of Cosmic Strings," *Phys. Rev. Lett.* **54** (1985) 1868–1871.

[177] D. P. Bennett and F. R. Bouchet, "Evidence for a Scaling Solution in Cosmic String Evolution," *Phys. Rev. Lett.* **60** (1988) 257.

[178] B. Allen and E. P. S. Shellard, "Cosmic string evolution: a numerical simulation," *Phys. Rev. Lett.* **64** (1990) 119–122.

[179] G. R. Vincent, M. Hindmarsh, and M. Sakellariadou, "Scaling and small scale structure in cosmic string networks," *Phys. Rev. D* **56** (1997) 637–646, arXiv:astro-ph/9612135.

[180] C. J. A. P. Martins and E. P. S. Shellard, "Extending the velocity dependent one scale string evolution model," *Phys. Rev. D* **65** (2002) 043514, arXiv:hep-ph/0003298.

[181] A. Vilenkin and E. P. S. Shellard, *Cosmic Strings and Other Topological Defects*. Cambridge University Press, 7, 2000.

[182] L. Fleury and G. D. Moore, "Axion dark matter: strings and their cores," *JCAP* **01** (2016) 004, arXiv:1509.00026 [hep-ph].

[183] V. B. . Klaer and G. D. Moore, "The dark-matter axion mass," *JCAP* **11** (2017) 049, arXiv:1708.07521 [hep-ph].

[184] A. Vaquero, J. Redondo, and J. Stadler, "Early seeds of axion miniclusters," *JCAP* **04** (2019) 012, arXiv:1809.09241 [astro-ph.CO].

[185] M. Kawasaki, T. Sekiguchi, M. Yamaguchi, and J. Yokoyama, "Long-term dynamics of cosmological axion strings," *PTEP* **2018** no. 9, (2018) 091E01, arXiv:1806.05566 [hep-ph].

[186] M. Gorghetto, E. Hardy, and G. Villadoro, "Axions from Strings: the Attractive Solution," *JHEP* **07** (2018) 151, arXiv:1806.04677 [hep-ph].

[187] M. Buschmann, J. W. Foster, and B. R. Safdi, "Early-Universe Simulations of the Cosmological Axion," *Phys. Rev. Lett.* **124** no. 16, (2020) 161103, arXiv:1906.00967 [astro-ph.CO].

[188] M. Gorghetto, E. Hardy, and G. Villadoro, "More axions from strings," *SciPost Phys.* **10** no. 2, (2021) 050, arXiv:2007.04990 [hep-ph].

[189] M. Buschmann, J. W. Foster, A. Hook, A. Peterson, D. E. Willcox, W. Zhang, and B. R. Safdi, "Dark matter from axion strings with adaptive mesh refinement," *Nature Commun.* **13** no. 1, (2022) 1049, arXiv:2108.05368 [hep-ph].

[190] G. B. Gelmini, M. Gleiser, and E. W. Kolb, "Cosmology of Biased Discrete Symmetry Breaking," *Phys. Rev. D* **39** (1989) 1558.

[191] T. Hiramatsu, M. Kawasaki, K. Saikawa, and T. Sekiguchi, "Axion cosmology with long-lived domain walls," *JCAP* **01** (2013) 001, arXiv:1207.3166 [hep-ph].

[192] M. Axenides, R. H. Brandenberger, and M. S. Turner, "Development of Axion Perturbations in an Axion Dominated Universe," *Phys. Lett. B* **126** (1983) 178–182.

[193] A. D. Linde, "Generation of Isothermal Density Perturbations in the Inflationary Universe," *Phys. Lett. B* **158** (1985) 375–380.

[194] D. Seckel and M. S. Turner, "Isothermal Density Perturbations in an Axion Dominated Inflationary Universe," *Phys. Rev. D* **32** (1985) 3178.

[195] D. H. Lyth, "A Limit on the Inflationary Energy Density From Axion Isocurvature Fluctuations," *Phys. Lett. B* **236** (1990) 408–410.

[196] M. S. Turner and F. Wilczek, "Inflationary axion cosmology," *Phys. Rev. Lett.* **66** (1991) 5–8.

[197] A. D. Linde and D. H. Lyth, "Axionic domain wall production during inflation," *Phys. Lett. B* **246** (1990) 353–358.

[198] D. H. Lyth, "Axions and inflation: Sitting in the vacuum," *Phys. Rev. D* **45** (1992) 3394–3404.

[199] M. Beltran, J. Garcia-Bellido, and J. Lesgourgues, "Isocurvature bounds on axions revisited," *Phys. Rev. D* **75** (2007) 103507, arXiv:hep-ph/0606107.

[200] M. P. Hertzberg, M. Tegmark, and F. Wilczek, "Axion Cosmology and the Energy Scale of Inflation," *Phys. Rev. D* **78** (2008) 083507, arXiv:0807.1726 [astro-ph].

[201] T. Kobayashi, R. Kurematsu, and F. Takahashi, "Isocurvature Constraints and Anharmonic Effects on QCD Axion Dark Matter," *JCAP* **09** (2013) 032, arXiv:1304.0922 [hep-ph].

[202] K. Schmitz and T. T. Yanagida, "Axion Isocurvature Perturbations in Low-Scale Models of Hybrid Inflation," *Phys. Rev. D* **98** no. 7, (2018) 075003, arXiv:1806.06056 [hep-ph].

[203] L. Jukko and A. Rajantie, "Stochastic isocurvature constraints for axion dark matter with high-scale inflation," arXiv:2107.07948 [astro-ph.CO].

[204] **WMAP** Collaboration, E. Komatsu *et al.*, "Five-Year Wilkinson Microwave Anisotropy Probe (WMAP) Observations: Cosmological Interpretation," *Astrophys. J. Suppl.* **180** (2009) 330–376, arXiv:0803.0547 [astro-ph].

[205] **Planck** Collaboration, Y. Akrami *et al.*, "Planck 2018 results. X. Constraints on inflation," *Astron. Astrophys.* **641** (2020) A10, arXiv:1807.06211 [astro-ph.CO].

[206] H. Primakoff, "Photoproduction of neutral mesons in nuclear electric fields and the mean life of the neutral meson," *Phys. Rev.* **81** (1951) 899.

[207] P. Sikivie, "Experimental Tests of the Invisible Axion," *Phys. Rev. Lett.* **51** (1983) 1415–1417. [Erratum: Phys.Rev.Lett. 52, 695 (1984)].

[208] K. Van Bibber, N. R. Dagdeviren, S. E. Koonin, A. Kerman, and H. N. Nelson, "Proposed experiment to produce and detect light pseudoscalars," *Phys. Rev. Lett.* **59** (1987) 759–762.

[209] **CAST** Collaboration, K. Zioutas *et al.*, "First results from the CERN Axion Solar Telescope (CAST)," *Phys. Rev. Lett.* **94** (2005) 121301, arXiv:hep-ex/0411033.

[210] **CAST** Collaboration, S. Andriamonje *et al.*, "An Improved limit on the axion-photon coupling from the CAST experiment," *JCAP* **04** (2007) 010, arXiv:hep-ex/0702006.

[211] **CAST** Collaboration, M. Arik *et al.*, "Search for Solar Axions by the CERN Axion Solar Telescope with ^{3}He Buffer Gas: Closing the Hot Dark Matter Gap," *Phys. Rev. Lett.* **112** no. 9, (2014) 091302, arXiv:1307.1985 [hep-ex].

[212] **IAXO** Collaboration, E. Armengaud *et al.*, "Physics potential of the International Axion Observatory (IAXO)," *JCAP* **06** (2019) 047, arXiv:1904.09155 [hep-ph].

[213] K. Ehret *et al.*, "New ALPS Results on Hidden-Sector Lightweights," *Phys. Lett. B* **689** (2010) 149–155, arXiv:1004.1313 [hep-ex].

[214] **ADMX** Collaboration, S. J. Asztalos *et al.*, "A SQUID-based microwave cavity search for dark-matter axions," *Phys. Rev. Lett.* **104** (2010) 041301, arXiv:0910.5914 [astro-ph.CO].

[215] **ADMX** Collaboration, N. Du *et al.*, "A Search for Invisible Axion Dark Matter with the Axion Dark Matter Experiment," *Phys. Rev. Lett.* **120** no. 15, (2018) 151301, arXiv:1804.05750 [hep-ex].

[216] **ADMX** Collaboration, T. Braine *et al.*, "Extended Search for the Invisible Axion with the Axion Dark Matter Experiment," *Phys. Rev. Lett.* **124** no. 10, (2020) 101303, arXiv:1910.08638 [hep-ex].

[217] **ADMX** Collaboration, C. Bartram *et al.*, "Search for Invisible Axion Dark Matter in the 3.3–4.2 μeV Mass Range," *Phys. Rev. Lett.* **127** no. 26, (2021) 261803, arXiv:2110.06096 [hep-ex].

[218] I. Stern, "ADMX Status," *PoS* **ICHEP2016** (2016) 198, arXiv:1612.08296 [physics.ins-det].

[219] B. T. McAllister, G. Flower, J. Kruger, E. N. Ivanov, M. Goryachev, J. Bourhill, and M. E. Tobar, "The ORGAN Experiment: An axion haloscope above 15 GHz," *Phys. Dark Univ.* **18** (2017) 67–72, arXiv:1706.00209 [physics.ins-det].

[220] M. Lawson, A. J. Millar, M. Pancaldi, E. Vitagliano, and F. Wilczek, "Tunable axion plasma haloscopes," *Phys. Rev. Lett.* **123** no. 14, (2019) 141802, arXiv:1904.11872 [hep-ph].

[221] S. Beurthey *et al.*, "MADMAX Status Report," arXiv:2003.10894 [physics.ins-det].

[222] **BREAD** Collaboration, J. Liu *et al.*, "Broadband Solenoidal Haloscope for Terahertz Axion Detection," *Phys. Rev. Lett.* **128** no. 13, (2022) 131801, arXiv:2111.12103 [physics.ins-det].

[223] G. G. Raffelt and D. S. P. Dearborn, "Bounds on Hadronic Axions From Stellar Evolution," *Phys. Rev. D* **36** (1987) 2211.

[224] A. Ayala, I. Domínguez, M. Giannotti, A. Mirizzi, and O. Straniero, "Revisiting the bound on axion-photon coupling from Globular Clusters," *Phys. Rev. Lett.* **113** no. 19, (2014) 191302, arXiv:1406.6053 [astro-ph.SR].

[225] G. G. Raffelt, "Astrophysical axion bounds," *Lect. Notes Phys.* **741** (2008) 51–71, arXiv:hep-ph/0611350.

[226] J. H. Chang, R. Essig, and S. D. McDermott, "Supernova 1987A Constraints on Sub-GeV Dark Sectors, Millicharged Particles, the QCD Axion, and an Axion-like Particle," *JHEP* **09** (2018) 051, arXiv:1803.00993 [hep-ph].

[227] P. Carenza, T. Fischer, M. Giannotti, G. Guo, G. Martínez-Pinedo, and A. Mirizzi, "Improved axion emissivity from a supernova via nucleon-nucleon bremsstrahlung," *JCAP* **10** no. 10, (2019) 016, arXiv:1906.11844 [hep-ph]. [Erratum: JCAP 05, E01 (2020)].

[228] N. Bar, K. Blum, and G. D'Amico, "Is there a supernova bound on axions?," *Phys. Rev. D* **101** no. 12, (2020) 123025, arXiv:1907.05020 [hep-ph].

[229] R. Penrose, "Gravitational collapse: The role of general relativity," *Riv. Nuovo Cim.* **1** (1969) 252–276.

[230] D. Christodoulou, "Reversible and irreversible transforations in black hole physics," *Phys. Rev. Lett.* **25** (1970) 1596–1597.

[231] W. H. Press and S. A. Teukolsky, "Floating Orbits, Superradiant Scattering and the Black-hole Bomb," *Nature* **238** (1972) 211–212.

[232] W. H. Press and S. A. Teukolsky, "Perturbations of a Rotating Black Hole. II. Dynamical Stability of the Kerr Metric," *Astrophys. J.* **185** (1973) 649–674.

[233] A. Arvanitaki and S. Dubovsky, "Exploring the String Axiverse with Precision Black Hole Physics," *Phys. Rev. D* **83** (2011) 044026, arXiv:1004.3558 [hep-th].

[234] P. Pani, V. Cardoso, L. Gualtieri, E. Berti, and A. Ishibashi, "Black hole bombs and photon mass bounds," *Phys. Rev. Lett.* **109** (2012) 131102, arXiv:1209.0465 [gr-qc].

[235] A. Arvanitaki, M. Baryakhtar, and X. Huang, "Discovering the QCD Axion with Black Holes and Gravitational Waves," *Phys. Rev. D* **91** no. 8, (2015) 084011, arXiv:1411.2263 [hep-ph].

[236] R. Brito, V. Cardoso, and P. Pani, "Black holes as particle detectors: evolution of superradiant instabilities," *Class. Quant. Grav.* **32** no. 13, (2015) 134001, arXiv:1411.0686 [gr-qc].

[237] M. J. Stott and D. J. Marsh, "Black hole spin constraints on the mass spectrum and number of axionlike fields," *Phys. Rev. D* **98** no. 8, (2018) 083006, arXiv:1805.02016 [hep-ph].

[238] M. Baryakhtar, M. Galanis, R. Lasenby, and O. Simon, "Black hole superradiance of self-interacting scalar fields," arXiv:2011.11646 [hep-ph].

[239] C. O'Hare, "cajohare/axionlimits: Axionlimits." https://cajohare.github.io/AxionLimits/, July, 2020.

[240] A. Riotto, "Inflation and the theory of cosmological perturbations," *ICTP Lect. Notes Ser.* **14** (2003) 317–413, arXiv:hep-ph/0210162.

[241] D. Baumann, "Inflation," in *Theoretical Advanced Study Institute in Elementary Particle Physics: Physics of the Large and the Small*, pp. 523–686. 2011. arXiv:0907.5424 [hep-th].

[242] T. S. Bunch and P. C. W. Davies, "Quantum Field Theory in de Sitter Space: Renormalization by Point Splitting," *Proc. Roy. Soc. Lond. A* **360** (1978) 117–134.

[243] A. A. Starobinsky, "Dynamics of Phase Transition in the New Inflationary Universe Scenario and Generation of Perturbations," *Phys. Lett. B* **117** (1982) 175–178.

[244] A. A. Starobinsky and J. Yokoyama, "Equilibrium state of a selfinteracting scalar field in the De Sitter background," *Phys. Rev. D* **50** (1994) 6357–6368, arXiv:astro-ph/9407016.

[245] M. Sasaki, H. Suzuki, K. Yamamoto, and J. Yokoyama, "Superexpansionary divergence: Breakdown of perturbative quantum field theory in space-time with accelerated expansion," *Class. Quant. Grav.* **10** (1993) L55–L60.

[246] S. Stopyra, "Higgs dynamics during inflation (master thesis)," 2014. https://www.imperial.ac.uk/media/imperial-college/research-centres-and-groups/theoretical-physics/msc/dissertations/2014/Stephen-Stopyra-Dissertation.pdf.

[247] D. Tong, "Lectures on kinetic theory," 2012. https://www.damtp.cam.ac.uk/user/tong/kintheory/.

[248] P. W. Graham and A. Scherlis, "Stochastic axion scenario," *Phys. Rev. D* **98** no. 3, (2018) 035017, arXiv:1805.07362 [hep-ph].

[249] F. Takahashi, W. Yin, and A. H. Guth, "QCD axion window and low-scale inflation," *Phys. Rev. D* **98** no. 1, (2018) 015042, arXiv:1805.08763 [hep-ph].

[250] J. M. Bardeen, J. R. Bond, N. Kaiser, and A. S. Szalay, "The Statistics of Peaks of Gaussian Random Fields," *Astrophys. J.* **304** (1986) 15–61.

[251] D. H. Lyth and E. D. Stewart, "Axions and inflation: String formation during inflation," *Phys. Rev. D* **46** (1992) 532–538.

[252] M. Fairbairn, R. Hogan, and D. J. E. Marsh, "Unifying inflation and dark matter with the Peccei-Quinn field: observable axions and observable tensors," *Phys. Rev. D* **91** no. 2, (2015) 023509, arXiv:1410.1752 [hep-ph].

[253] C. Han, "QCD axion dark matter and the cosmic dipole anomaly," arXiv:2211.06912 [hep-ph].

[254] W. R. Inc., "Mathematica, Version 13.3." https://www.wolfram.com/mathematica. Champaign, IL, 2023.

[255] G. B. Gelmini, S. Pascoli, E. Vitagliano, and Y.-L. Zhou, "Gravitational wave signatures from discrete flavor symmetries," *JCAP* **02** (2021) 032, arXiv:2009.01903 [hep-ph].

[256] C. Hogan and M. Rees, "AXION MINICLUSTERS," *Phys. Lett. B* **205** (1988) 228–230.

[257] J. Enander, A. Pargner, and T. Schwetz, "Axion minicluster power spectrum and mass function," *JCAP* **12** (2017) 038, arXiv:1708.04466 [astro-ph.CO].

[258] M. Feix, J. Frank, A. Pargner, R. Reischke, B. M. Schäfer, and T. Schwetz, "Isocurvature bounds on axion-like particle dark matter in the post-inflationary scenario," *JCAP* **05** (2019) 021, arXiv:1903.06194 [astro-ph.CO].

[259] M. Feix, S. Hagstotz, A. Pargner, R. Reischke, B. M. Schäfer, and T. Schwetz, "Post-inflationary axion isocurvature perturbations facing CMB and large-scale structure," *JCAP* **11** (2020) 046, arXiv:2004.02926 [astro-ph.CO].

[260] R. Murgia, G. Scelfo, M. Viel, and A. Raccanelli, "Lyman-α forest constraints on primordial black holes as dark matter," *Physical Review Letters* **123** no. 7, (Aug, 2019) . http://dx.doi.org/10.1103/PhysRevLett.123.071102.

[261] V. Irˇ sič, H. Xiao, and M. McQuinn, "Early Structure Formation Constraints on the Ultra-Light Axion in the Post-Inflation Scenario," arXiv:1911.11150 [astro-ph.CO].

[262] E. W. Kolb and I. I. Tkachev, "Large amplitude isothermal fluctuations and high density dark matter clumps," *Phys. Rev. D* **50** (1994) 769–773, arXiv:astro-ph/9403011.

[263] E. W. Kolb and I. I. Tkachev, "Femtolensing and picolensing by axion miniclusters," *Astrophys. J. Lett.* **460** (1996) L25–L28, arXiv:astro-ph/9510043.

[264] K. Strobl and T. J. Weiler, "Anharmonic evolution of the cosmic axion density spectrum," *Phys. Rev. D* **50** (1994) 7690–7702, arXiv:astro-ph/9405028.

[265] K. J. Bae, J.-H. Huh, and J. E. Kim, "Update of axion CDM energy," *JCAP* **09** (2008) 005, arXiv:0806.0497 [hep-ph].

[266] L. Visinelli and P. Gondolo, "Dark Matter Axions Revisited," *Phys. Rev. D* **80** (2009) 035024, arXiv:0903.4377 [astro-ph.CO].

[267] A. Arvanitaki, S. Dimopoulos, M. Galanis, L. Lehner, J. O. Thompson, and K. Van Tilburg, "Large-misalignment mechanism for the formation of compact axion structures: Signatures from the QCD axion to fuzzy dark matter," *Phys. Rev. D* **101** no. 8, (2020) 083014, arXiv:1909.11665 [astro-ph.CO].

[268] P. Sikivie, "Of Axions, Domain Walls and the Early Universe," *Phys. Rev. Lett.* **48** (1982) 1156–1159.

[269] S. M. Barr and D. Seckel, "Planck scale corrections to axion models," *Phys. Rev. D* **46** (1992) 539–549.

[270] S. E. Larsson, S. Sarkar, and P. L. White, "Evading the cosmological domain wall problem," *Phys. Rev. D* **55** (1997) 5129–5135, arXiv:hep-ph/9608319.

[271] S. Chang, C. Hagmann, and P. Sikivie, "Studies of the motion and decay of axion walls bounded by strings," *Phys. Rev. D* **59** (1999) 023505, arXiv:hep-ph/9807374.

[272] J. Garriga and M. Sakellariadou, "Effects of friction on cosmic strings," *Phys. Rev. D* **48** (1993) 2502–2515, arXiv:hep-th/9303024.

[273] R. Battye and E. Shellard, "Axion string constraints," *Phys. Rev. Lett.* **73** (1994) 2954–2957, arXiv:astro-ph/9403018. [Erratum: Phys.Rev.Lett. 76, 2203–2204 (1996)].

[274] A. Vilenkin, "Cosmic string dynamics with friction," *Phys. Rev. D* **43** (1991) 1060–1062.

[275] C. Martins and E. Shellard, "String evolution with friction," *Phys. Rev. D* **53** (1996) 575–579, arXiv:hep-ph/9507335.

[276] P. Agrawal, A. Hook, J. Huang, and G. Marques-Tavares, "Axion string signatures II: A cosmological plasma collider," arXiv:2010.15848 [hep-ph].

[277] A. D. Linde, "Axions in inflationary cosmology," *Phys. Lett. B* **259** (1991) 38–47.

[278] A. D. Linde, "Hybrid inflation," *Phys. Rev. D* **49** (1994) 748–754, arXiv:astro-ph/9307002.

[279] E. J. Copeland, A. R. Liddle, D. H. Lyth, E. D. Stewart, and D. Wands, "False vacuum inflation with Einstein gravity," *Phys. Rev. D* **49** (1994) 6410–6433, arXiv:astro-ph/9401011.

[280] D. H. Lyth and A. Riotto, "Particle physics models of inflation and the cosmological density perturbation," *Physics Reports* **314** no. 1-2, (1999) 1–146.

[281] R. Allahverdi and M. Drees, "Thermalization after inflation and production of massive stable particles," *Phys. Rev. D* **66** (2002) 063513, arXiv:hep-ph/0205246.

[282] A. Mazumdar and B. Zaldivar, "Quantifying the reheating temperature of the universe," *Nucl. Phys. B* **886** (2014) 312–327, arXiv:1310.5143 [hep-ph].

[283] D. Kirzhnits and A. D. Linde, "Macroscopic Consequences of the Weinberg Model," *Phys. Lett. B* **42** (1972) 471–474.

[284] D. Kirzhnits and A. D. Linde, "A Relativistic phase transition," *Sov. Phys. JETP* **40** (1975) 628.

[285] S. Weinberg, "Gauge and Global Symmetries at High Temperature," *Phys. Rev. D* **9** (1974) 3357–3378.

[286] G. Dvali and G. Senjanovic, "Is there a domain wall problem?," *Phys. Rev. Lett.* **74** (1995) 5178–5181, arXiv:hep-ph/9501387.

[287] A. Albrecht, P. J. Steinhardt, M. S. Turner, and F. Wilczek, "Reheating an Inflationary Universe," *Phys. Rev. Lett.* **48** (1982) 1437.

[288] A. D. Dolgov and A. D. Linde, "Baryon Asymmetry in Inflationary Universe," *Phys. Lett. B* **116** (1982) 329.

[289] L. F. Abbott, E. Farhi, and M. B. Wise, "Particle Production in the New Inflationary Cosmology," *Phys. Lett. B* **117** (1982) 29.

[290] G. F. Giudice, E. W. Kolb, and A. Riotto, "Largest temperature of the radiation era and its cosmological implications," *Phys. Rev. D* **64** (2001) 023508, arXiv:hep-ph/0005123.

[291] Y. Shtanov, J. H. Traschen, and R. H. Brandenberger, "Universe reheating after inflation," *Phys. Rev. D* **51** (1995) 5438–5455, arXiv:hep-ph/9407247.

[292] L. Kofman, A. D. Linde, and A. A. Starobinsky, "Nonthermal phase transitions after inflation," *Phys. Rev. Lett.* **76** (1996) 1011–1014, arXiv:hep-th/9510119.

[293] I. I. Tkachev, "Phase transitions at preheating," *Phys. Lett. B* **376** (1996) 35–40, arXiv:hep-th/9510146.

[294] I. Tkachev, S. Khlebnikov, L. Kofman, and A. D. Linde, "Cosmic strings from preheating," *Phys. Lett. B* **440** (1998) 262–268, arXiv:hep-ph/9805209.

[295] M. F. Parry and A. T. Sornborger, "Domain wall production during inflationary reheating," *Phys. Rev. D* **60** (1999) 103504, arXiv:hep-ph/9805211.

[296] G. F. Giudice, A. Riotto, and I. Tkachev, "Thermal and nonthermal production of gravitinos in the early universe," *JHEP* **11** (1999) 036, arXiv:hep-ph/9911302.

[297] G. F. Giudice, I. Tkachev, and A. Riotto, "Nonthermal production of dangerous relics in the early universe," *JHEP* **08** (1999) 009, arXiv:hep-ph/9907510.

[298] L. Kofman, A. D. Linde, and A. A. Starobinsky, "Towards the theory of reheating after inflation," *Phys. Rev. D* **56** (1997) 3258–3295, arXiv:hep-ph/9704452.

[299] N. W. McLachlan, *Theory and application of Mathieu functions*. Clarendon Press, Oxford, 1951. https://cds.cern.ch/record/104546.

[300] P. B. Greene, L. Kofman, A. D. Linde, and A. A. Starobinsky, "Structure of resonance in preheating after inflation," *Phys. Rev. D* **56** (1997) 6175–6192, arXiv:hep-ph/9705347.

[301] S. Khlebnikov and I. Tkachev, "The Universe after inflation: The Wide resonance case," *Phys. Lett. B* **390** (1997) 80–86, arXiv:hep-ph/9608458.

[302] G. D'Amico and N. Kaloper, "Rollercoaster cosmology," *JCAP* **08** (2021) 058, arXiv:2011.09489 [hep-th].

[303] L. Dolan and R. Jackiw, "Symmetry Behavior at Finite Temperature," *Phys. Rev. D* **9** (1974) 3320–3341.

[304] P. B. Arnold and C.-X. Zhai, "The Three loop free energy for pure gauge QCD," *Phys. Rev. D* **50** (1994) 7603–7623, arXiv:hep-ph/9408276.

[305] G. B. Gelmini, A. Simpson, and E. Vitagliano, "Catastrogenesis: DM, GWs, and PBHs from ALP string-wall networks," arXiv:2207.07126 [hep-ph].

[306] F. Lund and T. Regge, "Unified Approach to Strings and Vortices with Soliton Solutions," *Phys. Rev. D* **14** (1976) 1524.

[307] M. Kalb and P. Ramond, "Classical direct interstring action," *Phys. Rev. D* **9** (1974) 2273–2284.

[308] R. Davis and E. Shellard, "Antisymmetric Tensors and Spontaneous Symmetry Breaking," *Phys. Lett. B* **214** (1988) 219–222.

[309] A. Dabholkar and J. M. Quashnock, "Pinning Down the Axion," *Nucl. Phys. B* **333** (1990) 815–832.

[310] B. Horn, A. Nicolis, and R. Penco, "Effective string theory for vortex lines in fluids and superfluids," *JHEP* **10** (2015) 153, arXiv:1507.05635 [hep-th].

[311] T. Vachaspati and A. Vilenkin, "Gravitational Radiation from Cosmic Strings," *Phys. Rev. D* **31** (1985) 3052.

[312] A. Vilenkin and T. Vachaspati, "Radiation of Goldstone Bosons From Cosmic Strings," *Phys. Rev. D* **35** (1987) 1138.

[313] E. J. Copeland, D. Haws, and M. Hindmarsh, "Classical theory of radiating strings," *Phys. Rev. D* **42** (1990) 726–730.

[314] J. M. Quashnock and D. N. Spergel, "Gravitational Selfinteractions of Cosmic Strings," *Phys. Rev. D* **42** (1990) 2505–2520.

[315] P. Auclair *et al.*, "Probing the gravitational wave background from cosmic strings with LISA," *JCAP* **04** (2020) 034, arXiv:1909.00819 [astro-ph.CO].

[316] C. Caprini, R. Durrer, T. Konstandin, and G. Servant, "General Properties of the Gravitational Wave Spectrum from Phase Transitions," *Phys. Rev. D* **79** (2009) 083519, arXiv:0901.1661 [astro-ph.CO].

[317] **NANOGrav** Collaboration, Z. Arzoumanian *et al.*, "The NANOGrav 12.5-year Data Set: Search For An Isotropic Stochastic Gravitational-Wave Background," arXiv:2009.04496 [astro-ph.HE].

[318] E. Thrane and J. D. Romano, "Sensitivity curves for searches for gravitational-wave backgrounds," *Phys. Rev. D* **88** no. 12, (2013) 124032, arXiv:1310.5300 [astro-ph.IM].

[319] C. Moore, R. Cole, and C. Berry, "Gravitational-wave sensitivity curves," *Class. Quant. Grav.* **32** no. 1, (2015) 015014, arXiv:1408.0740 [gr-qc].

[320] J. D. Romano and N. J. Cornish, "Detection methods for stochastic gravitational-wave backgrounds: a unified treatment," *Living Rev. Rel.* **20** no. 1, (2017) 2, arXiv:1608.06889 [gr-qc].

[321] Y. Gouttenoire, G. Servant, and P. Simakachorn, "Beyond the Standard Models with Cosmic Strings," *JCAP* **07** (2020) 032, arXiv:1912.02569 [hep-ph].

[322] D. P. Bennett and F. R. Bouchet, "High resolution simulations of cosmic string evolution. 1. Network evolution," *Phys. Rev. D* **41** (1990) 2408.

[323] V. B. Klaer and G. D. Moore, "How to simulate global cosmic strings with large string tension," *JCAP* **10** (2017) 043, arXiv:1707.05566 [hep-ph].

[324] V. B. Klaer and G. D. Moore, "Global cosmic string networks as a function of tension," *JCAP* **06** (2020) 021, arXiv:1912.08058 [hep-ph].

[325] M. Giovannini, "Gravitational waves constraints on postinflationary phases stiffer than radiation," *Phys. Rev. D* **58** (1998) 083504, arXiv:hep-ph/9806329.

[326] A. Riazuelo and J.-P. Uzan, "Quintessence and gravitational waves," *Phys. Rev. D* **62** (2000) 083506, arXiv:astro-ph/0004156.

[327] Y. Cui, M. Lewicki, D. E. Morrissey, and J. D. Wells, "Probing the pre-BBN universe with gravitational waves from cosmic strings," *JHEP* **01** (2019) 081, arXiv:1808.08968 [hep-ph].

[328] N. Ramberg and L. Visinelli, "Probing the Early Universe with Axion Physics and Gravitational Waves," *Phys. Rev. D* **99** no. 12, (2019) 123513, arXiv:1904.05707 [astro-ph.CO].

[329] R. Battye, R. Caldwell, and E. Shellard, "Gravitational waves from cosmic strings," in *Conference on Topological Defects and CMB*, pp. 11–31. 6, 1997. arXiv:astro-ph/9706013.

[330] P. Arias, D. Cadamuro, M. Goodsell, J. Jaeckel, J. Redondo, and A. Ringwald, "WISPy Cold Dark Matter," *JCAP* **06** (2012) 013, arXiv:1201.5902 [hep-ph].

[331] R. Hlozek, D. J. E. Marsh, and D. Grin, "Using the Full Power of the Cosmic Microwave Background to Probe Axion Dark Matter," *Mon. Not. Roy. Astron. Soc.* **476** no. 3, (2018) 3063–3085, arXiv:1708.05681 [astro-ph.CO].

[332] C. Dvorkin *et al.*, "Dark Matter Physics from the CMB-S4 Experiment," in *Snowmass 2021*. 3, 2022. arXiv:2203.07064 [hep-ph].

[333] L. Hui, J. P. Ostriker, S. Tremaine, and E. Witten, "Ultralight scalars as cosmological dark matter," *Phys. Rev. D* **95** no. 4, (2017) 043541, arXiv:1610.08297 [astro-ph.CO].

[334] V. Irˇ sič, M. Viel, M. G. Haehnelt, J. S. Bolton, and G. D. Becker, "First constraints on fuzzy dark matter from Lyman-α forest data and hydrodynamical simulations," *Phys. Rev. Lett.* **119** no. 3, (2017) 031302, arXiv:1703.04683 [astro-ph.CO].

[335] T. Kobayashi, R. Murgia, A. De Simone, V. Irˇ sič, and M. Viel, "Lyman-α constraints on ultralight scalar dark matter: Implications for the early and late universe," *Phys. Rev. D* **96** no. 12, (2017) 123514, arXiv:1708.00015 [astro-ph.CO].

[336] K. K. Rogers and H. V. Peiris, "Strong bound on canonical ultra-light axion dark matter from the Lyman-alpha forest," arXiv:2007.12705 [astro-ph.CO].

[337] C. Pitrou, A. Coc, J.-P. Uzan, and E. Vangioni, "Precision big bang nucleosynthesis with improved Helium-4 predictions," *Phys. Rept.* **754** (2018) 1–66, arXiv:1801.08023 [astro-ph.CO].

[338] **Topical Conveners: K.N. Abazajian, J.E. Carlstrom, A.T. Lee** Collaboration, K. Abazajian *et al.*, "Neutrino Physics from the Cosmic Microwave Background and Large Scale Structure," *Astropart. Phys.* **63** (2015) 66–80, arXiv:1309.5383 [astro-ph.CO].

[339] J. A. Dror, H. Murayama, and N. L. Rodd, "The Cosmic Axion Background," arXiv:2101.09287 [hep-ph].

[340] Y. Zeldovich, "Cosmological fluctuations produced near a singularity," *Mon. Not. Roy. Astron. Soc.* **192** (1980) 663–667.

[341] A. Vilenkin, "Cosmological Density Fluctuations Produced by Vacuum Strings," *Phys. Rev. Lett.* **46** (1981) 1169–1172. [Erratum: Phys.Rev.Lett. 46, 1496 (1981)].

[342] N. Kaiser and A. Stebbins, "Microwave Anisotropy Due to Cosmic Strings," *Nature* **310** (1984) 391–393.

[343] A. Albrecht, D. Coulson, P. Ferreira, and J. Magueijo, "Causality and the microwave background," *Phys. Rev. Lett.* **76** (1996) 1413–1416, arXiv:astro-ph/9505030.

[344] J. Magueijo, A. Albrecht, D. Coulson, and P. Ferreira, "Doppler peaks from active perturbations," *Phys. Rev. Lett.* **76** (1996) 2617–2620, arXiv:astro-ph/9511042.

[345] U.-L. Pen, U. Seljak, and N. Turok, "Power spectra in global defect theories of cosmic structure formation," *Phys. Rev. Lett.* **79** (1997) 1611–1614, arXiv:astro-ph/9704165.

[346] R. Battye and A. Moss, "Updated constraints on the cosmic string tension," *Phys. Rev. D* **82** (2010) 023521, arXiv:1005.0479 [astro-ph.CO].

[347] T. Charnock, A. Avgoustidis, E. J. Copeland, and A. Moss, "CMB constraints on cosmic strings and superstrings," *Phys. Rev. D* **93** no. 12, (2016) 123503, arXiv:1603.01275 [astro-ph.CO].

[348] J. Lizarraga, J. Urrestilla, D. Daverio, M. Hindmarsh, and M. Kunz, "New CMB constraints for Abelian Higgs cosmic strings," *JCAP* **10** (2016) 042, arXiv:1609.03386 [astro-ph.CO].

[349] A. Lopez-Eiguren, J. Lizarraga, M. Hindmarsh, and J. Urrestilla, "Cosmic Microwave Background constraints for global strings and global monopoles," *JCAP* **07** (2017) 026, arXiv:1705.04154 [astro-ph.CO].

[350] L. Kofman and A. D. Linde, "Generation of Density Perturbations in the Inflationary Cosmology," *Nucl. Phys. B* **282** (1987) 555.

[351] E. T. Vishniac, K. A. Olive, and D. Seckel, "Cosmic Strings and Inflation," *Nucl. Phys. B* **289** (1987) 717–734.

[352] J. Yokoyama, "INFLATION CAN SAVE COSMIC STRINGS," *Phys. Rev. Lett.* **63** (1989) 712.

[353] H. M. Hodges and J. R. Primack, "Strings, texture and inflation," *Phys. Rev. D* **43** (1991) 3155–3172.

[354] A. Drew and E. P. S. Shellard, "Radiation from Global Topological Strings using Adaptive Mesh Refinement: Methodology and Massless Modes," arXiv:1910.01718 [astro-ph.CO].

[355] N. Ramberg and L. Visinelli, "The QCD Axion and Gravitational Waves in light of NANOGrav results," 12, 2020. arXiv:2012.06882 [astro-ph.CO].

[356] J. Halverson, C. Long, and P. Nath, "Ultralight axion in supersymmetry and strings and cosmology at small scales," *Phys. Rev. D* **96** no. 5, (2017) 056025, arXiv:1703.07779 [hep-ph].

[357] R. Alonso and A. Urbano, "Wormholes and masses for Goldstone bosons," *JHEP* **02** (2019) 136, arXiv:1706.07415 [hep-ph].

[358] L. E. Ibanez and F. Quevedo, "Anomalous U(1)'s and proton stability in brane models," *JHEP* **10** (1999) 001, arXiv:hep-ph/9908305.

[359] A. Khmelnitsky and V. Rubakov, "Pulsar timing signal from ultralight scalar dark matter," *JCAP* **02** (2014) 019, arXiv:1309.5888 [astro-ph.CO].

[360] V. S. Lee, A. Mitridate, T. Trickle, and K. M. Zurek, "Probing Small-Scale Power Spectra with Pulsar Timing Arrays," arXiv:2012.09857 [astro-ph.CO].

[361] C. Cutler and J. Harms, "BBO and the neutron-star-binary subtraction problem," *Phys. Rev. D* **73** (2006) 042001, arXiv:gr-qc/0511092.

[362] M. Frigo and S. G. Johnson, "The design and implementation of FFTW3," *Proceedings of the IEEE* **93** no. 2, (2005) 216–231. Special issue on "Program Generation, Optimization, and Platform Adaptation".

[363] R. Chandra, L. Dagum, D. Kohr, R. Menon, D. Maydan, and J. McDonald, *Parallel programming in OpenMP*. Morgan kaufmann, 2001.

[364] E. Gabriel, G. E. Fagg, G. Bosilca, T. Angskun, J. J. Dongarra, J. M. Squyres, V. Sahay, P. Kambadur, B. Barrett, A. Lumsdaine, R. H. Castain, D. J. Daniel, R. L. Graham, and T. S. Woodall, "Open MPI: Goals, concept, and design of a next generation MPI implementation," in *Proceedings, 11th European PVM/MPI Users' Group Meeting*, pp. 97–104. Budapest, Hungary, September, 2004.

[365] R. J. LeVeque, *Finite Difference Methods for Ordinary and Partial Differential Equations: Steady-State and Time-Dependent Problems*. Cambridge University Press, 2007.

[366] R. Courant, K. Friedrichs, and H. Lewy, "Über die partiellen Differenzengleichungen der mathematischen Physik," *Mathematische Annalen* **100** (Jan., 1928) 32–74.

[367] J. Garcia-Bellido, D. G. Figueroa, and A. Sastre, "A Gravitational Wave Background from Reheating after Hybrid Inflation," *Phys. Rev. D* **77** (2008) 043517, arXiv:0707.0839 [hep-ph].

[368] D. G. Figueroa, J. Garcia-Bellido, and A. Rajantie, "On the Transverse-Traceless Projection in Lattice Simulations of Gravitational Wave Production," *JCAP* **11** (2011) 015, arXiv:1110.0337 [astro-ph.CO].

[369] M. Dine, N. Fernandez, A. Ghalsasi, and H. H. Patel, "Comments on Axions, Domain Walls, and Cosmic Strings," arXiv:2012.13065 [hep-ph].

[370] J. F. Dufaux, A. Bergman, G. N. Felder, L. Kofman, and J.-P. Uzan, "Theory and Numerics of Gravitational Waves from Preheating after Inflation," *Phys. Rev. D* **76** (2007) 123517, arXiv:0707.0875 [astro-ph].

[371] J. B. Bauer, D. J. Marsh, R. Hloˇ zek, H. Padmanabhan, and A. Laguë, "Intensity Mapping as a Probe of Axion Dark Matter," arXiv:2003.09655 [astro-ph.CO].

[372] P. Agrawal, A. Hook, and J. Huang, "A CMB Millikan Experiment with Cosmic Axiverse Strings," arXiv:1912.02823 [astro-ph.CO].

[373] C. S. Machado, W. Ratzinger, P. Schwaller, and B. A. Stefanek, "Audible Axions," *JHEP* **01** (2019) 053, arXiv:1811.01950 [hep-ph].

[374] C. S. Machado, W. Ratzinger, P. Schwaller, and B. A. Stefanek, "Gravitational wave probes of axion-like particles," arXiv:1912.01007 [hep-ph].

[375] C.-F. Chang and Y. Cui, "Stochastic Gravitational Wave Background from Global Cosmic Strings," arXiv:1910.04781 [hep-ph].

[376] Y. Gouttenoire, G. Servant, and P. Simakachorn, "BSM with Cosmic Strings: Heavy, up to EeV mass, Unstable Particles," *JCAP* **07** (2020) 016, arXiv:1912.03245 [hep-ph].

[377] D. G. Figueroa, M. Hindmarsh, and J. Urrestilla, "Exact Scale-Invariant Background of Gravitational Waves from Cosmic Defects," *Phys. Rev. Lett.* **110** no. 10, (2013) 101302, arXiv:1212.5458 [astro-ph.CO].

[378] D. G. Figueroa, M. Hindmarsh, J. Lizarraga, and J. Urrestilla, "Irreducible background of gravitational waves from a cosmic defect network: update and comparison of numerical techniques," arXiv:2007.03337 [astro-ph.CO].

[379] M. Fairbairn, D. J. E. Marsh, J. Quevillon, and S. Rozier, "Structure formation and microlensing with axion miniclusters," *Phys. Rev. D* **97** no. 8, (2018) 083502, arXiv:1707.03310 [astro-ph.CO].

[380] B. Eggemeier, J. Redondo, K. Dolag, J. C. Niemeyer, and A. Vaquero, "First Simulations of Axion Minicluster Halos," *Phys. Rev. Lett.* **125** no. 4, (2020) 041301, arXiv:1911.09417 [astro-ph.CO].